# Design of Bi-based layered oxyhalide photocatalysts for efficient solar-to-chemical conversion

Kanta Ogawa

2022

# Table of Contents

## General Introduction

## Chapter 1

***Layered Perovskite Oxyiodide with Narrow Bandgap and Long Lifetime Carriers for Water Splitting Photocatalysis***

## Chapter 2

***Tuning of Conduction Band via Inter-layer Interaction in Layered Perovskite Oxyiodide Photocatalysts***

## Chapter 3

***Flux Synthesis of Layered Oxyhalide $Bi_4NbO_8Cl$ Photocatalyst for Efficient Z-Scheme Water Splitting Under Visible Light***

## Chapter 4

***Manipulation of charge carrier flow in $Bi_4NbO_8Cl$ nanoplate photocatalyst with metal loading***

## Chapter 5

***$CrO_x$ layer promoting electron transfer from photocatalyst to noble-metal cocatalysts for efficient charge separation and $H_2$ evolution***

## Chapter 6

***Earth-abundant iron(III) species serves as a cocatalyst boosting the multi-electron reduction of $IO_3^-/I^-$ redox shuttle in Z-scheme photocatalytic water splitting***

# *General Introduction*

# 1. Background of the work

## Solar-to-energy conversion

The sun provides the largest energy source on the earth, with more energy from sunlight striking the earth in 1 h than all of the energy consumed on the planet in an entire year.[1] Thus, considerable research efforts have been devoted to the field of solar energy capture and conversion in order to free us from the reliance on fossil fuels and reduce the carbon emission. In the past years, the remarkable development of the photovoltaic (PV) technologies enables the practical solar energy conversion into electricity.[2] Polycrystalline silicon is now widely used to make solar panels, while the metal-halide perovskite (MHP) solar cells have emerged as the next generation solar cells due to their low-cost solution fabrication process and efficient solar energy harvesting.[3–6] Other forms of the solar-to-energy conversion system are the particulate photocatalytic system[7–13] and the photoelectrocatalytic (PEC) system,[14–17] where solar energy is converted directly into a storable chemical energy form, such as $H_2$ produced via water splitting, as natural photosynthesis does (Figure 1).

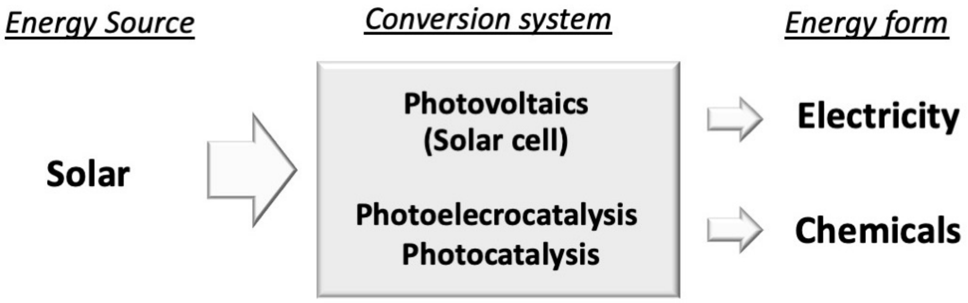

**Figure 1.** Solar-to-energy conversion systems, producing electricity or chemicals from abundant solar energy.

Although the energy form converted from solar energy depends on the system employed, the basic working principle is in common as they basically employ semiconductor materials to capture solar energy (Figure 2). Light irradiation, with energy more than the band gap of the semiconductor, generates electrons and holes excited in the conduction band (CB) and the valance band (VB), respectively. After rapid relaxation to the edges of their respective bands, these charge carriers migrate inside the semiconductor toward the interface with electrode or reactants, where the photoexcited carriers in the semiconductor is converted to electricity or chemicals. Using as much of the solar spectrum as possible and suppressing the recombination between the electrons and holes during their migration are essential for high efficiency in every solar-to-energy system.[18]

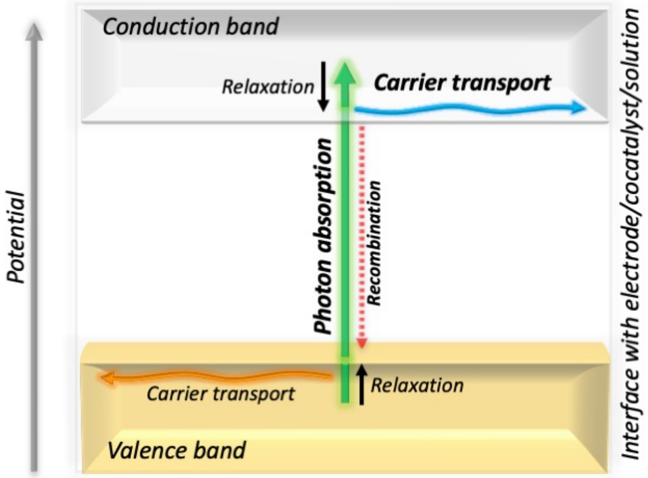

**Figure 2.** Schematic image if the solar-to-energy conversion system using semiconductor photoabsorber.

## Particulate semiconductor photocatalyst

The photocatalytic system using particulate semiconductor materials is one of the most simplest photoconversion system,[7–13,19,20] where light absorption and electron-to-chemical conversion take place on single particle. In other words, both the solar-to-electricity conversion by solar cells and the electricity-to-chemical conversion by electrochemical system are included in one particle (Figure 3). The system has attracted huge interest as the system design is simple, cheap, and easily scaled up, as demonstrated by Domen et.al., though further improvement of the solar-to-energy conversion is necessary for the practical use.[10,12,13,21,22]

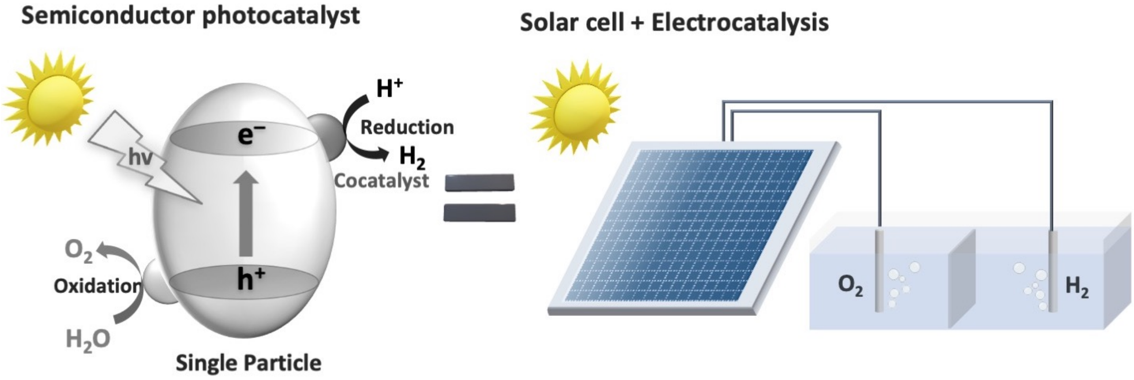

**Figure 3.** Solar-to-chemical conversion using a single particle semiconductor photocatalyst.

One of the requirements is to utilize wide range of the solar spectrum. Although photocatalytic water splitting with quantum efficiency with almost unity was achieved by using $SrTiO_3$:Al, the STH was only 0.65% under sunlight as $SrTiO_3$:Al having a wide bandgap of 3.2 eV captures only ultraviolet light.[12] As shown in Figure 4, the STH can be significantly enhanced by utilizing the visible light region in the solar spectrum.[23] Therefore, significant research efforts have been devoted to find new photocatalyst materials working under visible light.[7,20,24–39]

Not only finding new materials, design strategy is also important for efficient utilization of the charge carrier generated in the photocatalyst. The elaborated synthetic methods and the surface modification such as cocatalyst loading drastically affect the photocatalytic activity.[8,12,18,30,40–42]

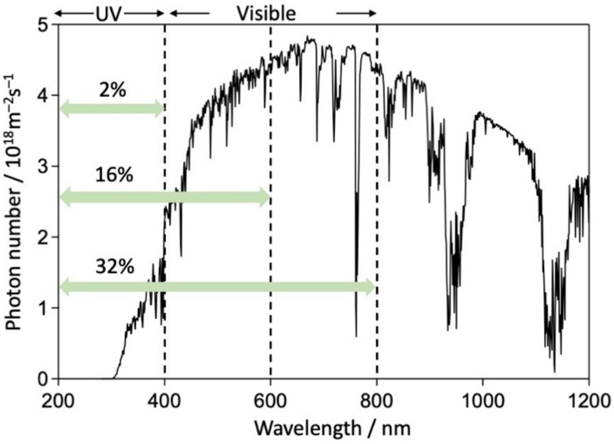

**Figure 4.** Solar spectrum and solar-to-hydrogen efficiency for photocatalytic water splitting with a quantum efficiency of 100%.

## Post transition-metal based semiconductor

Semiconductor materials containing post-transition cation with $ns^2np^0$ (i.e., Sn (II), Pb (II), Sb (III) and Bi (III)) have emerged as promising semiconductors for efficient solar-to-energy conversion system as represented by MHPs. One of the origin of the high performance in $MAPbX_3$ has been reported to be the defect tolerant nature owing to the Pb-$6s^2$ – X-$n$p (e.g., I-5p) hybridization.[43] The VBMs of the $MAPbX_3$ are composed of anti-bonding states between filled Pb-6s and filled X-$n$p orbitals.[44] Therefore, the energy-level of the $X^-$ dangling bonds produced by Pb defect is below the VBM and thus the deep hole-traps inside the band gap is hardly produced in $MAPbX_3$. In $BiVO_4$, one of the most efficient water splitting photocatalyst, the $6s^2$ – O 2p hybridization causes not only the VBM more negative than the conventional $d^0$ metal oxide such as $TiO_2$ but also the light hole effective mass.[45] Notably, the CBM of $BiVO_4$ consist of a relatively localized V-3d band, although doped Nb with a more delocalized band can reduce the electron effective mass.[46] As in the MHPs, the CB contributed by p orbitals is more desirable due to good electron conductivity derived from the low effective mass of electron provided by the spatially delocalized p orbitals as compared the localized d orbital.[47,48] From the view points of the chemistry of $ns^2np^0$ cation,[47,49] the post-transition cation (e.g., Pb (II), and Bi (III)) based semiconductors are promising candidates for efficient solar-to energy conversion.

## Sillén–Aurivillius layered oxyhalides

In recent years, bismuth (or lead)-based oxyhalides with layered structure have emerged as promising photocatalysts for dye degradation,[50,51] water splitting,[32,52,53] and $CO_2$ reduction.[54] The bismuth/lead oxide based fluorite-like layer, $[M_2O_2]$, intergrown with single, double or triple halide layer, [X], $[X_2]$, or $[M'_xX_3]$ is the common moiety in their structures. The simple intergrowth phase between the fluorite layer and the halide layer, which is so-called Sillén phase, includes BiOCl, $PbBiO_2Cl$, and $PbBi_3O_4Cl_3$ photocatalysts (Figure 5a-d).[55,56] The Sillén phases intergrow with the Aurivillius phases, of general formula $[Bi_2O_2][A_{n-1}B_nO_{3n+1}]$, producing Sillén–Aurivillius (S–A) phases, of the general formula $[A_2O_2][X_n][A_2O_2][A'_{m-1}B_mO_{3m+1}]$ (Figure 5e-h).[57] The Sillén–Aurivillius phase is represented by its simplest member $Bi_4NbO_8Cl$ (i.e, $n = 1$, $m = 1$),[58] a promising photocatalyst for visible light water splitting for clean production of hydrogen (Figure 5e).[32]

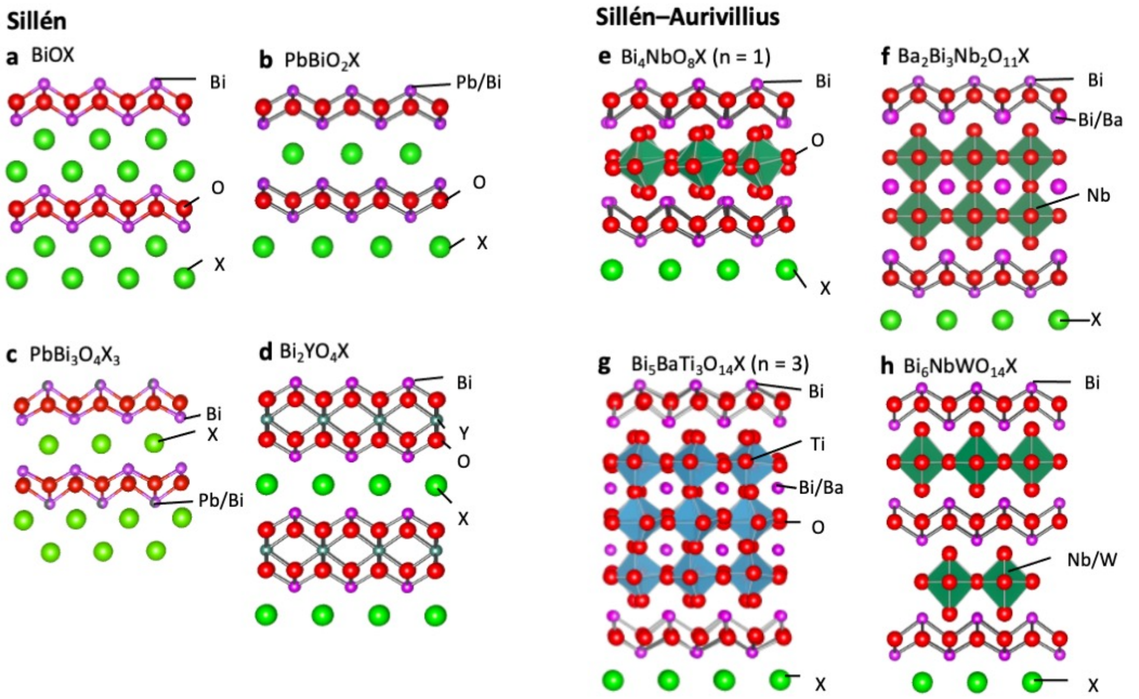

**Figure 5.** Crystal structure of Sillén and v Sillén–Aurivillius layered oxyhalides; (a) BiOX, (b)$PbBiO_2Cl$, (c)$Bi_2YO_4Cl$, (d) $PbBi_3O_4Cl_3$, (e) $Bi_4NbO_8X$ (n = 1), (f) $Bi_3Ba_2Nb_2O_{11}X$ (n = 2), (g) $Bi_5BaTi_3O_{14}X$ (n = 3) and (h) Sillén-Aurivillus-related oxyhalide $Bi_6NbWO_{14}X$.

The electronic structures of these bismuth/lead-based oxyhalides are characterized by participation by Bi(Ⅲ) or Pb ( Ⅱ ) with $6s^2p^0$ electronic configuration.[59,60] The $6s^2$ – O 2p hybridization reduces O 2p localization, resulting in their valence band maxima (VBM) located more negative than that of the conventional oxide based photocatalysts, such as $TiO_2$, $SrTiO_3$, which affords visible light responsibility to the bismuth/lead base photocatalysts (e.g., $Bi_4NbO_8Cl$,[32,59] $Bi_2YO_4Cl$,[61] $PbBiO_2Cl$[60] and $PbBi_3O_4Cl_3$[62]). Their VBMs composed of Bi/Pb-6s and O-2p not of halide (chloride) afford stability of these oxyhalides during photocatalytic reaction, while other visible-light responsible mix-oxides or non-oxide materials with the VBMs composed of non-oxide orbitals (e.g., S, Se, and N) often suffer from self-oxidation of these anions caused by the holes photoexcited in the VBM, which is so-called self-oxidation.[63,64] It is noteworthy that the

CBMs of these oxyhalides mainly consist of Bi/Pb-6p orbitals. The chemistry of $ns^2np^0$ cation suggests that the electronic structures where s and p orbital contribute to the VBM and CBM, respectively, allow the favorable optoelectronic properties for solar-to-energy conversion system,[47,49] while, in the conventional photocatalysts, more-localized anion p (O-2p, S-3p, N-2p) and cation d (Ti-3d, V-3d, Nb-4d, Ta-5d, W-5d) orbitals mainly contribute to the VBM and CBM, respectively (Figure 6).[18] The unique electronic structure owing to the $ns^2np^0$ electronic configuration provides Sillén–(Aurivillius) oxyhalides with the visible-light responsibility and the stability under light irradiation, setting them as a plausible candidate for solar-to-energy conversion.

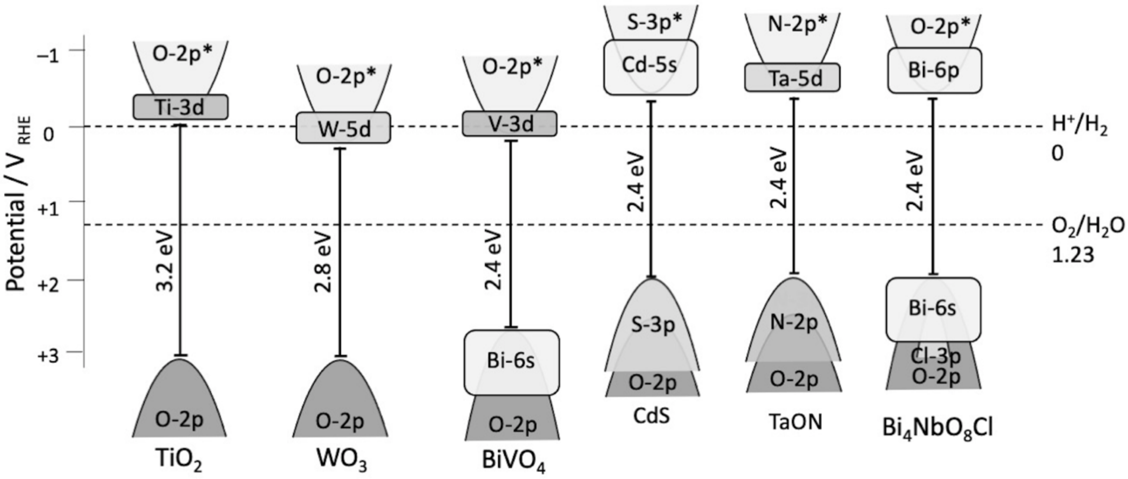

**Figure 6.** Band alignment and electronic structure of the typical semiconductor photocatalysts for water splitting.

## 2. Outline of the work

In the present thesis, the design strategies for Sillén–Aurivillius oxyhalides are developed, especially focusing on the exploitation of the wide range of visible-light and efficient utilization of the charge carrier generated in a particulate photocatalyst. The thesis consists of the following six chapters.

In Chapter 1, the author demonstrates that a Sillén–Aurivillius oxyiodide functions as water oxidation photocatalyst under visible-light. Thus far, semiconductors containing iodine have been rarely used for photocatalytic water splitting because of the facile self-oxidation of iodide under light irradiation. Herein, the introduction of iodine narrows the band gap of the Sillén–Aurivillius oxyhalide with double perovskite layer without sacrifice of the stability under light irradiation.[33] The highly polarizable iodide causes the electrostatic destabilization of O 2p orbitals in perovskite layer and successfully increases the VBM composed of O-2p band. This is in stark contrast to conventional band control where the non-oxide anion orbital (e.g., S-3p, N-2p, I-6p) with a lower electron affinity occupies the VBM, shifting VBM position negatively, but leading to self-decomposition by photo-excited carriers.[65] The iodide in the Sillén–Aurivillius oxyhalide also provides longer carrier lifetime, leading to significantly higher quantum efficiency and photocatalytic activity as compared to the Cl/Br counterparts. Chapter 1 demonstrates that the iodine introduction enables both the exploitation of the wide range of visible-light and efficient utilization of the photoexcited carrier of Sillén–Aurivillius oxyhalide.

In Chapter 2, the introduction of iodine is applied to other Sillén–Aurivillius oxyhalides and three novel oxyiodides are successfully synthesized. In contrast to the case with n = 2 in Chapter 1, their CBMs, as well as VBMs, are negatively shifted as compared to the chloride counterparts. The origin of the CBM shift by iodine introduction is discussed based on the interlayer Bi-Bi interaction and revised lone pair (RLP) model.[47] The novel oxyiodides function as visible light water oxidation photocatalyst, showing much higher $O_2$ evolution activities than their chloride counterparts. Chapter 2 offers a strategy for shifting CBM negatively without sacrifice of visible light absorbability and photocatalytic activity of Sillén–Aurivillius oxyhalides.

In Chapter 3, the flux synthetic method, using molten salts, of $Bi_4NbO_8Cl$ particles is developed.[66] The obtained particles with nanoplate morphology are featured by a larger surface and higher crystal quality than those prepared via the conventional solid-state reaction. The flux synthesis much improves the photoconductivity and thus the photocatalytic activity of $Bi_4NbO_8Cl$. Chapter 3 demonstrates that the elaborated synthesis enables the efficient utilization of the photoexcited carriers in the oxyhalide.

In Chapter 4, the carrier dynamics in the $Bi_4NbO_8Cl$ nanoplate is unveiled and successfully modified for efficient charge separation in a particle. In the pristine $Bi_4NbO_8Cl$, the parallel flow of the electrons and holes ends in the recombination at the edge of the nanoplate. Depositing Rh cocatalyst at the edges of nanoplates manipulates the carrier flow of layered $Bi_4NbO_8Cl$; the intrinsic but undesirable parallel carrier flow is changed into the orthogonal one, resulting in spatial charge separation and a significant enhancement of the photocatalytic activity. Chapter 4 shows the carrier flow inside a $Bi_4NbO_8Cl$ nanoplate can be modified via cocatalyst deposition for efficient charge separation.

In Chapter 5, the charge transfer at the interface of $Bi_4NbO_8Cl$ and Rh cocatalyst is further improved. The chromium oxide lying between $Bi_4NbO_8Cl$ and Rh acts as an electron transport layer, enhancing the selectivity of electron transfer from the CB of the photocatalyst to cocatalyst by suppressing the undesirable hole transfer, which results in the improved photocatalytic activity. Chapter 5 introduces the electron transport layer as employed in the field of solar cells to the particulate photocatalyst system for efficient utilization of the photoexcited carrier.

In Chapter 6, not only the chromium oxide shown in Chapter 5, earth abundant iron oxide can be applied to facilitate the charge separation in an oxychloride.[67] The iron oxide loaded on the oxychloride photocatalyst selectively captures photoexcited electrons in the CBM, enhancing the charge separation in the photocatalyst. In addition, the iron oxide catalyzes the multi-electron reduction of $IO_3^-$ on the surface of the oxychloride. Chapter 6, in combination with Chapter 5, shows transition metal oxide loaded on the Sillén–Aurivillius oxyhalides facilitates the charge separation in the photocatalyst by selectively capturing one of the photoexcited carriers.

These strategies developed thorough the present thesis for broadening the absorption range of visible-light (Chapter 1, 2) and efficient utilization of the photoexcited carrier of Sillén–Aurivillius oxyhalide (Chapter 3-6) paving the way of the future of the Sillén–Aurivillius photocatalysts.

# References

(1) Lewis, N. S. Introduction: Solar Energy Conversion. *Chem. Rev.* **2015**, *115*, 12631–12632.

(2) Nayak, P. K.; Mahesh, S.; Snaith, H. J.; Cahen, D. Photovoltaic Solar Cell Technologies: Analysing the State of the Art. *Nat Rev Mater* **2019**, *4*, 269–285.

(3) Kojima, A.; Teshima, K.; Shirai, Y.; Miyasaka, T. Organometal Halide Perovskites as Visible-Light Sensitizers for Photovoltaic Cells. *J. Am. Chem. Soc.* **2009**, *131*, 6050–6051.

(4) Lee, M. M.; Teuscher, J.; Miyasaka, T.; Murakami, T. N.; Snaith, H. J. Efficient Hybrid Solar Cells Based on Meso-Superstructured Organometal Halide Perovskites. *Science* **2012**, *338*, 643–647.

(5) Yan, J.; Saunders, B. R. Third-Generation Solar Cells: A Review and Comparison of Polymer:Fullerene, Hybrid Polymer and Perovskite Solar Cells. *RSC Adv.* **2014**, *4*, 43286–43314.

(6) Kim, J. Y.; Lee, J.-W.; Jung, H. S.; Shin, H.; Park, N.-G. High-Efficiency Perovskite Solar Cells. *Chem. Rev.* **2020**, *120*, 7867–7918.

(7) Kudo, A.; Miseki, Y. Heterogeneous Photocatalyst Materials for Water Splitting. *Chem. Soc. Rev.* **2009**, *38*, 253–278.

(8) Maeda, K.; Domen, K. Development of Novel Photocatalyst and Cocatalyst Materials for Water Splitting under Visible Light. *BCSJ* **2016**, *89*, 627–648.

(9) Chen, S.; Takata, T.; Domen, K. Particulate Photocatalysts for Overall Water Splitting. *Nat Rev Mater* **2017**, *2*, 17050.

(10) Wang, Q.; Domen, K. Particulate Photocatalysts for Light-Driven Water Splitting: Mechanisms, Challenges, and Design Strategies. *Chem. Rev.* **2020**, *120*, 919−985.

(11) Wang, Z.; Li, C.; Domen, K. Recent Developments in Heterogeneous Photocatalysts for Solar-Driven Overall Water Splitting. *Chem. Soc. Rev.* **2019**, *48*, 2109–2125.

(12) Takata, T.; Jiang, J.; Sakata, Y.; Nakabayashi, M.; Shibata, N.; Nandal, V.; Seki, K.; Hisatomi, T.; Domen, K. Photocatalytic Water Splitting with a Quantum Efficiency of Almost Unity. *Nature* **2020**, *581*, 411–414.

(13) Nishiyama, H.; Yamada, T.; Nakabayashi, M.; Maehara, Y.; Yamaguchi, M.; Kuromiya, Y.; Nagatsuma, Y.; Tokudome, H.; Akiyama, S.; Watanabe, T.; Narushima, R.; Okunaka, S.; Shibata, N.; Takata, T.; Hisatomi, T.; Domen, K. Photocatalytic Solar Hydrogen Production from Water on a 100-m$^2$ Scale. *Nature* **2021**, *598*, 304–307.

(14) Moniz, S. J. A.; Shevlin, S. A.; Martin, D. J.; Guo, Z.-X.; Tang, J. Visible-Light Driven Heterojunction Photocatalysts for Water Splitting – a Critical Review. *Energy Environ. Sci.* **2015**, *8*, 731–759.

(15) Jiang, C.; Moniz, S. J. A.; Wang, A.; Zhang, T.; Tang, J. Photoelectrochemical Devices

for Solar Water Splitting – Materials and Challenges. *Chem. Soc. Rev.* **2017**, *46*, 4645–4660.

(16) Gong, J.; Li, C.; Wasielewski, M. R. Advances in Solar Energy Conversion. *Chem. Soc. Rev.* **2019**, *48*, 1862–1864.

(17) Yang, W.; Prabhakar, R. R.; Tan, J.; Tilley, S. D.; Moon, J. Strategies for Enhancing the Photocurrent, Photovoltage, and Stability of Photoelectrodes for Photoelectrochemical Water Splitting. *Chem. Soc. Rev.* **2019**, *48*, 4979–5015.

(18) Takanabe, K. Photocatalytic Water Splitting: Quantitative Approaches toward Photocatalyst by Design. *ACS Catal.* **2017**, *7*, 8006–8022.

(19) Abe, R. Recent Progress on Photocatalytic and Photoelectrochemical Water Splitting under Visible Light Irradiation. *Journal of Photochemistry and Photobiology C: Photochemistry Reviews* **2010**, *11*, 179–209.

(20) Wang, Y.; Suzuki, H.; Xie, J.; Tomita, O.; Martin, D. J.; Higashi, M.; Kong, D.; Abe, R.; Tang, J. Mimicking Natural Photosynthesis: Solar to Renewable $H_2$ Fuel Synthesis by Z-Scheme Water Splitting Systems. *Chem. Rev.* **2018**, *118*, 5201–5241.

(21) Wang, Q.; Hisatomi, T.; Jia, Q.; Tokudome, H.; Zhong, M.; Wang, C.; Pan, Z.; Takata, T.; Nakabayashi, M.; Shibata, N.; Li, Y.; Sharp, I. D.; Kudo, A.; Yamada, T.; Domen, K. Scalable Water Splitting on Particulate Photocatalyst Sheets with a Solar-to-Hydrogen Energy Conversion Efficiency Exceeding 1%. *Nature Mater* **2016**, *15*, 611–615.

(22) Wang, Q.; Warnan, J.; Rodríguez-Jiménez, S.; Leung, J. J.; Kalathil, S.; Andrei, V.; Domen, K.; Reisner, E. Molecularly Engineered Photocatalyst Sheet for Scalable Solar Formate Production from Carbon Dioxide and Water. *Nat Energy* **2020**, *5*, 703–710.

(23) Abe, R. Development of a New System for Photocatalytic Water Splitting into $H_2$ and $O_2$ under Visible Light Irradiation. *BCSJ* **2011**, *84*, 1000–1030.

(24) Maeda, K.; Teramura, K.; Lu, D.; Takata, T.; Saito, N.; Inoue, Y.; Domen, K. Photocatalyst Releasing Hydrogen from Water. *Nature* **2006**, *440*, 295–295.

(25) Osterloh, F. E. Inorganic Materials as Catalysts for Photochemical Splitting of Water. *Chem. Mater.* **2008**, *20*, 35–54.

(26) Wang, X.; Maeda, K.; Thomas, A.; Takanabe, K.; Xin, G.; Carlsson, J. M.; Domen, K.; Antonietti, M. A Metal-Free Polymeric Photocatalyst for Hydrogen Production from Water under Visible Light. *Nature Mater* **2009**, *8*, 76–80.

(27) Horiuchi, Y.; Toyao, T.; Saito, M.; Mochizuki, K.; Iwata, M.; Higashimura, H.; Anpo, M.; Matsuoka, M. Visible-Light-Promoted Photocatalytic Hydrogen Production by Using an Amino-Functionalized Ti(IV) Metal–Organic Framework. *J. Phys. Chem. C* **2012**, *116*, 20848–20853.

(28) Fu, Y.; Sun, D.; Chen, Y.; Huang, R.; Ding, Z.; Fu, X.; Li, Z. An Amine-Functionalized Titanium Metal-Organic Framework Photocatalyst with Visible-Light-Induced Activity for $CO_2$

Reduction. *Angew. Chem. Int. Ed.* **2012**, *51*, 3364–3367.

(29) Fu, C.-F.; Wu, X.; Yang, J. Material Design for Photocatalytic Water Splitting from a Theoretical Perspective. *Adv. Mater.* **2018**, *30*, 1802106.

(30) Wang, Z.; Inoue, Y.; Hisatomi, T.; Ishikawa, R.; Wang, Q.; Takata, T.; Chen, S.; Shibata, N.; Ikuhara, Y.; Domen, K. Overall Water Splitting by $Ta_3N_5$ Nanorod Single Crystals Grown on the Edges of $KTaO_3$ Particles. *Nat Catal* **2018**, *1*, 756–763.

(31) Wang, Q.; Nakabayashi, M.; Hisatomi, T.; Sun, S.; Akiyama, S.; Wang, Z.; Pan, Z.; Xiao, X.; Watanabe, T.; Yamada, T.; Shibata, N.; Takata, T.; Domen, K. Oxysulfide Photocatalyst for Visible-Light-Driven Overall Water Splitting. *Nat. Mater.* **2019**, *18*, 827–832.

(32) Fujito, H.; Kunioku, H.; Kato, D.; Suzuki, H.; Higashi, M.; Kageyama, H.; Abe, R. Layered Perovskite Oxychloride $Bi_4NbO_8Cl$: A Stable Visible Light Responsive Photocatalyst for Water Splitting. *J. Am. Chem. Soc.* **2016**, *138*, 2082–2085.

(33) Ogawa, K.; Suzuki, H.; Zhong, C.; Sakamoto, R.; Tomita, O.; Saeki, A.; Kageyama, H.; Abe, R. Layered Perovskite Oxyiodide with Narrow Band Gap and Long Lifetime Carriers for Water Splitting Photocatalysis. *J. Am. Chem. Soc.* **2021**, *143*, 8446–8453.

(34) Zhao, Y.; Zhang, S.; Shi, R.; Waterhouse, G. I. N.; Tang, J.; Zhang, T. Two-Dimensional Photocatalyst Design: A Critical Review of Recent Experimental and Computational Advances. *Materials Today* **2020**, *34*, 78–91.

(35) Ghosh, S.; Nakada, A.; Springer, M. A.; Kawaguchi, T.; Suzuki, K.; Kaji, H.; Baburin, I.; Kuc, A.; Heine, T.; Suzuki, H.; Abe, R.; Seki, S. Identification of Prime Factors to Maximize the Photocatalytic Hydrogen Evolution of Covalent Organic Frameworks. *J. Am. Chem. Soc.* **2020**, *142*, 9752−9762.

(36) Wang, Q.; Gao, Q.; Al-Enizi, A. M.; Nafady, A.; Ma, S. Recent Advances in MOF-Based Photocatalysis: Environmental Remediation under Visible Light. *Inorg. Chem. Front.* **2020**, *7*, 300–339.

(37) Song, X.; Wei, G.; Sun, J.; Peng, C.; Yin, J.; Zhang, X.; Jiang, Y.; Fei, H. Overall Photocatalytic Water Splitting by an Organolead Iodide Crystalline Material. *Nat Catal* **2020**, *3*, 1027–1033.

(38) Wang, H.; Wang, H.; Wang, Z.; Tang, L.; Zeng, G.; Xu, P.; Chen, M.; Xiong, T.; Zhou, C.; Li, X.; Huang, D.; Zhu, Y.; Wang, Z.; Tang, J. Covalent Organic Framework Photocatalysts: Structures and Applications. *Chem. Soc. Rev.* **2020**, *49*, 4135–4165.

(39) Bai, Y.; Wilbraham, L.; Slater, B. J.; Zwijnenburg, M. A.; Sprick, R. S.; Cooper, A. I. Accelerated Discovery of Organic Polymer Photocatalysts for Hydrogen Evolution from Water through the Integration of Experiment and Theory. *J. Am. Chem. Soc.* **2019**, *141*, 9063–9071.

(40) Fajrina, N.; Tahir, M. A Critical Review in Strategies to Improve Photocatalytic Water Splitting towards Hydrogen Production. *International Journal of Hydrogen Energy* **2019**, *44*,

540–577.

(41) Ham, Y.; Hisatomi, T.; Goto, Y.; Moriya, Y.; Sakata, Y.; Yamakata, A.; Kubota, J.; Domen, K. Flux-Mediated Doping of $SrTiO_3$ Photocatalysts for Efficient Overall Water Splitting. *J. Mater. Chem. A* **2016**, *4*, 3027–3033.

(42) Wang, Z.; Luo, Y.; Hisatomi, T.; Vequizo, J. J. M.; Suzuki, S.; Chen, S.; Nakabayashi, M.; Lin, L.; Pan, Z.; Kariya, N.; Yamakata, A.; Shibata, N.; Takata, T.; Teshima, K.; Domen, K. Sequential Cocatalyst Decoration on $BaTaO_2N$ towards Highly-Active Z-Scheme Water Splitting. *Nat Commun* **2021**, *12*, 1005.

(43) Brandt, R. E.; Stevanović, V.; Ginley, D. S.; Buonassisi, T. Identifying Defect-Tolerant Semiconductors with High Minority-Carrier Lifetimes: Beyond Hybrid Lead Halide Perovskites. *MRS Communications* **2015**, *5*, 265–275.

(44) Kang, J.; Wang, L.-W. High Defect Tolerance in Lead Halide Perovskite $CsPbBr_3$. *J. Phys. Chem. Lett.* **2017**, *8*, 489–493.

(45) Walsh, A.; Yan, Y.; Huda, M. N.; Al-Jassim, M. M.; Wei, S.-H. Band Edge Electronic Structure of $BiVO_4$: Elucidating the Role of the Bi s and V d Orbitals. *Chem. Mater.* **2009**, *21*, 547–551.

(46) Sarker, H. P.; Rao, P. M.; Huda, M. N. Niobium Doping in $BiVO_4$ : Interplay Between Effective Mass, Stability, and Pressure. *ChemPhysChem* **2019**, *20*, 773–784.

(47) Walsh, A.; Payne, D. J.; Egdell, R. G.; Watson, G. W. Stereochemistry of Post-Transition Metal Oxides: Revision of the Classical Lone Pair Model. *Chem. Soc. Rev.* **2011**, *40*, 4455.

(48) Du, M. H. Efficient Carrier Transport in Halide Perovskites: Theoretical Perspectives. *J. Mater. Chem. A* **2014**, *2*, 9091–9098.

(49) Bainglass, E.; Walsh, A.; Huda, M. N. $BiSbWO_6$: Properties of a Mixed 5s/6s Lone-Pair-Electron System. *Chemical Physics* **2021**, *544*, 111117.

(50) Lin, X.; Huang, T.; Huang, F.; Wang, W.; Shi, J. Photocatalytic Activity of a Bi-Based Oxychloride $Bi_4NbO_8Cl$. *J. Mater. Chem.* **2007**, *17*, 2145.

(51) Wei, X.; Akbar, M. U.; Raza, A.; Li, G. A Review on Bismuth Oxyhalide Based Materials for Photocatalysis. *Nanoscale Adv.* **2021**, *3*, 3353–3372.

(52) Nakada, A.; Higashi, M.; Kimura, T.; Suzuki, H.; Kato, D.; Okajima, H.; Yamamoto, T.; Saeki, A.; Kageyama, H.; Abe, R. Band Engineering of Double-Layered Sillén–Aurivillius Perovskite Oxychlorides for Visible-Light-Driven Water Splitting. *Chem. Mater.* **2019**, *31*, 3419–3429.

(53) Ozaki, D.; Suzuki, H.; Ogawa, K.; Sakamoto, R.; Inaguma, Y.; Nakashima, K.; Tomita, O.; Kageyama, H.; Abe, R. Synthesis, Band Structure and Photocatalytic Properties of Sillén–Aurivillius Oxychlorides $BaBi_5Ti_3O_{14}Cl$, $Ba_2Bi_5Ti_4O_{17}Cl$ and $Ba_3Bi_5Ti_5O_{20}Cl$ with Triple-,

Quadruple- and Quintuple-Perovskite Layers. *J. Mater. Chem. A* **2021**, *9*, 8332–8340.

(54) Shi, Y.; Li, J.; Mao, C.; Liu, S.; Wang, X.; Liu, X.; Zhao, S.; Liu, X.; Huang, Y.; Zhang, L. Van Der Waals Gap-Rich BiOCl Atomic Layers Realizing Efficient, Pure-Water $CO_2$-to-CO Photocatalysis. *Nat Commun* **2021**, *12*, 5923.

(55) Sillén, L. G. Uber eine Familie yon Oxyhalogeniden. *Die Naturwissenschaften 30*, 318–324.

(56) Dolgikh, V. A.; Kholodkovskaya, L. N. The Crystal Chemistry of Metal Oxide Halides and Oxides Chalcogenides. *Russ. J. Inorg. Chem* **1992**, *37*, 488.

(57) Aurivillius, B. Intergrowth Compounds between Members of Te Bismuth Titanate Family and Structures of the $LiBi_2O_4Cl_2$ Type - an Architectural Approach. *Chem. Scr.* **1984**, *23*, 143.

(58) Kusainova, A. M.; Stefanovich, S. Yu.; Dolgikh, V. A.; Mosunov, A. V.; Hervoches, C. H.; Lightfoot, P. Dielectric Properties and Structure of $Bi_4NbO_8Cl$ and $Bi_4TaO_8Cl$. *J. Mater. Chem.* **2001**, *11*, 1141–1145.

(59) Kunioku, H.; Higashi, M.; Tomita, O.; Yabuuchi, M.; Kato, D.; Fujito, H.; Kageyama, H.; Abe, R. Strong Hybridization between Bi-6s and O-2p Orbitals in Sillén–Aurivillius Perovskite $Bi_4MO_8X$ (M = Nb, Ta; X = Cl, Br), Visible Light Photocatalysts Enabling Stable Water Oxidation. *J. Mater. Chem. A* **2018**, *6*, 3100–3107.

(60) Suzuki, H.; Kunioku, H.; Higashi, M.; Tomita, O.; Kato, D.; Kageyama, H.; Abe, R. Lead Bismuth Oxyhalides $PbBiO_2X$ (X = Cl, Br) as Visible-Light-Responsive Photocatalysts for Water Oxidation: Role of Lone-Pair Electrons in Valence Band Engineering. *Chem. Mater.* **2018**, *30*, 5862–5869.

(61) Nakada, A. Conduction Band Control of Oxyhalides with a Triple-Fluorite Layer for Visible Light Photocatalysis. *Journal of the American Chemical Society* 9.

(62) Suzuki, H.; Higashi, M.; Tomita, O.; Ishii, Y.; Yamamoto, T.; Kato, D.; Kotani, T.; Ozaki, D.; Nozawa, S.; Nakashima, K.; Fujita, K.; Saeki, A.; Kageyama, H.; Abe, R. $PbBi_3O_4X_3$ (X = Cl, Br) with Single/Double Halogen Layers as a Photocatalyst for Visible-Light-Driven Water Splitting: Impact of a Halogen Layer on the Band Structure and Stability. *Chem. Mater.* **2021**, acs.chemmater.1c02876.

(63) Buehler, N.; Meier, K.; Reber, J. F. Photochemical Hydrogen Production with Cadmium Sulfide Suspensions. *J. Phys. Chem.* **1984**, *88*, 3261–3268.

(64) Kasahara, A.; Nukumizu, K.; Hitoki, G.; Takata, T.; Kondo, J. N.; Hara, M.; Kobayashi, H.; Domen, K. Photoreactions on $LaTiO_2N$ under Visible Light Irradiation. *J. Phys. Chem. A,* **2002**, *106*, 6750–6753.

(65) Kunioku, H.; Higashi, M.; Abe, R. Low-Temperature Synthesis of Bismuth Chalcohalides: Candidate Photovoltaic Materialswith Easily, Continuously Controllable Band

Gap. *Sci Rep* **2016**, *6*, 32664.

(66) Ogawa, K.; Nakada, A.; Suzuki, H.; Tomita, O.; Higashi, M.; Saeki, A.; Kageyama, H.; Abe, R. Flux Synthesis of Layered Oxyhalide $Bi_4NbO_8Cl$ Photocatalyst for Efficient *Z* -Scheme Water Splitting under Visible Light. *ACS Appl. Mater. Interfaces* **2019**, *11*, 5642–5650.

(67) Murofushi, K.; Ogawa, K.; Suzuki, H.; Sakamoto, R.; Tomita, O.; Kato, K.; Yamakata, A.; Saeki, A.; Abe, R. Earth-Abundant Iron(III) Species Serves as a Cocatalyst Boosting the Multielectron Reduction of $IO_3^-/I^-$ Redox Shuttle in Z-Scheme Photocatalytic Water Splitting. *J. Mater. Chem. A* **2021**, *9*, 11718–11725.

# *Chapter 1*

## *Layered Perovskite Oxyiodide with Narrow Bandgap and Long Lifetime Carriers for Water Splitting Photocatalysis*

## 1.1. Introduction

Iodine (I) is a key element for realizing various functionalities, such as high ionic conductivity and efficient photoelectric conversion.[1–4] These properties frequently result from the "soft" characteristics of iodide ion ($I^-$) arising from low electronegativity and high polarizability. The low electronegativity causes iodine-based semiconductors to exhibit band gaps much narrower than their chloride or bromide counterparts, as seen in metal halide perovskites (MHPs), including $CH_3NH_3PbI_3$ ($MAPbI_3$), $HC(NH_2)_2PbI_3$($FAPbI_3$), and $CsPbI_3$. These materials are promising photo-absorbers for next-generation solar cells.[5,6] In these materials, the high polarizability of the Pb–I sublattice contributes to protecting the carriers from scattering by charged defects and optical phonons, thereby increasing the carrier lifetimes.[2,6,7] Furthermore, smaller elastic moduli and lower thermal conductivities[8] induce a strong phonon bottleneck effect, which allows a long-lived hot carrier population for photovoltaic energy conversion.[9]

Despite such interesting features of iodine-based semiconductors, they have been rarely used for photocatalytic water splitting (involving oxygen ($O_2$) evolution).[10–12] This is because of the facile self-oxidation of iodide compared to water oxidation.[10] The valance band maximum (VBM) is shifted upward due to the dominant contribution of the high-energy I 5p band, thereby reducing the band gap. However, the iodide ions are preferentially oxidized by photo-generated holes, which decomposes the photocatalyst itself and deactivates water oxidation.[10] This problem, i.e., the tradeoff between a narrow band gap and photostability, is common to other photocatalysts with low-electronegativity anions (e.g., $S^{2-}$, $N^{3-}$, $Cl^-$, $Br^-$).[13–15]

Sillén–(Aurivillius) oxychlorides and oxybromides (e.g., $Bi_4NbO_8X$,[16] $PbBiO_2X$[10]) offer an effective strategy to overcome this tradeoff problem, serving as stable visible-light water oxidation photocatalysts. Here, the VBM is dominated by an elevated O 2p band (vs. halogen (Cl or Br) bands), which is robust against self-oxidation by holes and achieves photostability, along with ensuring suitable band levels.[16] The unique valence band structure, or the elevated O 2p band is interpreted in terms of Pb/Bi 6s electrons (revised lone pair (RLP) model)[17,15] and Madelung site potential (MP) of oxygen.[18] Their VBMs (typically 2.4 V vs. RHE) are more favorable than those of conventional oxides (3.0 V vs. RHE), but still higher than the requirement for water oxidation (1.23 V vs.

RHE). Some iodine-containing Sillen-based compounds, e.g., $PbBiO_2I$,[13] have higher VBM due to the I 5p band, which causes, as mentioned above, a self-oxidative deactivation by photogenerated holes.

In the present study, we demonstrate that a Sillén–Aurivillius oxyiodide, $Bi_3Ba_2Nb_2O_{11}I$, has an unusually high-energy O 2p band that surpasses the I 5p band level, thus avoiding photoinstability and achieving more efficient water oxidation activity. The unexpected O-2p band location is rationalized by incorporating the high polarizability of iodide in the MP analysis, thus providing a new pathway to design narrow-band gap photocatalysts with intrinsic high stability. The high polarizability of iodide in $Bi_3Ba_2Nb_2O_{11}I$ affect the carrier dynamics – it leads to longer carrier lifetime than the chloride and bromide-based counterparts. Furthermore, visible light-driven Z-scheme water splitting was realized for the first time in an iodine-based system using $Bi_3Ba_2Nb_2O_{11}I$ as an oxygen-evolution photocatalyst.

## 1.2. Experimental

### Synthesis.

All the oxyhalides were prepared by solid-state reactions. In the case of $Bi_3Ba_2Nb_2O_{11}X$ (X = Cl, Br, I), the Sillén-type $BaBiO_2X$ and Aurivillius-type $Bi_3BaNb_2O_9$ were mixed in 1.05 : 1 composition, heated in air (X = Cl, Br) an evacuated silica tube (X = I, and Cl for a certain case) at 800 °C for 20 h.[19] $BaBiO_2X$ precursors were prepared by calcining a stoichiometric mixture of $BaCO_3$ (FUJIFILM Wako Pure Chemical Corporation) and BiOX in air (X = Cl, Br) an evacuated silica tube (X = I) at 800 °C for 20 h. BiOCl was purchased from FUJIFILM Wako Pure Chemical Corporation, while BiOBr and BiOI were synthesized by a soft liquid deposition method;[20] 5 mmol of $Bi(NO_3)_3{\cdot}5H_2O$ (FUJIFILM Wako Pure Chemical Corporation) was dispersed in 30 mL of ethanol and mixed with the solution of 5 mmol of KX (X = Br or I) (FUJIFILM Wako Pure Chemical Corporation) dissolved in 10 mL of pure water. After 5 h stirring at room temperature, the precipitate was collected by centrifugation, washed several times with water and ethanol, and finally dried in air at 60 °C. $Bi_3BaNb_2O_9$ was prepared by calcinating the mixture of $Bi_2O_3$ (FUJIFILM Wako Pure Chemical Corporation), $BaCO_3$ and $Nb_2O_5$ (FUJIFILM Wako Pure Chemical Corporation) at 1000 °C for 24 h.[21]

$SrTiO_3$:Rh[22] was prepared by solid-state reaction. A mixture of $TiO_2$, $SrCO_3$ and $Rh_2O_3$ (Ti : Sr : Rh = 1 : 1.07 : 0.01) was calcined in air at 800 °C for 1 h and subsequently at 1000 °C for 10 h. A Ru-based cocatalyst (0.7 wt% calculated as metal) was loaded onto $SrTiO_3$:Rh by photo-deposition using $RuCl_3\cdot nH_2O$ (FUJIFILM Wako Pure Chemical Corporation) as a precursor.[23]

### Characterization.

Powder XRD (MiniFlex II, Rigaku, X-ray source: Cu Kα), UV−visible diffuse reflectance spectroscopy (V-650, JASCO), SEM-EDX (NVision 40, Carl Zeiss-SIINT) were used for characterization of samples. SXRD patterns were collected at the BL02B2 in SPring-8, Japan ($\lambda$ = 0.41943 Å) and were analyzed by the Rietveld method using the RIETAN-FP program.[24] The energy levels of each anion in the oxy-halides were determined by the sum of electron affinities and Madelung site potential calculated using VESTA.[25]

### Mott–Schottky Measurement.

The sample was mixed with a small amount of water, then the obtained paste was coated on a fluorine-doped tin oxide (FTO) conductive substrate via a squeezing method and dried in air at 60 °C. The Mott−Schottky plots were recorded on an electrochemical analyzer (PARSTAT2263, Princeton Applied Research). Electrochemical measurements were performed in a three-electrode cell using a Pt wire counter-electrode, a Ag/AgCl reference electrode, and a phosphate-buffered solution (0.1 M, pH = 2.5–8.0) with 10 mV amplitude and a frequency of 1 kHz. The flat-band potentials are assumed to be CBMs due to the n-type nature of the samples.

### Time-Resolved Microwave Conductivity (TRMC) Measurement.

The X-band microwave (~9.1 GHz) was as the probe. The third harmonic generation (THG; 355 nm) of a Nd:YAG laser (Continuum Inc., Surelite II, 5−8 ns pulse duration, 10 Hz) or visible light (440–600 nm) from an optical parametric oscillator (Continuum Inc., Panther) seeded by a Nd:YAG laser were used as the and excitation. The THG ($4.6 \times 10^{15}$ photons $cm^{-2}$ $pulse^{-1}$) was used unless otherwise note. The powdered samples were fixed to quartz substrates using optically clear adhesive tape (the tape does not interfere with any TRMC signal). The photoconductivity $\Delta\sigma$ was calculated by the following formula: $\Delta\sigma = \Delta P_r/(AP_r)$, where $\Delta P_r$, $A$, and $P_r$ are the transient power change of microwave reflected, the sensitivity factor, and the power of microwave reflected, respectively. The obtained $\Delta\sigma$ values were then converted to the product of the quantum yield ($\varphi$) and the sum of the charge carrier mobilities ($\sum\mu = \mu_+ + \mu_-$) by the following formula: $\varphi\sum\mu = \Delta\sigma(eI_0F_{\mathrm{light}})^{-1}$, in which $e$ and $F_{\mathrm{light}}$ are the unit charge of a single electron and a correction (or filling) factor, respectively. All of the TRMC measurements were performed in ambient atmosphere at room temperature (25 °C). Fitting of TRMC transients was conducted using a stretched exponential function, α exp(–(kt) β), where α, k, and β are the coefficient, the rate constant, and the power factor of the exponent, respectively. The β was fixed at 0.20 to secure the consistency in the comparison of the decays. The lifetime (τ) is defined by the inverse of k (τ = 1/k).

**Density Functional Theory Calculation.**

The band structure calculation of the oxyhalides was performed within the framework of density functional theory (DFT) using plane-wave pseudopotential method as implemented in the Cambridge Serial Total Energy Package (CASTEP) code of BIOVIA's Material Studio 2020.[26] The interaction between the ionic core and valence electrons is treated with the OTFG ultra-soft pseudopotential with the scalar relativistic Kolling-Harmon approximation. The Perdew-Burke-Ernzerhof (PBE) function of generalized gradient apporoximation (GGA) was employed as exchange-correlation functional. An energy cut off and the Monkhorst-Pack k-point mesh of a plane wave 700 eV and 6×6×2, respectively. The minimization algorithm of Broyden–Fletcher–Goldfarb–Shanno (BFGS) was employed for geometry optimizations with total energy convergence tolerance $10^{-6}$ eV per atom. Other convergence parameters were as follows: self-consistent field tolerance $1 \times 10^{-5}$ eV per atom, maximum stress 0.05 GPa, and maximum ionic displacement $1 \times 10^{-3}$ Å.

Effective mass $m^*$ was calculated according to the obtained band structure. $m^*$ is defined by the following equation:

$$\frac{m_0}{m^*} = \frac{m_0}{\hbar^2}\frac{d^2\varepsilon}{dk^2}$$

where $m_0$ is the free electron mass, $k$ is the reciprocal lattice vector in the direction of interest, and $d^2\varepsilon/dk^2$ is the curvature of band at a maximum or a minimum, respectively. Assuming the band around their minima/maxima to be parabolic, we estimate the curvature of the band using the finite differences approximation:

$$\frac{d^2\varepsilon}{dk^2} \approx \frac{2[\varepsilon(k + \Delta k) - \varepsilon(k)]}{\Delta k^2}$$

**Photocatalytic Reaction.**

The photocatalytic reactions were performed in a gas closed-circulation system. Photocatalyst powders (0.1 g) were dispersed in an aqueous $AgNO_3$ solution (8 mM, 100 mL) in a Pyrex top-window cell. The photocatalysts were irradiated with visible light ($\lambda$ > 400 nm) through a cutoff filter (HOYA; L42) from a 300-W Xe-arc lamp (PerkinElmer; Cermax- PE300BF). The quantity of the evolved gases was determined using an online gas chromatograph (thermal conductivity detector; molecular sieve 5 Å column packing; Ar carrier gas). The apparent quantum efficiency (AQE) was evaluated using a 405 nm monochromatic LED light source (ASAHI SPECTRA, CL-1501).

For hydrogen evolution reaction, Rh co-catalyst was loaded on $Bi_3Ba_2Nb_2O_{11}X$ particles by photoreduction method using $Rh(NO_3)_3$ as metal sources. $Bi_3Ba_2Nb_2O_{11}X$ powder (0.2 g) and metal precursors (1 wt%) were mixed in 20 vol% MeOH aqueous solution. For photocatalytic reaction, photocatalyst powder (0.1 g) was dispersed in an aqueous methanol solution (20 vol%, 100 mL), irradiated with UV and visible light ($\lambda$> 300 nm).

For water oxidation reaction in the presence of $Fe^{3+}$ electron acceptor, ruthenium oxide ($RuO_2$) was loaded as a cocatalyst (0.5 wt% calculated as). $Ru(acac)_3$ for $RuO_2$ deposition and $Fe(NO_3)_3$ for $Fe^{3+}$ source were employed to exclude the possibility of anion exchange from $I^-$ to, for example, smaller $Cl^-$ in precursors. Small amount of sample was mixed with an aqueous solution containing Ru (III) acetylacetonate ($Ru(acac)_3$) (Sigma-Aldrich) followed by heating under an Ar flow at 450 °C for 30 min.

Z-scheme water-splitting reaction was conducted using $RuO_2$-loaded $Bi_3Ba_2Nb_2O_{11}I$, Ru-loaded $SrTiO_3$:Rh (50 mg each), as $H_2$- and $O_2$-evolving photocatalysts, respectively.

They were suspended in an aqueous $Fe(NO_3)_3$ solution (2 mM, 100 mL). The solution pH was adjusted to ~2.4 with diluted aqueous $HNO_3$ solution. The suspension was irradiated with visible light ($\lambda > 400$ nm).

### Complexometric Titration of $Fe^{2+}$.

The amount of $Fe^{2+}$ produced from $Fe^{3+}$ reduction during the $O_2$ evolution reaction was quantified as follows. After the photocatalytic reactions, the powdery sample were removed from the solution by filtration. The concentrations of Fe cations remaining in the solutions were determined from the absorption spectra of the solutions measured by UV−vis spectroscopy (Shimadzu, UV-1800). The reaction solution (50 μL), 2 M acetate buffer solution (2.1 mL) and $9.6\times10^{-4}$ M TPTZ solution (0.7 mL) were mixed, then produced amount of $Fe^{2+}$ was determined on the basis of the absorbance at 596.5 nm.

## 1.3. Results and Discussion

### Photoabsorption and Band Alignment

$Bi_3Ba_2Nb_2O_{11}I$ is a double-perovskite layered Sillén–Aurivillius oxyhalide comprising perovskite, fluorite, and halide layers (Figure 1-1a). Photocatalytic properties of the oxyiodide, including its optical absorption and band structure, have remained elusive. $Bi_3Ba_2Nb_2O_{11}X$ (X = Cl, Br, I) were synthesized based on reported literature (see X-ray diffraction (XRD) and scanning electron microscopy–energy dispersive X-ray spectroscopy (SEM-EDX)) in Figures 2 and 3).[19] The oxyiodide absorbs longer wavelength light (Figure 1-1b), and its bandgap is determined to be approximately 2.3 eV. We estimated the conduction band minimum (CBM) from the flat-band potential determined based on a Mott–Schottky analysis (Figure 1-4). As presented in Figure 1-1c, the negative shift in the VBM of $Bi_3Ba_2Nb_2O_{11}I$ accounts for the narrowed band gap. $Bi_3Ba_2Nb_2O_{11}I$ possesses a much more negative VBM (+1.78 V at pH 6, which corresponds to +2.13 V vs. RHE based on its Nernstian response slope (Figure 1-4d)) than previously reported Sillén–Aurivillius oxyhalides (typically 2.4 V vs. RHE).[15,10,27]

Notably, the band positions (VBM/CBM) meet the thermodynamic requirements for both water reduction and oxidation (i.e., −0.35 V and +0.88 V vs. SHE at pH 6 for $H^+/H_2$ and $O_2/H_2O$, respectively). Note that both $Bi_3Ba_2Nb_2O_{11}Cl$ and $Bi_3Ba_2Nb_2O_{11}Br$ have VBMs similar (approximately +2.46 V vs. RHE) to other Br/Cl-based compounds.

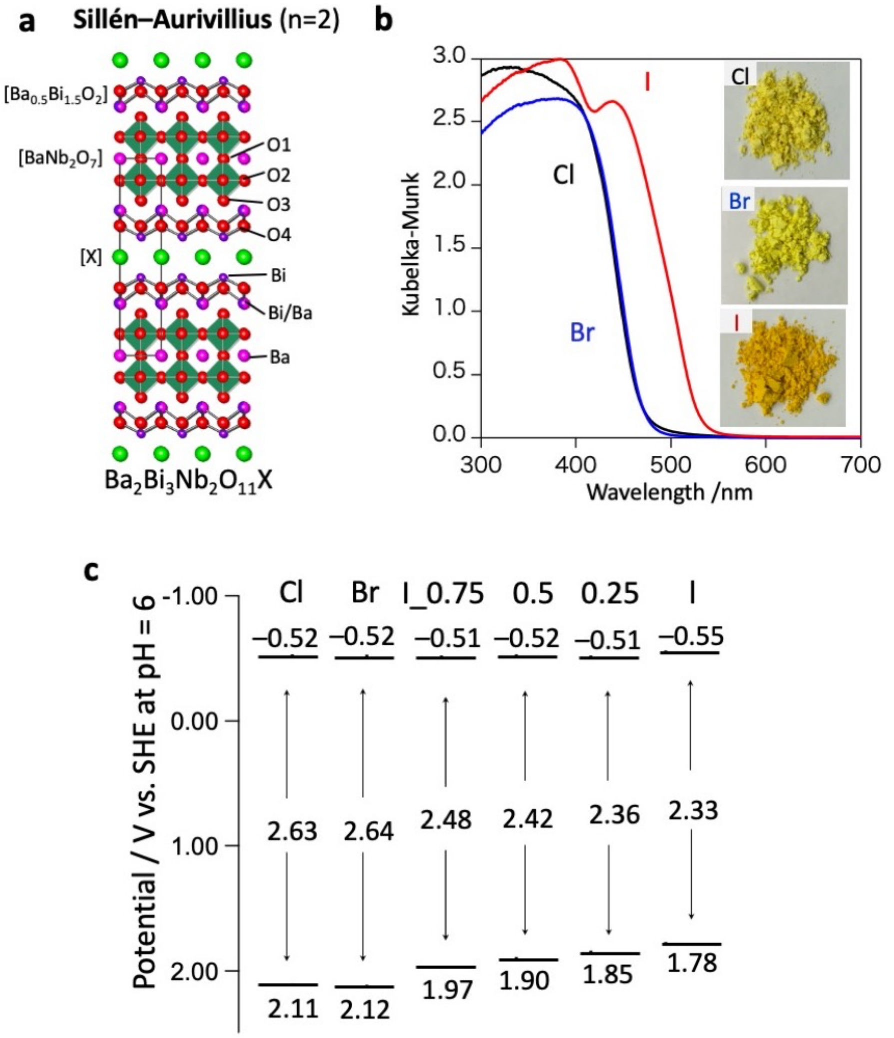

**Figure 1-1.** a, Crystal structure of Sillén–Aurivillus (n = 2) oxyhalide. b, Diffuse reflectance spectra and product color of $Ba_2Bi_3Nb_2O_{11}X$ (X = Cl, Br or I). c, Band edge positions of $Ba_2Bi_3Nb_2O_{11}X$ (X = Cl, Br or I) and $Ba_2Bi_3Nb_2O_{11}Br_{1-x}I_x$ (x = 0.25, 0.5, and 0.75) (denotes as I_0.25, I_0.5, and I_0.75, respectively) estimated from Mott–Schottoky plots in 0.1 M phosphate buffer solution (pH = 6). Flat-band potentials are considered as CBMs.

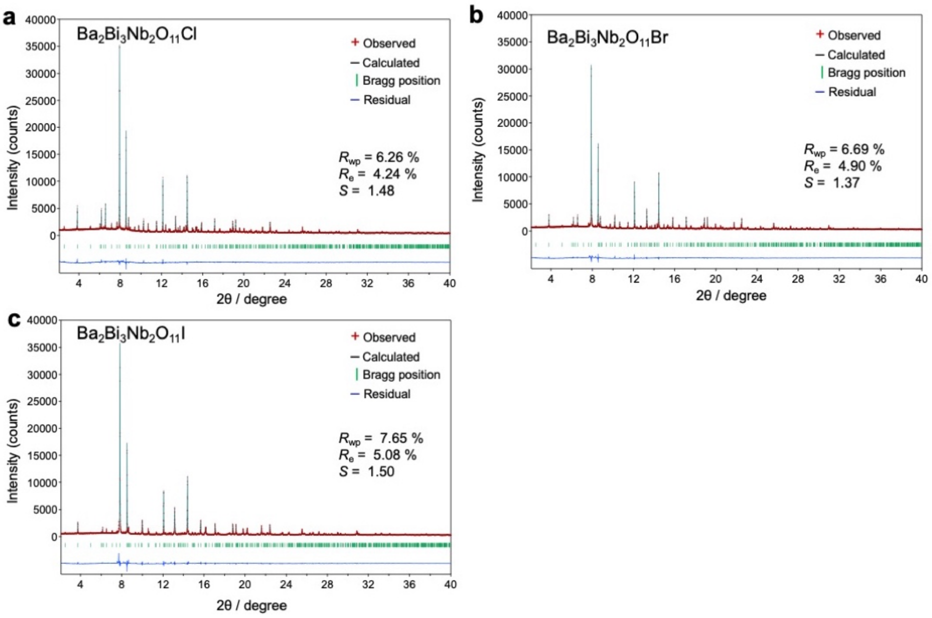

**Figure 1-2.** Rietveld refinement of SXRD pattern of $Ba_2Bi_3Nb_2O_{11}X$ (X = (a) Cl, (b) Br or (c) I) using a proposed model with a tetragonal system (space group: *P4/mmm*).

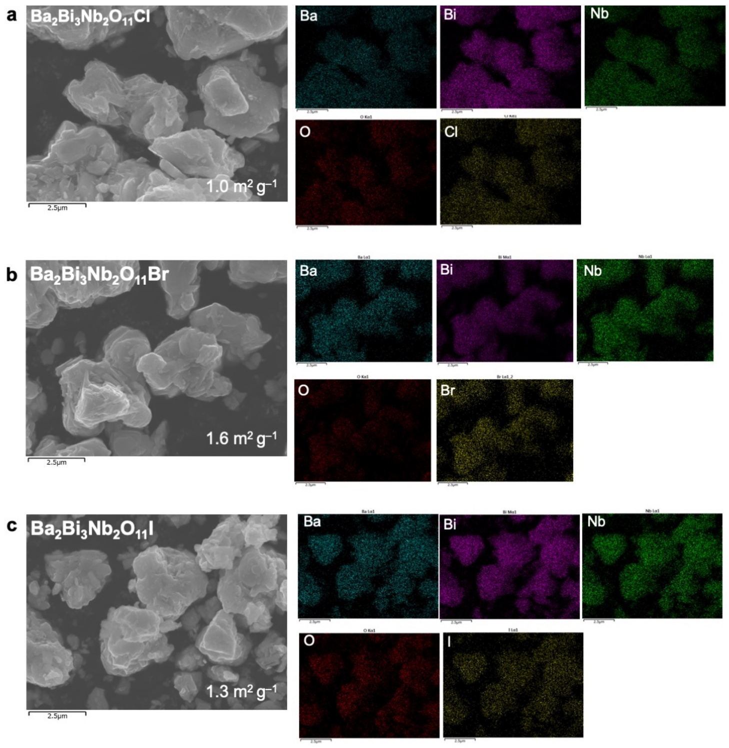

**Figure 1-3.** SEM images and SEM-EDS elemental mapping of $Ba_2Bi_3Nb_2O_{11}X$ (X = Cl (a), Br (b) or I (c)) samples.

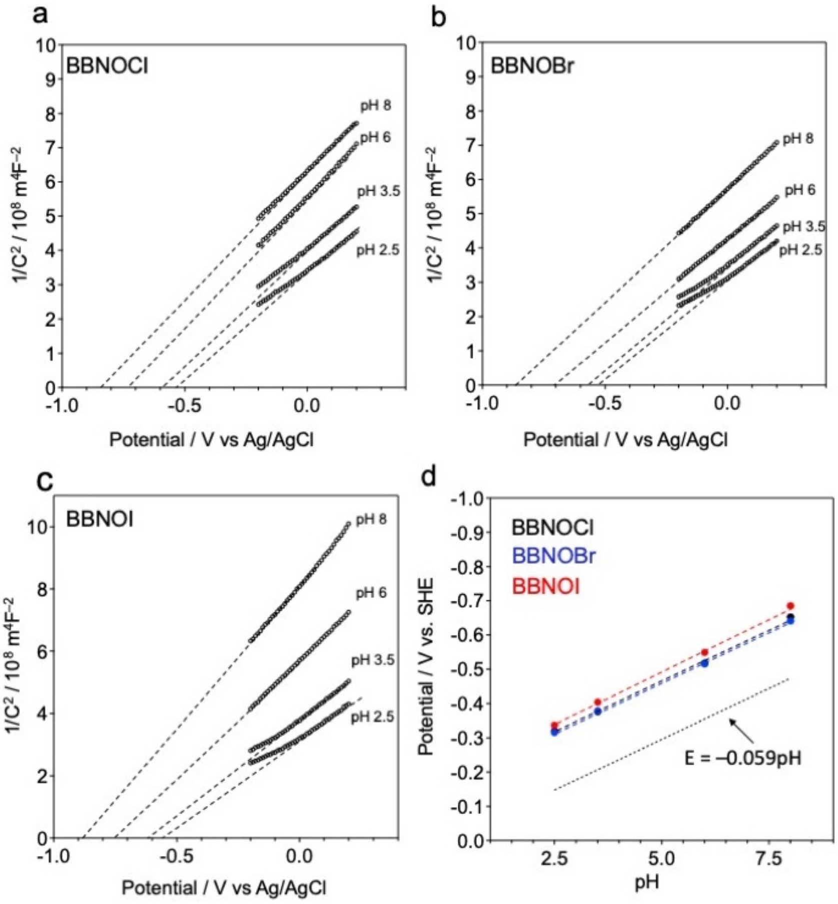

**Figure 1-4.** The pH dependence of the flat band potentials of $Ba_2Bi_3Nb_2O_{11}X$ (X = Cl (a), Br (b) or I (c)) in 0.1 M phosphate buffer solution (pH = 2.5, 3.5, 6 and 8). d, The flat band potentials are dependent on the pH with a Nernstian gradient of 59 mV $pH^{-1}$ like metal oxides.

## Photocatalytic Activity

We evaluated the photocatalytic water oxidation activity under visible light in the presence of electron acceptors, $Ag^+$ ions. $Bi_3Ba_2Nb_2O_{11}I$ exhibited $O_2$ evolution along with $Ag^+$ reduction (Figures 5 and 6). The X-ray photoelectron spectroscopy (XPS) and SEM–EDX analyses confirmed that iodide ions do not elute from $Bi_3Ba_2Nb_2O_{11}I$ under photoirradiation (Table 1-1), showing its photostability, in contrast to $PbBiO_2I$.[10] Note that the oxyiodide exhibited much more $O_2$ generation than its chloride and bromide counterparts (Figure 1-5a), partly because it can utilize visible light with wavelength up to ~500 nm (Figure 1-5b). We confirmed that the surface area is not the determining factor for the significant water oxidation activity of the oxyiodide (Figure 1-3). $Bi_3Ba_2Nb_2O_{11}I$

also presented a higher $H_2$ evolution activity than the oxychloride (Figure 1-7), reflecting the suitable band-edge positions for water splitting.

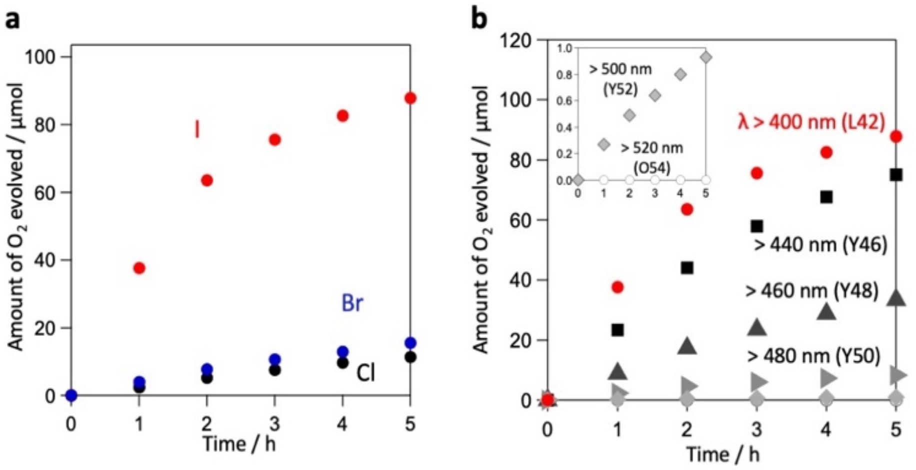

**Figure 1-5.** a, Time course of $O_2$ evolution over $Ba_2Bi_3Nb_2O_{11}X$ (X = Cl (black), Br (blue), or I (red)) in $AgNO_3$ (aq.) (8 mM) under visible light (λ > 400) irradiation. b, Wavelength dependence of photocatalytic activity of $Ba_2Bi_3Nb_2O_{11}I$.

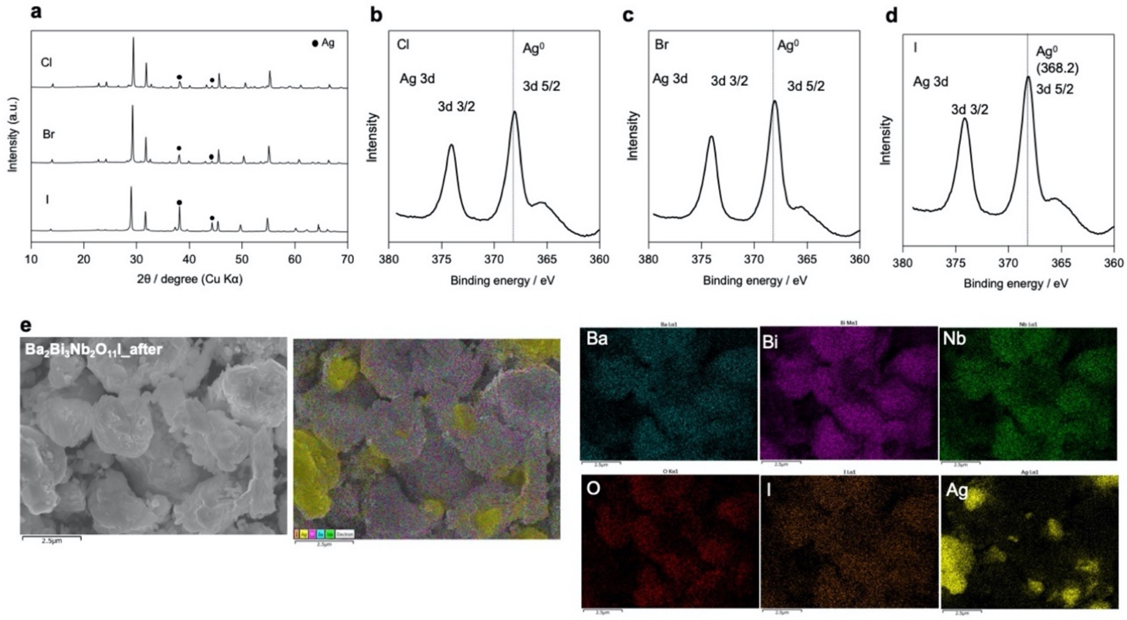

**Figure 1-6.** XRD patterns (a) and XPS spectra of Ag 3d region (b-d) of $Ba_2Bi_3Nb_2O_{11}X$ (X = Cl, Br or I) samples after the photocatalytic water oxidation in aqueous $AgNO_3$ solution (8 mM). e, SEM images and SEM-EDS elemental mapping of $Ba_2Bi_3Nb_2O_{11}I$ sample after the photocatalytic reaction.

**Table 1-1.** X/Bi ratios of $Ba_2Bi_3Nb_2O_{11}X$ (X = Cl, Br or I) before and after $O_2$ evolution along with those after stirring in the $AgNO_3$(aq) under dark conditions.

| | | Cl | | |
|---|---|---|---|---|
| | | before | after | dark |
| Cl/Bi | XPS | 0.3 | 0.3 | 0.3 |
| | EDX | 0.3 | 0.3 | |

| | | Br | | |
|---|---|---|---|---|
| | | before | after | dark |
| Br/Bi | XPS | 0.4 | 0.2 | 0.2 |
| | EDX | 0.3 | 0.3 | |

| | | I | | |
|---|---|---|---|---|
| | | Before | after | dark |
| I/Bi | XPS | 0.4 | 0.3 | 0.3 |
| | EDX | 0.3 | 0.3 | |

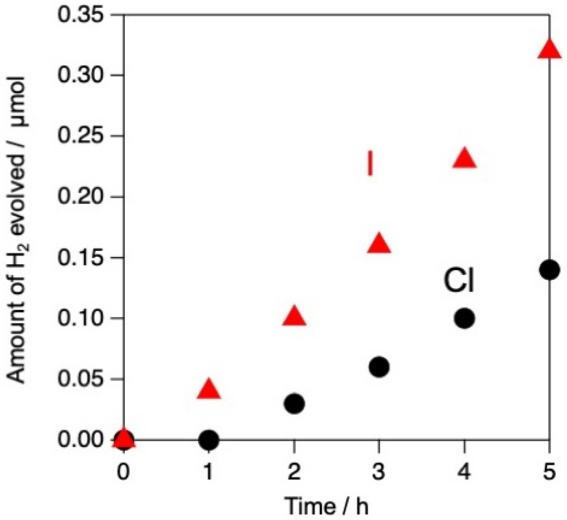

**Figure 1-7.** Time courses of $H_2$ evolution over Rh (1 wt%)-modified $Ba_2Bi_3Nb_2O_{11}X$ (X = Cl or I) in methanol-water mixed solution (1:4, v/v) under UV-visible light irradiation ($\lambda > 300$ nm).

We used $Ba_2Bi_3Nb_2O_{11}I$ as an $O_2$ evolution photocatalyst in Z-scheme water splitting. $RuO_2$-loaded $Bi_3Ba_2Nb_2O_{11}I$ achieved $O_2$ evolution in the presence of $Fe^{3+}$, which is the oxidant of the $Fe^{3+}/Fe^{2+}$ redox mediator, under visible-light illumination (Figure 1-8a). The amount of $Fe^{2+}$ ions converted from $Fe^{3+}$ ions by the photoexcited electrons in this half reaction was estimated by complexometric determination (Figure 1-8b), which was exactly four times the $O_2$ evolved, confirming the stoichiometric redox reaction (e.g., $4Fe^{3+} + 2H_2O \rightarrow O_2 + 4Fe^{2+} + 4H^+$), free from self-oxidation. Subsequently, visible-light water splitting using $RuO_2$-loaded $Bi_3Ba_2Nb_2O_{11}I$ (Figure 1-9) was conducted with the $Fe^{3+}/Fe^{2+}$ couple as the redox mediator and Ru-loaded strontium titanate doped with Rh cations[23] (Ru/$SrTiO_3$:Rh, Fig. 10) as the $H_2$-evolution photocatalyst. As shown in Figure 1-8c, $H_2$ and $O_2$ evolve stoichiometrically at steady rates, demonstrating Z-scheme water splitting using oxyiodide photocatalysts for the first time. The present apparent quantum yield (AQY) at 420 nm is approximately 0.1 %.

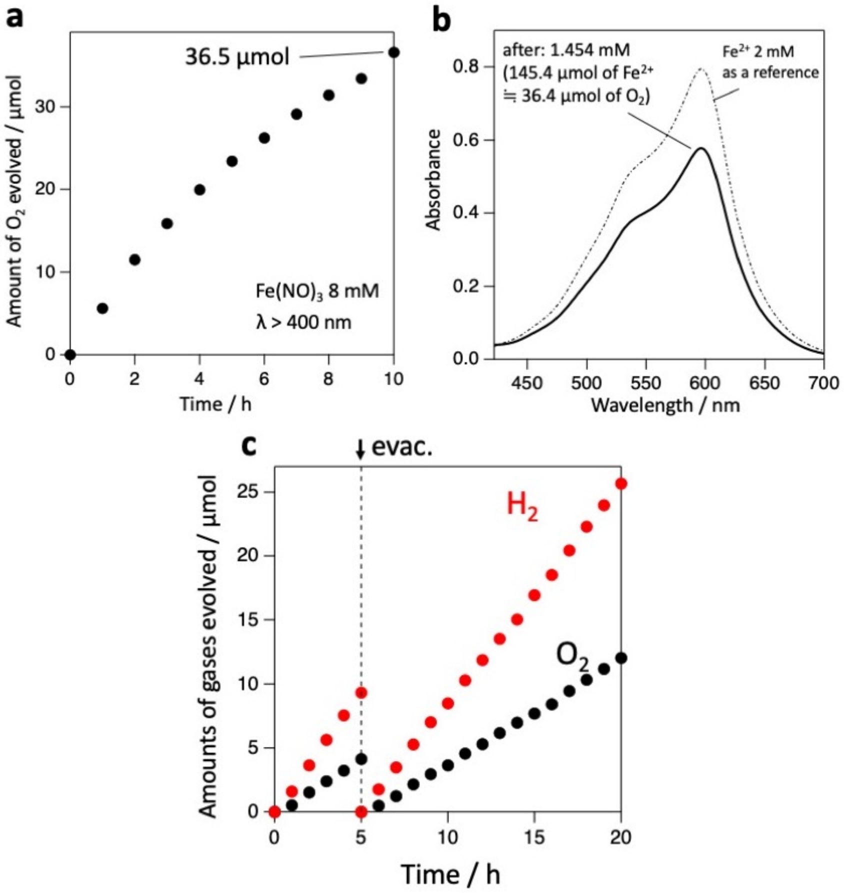

**Figure 1-8.** a, Time course of $O_2$ evolution over $RuO_2$-loaded $Ba_2Bi_3Nb_2O_{11}I$ in $Fe(NO_3)_3$ (aq.) (8 mM, 100 mL) at pH 2.4 under visible light irradiation (λ > 400 nm). b, Absorption spectra of $Fe^{2+}$ after photocatalytic reaction, which is detected as $Fe^{2+}$–2,4,6-tris(2-pyridyl)-1,3,5-triazine (TPTZ) complex. c, Time courses of $H_2$ and $O_2$ evolution over mixture of $RuO_2$-loaded $Ba_2Bi_3Nb_2O_{11}I$ (50 mg) and Ru/$SrTiO_3$:Rh (50 mg) in $FeCl_3$ (aq.) (2 mM, 100 mL) at pH 2.4 under visible light irradiation (λ > 400 nm). The gas phases were evacuated after the initial 5 h operation. Note that the ratio of $H_2$ to $O_2$ produced during the 20 h operation was approximately 2.1.

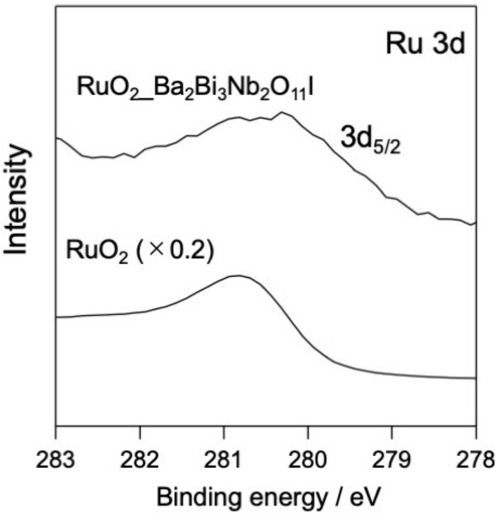

**Figure 1-9.** XPS spectra of Ru 3d region of Ru-species loaded $Ba_2Bi_3Nb_2O_{11}I$. This result shows that the valence state of Ru species loaded via impregnation method with $Ru(acac)_3$ is similar to that of $RuO_2$.

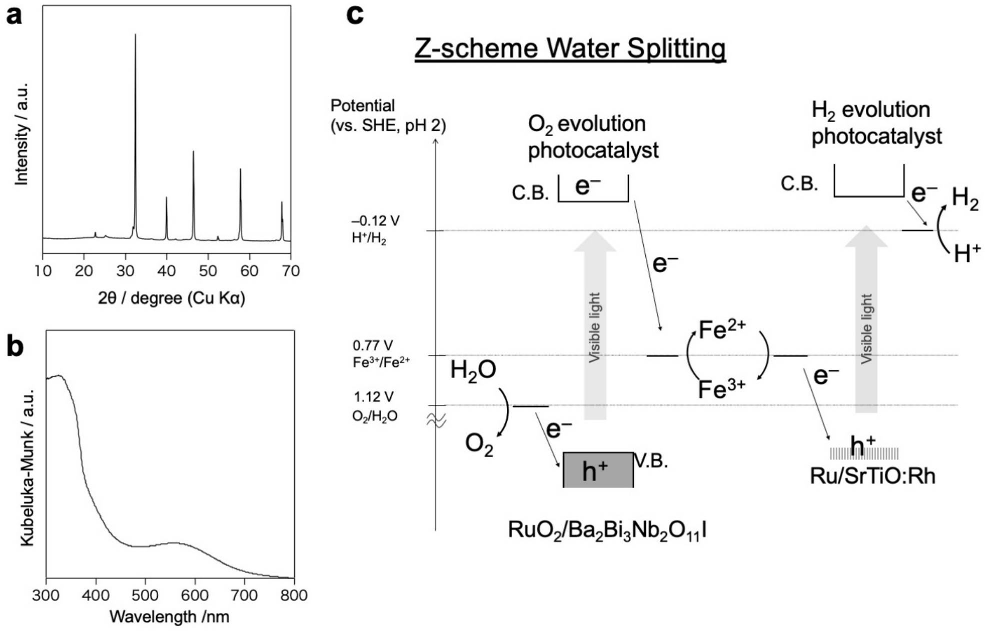

**Figure 1-10.** XRD pattern (a) and DRS (b) of as-prepared SrTiO3:Rh. c, Schematic energy diagram of the Z-scheme water splitting system composed of $RuO_2/Ba_2Bi_3Nb_2O_{11}I$, $Ru/SrTiO_3$:Rh and $Fe^{3+}/Fe^{2+}$ redox.

## Band Structure of $Bi_3Ba_2Nb_2O_{11}I$

The electronic structure of $Bi_3Ba_2Nb_2O_{11}I$ was obtained by density functional theory (DFT) calculations. The DOS shows that its VBM consists of O 2p levels (Figure 1-11a), with the primary contribution from the O atoms in the middle of the $[BaNb_2O_7]$ perovskite slab (O1, O2, and O3), instead of that in the $[Bi_2O_2]$ fluorite layer (O4) (Figure 1-11b). Specifically, the O 2p in the perovskite layer energetically lies above I 5p, despite lower electronegativity of iodine (vs. oxygen), which prevents self-oxidation of iodide ions in this oxyiodide. The obtained electronic structure differs from those of Sillén BiOI and $PbBiO_2I$, whose I 5p-dominated VBMs are responsible for their negligible water oxidation activity[10] (Figure 1-12). The difference between $Bi_3Ba_2Nb_2O_{11}I$ and these Sillén oxyiodides appears to be related to the included perovskite layer in the former structure, implying that the perovskite layer is a key factor in the oxygen participation in the VBM and the excellent photocatalytic function.

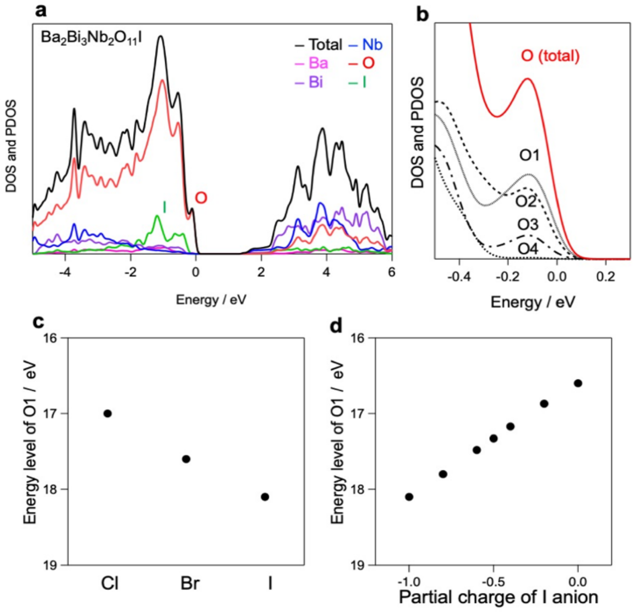

**Figure 1-11.** a, Electronic density of state (DOS) projected for $Ba_2Bi_3Nb_2O_{11}I$. b, Site-projected DOS for oxygen. c, Ionic orbital energy levels of $O^{2-}$ at O1 site in $Ba_2Bi_3Nb_2O_{11}X$ (X = Cl, Br and I) calculated by the sum of Madelung potential and second electron affinity of oxygen. d, The effect of the partial charge of I anion on the energy levels of O1 site in the Madelung potential analysis.

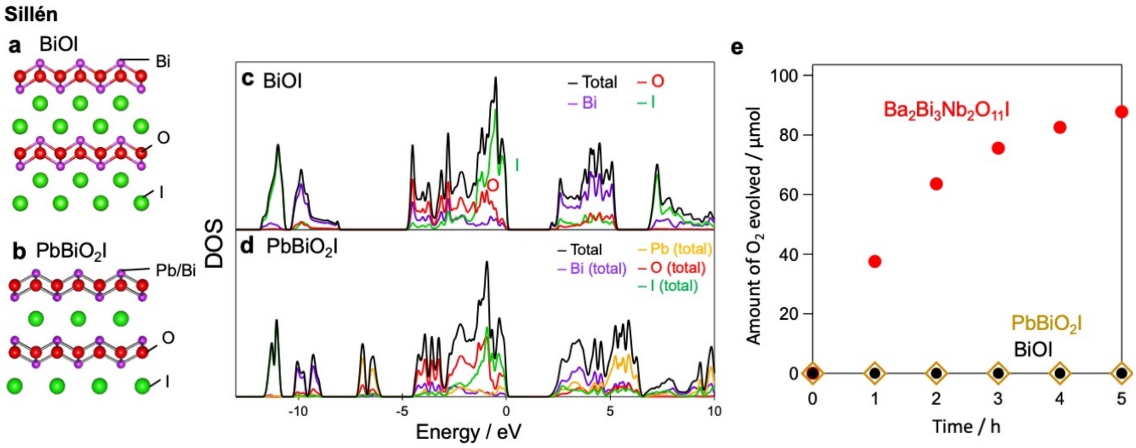

**Figure 1-12.** Crystal structure of Sillén oxyhalides BiOI (a) and PbBiO$_2$I (b). Electronic density of state projected for BiOI (c) and PbBiO$_2$I (d). e, Time courses of O$_2$ evolution over BiOI and PbBiO$_2$I in aqueous AgNO$_3$ solution (8 mM) under visible-light ($\lambda > 400$) irradiation.

Let us discuss why the VBM of $Bi_3Ba_2Nb_2O_{11}I$ is elevated compared to its chloride and bromide counterparts. In our previous study, the elevated VBMs of the Sillén and Sillén–Aurivillius oxyhalides have been attributed mainly to the destabilization of the oxide anion in the $Bi_2O_2$ fluorite block, based on the Bi 6s lone-pair effect[15,17] and the electrostatic effect.[18,28] In contrast, the DFT result on $Bi_3Ba_2Nb_2O_{11}I$ shows that the VBM position is governed primarily by the oxide ions in the perovskite block, rather than those in the fluorite block. Thus, we performed the MP analysis, focusing on O1 in the middle of the perovskite layer (see Figure 1-1a). However, as shown in Figure 1-11c, the ionic energy level of O1 site decreases from X = Cl to I due to the increased O1–X distance and the resultant decreased charge repulsion. This tendency is inconsistent with their VBM positions (Figure 1-1c), which, in turn, implies that the nonionic (highly polarizable) character of iodine must to be taken into consideration, since Madelung site potentials are entirely based on an ionic basis.

The polarizability of the iodide anion, relative to other halide anions, has been addressed theoretically. For example, Bichoutskaia[23] has discussed the contribution of polarization of iodide and electron correlations by ab initio calculations for Alkali metal halides (F, Cl, Br, I) in rock salt and CsCl type structures. Huang[24] performed DFT calculations for Sillen-type BiOX (X = F, Cl, Br, I) and estimated the effective charges to be −0.7 (F), −0.5 (Cl), −0.4 (Br), and −0.3 (I). $Bi_3Ba_2Nb_2O_{11}I$ consists of a stacking sequence of $[Ba_{0.5}Bi_{1.5}O_2]^{+1.5}$–$[BaNb_2O_7]^{-2}$–$[Ba_{0.5}Bi_{1.5}O_2]^{+1.5}$–$[I]^{-1}$. However, given the high polarizability of iodide, let us assume here that the iodide layer possesses an effective valence of $-1+\delta$. It also is natural to assume that the adjacent bismuth ions with a moderate electronegativity of 2.02 has a reduced charge, namely, $[Ba_{0.5}Bi^{+3}{}_{0.5}Bi^{+3-\delta/2}O_2]^{+1.5-\delta/2}$. Then, the $[BaNb_2O_7]^{-2}$ perovskite layer, which is sandwiched by the $[Ba_{0.5}Bi_{1.5}O_2]^{+1.5-\delta/2}$ fluorite layers, should be less electrostatically stabilized, leading to the elevated oxygen band in the perovskite block. By changing the formal charge of iodide ($-1+\delta$), we calculated the Madelung site potential at O1 site, and found that, as $\delta$ increases from 0 to 1, O1 is destabilized, as shown in Figure 1-11d. We thus conclude that the energy level of O1 is determined by the balance between the destabilizing effect of the ionic radius (Figure 1-11c) and the stabilizing effect of the polarizability (Figure 1-11d), and the latter effect is dominant in $Bi_3Ba_2Nb_2O_{11}I$.

It should be noted that in $Bi_3Ba_2Nb_2O_{11}X$ ($n = 2$) (Cl, Br) (Figure 1-13) and other oxyhalides ($n = 3$-5) with perovskite layers, the electronic structures by DFT show that the oxygen in the perovskite layer makes a substantial contribution.[27,29] This means that, by using a perovskite layer as a base of the fluorite-type $Bi_2O_2$ layer that has been emphasized, it will be possible to control the band gap reasonably and extensively with other materials.

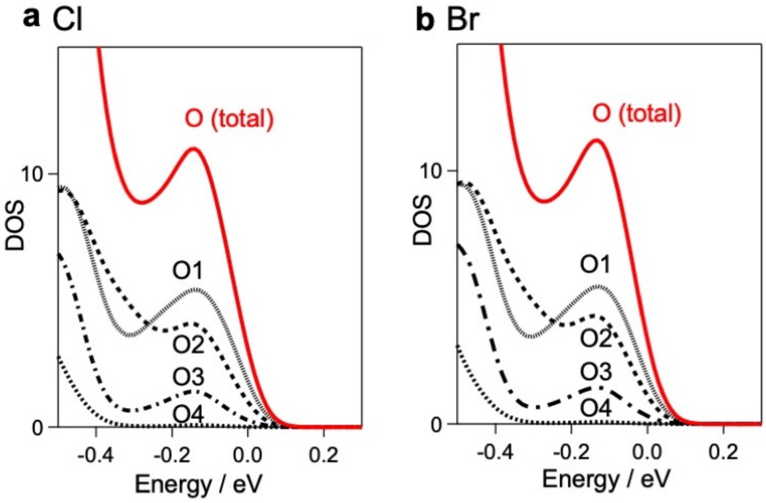

**Figure 1-13.** Site-projected DOS for oxygens in $Ba_2Bi_3Nb_2O_{11}X$ (X = Cl, Br).

### Carrier Lifetime in $Bi_3Ba_2Nb_2O_{11}X$

The observation of the highest apparent quantum efficiency (AQE) of $Bi_3Ba_2Nb_2O_{11}I$ at 405 nm among the other oxyhalides (Table 1-2) suggests that the iodine introduction not only reduces the band gap but also affects the carrier dynamics. Again, the high polarizability of the iodide is at play, which is also inferred from long-life carriers in the iodine-based MHPs. Hence, we compared the carrier dynamics of $Bi_3Ba_2Nb_2O_{11}X$, using a time-resolved microwave conductivity (TRMC) method,[30–32] where photoconductivity $\varphi\sum\mu$ is given by the product of charge carrier photogeneration efficiency $\varphi$ and sum of the photogenerated charge carrier mobilities $\sum\mu$.[31–33] From the decay profile of $\varphi\sum\mu$ at 355 nm excitation (Figure 1-14a), we extracted $\varphi\sum\mu_{\max}$ and carrier lifetime τ (see the details in the Experimental section). Figure 1-14b shows that $\varphi\sum\mu_{\max}$ is improved in $Bi_3Ba_2Nb_2O_{11}I$, though it includes contributions from both carrier mobility and lifetime owing to the problem of time resolution (~ 40 ns).[34] However, Figure 1-14c clearly shows that the carrier lifetime τ is greatly prolonged by introducing iodine. Notably, the carrier lifetime of $Bi_3Ba_2Nb_2O_{11}I$ is approximately 3.3 μs, which is similar in the carrier lifetime order of MHPs[35–38] and is one-order magnitude longer than those of previously reported oxychlorides such as $Bi_4TaO_8Cl$.[39]

**Table 1-2.** AQEs at 405 nm for water oxidation over $Ba_2Bi_3Nb_2O_{11}X$ (X = Cl, Br or I) and $Ba_2Bi_3Nb_2O_{11}Br_{1-x}I_x$ ($x$ = 0.25, 0.5, 0.75).

|  | Cl | Br | $Ba_2Bi_3Nb_2O_{11}Br_{1-x}I_x$ |  |  | I |
|---|---|---|---|---|---|---|
|  |  |  | $x$ = 0.25 | 0.5 | 0.75 |  |
| % | 0.25 | 0.27 | 0.35 | 0.66 | 0.99 | 1.12 |

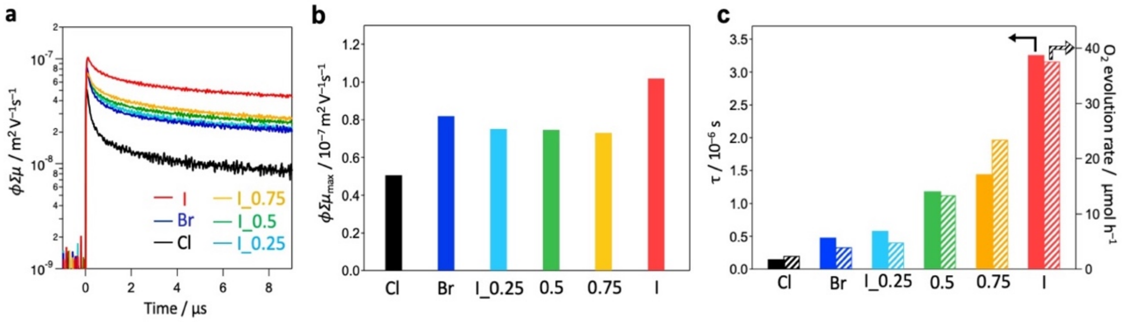

**Figure 1-14**. a, TRMC transients of $Ba_2Bi_3Nb_2O_{11}X$ (X = Cl, Br or I) and $Ba_2Bi_3Nb_2O_{11}Br_{1-x}I_x$ (x = 0.25, 0.5, 0.75) samples ($\lambda_{ex}$ = 355 nm, $I_0 = 4.6 \times 10^{15}$ photons $cm^{-2}$ $pulse^{-1}$). Inset: a zoomed view of initial decays. TRMC transient maxima ($\varphi\Sigma\mu_{max}$). c, Lifetimes ($\tau$) of signal in (a) correlation with $O_2$ evolution rate over $Ba_2Bi_3Nb_2O_{11}X$ in $AgNO_3$ (aq.) (striped bars). The onset wavelength of the TRMC signal is consistent with the absorption of $Bi_3Ba_2Nb_2O_{11}I$ (Figure 1-15).

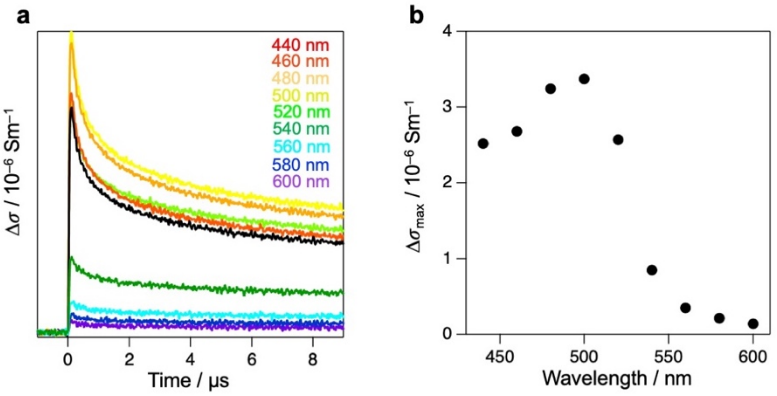

**Figure 1-15.** Wavelength dependence of TRMC signal. **a,** Photoconductivity transients: $\Delta\sigma$ ($\lambda_{ex}$ = 440–600 nm, $I_0 = 5.0 \times 10^{15}$ photons $cm^{-2}$ $pulse^{-1}$) of $Ba_2Bi_3Nb_2O_{11}I$. **b,** The photoconductivity maxima ($\Delta\sigma_{max}$).

To ensure the impact of the iodine introduction on the carrier dynamics and other properties, solid solutions of $Ba_2Bi_3Nb_2O_{11}Br_{1-x}I_x$ ($x$ = 0.25, 0.5, 0.75) were synthesized (Figures 16 and 17 and Table 1-3). The solid solution presents a continuous evolution; as $x$ increases, the VBM level experiences a negative shift (Figure 1-1c), offering a precise control of the VBMs, which cannot be achieved by changing the Cl/Br ratio. Importantly, the TRMC investigation shows that τ gradually increases with increasing $x$. As a result, the photocatalytic activity and the AQE value also increase with increasing $x$ (Figure 1-14c and Table 1-2). The positive correlation between the $O_2$ evolution activity and τ further supports the role of iodine in prolonging the carrier lifetime for realizing efficient photocatalytic reaction (Figure 1-14c). It is likely that the high polarizability of the iodide can protect the photoexcited carrier from recombination by screening the Coulomb potential, as discussed for MHPs and other materials.[40–42]

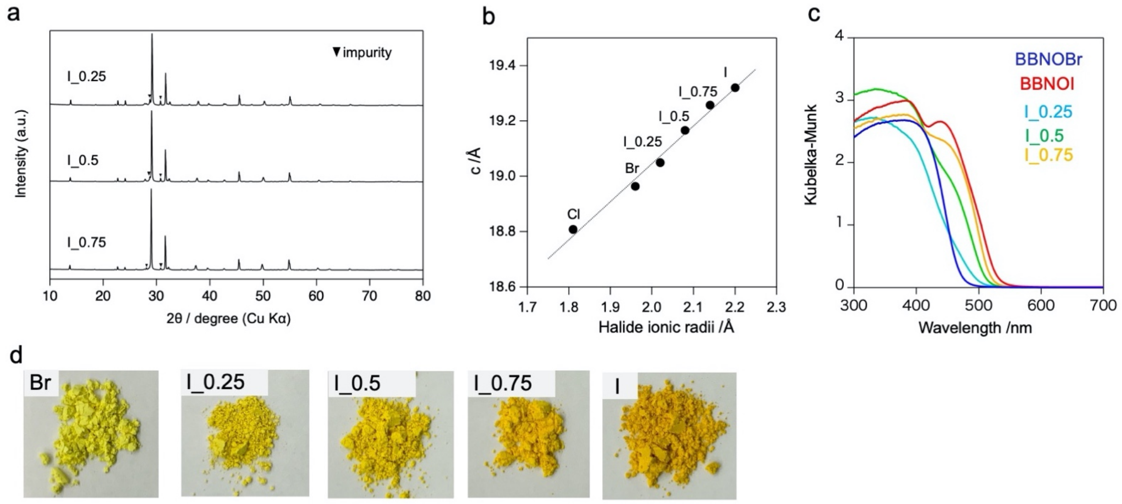

**Figure 1-16. a**, XRD patterns of $Ba_2Bi_3Nb_2O_{11}Br_{1-x}I_x$ ($x$ = 0.25, 0.5, 0.75). **b**, Lattice parameter c vs. the halide ionic radii. Diffuse reflectance spectra (c), and product color (d) of $Ba_2Bi_3Nb_2O_{11}Br_{1-x}I_x$ ($x$ = 0.25, 0.5, 0.75).

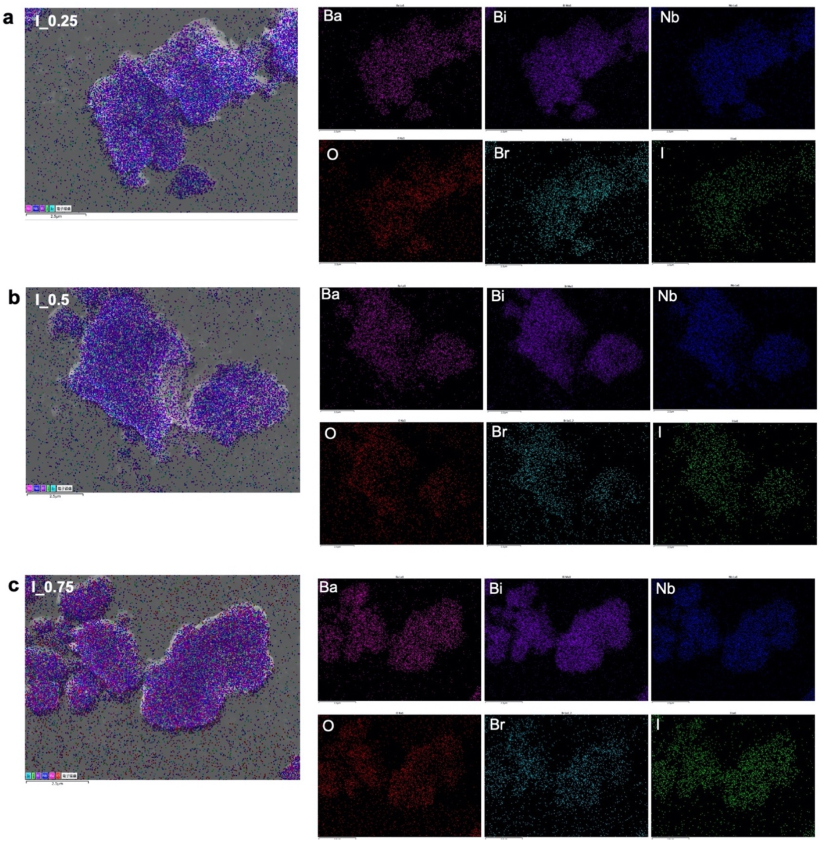

**Figure 1-17.** SEM images and SEM-EDS elemental mapping of $Ba_2Bi_3Nb_2O_{11}Br_{1-x}I_x$ ($x$ = 0.25 (a), 0.5 (b), 0.75 (c)).

**Table 1-3.** X/Bi Ratios of $Ba_2Bi_3Nb_2O_{11}Br_{1-x}I_x$ ($x$ = 0.25, 0.5, 0.75) determined SEM-EDS analysis as shown in Figure 1-17.

| | **I_0.25** | **I_0.5** | **I_0.75** |
|---|---|---|---|
| Br:I | 3.2:1 | 1.3:1 | 1.3:3 |
| ideal | 3:1 | 1:1 | 1:3 |

## 1.4. Conclusion

In summary, we propose a novel approach to manipulate the band structure and carrier dynamics by incorporating polarizable "soft" anions into the building blocks of layered materials. $Bi_3Ba_2Nb_2O_{11}I$ functions as an $O_2$ evolution photocatalyst with much higher activity than its chloride or bromide counterparts. The highly polarizable iodide (or low effective valence) significantly suppresses the electrostatic stabilization of O 2p orbitals in perovskite layer and successfully increases the VBM. This is in stark contrast to conventional band control, which takes advantage of the destabilization of the 6p orbital of iodine (but leads to self-decomposition by photo-excited carriers). This study provides a different design principle based on perovskite layers instead of the previously used fluorite layers. The high polarizability of iodide provides not only a static effect (narrower gap) but also a dynamic effect, i.e., longer carrier lifetime, leading to significantly higher quantum efficiency compared to the Cl/Br counterparts. Visible light-driven Z-scheme water splitting is realized for the first time in an iodine-based system, by using $Bi_3Ba_2Nb_2O_{11}I$ as an oxygen-evolution photocatalyst.

Considering that most of the reported Sillén-Aurivillius-type compounds are chlorides and bromides,[43] we can expect to develop more efficient water splitting systems by increasing the repertoire of iodides. It is noteworthy that $Bi_3Ba_2Nb_2O_{11}I$ was prepared in this study by the conventional solid-state reaction method. More elaborate synthetic methods, such as a two-step method using a polymerized-complex reaction[39] and the flux method[30], would improve its crystallinity and enhance the carrier lifetime and photocatalytic activity. The new approach of the Sillen-Aurivillius system using iodine will be an important strategy for solar energy conversion systems using other reactions. The modified MP analysis considering the effective charge can be applied to the layer-by-layer method shown previously,[28] and thus is a simple tool for screening and predicting the band structure.

# Reference

(1) Kojima, A.; Teshima, K.; Shirai, Y.; Miyasaka, T. Organometal Halide Perovskites as Visible-Light Sensitizers for Photovoltaic Cells. *J. Am. Chem. Soc.* **2009**, *131*, 6050–6051.

(2) Zhang, W.; Eperon, G. E.; Snaith, H. J. Metal Halide Perovskites for Energy Applications. *Nat Energy* **2016**, *1*, 16048.

(3) Veldhuis, S. A.; Boix, P. P.; Yantara, N.; Li, M.; Sum, T. C.; Mathews, N.; Mhaisalkar, S. G. Perovskite Materials for Light-Emitting Diodes and Lasers. *Adv. Mater.* **2016**, *28*, 6804–6834.

(4) Kraft, M. A.; Culver, S. P.; Calderon, M.; Böcher, F.; Krauskopf, T.; Senyshyn, A.; Dietrich, C.; Zevalkink, A.; Janek, J.; Zeier, W. G. Influence of Lattice Polarizability on the Ionic Conductivity in the Lithium Superionic Argyrodites $Li_6PS_5X$ (X = Cl, Br, I). *J. Am. Chem. Soc.* **2017**, *139*, 10909–10918.

(5) Lee, M. M.; Teuscher, J.; Miyasaka, T.; Murakami, T. N.; Snaith, H. J. Efficient Hybrid Solar Cells Based on Meso-Superstructured Organometal Halide Perovskites. *Science* **2012**, *338*, 643–647.

(6) Miyata, K.; Atallah, T. L.; Zhu, X.-Y. Lead Halide Perovskites: Crystal-Liquid Duality, Phonon Glass Electron Crystals, and Large Polaron Formation. *Sci. Adv.* **2017**, *3*, e1701469.

(7) Frolova, L. A.; Anokhin, D. V.; Piryazev, A. A.; Luchkin, S. Yu.; Dremova, N. N.; Stevenson, K. J.; Troshin, P. A. Highly Efficient All-Inorganic Planar Heterojunction Perovskite Solar Cells Produced by Thermal Coevaporation of CsI and $PbI_2$. *J. Phys. Chem. Lett.* **2017**, *8*, 67–72.

(8) Wang, M.; Lin, S. Anisotropic and Ultralow Phonon Thermal Transport in Organic-Inorganic Hybrid Perovskites: Atomistic Insights into Solar Cell Thermal Management and Thermoelectric Energy Conversion Efficiency. *Adv. Funct. Mater.* **2016**, *26*, 5297–5306.

(9) Yang, J.; Wen, X.; Xia, H.; Sheng, R.; Ma, Q.; Kim, J.; Tapping, P.; Harada, T.; Kee, T. W.; Huang, F.; Cheng, Y.-B.; Green, M.; Ho-Baillie, A.; Huang, S.; Shrestha, S.; Patterson, R.; Conibeer, G. Acoustic-Optical Phonon up-Conversion and Hot-Phonon Bottleneck in Lead-Halide Perovskites. *Nat Commun* **2017**, *8*, 14120.

(10) Suzuki, H.; Kunioku, H.; Higashi, M.; Tomita, O.; Kato, D.; Kageyama, H.; Abe, R. Lead Bismuth Oxyhalides $PbBiO_2X$ (X = Cl, Br) as Visible-Light-Responsive Photocatalysts for Water Oxidation: Role of Lone-Pair Electrons in Valence Band Engineering. *Chem. Mater.* **2018**, *30*, 5862–5869.

(11) Luo, J.; Im, J.-H.; Mayer, M. T.; Schreier, M.; Nazeeruddin, M. K.; Park, N.-G.; Tilley, S. D.; Fan, H. J.; Gratzel, M. Water Photolysis at 12.3% Efficiency via Perovskite Photovoltaics and Earth-Abundant Catalysts. *Science* **2014**, *345*, 1593–1596.

(12) Gao, P. A Critical Review on Bismuth Oxyhalide Based Photocatalysis for

Pharmaceutical Active Compounds Degradation: Modifications, Reactive Sites, and Challenges. *Journal of Hazardous Materials* **2021**, 30.

(13) Buehler, N.; Meier, K.; Reber, J. F. Photochemical Hydrogen Production with Cadmium Sulfide Suspensions. *J. Phys. Chem.* **1984**, *88*, 3261–3268.

(14) Xu, J.; Pan, C.; Takata, T.; Domen, K. Photocatalytic Overall Water Splitting on the Perovskite-Type Transition Metal Oxynitride $CaTaO_2N$ under Visible Light Irradiation. *Chem. Commun.* **2015**, *51*, 7191–7194.

(15) Kunioku, H.; Higashi, M.; Tomita, O.; Yabuuchi, M.; Kato, D.; Fujito, H.; Kageyama, H.; Abe, R. Strong Hybridization between Bi-6s and O-2p Orbitals in Sillén–Aurivillius Perovskite $Bi_4MO_8X$ (M = Nb, Ta; X = Cl, Br), Visible Light Photocatalysts Enabling Stable Water Oxidation. *J. Mater. Chem. A* **2018**, *6*, 3100–3107.

(16) Fujito, H.; Kunioku, H.; Kato, D.; Suzuki, H.; Higashi, M.; Kageyama, H.; Abe, R. Layered Perovskite Oxychloride $Bi_4NbO_8Cl$: A Stable Visible Light Responsive Photocatalyst for Water Splitting. *J. Am. Chem. Soc.* **2016**, *138*, 2082–2085.

(17) Walsh, A.; Payne, D. J.; Egdell, R. G.; Watson, G. W. Stereochemistry of Post-Transition Metal Oxides: Revision of the Classical Lone Pair Model. *Chem. Soc. Rev.* **2011**, *40*, 4455.

(18) Kato, D.; Hongo, K.; Maezono, R.; Higashi, M.; Kunioku, H.; Yabuuchi, M.; Suzuki, H.; Okajima, H.; Zhong, C.; Nakano, K.; Abe, R.; Kageyama, H. Valence Band Engineering of Layered Bismuth Oxyhalides toward Stable Visible-Light Water Splitting: Madelung Site Potential Analysis. *J. Am. Chem. Soc.* **2017**, *139*, 18725–18731.

(19) Charkin, D. O.; Akinfiev, V. S.; Alekseeva, A. M.; Batuk, M.; Abakumov, A. M.; Kazakov, S. M. Synthesis and Cation Distribution in the New Bismuth Oxyhalides with the Sillén–Aurivillius Intergrowth Structures. *Dalton Trans.* **2015**, *44*, 20568–20576.

(20) Shannon, R. D.; Waring, R. K. Synthesis and Characterization of a New Series of $BiOI_{1-x-y}Br_xCl_y$, Pigment. *J. Phys. Chem. Solids.* **1985**, *46*, 325–330.

(21) Blake, S. M.; Falconer, M. J.; Mark, M.; Lightfoot, P. Cation Disorder in Ferroelectric Aurivillius Phases of the Type $Bi_2ANb_2O_9$ (A=Ba, Sr, Ca). *J. Mater. Chem.* **1997**, *7*, 1609–1613.

(22) Konta, R.; Ishii, T.; Kato, H.; Kudo, A. Photocatalytic Activities of Noble Metal Ion Doped $SrTiO_3$ under Visible Light Irradiation. *J. Phys. Chem. B* **2004**, *108*, 8992–8995.

(23) Sasaki, Y.; Iwase, A.; Kato, H.; Kudo, A. The Effect of Co-Catalyst for Z-Scheme Photocatalysis Systems with an $Fe^{3+}/Fe^{2+}$ Electron Mediator on Overall Water Splitting under Visible Light Irradiation. *Journal of Catalysis* **2008**, *259*, 133–137.

(24) Izumi, F.; Momma, K. Three-Dimensional Visualization in Powder Diffraction. *Solid State Phenom.* **2007**, *130*, 15–20.

(25) Momma, K.; Izumi, F. *VESTA 3* for Three-Dimensional Visualization of Crystal,

Volumetric and Morphology Data. *J Appl Crystallogr* **2011**, *44*, 1272–1276.

(26) Clark, S. J.; Segall, M. D.; Pickard, C. J.; Hasnip, P. J.; Probert, M. I. J.; Refson, K.; Payne, M. C. First Principles Methods Using CASTEP. *Z. Kristallogr.* **2005**, *220*, 567–570.

(27) Ozaki, D.; Suzuki, H.; Tomita, O.; Inaguma, Y.; Nakashima, K.; Kageyama, H.; Abe, R. A New Lead-Free Sillén–Aurivillius Oxychloride $Bi_5SrTi_3O_{14}Cl$ with Triple-Perovskite Layers for Photocatalytic Water Splitting under Visible Light. *Journal of Photochemistry and Photobiology A: Chemistry* **2021**, *408*, 113095.

(28) Kato, D.; Abe, R.; Kageyama, H. Extended Layer-by-Layer Madelung Potential Analysis of Layered Oxyhalide Photocatalysts and Other Layered Systems. *J. Mater. Chem. A* **2019**, *7*, 19846–19851.

(29) Ozaki, D.; Suzuki, H.; Ogawa, K.; Sakamoto, R.; Inaguma, Y.; Nakashima, K.; Tomita, O.; Kageyama, H.; Abe, R. Synthesis, Band Structure and Photocatalytic Properties of Sillén–Aurivillius Oxychlorides $BaBi_5Ti_3O_{14}Cl$, $Ba_2Bi_5Ti_4O_{17}Cl$ and $Ba_3Bi_5Ti_5O_{20}Cl$ with Triple-, Quadruple- and Quintuple-Perovskite Layers. *J. Mater. Chem. A* **2021**, *DOI: 10.1039/d0ta12550d*.

(30) Ogawa, K.; Nakada, A.; Suzuki, H.; Tomita, O.; Higashi, M.; Saeki, A.; Kageyama, H.; Abe, R. Flux Synthesis of Layered Oxyhalide $Bi_4NbO_8Cl$ Photocatalyst for Efficient *Z* -Scheme Water Splitting under Visible Light. *ACS Appl. Mater. Interfaces* **2019**, *11*, 5642–5650.

(31) Saeki, A.; Yoshikawa, S.; Tsuji, M.; Koizumi, Y.; Ide, M.; Vijayakumar, C.; Seki, S. A Versatile Approach to Organic Photovoltaics Evaluation Using White Light Pulse and Microwave Conductivity. *J. Am. Chem. Soc.* **2012**, *134*, 19035–19042.

(32) Suzuki, H.; Kanno, S.; Hada, M.; Abe, R.; Saeki, A. Exploring the Relationship between Effective Mass, Transient Photoconductivity, and Photocatalytic Activity of $Sr_xPb_{1-x}BiO_2Cl$($x$ = 0–1) Oxyhalides. *Chem. Mater.* **2020**, *32*, 4166–4173.

(33) Suzuki, H.; Higashi, M.; Kunioku, H.; Abe, R.; Saeki, A. Photoconductivity–Lifetime Product Correlates Well with the Photocatalytic Activity of Oxyhalides $Bi_4TaO_8Cl$ and $PbBiO_2Cl$: An Approach to Boost Their $O_2$ Evolution Rates. *ACS Energy Lett.* **2019**, *4*, 1572–1578.

(34) Saeki, A. Evaluation-Oriented Exploration of Photo Energy Conversion Systems: From Fundamental Optoelectronics and Material Screening to the Combination with Data Science. *Polym J* **2020**, *52*, 1307–1321.

(35) Bi, Y.; Hutter, E. M.; Fang, Y.; Dong, Q.; Huang, J.; Savenije, T. J. Charge Carrier Lifetimes Exceeding 15 Ms in Methylammonium Lead Iodide Single Crystals. *J. Phys. Chem. Lett.* **2016**, *7*, 923–928.

(36) Hutter, E. M.; Sutton, R. J.; Chandrashekar, S.; Abdi-Jalebi, M.; Stranks, S. D.; Snaith, H. J.; Savenije, T. J. Vapour-Deposited Cesium Lead Iodide Perovskites: Microsecond Charge Carrier Lifetimes and Enhanced Photovoltaic Performance. *ACS Energy Lett.* **2017**, *2*, 1901–1908.

(37) Tong, J.; Song, Z.; Kim, D. H.; Chen, X.; Chen, C.; Palmstrom, A. F.; Ndione, P. F.;

Reese, M. O.; Dunfield, S. P.; Reid, O. G.; Liu, J.; Zhang, F.; Harvey, S. P.; Li, Z.; Christensen, S. T.; Teeter, G.; Zhao, D.; Al-Jassim, M. M. Carrier Lifetimes of >1 Ms in Sn-Pb Perovskites Enable Efficient All-Perovskite Tandem Solar Cells. *Science* **2019**, *364*, 475–479.

(38) Nakanishi, E.; Nishikubo, R.; Wakamiya, A.; Saeki, A. How the Mixed Cations (Guanidium, Formamidinium, and Phenylethylamine) in Tin Iodide Perovskites Affect Their Charge Carrier Dynamics and Solar Cell Characteristics. *J. Phys. Chem. Lett.* **2020**, *11*, 4043–4051.

(39) Nakada, A.; Saeki, A.; Higashi, M.; Kageyama, H.; Abe, R. Two-Step Synthesis of Sillén–Aurivillius Type Oxychlorides to Enhance Their Photocatalytic Activity for Visible-Light-Induced Water Splitting. *J. Mater. Chem. A* **2018**, *6*, 10909–10917.

(40) Miyata, K.; Meggiolaro, D.; Trinh, M. T.; Joshi, P. P.; Mosconi, E.; Jones, S. C.; De Angelis, F.; Zhu, X.-Y. Large Polarons in Lead Halide Perovskites. *Sci. Adv.* **2017**, *3*, e1701217.

(41) Zhu, H.; Trinh, M. T.; Wang, J.; Fu, Y.; Joshi, P. P.; Miyata, K.; Jin, S.; Zhu, X.-Y. Organic Cations Might Not Be Essential to the Remarkable Properties of Band Edge Carriers in Lead Halide Perovskites. *Adv. Mater.* **2017**, *29*, 1603072.

(42) Bechstedt, F.; Furthmüller, J. Influence of Screening Dynamics on Excitons in $Ga_2O_3$ Polymorphs. *Appl. Phys. Lett.* **2019**, *114*, 122101.

(43) Aurivillius, B. Intergrowth Compounds between Members of Te Bismuth Titanate Family and Structures of the $LiBi_2O_4Cl_2$ Type - an Architectural Approach. *Chem. Scr.* **1984**, *23*, 143.

# Chapter 2

## Tuning of Conduction Band via Inter-layer Interaction in Layered Perovskite Oxyiodide Photocatalysts

## 2.1. Introduction

Interlayer interaction in 2D layered materials affect their electronic structure, changing electron conductivity, band gaps, and photoluminescence property.[1] For example, in bilayer graphene, which is originally semimetal, selective adjustment of the carrier concentration in each layer opens the gaps between the valence band (VB) and conduction band (CB), which can be achieved by breaking the inversion symmetry of the two layers and changing the interlayer interaction.[2] An electrical field applied perpendicularly to the sample can also be employed to tune the band gap.[3] Few-layered black phosphorus (BP) has sizable covalent interlayer interaction, exhibiting strongly layer-dependent electronic structures such as the hole effective mass.[4] Layer dependent bang gaps has been demonstrated in the transition metal dichalcogenides (TMDs),[5] which has emerged as a new class of semiconductors attracting huge interest as next-generation transistors,[6] light-emitting diodes,[7] photovoltaics,[8] and catalysts.[9] For example, the reduction of the layer number increases the band gap of $MoX_2$ owing to the quantum confinement effect.[5] Exfoliation of $MoS_2$ to a monolayer causes an indirect to direct bandgap transition, triggering the photoluminescence in the monolayer.[10] The heterostructure of two different TMDs such as $MoS_2/WS_2$ can facilitate electron-hole separation after photoexcitation between each layer, holding great promise for future optoelectronic and photovoltaic applications.[11]

In recent years, bismuth (or lead)-based oxyhalides with layered structure have emerged as promising photocatalysts for dye degradation,[12,13] water splitting,[14–16] and $CO_2$ reduction.[17] The bismuth/lead oxide based fluorite-like layer, $[M_2O_2]$, intergrown with single, double or triple halide layer, $[X]$, $[X_2]$, or $[M'_xX_3]$ is the common moiety in their structures. The simple intergrowth phase between the fluorite layer and the halide layer, which is so-called Sillén phase, includes BiOCl, $PbBiO_2Cl$, and $PbBi_3O_4Cl_3$ photocatalysts.[18,19] The Sillén phases intergrow with the Aurivillius phase, of general formula $[Bi_2O_2][A_{n-1}B_nO_{3n+1}]$, producing Sillén–Aurivillius (S–A) phases, of the general formula $[A_2O_2][X_n][A_2O_2][A'_{m-1}B_mO_{3m+1}]$.[20] The Sillén–Aurivillius phase is represented by its simplest member $Bi_4NbO_8Cl$ (i.e, $n = 1$, $m = 1$),[21] a promising photocatalyst for visible light water splitting for clean production of hydrogen.[14]

The electronic structure of the bismuth/lead-based oxyhalides characterized by participation by Bi(III) or Pb (II) with $6s^2p^0$ electronic configuration.[22,23] The $6s^2$ – O 2p hybridization reduces O 2p localization, resulting in their valence band maxima (VBM) located more negative than that of the conventional oxide based photocatalysts, such as $TiO_2$, $SrTiO_3$, which affords visible light responsibility to the bismuth/lead base photocatalyst (e.g., $Bi_4NbO_8Cl$,[14,22] $Bi_2YO_4Cl$,[24] $PbBiO_2Cl$[23] and $PbBi_3O_4Cl_3$[25]). Their conduction band minima (CBM) mainly consists of Bi/Pb-6p orbital. Notably, the electronic structures where s and p orbital contribute to the VBM and CBM, respectively, have been reported to allow the favorable optoelectronic properties for solar-to-energy conversion system.[26,27] This is in stark contrast to the conventional photocatalysts, where anion p (O-2p, S-3p, N-2p) and cation d (Ti-3d, V-3d, Nb-4d, Ta-5d, W-5d) orbitals mainly contribute the VBM and CBM, respectively.[28] The $6s^2$ – O 2p hybridization not only shifts the VBM negatively but also enlarges the hole mobility as reported in $PbWO_4$.[29] It was also reported that the defect tolerance of the lead-halide perovskites (LHPs) is provided by the $6s^2$ – X-$n$p (e.g., I-5p) hybridization.[30,31] In addition, the CB contributed by p orbitals affords good electron conductivity owing to the low effective mass of the carrier provided by the spatially delocalized conduction band as compared the localized d orbital.[26,32] From the view points of the chemistry of $ns^2np^0$ cation,[26,27] the bismuth/lead based semiconductors are promising candidates for efficient solar-to energy conversion.

In the present study, we demonstrate that the interlayer interaction of the bismuth-based layer in S–A compounds can shift the CBM position negatively. Although the negative shift of CBM of the bismuth based layered oxychloride has been achieved by changing the intralayer interaction of Bi and O, this negative shift is accompanied by the breaking the Bi–O bonds, the decreasing photoconductivity, and the widening the band bap, where the photocatalytic activity is significantly deteriorated.[33] Strategies for shifting CBM negatively without sacrifice of visible light absorbability and photocatalytic activity have not been established yet.

Recently, we have revealed that iodine introduced in S–A with double perovskite layer (n = 2), $Bi_3Ba_2Nb_2O_{11}X$, electronically destabilizes the oxygen in the perovskite layer, providing the negatively shifted VBM of the oxy-iodide as compared to its chloride and bromide counterparsts.[34] Therefore, the oxy-iodide has a narrower band gap and a much higher photocatalytic water oxidation activity under visible light than its chloride and bromide counterparts, while the chloride and the bromide have almost same band gaps and photocatalytic activities. Notably, the iodine introduction to this compound having double perovskite layer (n = 2) exerts little influence on the CBM position.[34]

S–A oxyhalides have many structural variety other than the double perovskite layer (n = 2) type.[20] However, most of the synthetic reports are for the chlorides, and there are few reports on synthesis of oxy-iodides.[35,36] In the present study, we synthesize three novel layered perovskite oxy-iodides, $Bi_4NbO_8I$, $Bi_5BaTi_3O_{14}I$ and $Bi_6NbWO_{14}I$ (Figure 2-1a-c) via replacing chloride by iodide in various S–A oxyhalides besides n = 2. In contrast to the case with n = 2, their CBMs, as well as VBMs, are negatively shifted as compared to the chloride counterparts. The negative shifts of both band edge positions via replacing the chloride by iodide are not accompanied by widening the band gaps, which allows the negative shift of CBM without sacrifice of visible light responsibility. We discuss the origin of the CBM shift by iodine introduction, focusing on the interlayer Bi-Bi interaction and revised lone pair (RLP) model.[26] In addition, they function as visible light water oxidation photocatalyst, showing much higher $O_2$ evolution activities than their chloride counterparts.

## 2.2. Experimental

**Synthesis**

All the oxyhalides were prepared by prepared by solid-state reactions. In the case of $Bi_3Ba_2Nb_2O_{11}X$ (X = Cl, Br, I), the Sillén-type $BaBiO_2X$ and Aurivillius-type $Bi_3BaNb_2O_9$ were mixed in 1.05 : 1 composition, heated in air (X = Cl, Br) an evacuated silica tube (X = I, and Cl for a certain case) at 800 °C for 20h.[36] $BaBiO_2X$ precursors were prepared by calcining a stoichiometric mixture of $BaCO_3$ (FUJIFILM Wako Pure Chemical Corporation) and BiOX in air (X = Cl, Br) an evacuated silica tube (X = I) at 800 °C for 20h. BiOCl was purchased from FUJIFILM Wako Pure Chemical Corporation, while BiOBr and BiOI were synthesized by a soft liquid deposition method;[37] 5 mmol of $Bi(NO_3)_3 \cdot 5H_2O$ (FUJIFILM Wako Pure Chemical Corporation) was dispersed in 30 mL of ethanol and mixed with the solution of 5 mmol of KX (X = Br or I) (FUJIFILM Wako Pure Chemical Corporation) dissolved in 10 mL of pure water. After 5 h stirring at room temperature, the precipitate was collected by centrifugation, washed several times with water and ethanol, and finally dried in air at 60 °C. $Bi_3BaNb_2O_9$ was prepared by calcinating the mixture of $Bi_2O_3$ (FUJIFILM Wako Pure Chemical Corporation), $BaCO_3$ and $Nb_2O_5$ (FUJIFILM Wako Pure Chemical Corporation) at 1000 °C for 24h.[38] $Bi_3BaMNb_2O_{11}X$ (M = Sr, Ca, X = Cl, I) were also prepared via similar procedures, where $Bi_3MNb_2O_9$ (M = Sr, Ca) were used as precursors. $SrCO_3$ (FUJIFILM Wako Pure Chemical Corporation) or $CaCO_3$ (FUJIFILM Wako Pure Chemical Corporation) was used instead of $BaCO_3$. The mixture of $BaBiO_2X$ (X = Cl, I) and $Bi_3MNb_2O_9$ were calcinated in an evacuated silica tube at 800 °C (M = Sr), or 850 °C (M = Ca) for 20h.

$Bi_4NbO_8X$ (X = Cl, I) were synthesized by solid-state reaction of $BiNbO_7$ and BiOX (X = Cl, I). These precursors were thoroughly mixed with a molar ratio of 1 : 1.05, heated in an evaluated silica tube at 700 °C for 10h. $BiNbO_7$ precursor was prepared by calcinating the mixture of $Bi_2O_3$ and $Nb_2O_5$ at 800°C for 5h. $Bi_5BaTi_3O_{14}I$ were synthesized by calcination of $Bi_2O_3$, $TiO_2$ (FUJIFILM Wako Pure Chemical Corporation), and $BaBiO_2X$ (10 mol% excess) in an evaluated silica tube at 850 °C for 20h. $Bi_6NbWO_{14}X$ (X = Cl, I) were prepared by calcinating the mixture of $Bi_2O_3$, $Nb_2O_5$, $WO_3$ (Kojundo Chemicals) and BiOX (5 mol% excess) in an evaluated silica tube at 800 °C for 20h.

$SrTiO_3$:Rh[39] was prepared by solid-state reaction. A mixture of $TiO_2$, $SrCO_3$ and $Rh_2O_3$ (Ti : Sr : Rh = 1 : 1.07 : 0.01) was calcined in air at 800 °C for 1 h and subsequently at 1000 °C for 10 h. A Ru-based cocatalyst (0.7 wt% calculated as metal) was loaded onto $SrTiO_3$:Rh by photo-deposition using $RuCl_3 \cdot nH_2O$ (FUJIFILM Wako Pure Chemical Corporation) as a precursor.[40]

**Density Functional Theory Calculation**

The band structure calculation of the oxyhalides was performed within the framework of density functional theory (DFT) using plane-wave pseudopotential method as implemented in the Cambridge Serial Total Energy Package (CASTEP) code of BIOVIA's Material Studio 2020.[41] The interaction between the ionic core and valence electrons is treated with the OTFG ultra-soft pseudopotential with the scalar relativistic Kolling-Harmon approximation. The Perdew-Burke-Ernzerhof (PBE) function of generalized gradient apporoximation (GGA) was employed as exchange-correlation functional. An energy cut off and the Monkhorst-Pack *k*-point mesh of a plane wave basis set were as follows; 700 eV 6×6×2 for $Bi_3Ba_2Nb_2O_{11}X$, 700 eV 6×6×2 for $Bi_4NbO_8I$, 700 eV 3×3×2 for $Bi_5BaTi_3O_{14}I$, 700 eV 6×2×6 for $Bi_6NbWO_{14}I$. The minimization algorithm of Broyden–Fletcher–Goldfarb–Shanno (BFGS) was employed for geometry optimizations with total energy convergence tolerance $10^{-6}$ eV per atom. Other convergence parameters were as follows: self-consistent field tolerance $1 \times 10^{-5}$ eV per atom, maximum stress 0.05 GPa, and maximum ionic displacement $1 \times 10^{-3}$ Å.

### Characterization

Powder XRD (MiniFlex II, Rigaku, X-ray source: Cu Kα), UV−visible diffuse reflectance spectroscopy (V-650, JASCO), SEM-EDX (NVision 40, Carl Zeiss-SIINT) were used for characterization of samples. High-angle annular dark-field scanning transmission electron microscopy (HAADF-STEM) and annular bright-field scanning transmission electron microscopy (ABF-STEM) images were collected using a JEM-ARM200CF (JEOL Ltd., Tokyo, Japan) operating at an accelerating voltage of 200 kV and equipped with a cold field emission gun and a Cs corrector in order to observe atomic columns of $Bi_4NbO_8Cl$. Elemental analysis was carried out using JEM-ARM200CF equipped with energy dispersive X-ray spectroscopy (EDX). Samples were prepared by grinding the material and depositing a few drops of the suspension onto a holey copper grid covered with a thin carbon film. SXRD patterns were collected at the BL02B2 in SPring-8, Japan ($\lambda$ = 0.419432 Å) and were analyzed by the Rietveld method using the RIETAN-FP program.[42]

### Mott–Schottky measurement

The sample was mixed with a small amount of water, then the obtained paste was coated on a fluorine-doped tin oxide (FTO) conductive substrate via a squeezing method and dried in air at 60 °C. The Mott−Schottky plots were recorded on an electrochemical analyzer (PARSTAT2263, Princeton Applied Research). Electrochemical measurements were performed in a three-electrode cell using a Pt wire counter-electrode, a Ag/AgCl reference electrode, and a phosphate-buffered solution (0.1 M, pH = 2.5–8.0) with 10 mV amplitude and a frequency of 1 kHz.

### Photocatalytic reaction

The photocatalytic reactions were performed in a gas closed-circulation system. Photocatalyst powders (0.1 g) were dispersed in an aqueous $AgNO_3$ solution (8 mM, 100 mL) in a Pyrex top-window cell. The photocatalysts were irradiated with visible light ($\lambda > 400$ nm) through a cutoff filter (HOYA; L42) from a 300-W Xe-arc lamp (PerkinElmer; Cermax- PE300BF). The quantity of the evolved gases was determined using an online gas chromatograph (thermal conductivity detector; molecular sieve 5 Å column packing; Ar carrier gas). The apparent quantum efficiency (AQE) was evaluated using a 405 nm monochromatic LED light source (ASAHI SPECTRA, CL-1501).

For water oxidation reaction in the presence of $Fe^{3+}$ electron acceptor, ruthenium oxide ($RuO_2$) was loaded as a cocatalyst. Small amount of sample was mixed with an aqueous solution containing Ru (III) acetylacetonate ($Ru(acac)_3$) (Sigma-Aldrich) followed by heating under an Ar flow at 450 °C for 30 min.

Z-scheme water-splitting reaction was conducted using $RuO_2$-loaded $Bi_6NbWO_{14}I$ (0.05 g), Ru-loaded $SrTiO_3$:Rh (0.05 g), as $H_2$- and $O_2$-evolving photocatalysts, respectively. They were suspended in an aqueous $Fe(NO_3)_3$ solution (2 mM, 100 mL). The solution pH was adjusted to ~2.4 with diluted aqueous $HNO_3$ solution. The suspension was irradiated with visible light ($\lambda > 400$ nm).

### Complexometric titration of $Fe^{2+}$

The amount of $Fe^{2+}$ produced from $Fe^{3+}$ reduction during the $O_2$ evolution reaction was quantified as follows. After the photocatalytic reactions, the powdery sample were removed from the solution by filtration. The concentrations of Fe cations remaining in the solutions were determined from the absorption spectra of the solutions measured by UV−vis spectroscopy (Shimadzu, UV-1800). The reaction solution (50 μL), 2 M acetate buffer solution (2.1 mL) and 9.6×10–4 M TPTZ solution (0.7 mL) were mixed, then produced amount of $Fe^{2+}$ was determined on the basis of the absorbance at 596.5 nm.

## 2.3. Results and Discussion

### Syntheses of the Novel Oxyiodides

We synthesized the S–A type layered perovskite oxyiodides with single perovskite layer (n = 1); $Bi_4NbO_8I$ (Figure 2-1a), triple perovskite layer (n = 3); $Bi_5BaTi_3O_{14}I$ (Figure 2-1c), and different staking pattern with Sillén–Aurivillius–Aurivillius (S–2A); $Bi_6NbWO_{14}I$ (Figure 2-1d). Their chloride counterparts function as water oxidation photocatalyst under visible light,[14,16,43,44] whereas the syntheses and, of course, the photocatalytic properties of these iodides have remained uninvestigated.

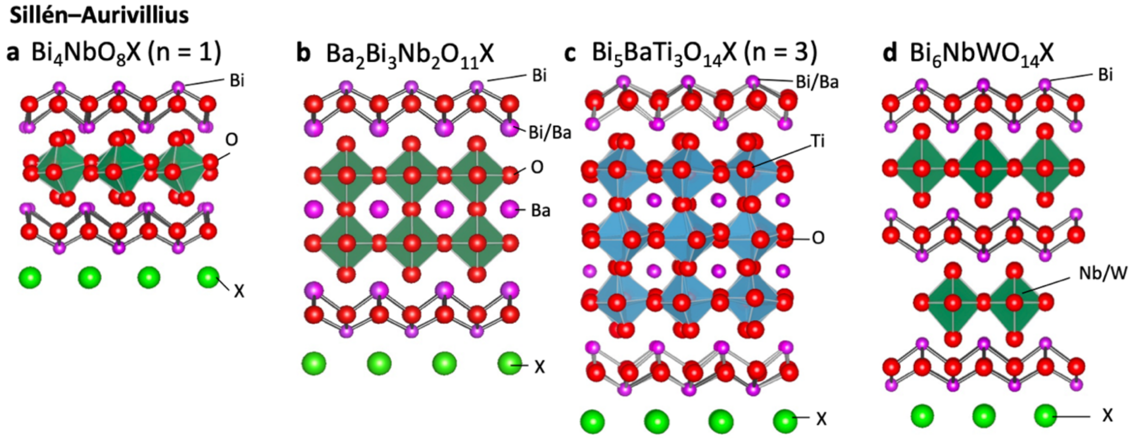

**Figure 2-1.** Crystal Structure of Sillén-Aurivillus oxyhalides (a) $Bi_4NbO_8X$ (n = 1), (b) $Bi_3Ba_2Nb_2O_{11}X$, (c) $Bi_5BaTi_3O_{14}X$ (n = 3) (b) and (d) Sillén-Aurivillus-related oxyhalide $Bi_6NbWO_{14}X$.

Figure 2-2a shows synchrotron powder X-ray diffraction (SXRD) pattern of $Bi_4NbO_8I$. Rietveld refinement was carried out in combination with neutron powder diffraction (NPD; Figure 2-3), testifying successful synthesis of the targeted material. Note that, $Bi_4NbO_8I$ has been considered to be difficult to synthesis due to the lattice mismatch between the perovskite $[NbO_4]$ layer and fluorite $[Bi_2O_2]$ layer.[35] To tackle this problem, we employed an oxygen-deficient fluorite type $Bi_3NbO_7$[45] as a precursor of Nb species (Figure 2-4), whereas the previous attempt did a “rigid” oxide already containing perovskite layer such as $BiNbO_4$.[35] The present result on $Bi_4NbO_8I$ synthesis indicates that, not only the lattice matching, but also the choice of the precursor materials affects the success or failure of the synthesis of the targeted layered structures. We also successfully synthesized $Bi_5BaTi_3O_{14}I$ (n = 3) and $Bi_6NbWO_{14}I$ (Figure 2-5: XRD patterns). HAADF-STEM images recorded parallel to the layers, along with the STEM/EDX line scan analysis and elemental maps (Figure 2-2b-d, Figure 2-6–8), are consistent with each crystal structures obtained from the XRD analysis. SEM-EDX mappings of these oxyhalides, showing the uniform distribution of the constitute elements at a stoichiometric elemental ratio, further confirm successful formation of these products (Figure 2-9).

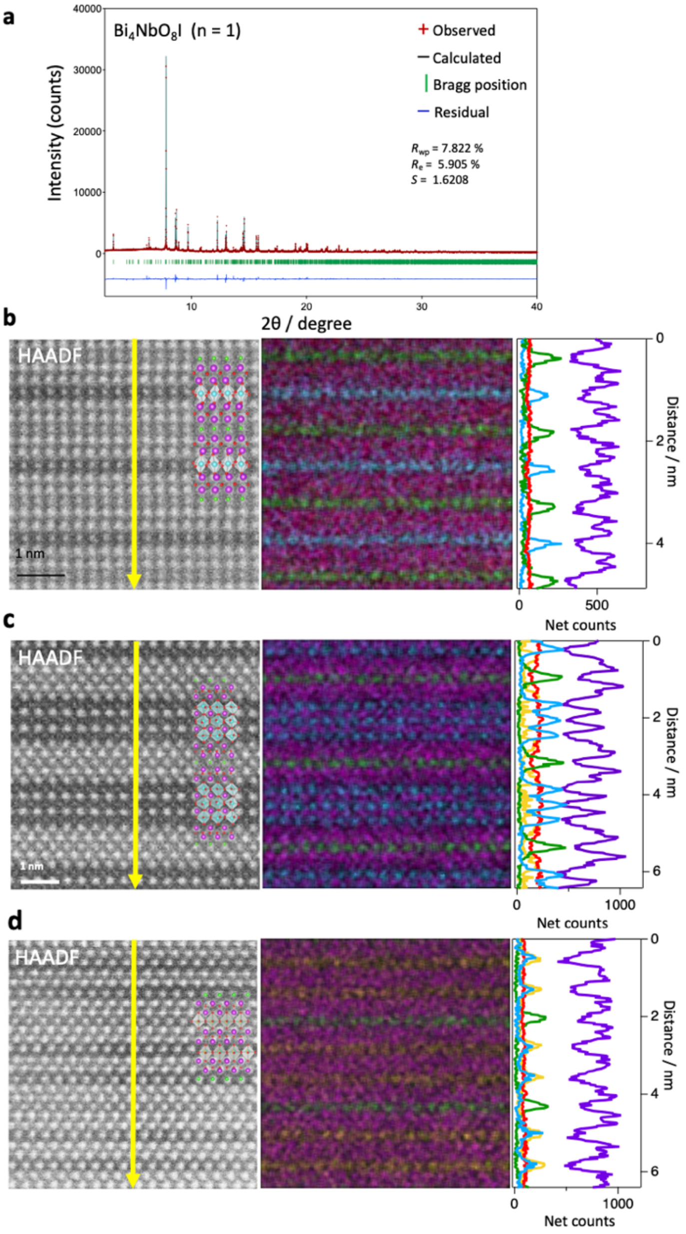

**Figure 2-2.** **a**, Rietveld refinement of SXRD pattern of prepared $Bi_4NbO_8I$. **h-j,** HAADF-STEM image, atomic resolution STEM-EDX elemental maps for $Bi_4NbO_8I$ (**h**) along the $[100]_t$ direction, $Bi_5BaTi_3O_{14}I$ (**i**) along the $[110]_t$ direction, $Bi_6NbWO_{14}I$ (**j**) along the $[110]_t$ direction.

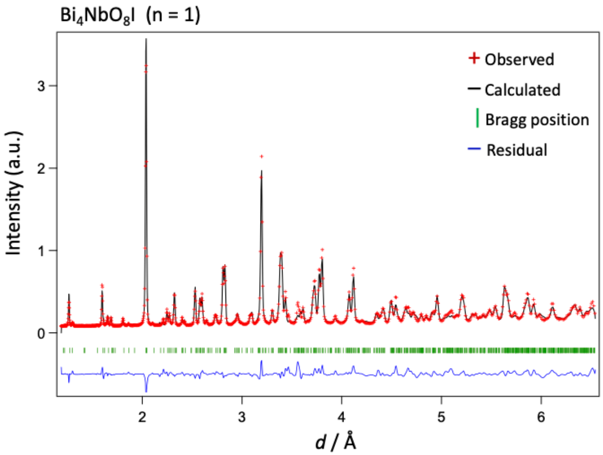

**Figure 2-3.** Final Rietveld plot for $Bi_4NbO_8I$ using the NPD pattern collected at room temperature; $R_p = 0.0754$, $R_{wp} = 0.0966$, $R_B = 0.0713$, $R_F = 0.0310$, $\chi^2 = 1.171$.

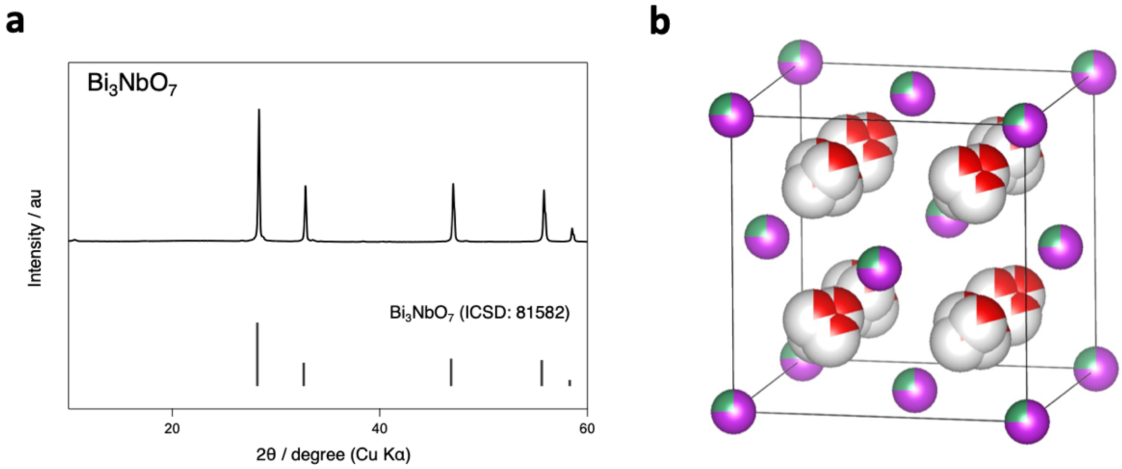

**Figure 2-4**. (a) XRD pattern and (b) Crystal structure of $Bi_3NbO_7$.

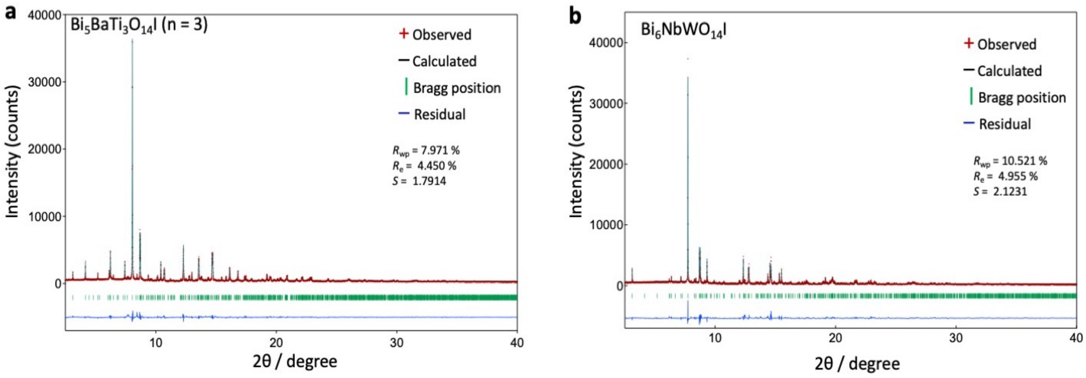

**Figure 2-5.** Rietveld refinement of SXRD pattern of prepared (a) $Bi_5BaTi_3O_{14}X$ (n = 3) and (b) $Bi_6NbWO_{14}X$.

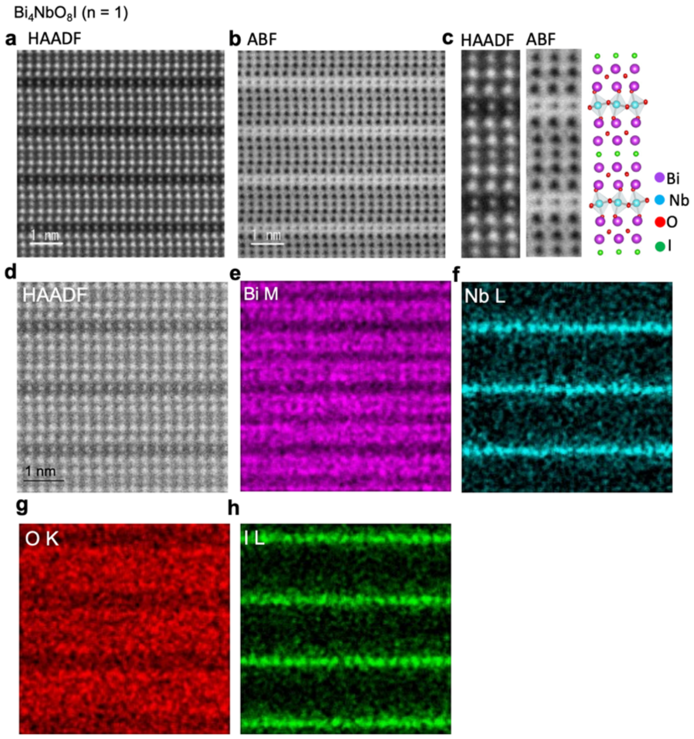

**Figure 2-6.** a,b, HAADF (a) and ABF (b) STEM images for $Bi_4NbO_8I$ particle. b, Close-up HAADF and blue ABF images together with the corresponding $Bi_4NbO_8I$ crystal structure. **d-h**, STEM-EDX atomic resolution elemental maps of the regions shown in d for Bi (**e**), Nb (**f**), O (**g**), I (**h**).

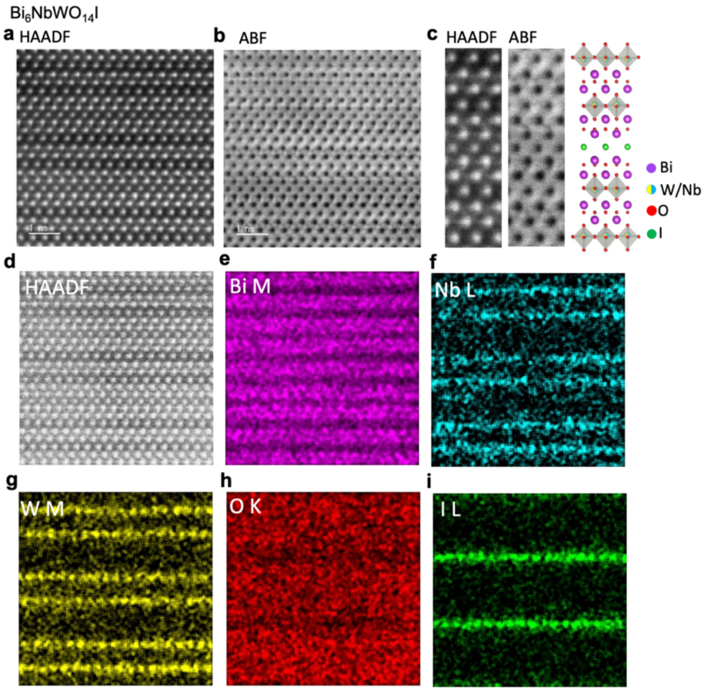

**Figure7.** a,b, HAADF (a) and ABF (b) STEM images for $Bi_5BaTi_3O_{14}I$ particle. b, Close-up HAADF and blue ABF images together with the corresponding $Bi_5BaTi_3O_{14}I$ crystal structure. **d-h**, STEM-EDX atomic resolution elemental maps of the regions shown in d for Bi (**e**), Ba (**f**), Ti (**g**), O (**h**), I (**i**).

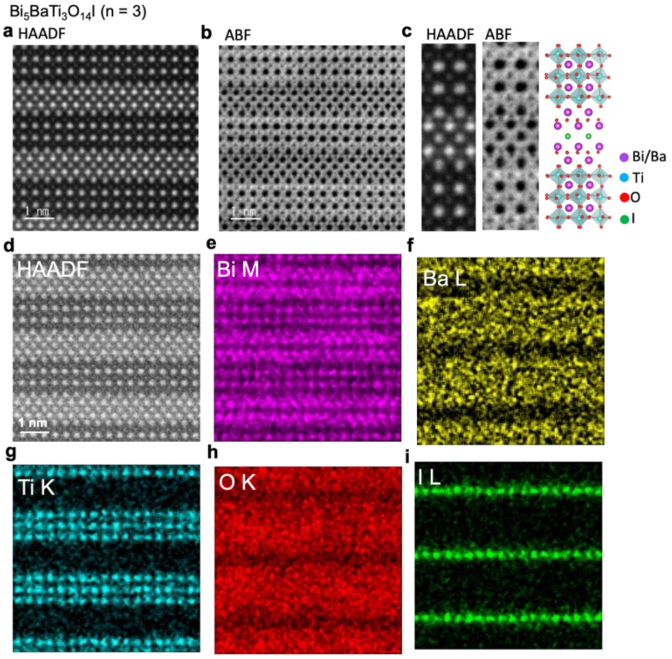

**Figure 2-8.** a,b, HAADF (a) and ABF (b) STEM images for $Bi_6NbWO_{14}I$ particle. b, Close-up HAADF and blue ABF images together with the corresponding $Bi_6NbWO_{14}I$ crystal structure. **d-h**, STEM-EDX atomic resolution elemental maps of the regions shown in d for Bi (**e**), Nb (**f**), W (**g**), O (**h**), I (**i**).

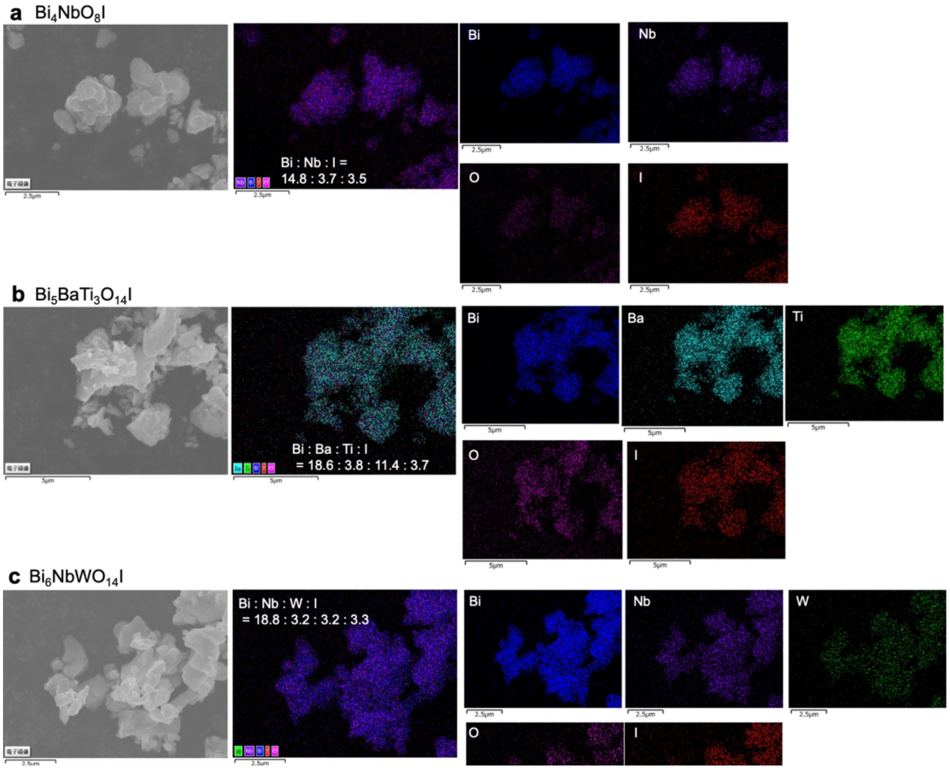

**Figure 2-9.** SEM images and SEM-EDS elemental mapping of of $Bi_4NbO_8I$, $Bi_5BaTi_3O_{14}I$ and $Bi_6NbWO_{14}I$ along with elemental molar ratios determined SEM-EDS analysis.

### Band Gaps and Positions

These oxyiodides absorb photons of longer wavelength and thus have narrower band gaps than the corresponding chloride counterparts (Figure 2-10a). In addition to the above three oxyioides, $BaMBi_3Nb_2O_{11}I$ (M = Ba, Sr, Ca) with double perovskite layer (n = 2) were also synthesized (Figure 2-11). While the n = 2 with M = Ba was reported as an active photocatalyst in our previous study,[34] the optical properties of its Sr and Ca substitutes have not investigated yet despite there being a synthetic report.[36] Figure 2-10b summarizes the band edge positions of these oxyiodides and the corresponding oxychloride, where VBMs of all the oxyiodides are negatively shifted as compared to the chloride counterparts. The VBMs of these oxyiodides are mainly composed of oxygen in the perovskite layers (Figure 2-12). As discussed in the previous report for n = 2, the high polarizability of iodine may energetically destabilize the oxygen in the perovskite layer, contributing to the negatively shifted VBM (Figure 2-13).

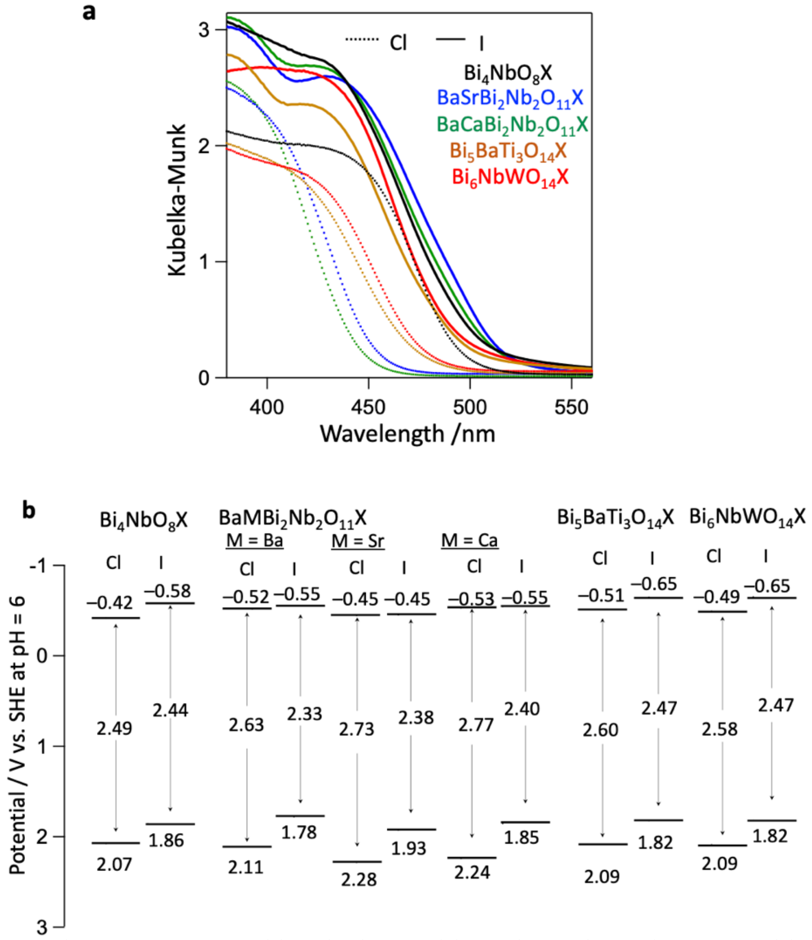

**Figure 2-10.** Absorption spectra (a) and band edge positions (b) of the series of oxychlorides and oxyiodides: $Bi_4NbO_8X$, $BaMBi_3Nb_2O_{11}X$ (M = Sr, Ca), $Bi_5BaTi_3O_{14}X$ and $Bi_6NbWO_{14}X$.

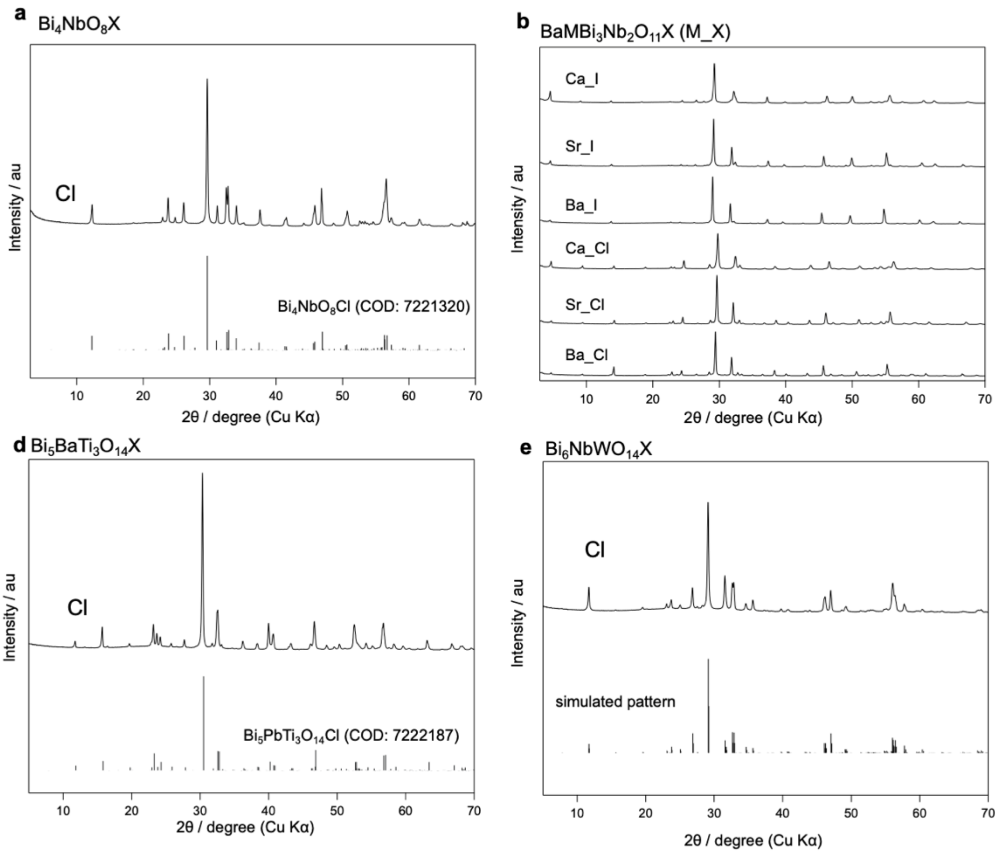

**Figure 2-11.** XRD patterns of $Bi_4NbO_8X$, $BaMBi_3Nb_2O_{11}X$ (M = Ca, Sr, Ba), $Bi_5BaTi_3O_{14}X$ and $Bi_6NbWO_{14}X$. As for $Bi_5BaTi_3O_{14}I$ and $Bi_6NbWO_{14}I$, the simulated diffraction patterns, with space group same as reported oxychloride (*P2an* and *Fmmm,* respectively) and lattice parameters determined by Le bail refinement, were shown.

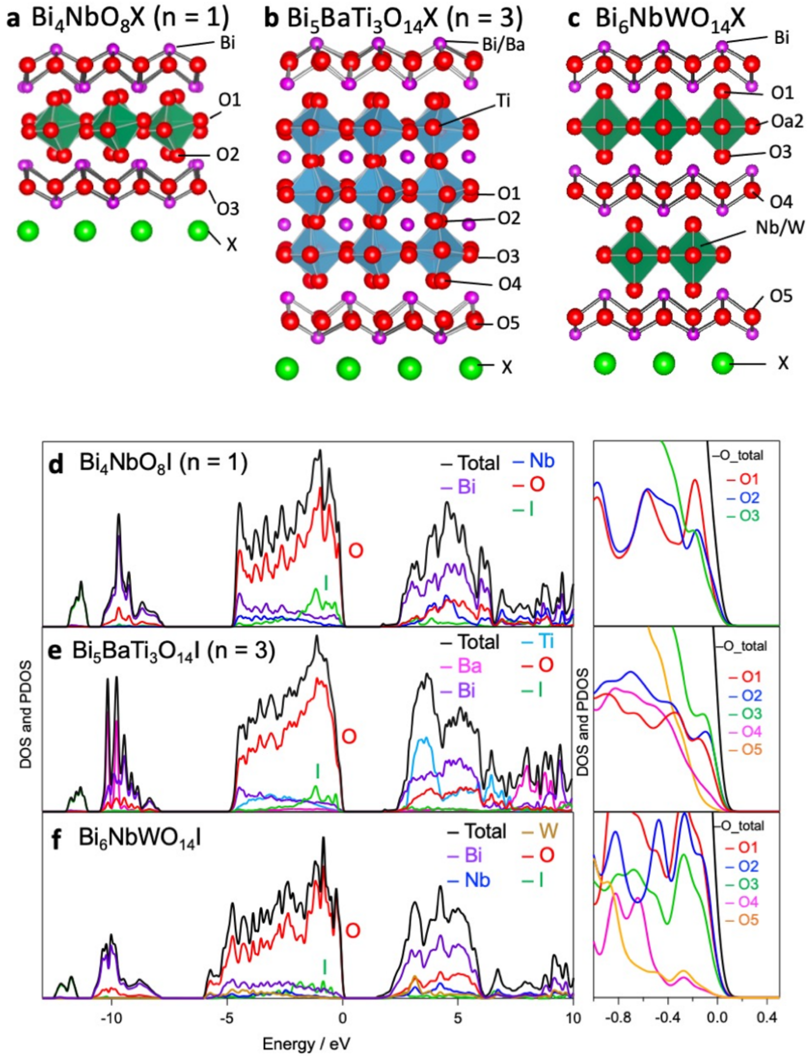

**Figure 2-12. a-b**, Crystal Structure and (d-f) electronic density of (a,d) $Bi_4NbO_8I$, (b,e) $Bi_5BaTi_3O_{14}I$ and (c,f) $Bi_6NbWO_{14}I$.

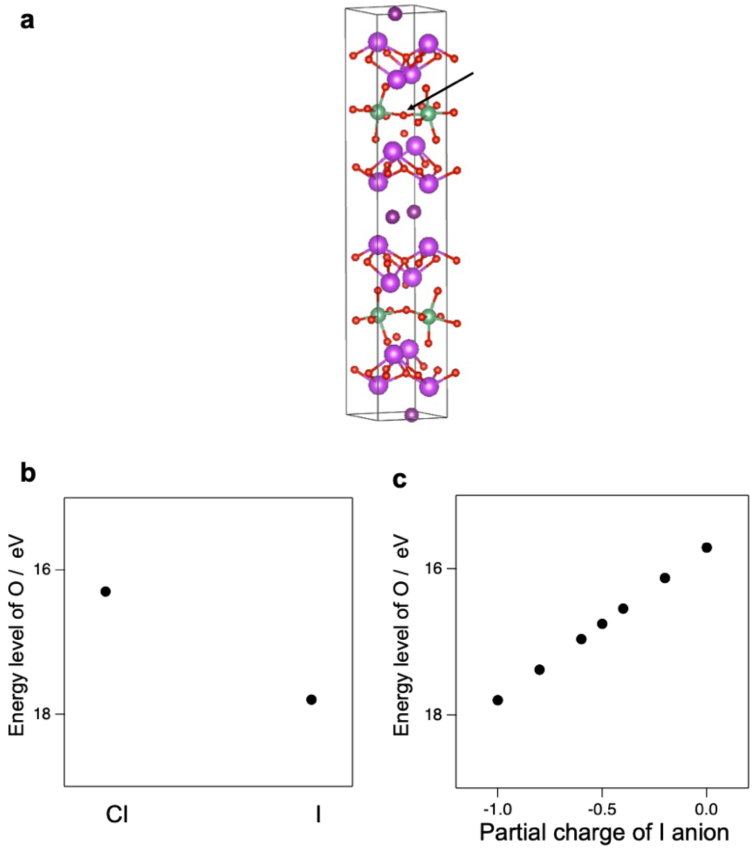

**Figure 2-13.** a, Crystal Structure of $Bi_4NbO_8I$. b, Ionic orbital energy levels of $O^{2-}$ at O site in $Bi_4NbO_8I$ (a) calculated by the sum of Madelung potential and second electron affinity of oxygen. d, The effect of the partial charge of I anion on the energy levels of O1 site in the Madelung potential analysis.

A notable difference from the case of n = 2 is the change of the CBM positions accompanied by replacing the chloride by iodide. While, in the case of n = 2, the iodine introduction exert little influence on the CBM position,[34] the other oxyiodides ($Bi_4NbO_8I$, $Bi_5BaTi_3O_{14}I$, and $Bi_6NbWO_{14}I$) have about 0.14~0.16 eV negatively shifted CBMs as compared its chloride counterparts (Figure 2-10b). Namely, both CBM and VBM are shifted by iodine introduction in the same direction, which enables negative CBM shift without sacrifice of the photo-absorption.

To elucidate the origin of the CBM shift accompanied by iodine introduction, we focused on the orbital interactions in the [$M_2O_2$] fluorite layer which mainly contributing to the CBMs of S–A compounds.[22,46] The characteristic structure of the fluorite like [$M_2O_2$] layer, where all four coordinated oxygen atoms are found on one side of M, is common in compounds containing post-transition metals with *n*s$^2$ electronic configuration, such as $Sn^{2+}$, $Pb^{2+}$ and $Bi^{3+}$, providing unique orbital interaction and band structures as intensively studied in various fields such as solar-to-energy conversion.[26] The key orbital interaction is the intra-layer interaction between metal-*n*s, -*n*p orbitals and anion orbitals, according to the RLP model proposed by Walsh *et al.*.[26] In addition to the intra-layer interaction, the inter-layer interaction between two *n*s$^2$ metals should be considered as Umezawa *et al.* demonstrated for the electronic structure of SnO.[47] Based on these reports, and by adding some modification, we can explain the origin of the CBM shift accompanied by iodine introduction.

Let us start with the intra-layer interaction between Bi and O in O-Bi-O block based on the RLP model. As illustrated in Figure 2-14a, Bi-6s orbital interacts with O-sp$^3$ orbital to form the bonding and antibonding states.[26] The latter is further interact with Bi-6p orbital (6$p_z$ in this case) to form (Antibonding + $p_z$) and (Antibonding + $p_z$)$^*$ state, while Bi-6$p_x$, $p_y$ have non-bonding characters. Although most studies have focused on the (Antibonding + $p_z$) state because their interests are mainly in the VBM (occupied state),[14,22,26] the (Antibonding + $p_z$)$^*$ state should be taken in to account to discuss about the CBM. Note that the (Antibonding + $p_z$)$^*$ state should not be energetically far from the non-bonding Bi-6$p_x$, 6$p_y$, because antibonding-nature of this state may be not so strong (Figure 2-14a).

Next, the inter-layer Bi-Bi interaction is considered for the conduction "band" formation.[48] Umezawa *et al.* showed that the CBM of the SnO is formed by the inter-layer Sn-Sn interaction.[47] The inter-layer Bi–Bi distance in the present materials (e.g., 3.9 Å in $Bi_4NbO_8Cl$)[21,49] is comparable to the Sn–Sn distance in SnO (3.8 Å),[47] which suggests that the inter-layer interaction should be considered also in the present case. In SnO, only the $p_x$–$p_x$ ($p_y$–$p_y$) interaction between $Sn^{2+}$ ions in different layers was discussed, because the $p_z$ orbitals in SnO are not facing each other and their orbital overlap is small. On the other hand, in the present S–A compounds, the $p_z$–$p_z$ interaction may be stronger than the $p_x$–$p_x$ ($p_y$–$p_y$) because $p_z$ orbitals of Bi in the different fluorite layers are facing each other. In other words, as shown in Figure 2-14b, the band width of the (Antibonding + $p_z$)$^*$ state may be wider than the $p_x$ ($p_y$) state. Note that the stronger the Bi-Bi interaction is, the wider the (Antibonding + $p_z$)$^*$ is (Figure 2-14b). Therefore, although the $p_x$ ($p_y$) state is energetically lower than the (Antibonding + $p_z$)$^*$ state without consideration of "band-width", the lower part of the unoccupied band can be contributed by the (Antibonding + $p_z$)$^*$ band if it has a wide band-width to overwhelm the $p_x$ ($p_y$) band (the right part of Figure 2-14b). In other words, the CBM composition depends on the strength of the Bi–Bi interaction; with weak interaction, the $p_x$ ($p_y$) state forms the CBM, while, with strong interaction, the (Antibonding + $p_z$)$^*$ state does.

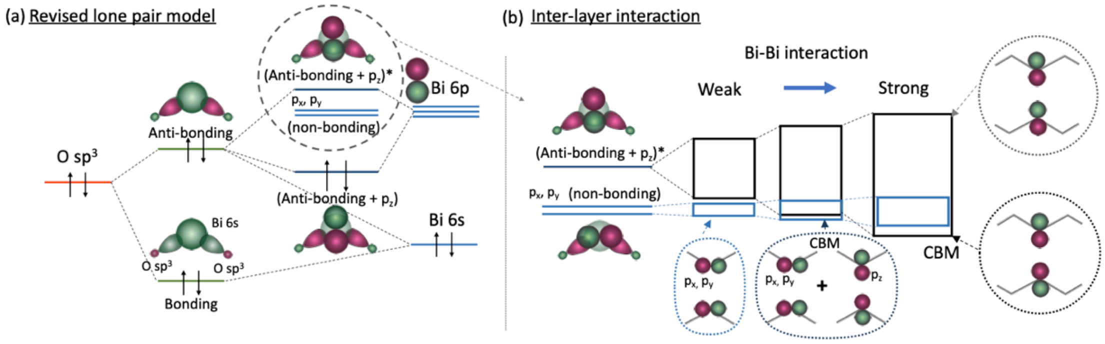

**Figure 2-14.** Formation of the conduction band of the S–A compounds via the (a) intra- and (b) inter-layer interaction.

The difference of CBM composition can explain whether the CBM is shifted or not by the iodine introduction. The replacement of Cl in a S–A compound by I increases the Bi–Bi distance, narrowing the band width of the (Antibonding + $p_z$)* band. Therefore, when the CBM of an oxy-chloride is composed of the (Antibonding + $p_z$)* band (the right side in Figure 2-14b), the iodine introduction will shift the CBM negatively by narrowing the band width. On the contrary, when the $p_x$ ($p_y$) band contributed to the CBM of an oxy-chloride (the middle or left side in Figure 2-14b), the iodine introduction will not strongly influence on the CBM position. As shown in Figure 2-15, the CBM of the n = 1 mainly comprises $p_z$ (Figure 2-15a). In addition, the density of state (DOS) that reveals the apparent participation of the antibonding state (Bi-6s and O orbital) to the CBM of the n = 1 (Figure 2-16), suggesting that the CBM is mainly composed of the (Antibonding + $p_z$)* band and therefore the CBM of n = 1 is negatively shifted by iodine introduction. On the other hand, for n = 2, x, y components of Bi-orbital apparently contribute to the CBM

(Figure 2-15c). These results suggest that the difference of the CBM component determines whether the CBM is shifted or not by the iodine introduction.

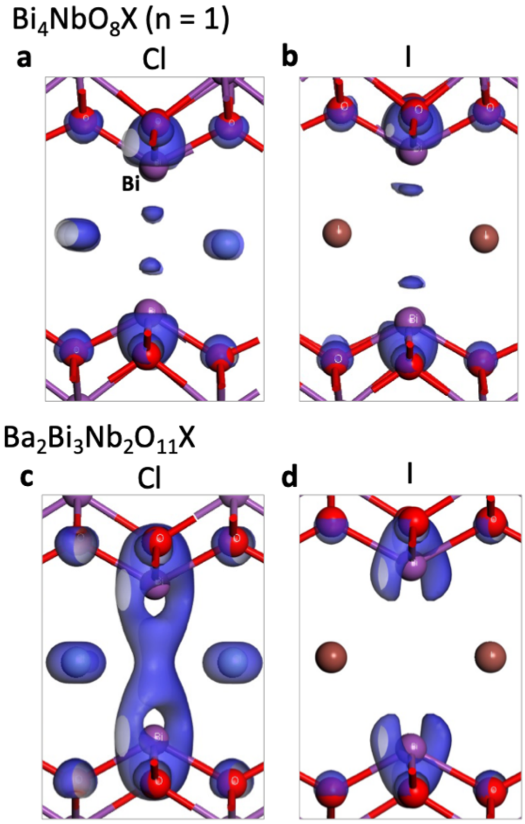

**Figure 2-15.** Orbital distribution of the lower parts of the conduction band of (a, b) $Bi_4NbO_8X$ (X = (a) Cl, (b) I) and (c, d,) $Bi_3Ba_2Nb_2O_{11}X$ (X = (c) Cl, (d) I) estimated by DFT calculation.

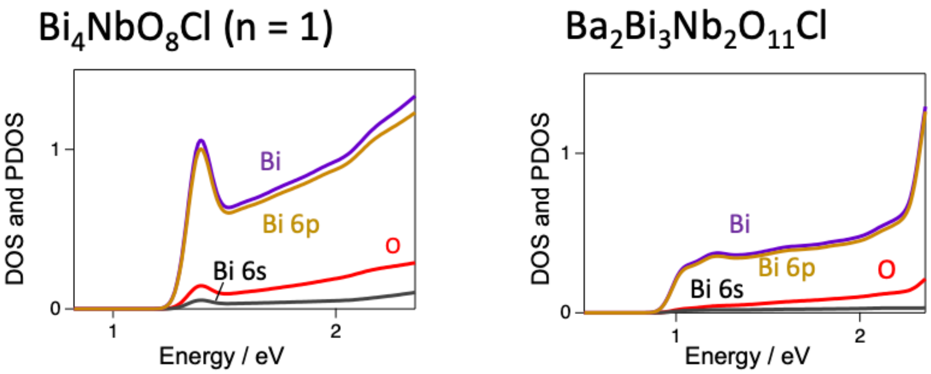

**Figure 2-16.** Density of state (DOS) around the CBM of $Bi_4NbO_8Cl$ and $Bi_3Ba_2Nb_2O_{11}Cl$.

The different composition of the CBM between the n = 1 and 2 may be associated with the inter-layer Bi–Bi distance in these chlorides. The n = 2 has the longer Bi–Bi distance than the n = 1, 3 and S–2A chlorides (Table 2-1). As shown in Figure 2-17, shortening Bi–Bi distance of the n = 2 chloride in DFT calculation with the strain-induced crystal structure increases Bi-$p_z$ component contributing to the CBM as in the n = 1. Therefore, the $p_z$–$p_z$ interaction in the n = 2 chloride having a long Bi–Bi distance may be relatively week, and thus the band width of the (Antibonding + $p_z$)* is narrow therein, which results in the CBM contributed by $p_x$ ($p_y$) component.

These results demonstrated that Bi–Bi distance controls the band width and the position of CBM of the S–A oxyhalides. It was theoretically reported that inter-layer Sn–Sn interaction determine the band gap of SnO, where the band-gap engineering can be realized by adjusting the number of the layers.[47] However, the CBM negative shift with this strategy is accompanied by widening the band gap because decreasing the Sn–Sn interaction narrows the band width of not only CBM but also VBM comprising (Antibonding + Sn–p) state. On the other hand, in the present S–A materials having unique electronic structures, the CBM is composed of the fluorite layer whereas the VBM is composed of the perovskite layer. The present study demonstrated that their positions are dominated by different factors; the former is affected by the interlayer Bi–Bi distance while the latter by the energetic stability of the oxygen in the perovskite layer. The iodine introduction exerts influence on the electronic structure of CB and VB thorough different mechanism, which enables the negative shift of both the CBM and VBM positions simultaneously and thus the CBM negative sift without the sacrifice of the photo-absorption.

**Table 2-1.** Interlayer Bi–Bi distance (Å) in each compound

| | $Bi_4NbO_8Cl$ | $Bi_3Ba_2Nb_2O_{11}Cl$ | $Bi_5BaTi_3O_{14}Cl$ | $Bi_6NbWO_{14}Cl$ |
|---|---|---|---|---|
| Cl | 3.895 | 3.934 | 3.8897 | 3.88566 |
| I | 4.621 | 4.566 | 4.62076 | 4.689 |

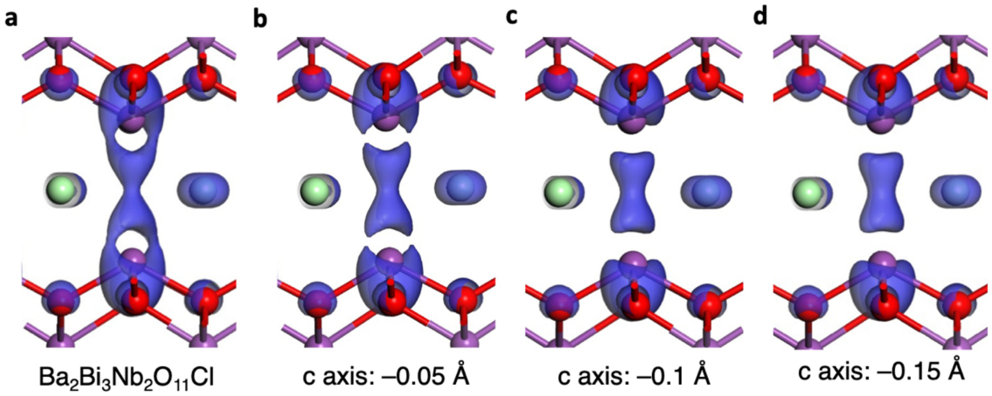

**Figure 2-17.** The effect of the decreased c lattice of the unit cell of the $Bi_3Ba_2Nb_2O_{11}Cl$ on the CBM distribution estimated by DFT calculation.

### Photocatalytic Activity

Table 2-2 summarizes the photocatalytic water oxidation activities of each sample under visible light in the presence of electron acceptors, $Ag^+$ ions. All the oxyiodides show $O_2$ evolution, functioning as water oxidation photocatalysts, which is in stark contrast to the case of negative shift of CBM by breaking Bi-O bonds, which results in the lost photocatalytic activity. Notably, the photocatalytic activity of each oxyiodide is superior to that of their oxychloride counterpart.

**Table 2-2.** The photocatalytic water oxidation activities of each sample under visible light in the presence of electron acceptors, $Ag^+$ ions.[a]

| no. | compound | Initial rate of $O_2$ evolution / μmol $h^{-1}$ | |
|---|---|---|---|
| | | I | Cl |
| 1 | $Bi_4NbO_8X$ (n = 1) | 41.5 | 4.8 |
| 2 | $Ba_2Bi_3Nb_2O_{11}X$ (n =2) | 37.6 | 4.7 |
| 3 | $BaSrBi_3Nb_2O_{11}X$ | 62.0 | 7.7 |
| 4 | $BaCaBi_3Nb_2O_{11}X$ | 32.3 | 6.2 |
| 5 | $Bi_5BaTi_3O_{14}X$ (n = 3) | 24.2 | 4.3 |
| 6 | $Bi_6NbWO_{14}X$ | 89.6 | 13.8 |

[a] Reaction condition: photocatalyst (0.1 g) dispersed in aqueous $AgNO_3$ solution (8 mM, 100 mL), light source: Xe lamp (300 W) fitted with L42 cutoff filter for visible-light irradiation ($\lambda > 400$ nm).

We used $Bi_6NbWO_{14}I$ showing the highest photocatalytic activity as an $O_2$ evolution photocatalyst in Z-scheme water splitting. $RuO_2$-loaded $Bi_6NbWO_{14}I$ achieved $O_2$ evolution in the presence of $Fe^{3+}$, which is the oxidant of the $Fe^{3+}/Fe^{2+}$ redox mediator, under visible-light illumination (Figure 2-18a). The amount of $Fe^{2+}$ ions converted from $Fe^{3+}$ ions by the photoexcited electrons in this half reaction was estimated by complexometric determination (Figure 2-18b), which was exactly four times the $O_2$ evolved, confirming the stoichiometric redox reaction (e.g., $4Fe^{3+} + 2H_2O \rightarrow O_2 + 4Fe^{2+} + 4H^+$). Subsequently, visible-light water splitting using $RuO_2$-loaded $Bi_6NbWO_{14}I$ was conducted with the $Fe^{3+}/Fe^{2+}$ couple as the redox mediator and Ru-loaded strontium titanate doped with Rh cations[40] ($Ru/SrTiO_3:Rh$) as the $H_2$-evolution photocatalyst. As shown in Figure 2-18c, $H_2$ and $O_2$ evolve stoichiometrically at steady rates, demonstrating Z-scheme water splitting.

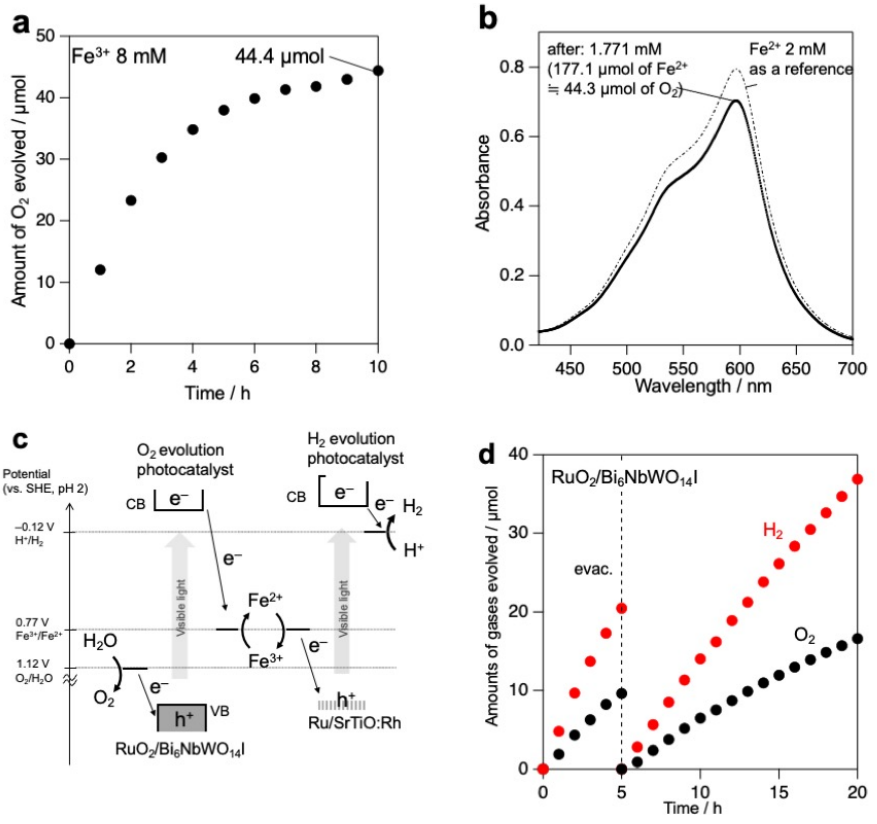

**Figure 2-18. a,** Time courses of $O_2$ evolution over $RuO_2$-loaded $Bi_6NbWO_{14}I$ sample in an aqueous $Fe(NO_3)_3$ solution (8 mM, 100 mL) at pH 2.4 under visible light irradiation (λ > 400 nm). **b,** Absorption spectra of $Fe^{2+}$ after the photocatalytic reaction of Fig. 3a detected as $Fe^{2+}$-2,4,6-tris(2-pyridyl)-1,3,5-triazine (TPTZ) complex complex. **c,** Time courses of $H_2$ and $O_2$ evolution over a mixture of $RuO_2$-loaded $Bi_6NbWO_{14}I$ and $Ru/SrTiO_3:Rh$ (50 mg each) in $FeCl_3$ aqueous solution (2 mM, 100 mL) at pH 2.4 under visible light irradiation (λ > 400 nm).

## 2.4. Conclusion

Three novel S–A oxyiodides was successfully synthesized. While the replacement of the chloride by iodide in S-A compound with n = 2 exerts little influence on the position of the CBM, the replacement by iodide negatively shift the CBM of n = 1, 3 and S–S–A, where the Bi–Bi interlayer interaction plays an important role. All the novel S–A oxyiodides show photocatalytic $O_2$ evolution activity much higher that their oxy chloride counterparts. The present study demonstrated the negative shift of the CBM by introducing iodine and changing the inter-layer interaction without sacrifice of the phot-absorptivity, and photocatalytic activity, which cannot be achieved via the previous strategy using the intra-layer interaction.[33] Further modification of the charge of each layer and making solid-solutions of Cl and I will control the Bi–Bi interlayer interaction, enabling fine tuning of the band positions. The present strategy using the interlayer interaction will offer a new insight into the controlling the optoelectronic property of $ns^2np^0$ semiconductors.

## Reference

(1) Zhao, Y.; Qiao, J.; Yu, P.; Hu, Z.; Lin, Z.; Lau, S. P.; Liu, Z.; Ji, W.; Chai, Y. Extraordinarily Strong Interlayer Interaction in 2D Layered $PtS_2$. *Adv. Mater.* **2016**, *28*, 2399–2407.

(2) Ohta, T.; Bostwick, A.; Seyller, T.; Horn, K.; Rotenberg, E. Controlling the Electronic Structure of Bilayer Graphene. *Science* **2006**, *313*, 951–954.

(3) Zhang, Y.; Tang, T.-T.; Girit, C.; Hao, Z.; Martin, M. C.; Zettl, A.; Crommie, M. F.; Shen, Y. R.; Wang, F. Direct Observation of a Widely Tunable Bandgap in Bilayer Graphene. *Nature* **2009**, *459*, 820–823.

(4) Qiao, J.; Kong, X.; Hu, Z.-X.; Yang, F.; Ji, W. High-Mobility Transport Anisotropy and Linear Dichroism in Few-Layer Black Phosphorus. *Nat Commun* **2014**, *5*, 4475.

(5) Kang, J.; Tongay, S.; Zhou, J.; Li, J.; Wu, J. Band Offsets and Heterostructures of Two-Dimensional Semiconductors. *Appl. Phys. Lett.* **2013**, *102*, 012111.

(6) Qian, X.; Liu, J.; Fu, L.; Li, J. Quantum Spin Hall Effect in Two-Dimensional Transition Metal Dichalcogenides. *Science* **2014**, *346*, 1344–1347.

(7) Withers, F.; Del Pozo-Zamudio, O.; Mishchenko, A.; Rooney, A. P.; Gholinia, A.; Watanabe, K.; Taniguchi, T.; Haigh, S. J.; Geim, A. K.; Tartakovskii, A. I.; Novoselov, K. S. Light-Emitting Diodes by Band-Structure Engineering in van Der Waals Heterostructures. *Nature Mater* **2015**, *14*, 301–306.

(8) Li, M.-Y.; Shi, Y.; Cheng, C.-C.; Lu, L.-S.; Lin, Y.-C.; Tang, H.-L.; Tsai, M.-L.; Chu,

C.-W.; Wei, K.-H.; He, J.-H.; Chang, W.-H.; Suenaga, K.; Li, L.-J. Epitaxial Growth of a Monolayer $WSe_2$-$MoS_2$ Lateral p-n Junction with an Atomically Sharp Interface. *Science* **2015**, *349*, 524–528.

(9) Jaramillo, T. F.; Jørgensen, K. P.; Bonde, J.; Nielsen, J. H.; Horch, S.; Chorkendorff, I. Identification of Active Edge Sites for Electrochemical $H_2$ Evolution from $MoS_2$ Nanocatalysts. *Science* **2007**, *317*, 100–102.

(10) Splendiani, A.; Sun, L.; Zhang, Y.; Li, T.; Kim, J.; Chim, C.-Y.; Galli, G.; Wang, F. Emerging Photoluminescence in Monolayer $MoS_2$. *Nano Lett.* **2010**, *10*, 1271–1275.

(11) Hong, X.; Kim, J.; Shi, S.-F.; Zhang, Y.; Jin, C.; Sun, Y.; Tongay, S.; Wu, J.; Zhang, Y.; Wang, F. Ultrafast Charge Transfer in Atomically Thin $MoS_2$/$WS_2$ Heterostructures. *Nature Nanotech* **2014**, *9*, 682–686.

(12) Lin, X.; Huang, T.; Huang, F.; Wang, W.; Shi, J. Photocatalytic Activity of a Bi-Based Oxychloride $Bi_4NbO_8Cl$. *J. Mater. Chem.* **2007**, *17*, 2145.

(13) Wei, X.; Akbar, M. U.; Raza, A.; Li, G. A Review on Bismuth Oxyhalide Based Materials for Photocatalysis. *Nanoscale Adv.* **2021**, *3*, 3353–3372.

(14) Fujito, H.; Kunioku, H.; Kato, D.; Suzuki, H.; Higashi, M.; Kageyama, H.; Abe, R. Layered Perovskite Oxychloride $Bi_4NbO_8Cl$: A Stable Visible Light Responsive Photocatalyst for Water Splitting. *J. Am. Chem. Soc.* **2016**, *138*, 2082–2085.

(15) Nakada, A.; Higashi, M.; Kimura, T.; Suzuki, H.; Kato, D.; Okajima, H.; Yamamoto, T.; Saeki, A.; Kageyama, H.; Abe, R. Band Engineering of Double-Layered Sillén–Aurivillius Perovskite Oxychlorides for Visible-Light-Driven Water Splitting. *Chem. Mater.* **2019**, *31*, 3419–3429.

(16) Ozaki, D.; Suzuki, H.; Ogawa, K.; Sakamoto, R.; Inaguma, Y.; Nakashima, K.; Tomita, O.; Kageyama, H.; Abe, R. Synthesis, Band Structure and Photocatalytic Properties of Sillén–Aurivillius Oxychlorides $BaBi_5Ti_3O_{14}Cl$, $Ba_2Bi_5Ti_4O_{17}Cl$ and $Ba_3Bi_5Ti_5O_{20}Cl$ with Triple-, Quadruple- and Quintuple-Perovskite Layers. *J. Mater. Chem. A* **2021**, *9*, 8332–8340.

(17) Shi, Y.; Li, J.; Mao, C.; Liu, S.; Wang, X.; Liu, X.; Zhao, S.; Liu, X.; Huang, Y.; Zhang, L. Van Der Waals Gap-Rich BiOCl Atomic Layers Realizing Efficient, Pure-Water $CO_2$-to-CO Photocatalysis. *Nat Commun* **2021**, *12*, 5923.

(18) Sillén, L. G. Uber eine Familie yon Oxyhalogeniden. *Die Naturwissenschaften 30*, 318–324.

(19) Dolgikh, V. A.; Kholodkovskaya, L. N. The Crystal Chemistry of Metal Oxide Halides and Oxides Chalcogenides. *Russ. J. Inorg. Chem* **1992**, *37*, 488.

(20) Aurivillius, B. Intergrowth Compounds between Members of Te Bismuth Titanate Family and Structures of the $LiBi_2O_4Cl_2$ Type - an Architectural Approach. *Chem. Scr.* **1984**, *23*, 143.

(21) Kusainova, A. M.; Stefanovich, S. Yu.; Dolgikh, V. A.; Mosunov, A. V.; Hervoches, C. H.; Lightfoot, P. Dielectric Properties and Structure of $Bi_4NbO_8Cl$ and $Bi_4TaO_8Cl$. *J. Mater. Chem.* **2001**, *11*, 1141–1145.

(22) Kunioku, H.; Higashi, M.; Tomita, O.; Yabuuchi, M.; Kato, D.; Fujito, H.; Kageyama, H.; Abe, R. Strong Hybridization between Bi-6s and O-2p Orbitals in Sillén–Aurivillius

Perovskite $Bi_4MO_8X$ (M = Nb, Ta; X = Cl, Br), Visible Light Photocatalysts Enabling Stable Water Oxidation. *J. Mater. Chem. A* **2018**, *6*, 3100–3107.

(23) Suzuki, H.; Kunioku, H.; Higashi, M.; Tomita, O.; Kato, D.; Kageyama, H.; Abe, R. Lead Bismuth Oxyhalides $PbBiO_2X$ (X = Cl, Br) as Visible-Light-Responsive Photocatalysts for Water Oxidation: Role of Lone-Pair Electrons in Valence Band Engineering. *Chem. Mater.* **2018**, *30*, 5862–5869.

(24) Nakada, A.; Kato, D.; Nelson, R.; Takahira, H.; Yabuuchi, M.; Higashi, M.; Suzuki, H.; Kirsanova, M.; Kakudou, N.; Tassel, C.; Yamamoto, T.; Brown, C. M.; Dronskowski, R.; Saeki, A.; Abakumov, A.; Kageyama, H.; Abe, R. Conduction Band Control of Oxyhalides with a Triple-Fluorite Layer for Visible Light Photocatalysis. *J. Am. Chem. Soc.* **2021**, *143*, 2491–2499.

(25) Suzuki, H.; Higashi, M.; Tomita, O.; Ishii, Y.; Yamamoto, T.; Kato, D.; Kotani, T.; Ozaki, D.; Nozawa, S.; Nakashima, K.; Fujita, K.; Saeki, A.; Kageyama, H.; Abe, R. $PbBi_3O_4X_3$ (X = Cl, Br) with Single/Double Halogen Layers as a Photocatalyst for Visible-Light-Driven Water Splitting: Impact of a Halogen Layer on the Band Structure and Stability. *Chem. Mater.* **2021**, acs.chemmater.1c02876.

(26) Walsh, A.; Payne, D. J.; Egdell, R. G.; Watson, G. W. Stereochemistry of Post-Transition Metal Oxides: Revision of the Classical Lone Pair Model. *Chem. Soc. Rev.* **2011**, *40*, 4455.

(27) Bainglass, E.; Walsh, A.; Huda, M. N. $BiSbWO_6$: Properties of a Mixed 5s/6s Lone-Pair-Electron System. *Chemical Physics* **2021**, *544*, 111117.

(28) Takanabe, K. Photocatalytic Water Splitting: Quantitative Approaches toward Photocatalyst by Design. *ACS Catal.* **2017**, *7*, 8006–8022.

(29) Kadowaki, H.; Saito, N.; Nishiyama, H.; Kobayashi, H.; Shimodaira, Y.; Inoue, Y. Overall Splitting of Water by $RuO_2$ -Loaded $PbWO_4$ Photocatalyst with $d^{10}s^2$-$d^0$ Configuration. *J. Phys. Chem. C* **2007**, *111*, 439–444.

(30) Brandt, R. E.; Stevanović, V.; Ginley, D. S.; Buonassisi, T. Identifying Defect-Tolerant Semiconductors with High Minority-Carrier Lifetimes: Beyond Hybrid Lead Halide Perovskites. *MRS Communications* **2015**, *5*, 265–275.

(31) Kang, J.; Wang, L.-W. High Defect Tolerance in Lead Halide Perovskite $CsPbBr_3$. *J. Phys. Chem. Lett.* **2017**, *8*, 489–493.

(32) Du, M. H. Efficient Carrier Transport in Halide Perovskites: Theoretical Perspectives. *J. Mater. Chem. A* **2014**, *2*, 9091–9098.

(33) Nakada, A. Conduction Band Control of Oxyhalides with a Triple-Fluorite Layer for Visible Light Photocatalysis. *Journal of the American Chemical Society* 9.

(34) Ogawa, K.; Suzuki, H.; Zhong, C.; Sakamoto, R.; Tomita, O.; Saeki, A.; Kageyama, H.; Abe, R. Layered Perovskite Oxyiodide with Narrow Band Gap and Long Lifetime Carriers for Water Splitting Photocatalysis. *J. Am. Chem. Soc.* **2021**, *143*, 8446–8453.

(35) Charkin, D. O.; Lebedev, D. N.; Kazakov, S. M. Multiple Cation and Anion Substitutions into the Structures of $Bi_2WO_6$ and $PbBi_3WO_8Cl$. *Journal of Alloys and Compounds* **2012**, *536*, 155–160.

(36) Charkin, D. O.; Akinfiev, V. S.; Alekseeva, A. M.; Batuk, M.; Abakumov, A. M.;

Kazakov, S. M. Synthesis and Cation Distribution in the New Bismuth Oxyhalides with the Sillén–Aurivillius Intergrowth Structures. *Dalton Trans.* **2015**, *44*, 20568–20576.

(37) Shannon, R. D.; Waring, R. K. Synthesis and Characterization of a New Series of $BiOI_{1-x-y}Br_xCl_y$, Pigment. *J. Phys. Chem. Solids.* **1985**, *46*, 325–330.

(38) Blake, S. M.; Falconer, M. J.; Mark, M.; Lightfoot, P. Cation Disorder in Ferroelectric Aurivillius Phases of the Type $Bi_2ANb_2O_9$ (A=Ba, Sr, Ca). *J. Mater. Chem.* **1997**, *7*, 1609–1613.

(39) Konta, R.; Ishii, T.; Kato, H.; Kudo, A. Photocatalytic Activities of Noble Metal Ion Doped $SrTiO_3$ under Visible Light Irradiation. *J. Phys. Chem. B* **2004**, *108*, 8992–8995.

(40) Sasaki, Y.; Iwase, A.; Kato, H.; Kudo, A. The Effect of Co-Catalyst for Z-Scheme Photocatalysis Systems with an $Fe^{3+}/Fe^{2+}$ Electron Mediator on Overall Water Splitting under Visible Light Irradiation. *Journal of Catalysis* **2008**, *259*, 133–137.

(41) Clark, S. J.; Segall, M. D.; Pickard, C. J.; Hasnip, P. J.; Probert, M. I. J.; Refson, K.; Payne, M. C. First Principles Methods Using CASTEP. *Z. Kristallogr.* **2005**, *220*, 567–570.

(42) Izumi, F.; Momma, K. Three-Dimensional Visualization in Powder Diffraction. *Solid State Phenom.* **2007**, *130*, 15–20.

(43) Kunioku, H.; Higashi, M.; Tassel, C.; Kato, D.; Tomita, O.; Kageyama, H.; Abe, R. Sillén–Aurivillius-Related Oxychloride $Bi_6NbWO_{14}Cl$ as a Stable $O_2$-Evolving Photocatalyst in Z-Scheme Water Splitting under Visible Light. *Chem. Lett.* **2017**, *46*, 583–586.

(44) Ozaki, D.; Suzuki, H.; Tomita, O.; Inaguma, Y.; Nakashima, K.; Kageyama, H.; Abe, R. A New Lead-Free Sillén–Aurivillius Oxychloride $Bi_5SrTi_3O_{14}Cl$ with Triple-Perovskite Layers for Photocatalytic Water Splitting under Visible Light. *Journal of Photochemistry and Photobiology A: Chemistry* **2021**, *408*, 113095.

(45) Aguado, E.; Enjalbert, R.; Rojo, J. M.; Castro, A. Síntesis, caracterización estructural y medidas de conductividad de $Bi_3NbO_7$. *Boletín de la Sociedad Española de Cerámica y Vidrio* **1995**, *34*, 417–420.

(46) Zhou, X.; Dong, H. Density Functional Studies on Layered Perovskite Oxyhalide $Bi_4MO_8X$ Photocatalysts (M = Nb and Ta, X = Cl, Br, and I). *J. Phys. Chem. C* **2017**, *121*, 20662–20672.

(47) Zhou, W.; Umezawa, N. Band Gap Engineering of Bulk and Nanosheet SnO: Insight into the Interlayer Sn-Sn Lone Pair Interactions. *Phys. Chem. Chem. Phys.* **2015**, 17816--17820.

(48) Hoffmann, R. *Solids and Surfaces: A Chemists View of Bonding in Extended Structures*; VCH Publishers, 1988.

(49) Zhong, C.; Kato, D.; Takeiri, F.; Fujii, K.; Yashima, M.; Nishiwaki, E.; Fujii, Y.; Koreeda, A.; Tassel, C.; Abe, R.; Kageyama, H. Single Crystal Growth of Sillén–Aurivillius Perovskite Oxyhalides $Bi_4NbO_8X$ (X = Cl, Br). *Inorganics* **2018**, *6*, 41.

# Chapter 3

## Flux Synthesis of Layered Oxyhalide $Bi_4NbO_8Cl$ Photocatalyst for Efficient Z-Scheme Water Splitting Under Visible Light

## 3.1. Introduction

Photocatalytic water splitting employing semiconductor materials is of great attractive because of the potential for clean $H_2$ production by harvesting abundant solar light.[1–6] The efficient utilization of visible light, which constitutes approximately half of the incident light of the solar spectrum, is indispensable for achieving a high efficiency in terms of solar to hydrogen conversion. Hence, various narrow bandgap semiconductors have been widely studied as potential candidates for visible-light responsible photocatalysts, which are subsequently applied to the conventional one-step or the two-step (i.e., Z-scheme) water splitting systems.[3,4,7–13] We have reported stable and efficient water oxidation by a layered Sillén−Aurivillius-type oxychloride $Bi_4NbO_8Cl$ under visible light. The stable Z-scheme water splitting was also demonstrated when combined with a $H_2$-evolving photocatalyst via an $Fe^{3+}/Fe^{2+}$ shuttle redox.[14] Subsequently, a series of isostructural $Bi_4MO_8X$ (M = Nb, Ta; X = Cl, Br)[15] are also found to function as stable photocatalysts for visible light $O_2$ evolution.[16] The valence band maxima (VBMs) in $Bi_4MO_8X$ consist primarily of O-2p orbitals, instead of Cl-3p or Br-4p orbitals, with much more negative potential than those of typical oxides or oxychlorides.[16,17] These features allow visible-light responsibility and high photostability, while maintaining sufficiently negative conduction band minimums (CBMs) even for water reduction.[16]

A following synthetic study on $Bi_4MO_8X$ via solid-state reaction (SSR) revealed that the photocatalytic activity of $Bi_4MO_8X$ particles is significantly affected by both the calcination temperature and the amount of halogen precursors.[18] When the stoichiometric precursors were heated at higher temperatures, the crystallite sizes of $Bi_4MO_8X$ decreased with the production of cleavages along the in-plane direction. In addition, higher temperature treatment led to the volatilization of halogen species, creating halogen defects that can act as recombination centers of photogenerated carriers and consequently lower the photocatalytic activity. Hence, adding excess amount of the precursor BiOX considerably improved the photocatalytic activities of $Bi_4MO_8X$, possibly due to the reduced halogen defects.[18]

Given the above, the flux synthesis with molten salts containing the halogen anions seems an effective strategy to improve the activity of such oxyhalide photocatalysts. The molten salts are expected to serve as a halogen source minimizing unfavorable halogen defects, not only working as a flux that provides high crystallinity with well-defined surfaces and thereby improving the activity as proven on some metal oxide and oxynitride photocatalysts.[19–21] An improved photocatalytic activity of $Bi_4TaO_8Cl$ was recently demonstrated by employing the KCl/NaCl molten salt as a flux at 700 °C.[22] It is however unfortunate that neither the influence of the preparation conditions nor the origin of the improved activity were presented.

Here, we report the synthesis of $Bi_4NbO_8Cl$ via a liquid-state flux method in air using three different molten salts: KCl, CsCl, and the eutectic mixture of CsCl/NaCl, under a range of calcination conditions, to systematically investigate their influence on the physicochemical properties of the obtained $Bi_4NbO_8Cl$ particles and the resultant photocatalytic activity. Time-resolved microwave conductivity (TRMC) was utilized to reveal the relation between the synthesis procedure and the charge dynamics in the $Bi_4NbO_8Cl$ photocatalyst, as well as the role of cocatalysts for enhancing the activity. Improved efficiency of the Z-scheme water splitting into $H_2$ and $O_2$ under visible light is achieved for optimized $Bi_4NbO_8Cl$ photocatalyst coupled with Ru-loaded $SrTiO_3$:Rh as a $H_2$-evolving photocatalyst and an $Fe^{3+}/Fe^{2+}$ electron mediator.

## 3.2. Experimental

### Sample Preparation

$Bi_4NbO_8Cl$ samples were prepared by a flux method using $Bi_2O_3$ (Wako Pure Chemicals Industries, Ltd., 99.99%), BiOCl (Wako Pure Chemicals Industries, Ltd., 99.5%), and $Nb_2O_5$ (Wako Pure Chemicals Industries, Ltd., 99.9%) as raw materials. A molten salt of an alkali metal chloride (KCl (Wako Pure Chemicals Industries, Ltd., 99.5%), CsCl (Wako Pure Chemicals Industries, Ltd., 99.0%)), or the eutectic mixture (65:35) of CsCl and NaCl (Wako Pure Chemicals Industries, Ltd., 99.5%) (CsCl/NaCl) was used as a flux. The flux was mixed with $Bi_2O_3$, BiOCl, and $Nb_2O_5$ at the stoichiometric molar ratio for $Bi_4NbO_8Cl$ (3:2:1), at a solute concentration ($Bi_4NbO_8Cl$/ ($Bi_4NbO_8Cl$ + flux)) of 5 mol% (0.5 and 1 mol% for CsCl/NaCl). The total mass was set as 25 g. The mixture was placed in an alumina crucible with a capacity of 30 $cm^3$, heated to a setting temperature (600–800 °C) at a heating rate of 50 °C $h^{-1}$, and held at the temperature for 10 h. After natural cooling, the product was thoroughly washed with deionized water and finally collected by filtration. The obtained powder samples were dried at room temperature. For the reaction with the CsCl/NaCl flux, various conditions (solute concentration: 0.5, 1, and 5 mol%, calcination time: 5, 10 and 20 h) were employed. For comparison, the $Bi_4NbO_8Cl$ sample was prepared by SSR;[15] A stoichiometric mixture of $Bi_2O_3$, BiOCl, and $Nb_2O_5$ was heated in an evacuated silica tube at 900 °C for 20 h.

As a cocatalyst on $Bi_4NbO_8Cl$ particles, ruthenium oxide (denoted hereafter as $RuO_2$) or platinum (Pt) was loaded. A small amount of $Bi_4NbO_8Cl$ specimen was mixed with an aqueous solution containing $RuCl_3 \cdot nH_2O$ (Wako Pure Chemicals Industries, Ltd., 99.9%) or $H_2PtCl_6 \cdot 6H_2O$ (Wako Pure Chemicals Industries, Ltd., 99.9%), followed by heating under an Ar flow at 450 °C for 30 min or a $H_2$ flow at 150 °C for 30 min. X-ray photoelectron spectroscopy showed that these metal species after the loading were $Ru^{4+}$ and $Pt^0$.

Rh-doped $SrTiO_3$ powder, with the atomic ratio of Sr/Ti/Rh of 1.07/1.0/0.01 was prepared by the following SSR.[23] The production of the intended $SrTiO_3$:Rh was confirmed using XRD and UV-visible DRS. Ru (0.7 wt%) was photodeposited on the photocatalyst as a cocatalyst in a 10 vol% aqueous MeOH solution containing $RuCl_3 \cdot nH_2O$, as reported in a previous paper.[24]

### Characterization

Powder X-ray diffraction (XRD) patterns were obtained by a Rigaku MiniFlex IIdiffractometer using Cu $K_a$ radiation. Scanning electron microscopy (SEM) images were collected using a Zeiss Nvision 40 microscope. Transmission electron microscopy (TEM) was carried out using a JEOL JEM-2100F microscope. The Brunauer-Emmett-Teller (BET) surface area was measured using a MicrotracBEL BELSORP–miniII instrument at the liquid nitrogen temperature. X-ray photoelectron spectroscopy (XPS) measurements were carried out using an ULVAC-PHI 5500MT system.

### Photocatalytic Reactions

The photocatalytic reactions were performed in a gas closed-circulation system. Photocatalyst powders (0.1 g) were dispersed in an aqueous $FeCl_3$ solution (100 mL) in a Pyrex top-window cell. The reactant solution pH was adjusted to ~2.4 with diluted aqueous HCl solution. The photocatalysts were irradiated with visible light ($\lambda > 420$ nm) through a cutoff filter (HOYA; L42) from a 300-W Xe-arc lamp (Perkin Elmer; Cermax-PE300BF). The quantity of the evolved gases was determined using an online gas chromatograph (thermal conductivity detector (TCD); molecular sieve 5 Å column packing; Ar carrier gas). The apparent quantum efficiency (AQE) was evaluated using a 420-nm monochromatic light source.

For the overall water-splitting reaction, the Ru-loaded $SrTiO_3$:Rh (0.05 g) and $Bi_4NbO_8Cl$ (0.05 g), as $H_2$- and $O_2$-evolving photocatalysts, respectively, were suspended in an aqueous $FeCl_3$ solution (2 mM, 100 mL). The solution pH was adjusted to ~2.4 with diluted aqueous HCl solution. The suspension was irradiated using a 300-W Xe-arc lamp. The evolved gases were analyzed using an online gas chromatograph.

### Adsorption Experiments

The amounts of $Fe^{3+}$ and $Fe^{2+}$ adsorbed onto each photocatalyst sample were qualified as follows. The photocatalyst particles (20 mg) were suspended in an aqueous solution (5 mL) containing different amounts of Fe cations ($FeCl_3$ or $FeCl_2$, 1–8 mM) in darkness at 20 °C for 15 h by use of a magnetic stirring. After filtrating the sample aliquots, the concentrations of Fe cations remained in the solutions were determined from the absorption spectra of the solutions measured by UV-vis spectroscopy (UV-1800, Shimadzu) to estimate the adsorption amounts.

### Time-resolved Microwave Conductivity (TRMC) Measurement

TRMC experiments were conducted to evaluate the charge dynamics of the samples. The X-band microwave (~9.1 GHz) and third harmonic generation (THG; 355 nm) of a Nd:YAG laser (Continuum Inc., Surelite II, 5–8 ns pulse duration, 10 Hz) were used as the probe and excitation ($4.6 \times 10^{15}$ photons $cm^{-2}$ $pulse^{-1}$), respectively. The photoconductivity $\Delta\sigma$ was calculated by the following formula: $\Delta\sigma = \Delta P_r/(AP_r)$, where $\Delta P_r$, $A$, and $P_r$ are the transient power change of microwave reflected, the sensitivity factor, and the power of microwave reflected, respectively. The obtained $\Delta\sigma$ values were then converted to the product of the quantum yield ($\varphi$) and the sum of the charge carrier mobilities [$\sum\mu$ ($= \mu_+ + \mu_-$)] by the following formula: $\phi\sum\mu = \Delta\sigma(eI_0F_{light})^{-1}$, in which $e$ and $F_{light}$ are the unit charge of a single electron and a correction (or filling) factor, respectively. All of the TRMC measurements were performed in ambient atmosphere at room temperature (25 °C).

**Electrochemical Measurement**

The catalytic ability of metal oxides ($RuO_2$) or metal (Pt) used as cocatalysts were evaluated by electrochemical measurements. Each particles was prepared on a conductive glass (FTO) substrate via the same procedure as that on $Bi_4NbO_8Cl$ as follows: A small amount (50 μL) of $RuCl_3$ or $H_2PtCl_6 \cdot 6H_2O$ aqueous solution (10 mM) was deposited on an FTO substrate, and the substrate was dried in air at room temperature and subsequently calcined under an Ar flow (20 mL $min^{-1}$) at 450 °C for 30 min or a $H_2$ flow (20 mL $min^{-1}$) at 150 °C for 30 min. It is confirmed that the valence states of the metal cations loaded on the FTO substrates were the same as those loaded on $Bi_4NbO_8Cl$ by XPS analysis. The electrochemical measurements were performed using a potentiostat (VersaSTAT3, Princeton Applied Research Co., Ltd.) and a cell consisted of a prepared electrode, a Pt wire and a Ag/AgCl electrode as the working electrode, the counter electrode and the reference electrode, respectively.

## 3.3. Results and Discussion

### Effect of the Kind of Molten Salts on the Formation of $Bi_4NbO_8Cl$ Particles

In the present study, three kinds of molten salts with different melting points (KCl: 771 °C, CsCl: 645 °C, CsCl/NaCl: 486 °C) were employed as a flux to prepare $Bi_4NbO_8Cl$ particles. Figure 3-1 shows the XRD patterns of the samples prepared with fluxes at different temperatures from 600 °C to 900 °C. It is noteworthy that the air calcination of the precursor mixture at 650 °C without any molten salts resulted in several strong impurity peaks, as shown in Figure 3-2. On the contrary, when the salts were used, the $Bi_4NbO_8Cl$ phase was observed as the primary product even at 650 °C, though some peaks derived from impurities were present. As shown in Figures 1a and 1b, the synthesis with KCl or CsCl at below 700 °C resulted in small but appreciable impurity peaks at approximately $2\theta = 29°$ (see the enlarged panels). Most remarkably, when a eutectic mixture CsCl/NaCl with a much lower melting point was used the impurity formation was drastically suppressed. As shown in Figure 3-1c, an almost pure $Bi_4NbO_8Cl$ phase was obtained at 650 °C. Clearly, the lower melting point of the CsCl/NaCl flux promotes the sufficient diffusion of precursor ions, affording the single-phase formation. A lower temperature treatment (e.g. 600 °C) gave again impurity reflections.

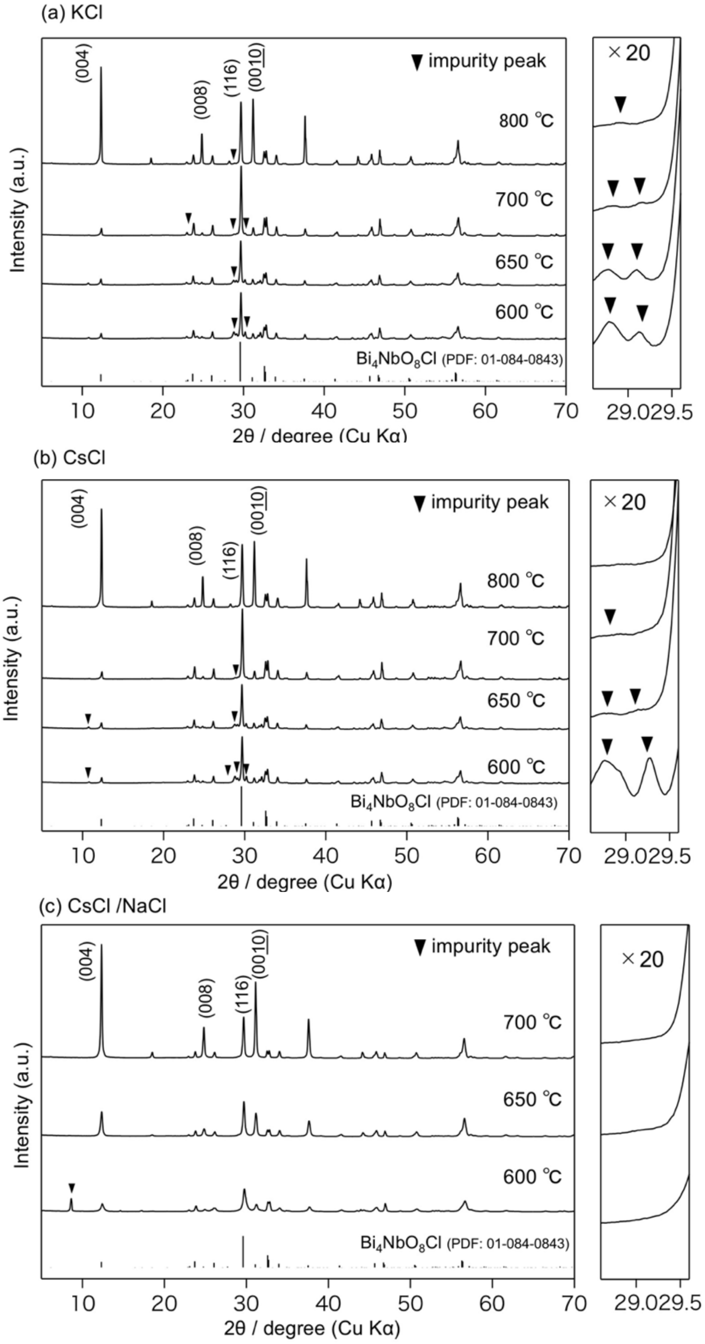

**Figure 3-1.** XRD patterns of $Bi_4NbO_8Cl$ samples prepared with (a) KCl, (b) CsCl or (c) CsCl/NaCl.

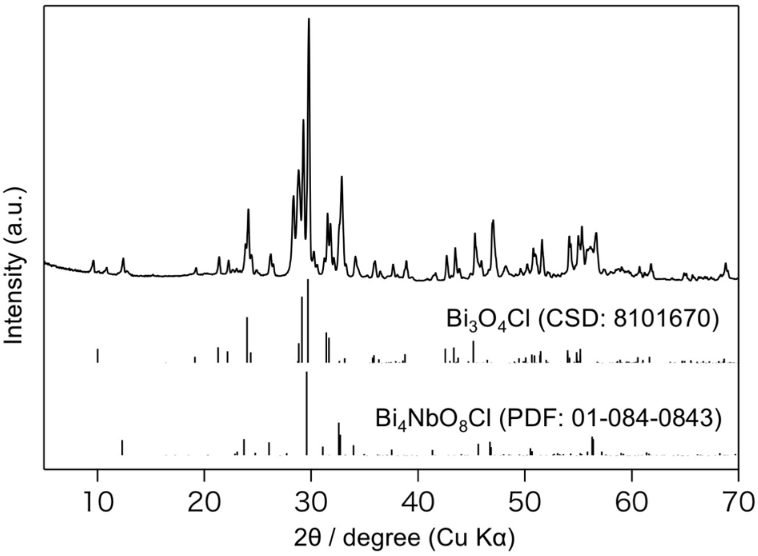

**Figure 3-2.** XRD patterns of $Bi_4NbO_8Cl$ prepared by calcination of the mixture of the materials in air at 650 °C without any flux.

Figure 3-3 shows the SEM images of the $Bi_4NbO_8Cl$ samples prepared at different conditions. The morphologies of the particles prepared with flux were different from those prepared via SSR; the synthesis above the melting points of molten salts resulted in plate-like shaped particles. For the CsCl/NaCl (m.p. 486 °C) flux, we found well-grown plate-like particles of $Bi_4NbO_8Cl$ when reacted at 650 °C. The TEM of the sample prepared with the CsCl/NaCl flux at 650 °C indicates that the major facet is the (00*l*) plane (Figure 3-4). For the CsCl or KCl flux (m.p. 645, 771 °C), however, many irregular shaped particles were observed when reacted at 650 °C and 700 °C, though plate-like particles become pronounced at higher temperatures (Figure 3-5). It seems reasonable to assume that the calcinations at the temperatures lower than (or close to) the melting point of salt result in the insufficient ionic diffusion of precursors, in other words, disable the salt to function as flux, consequently producing such irregular shaped particles. It is noteworthy that $Bi_4NbO_8Cl$ prepared with CsCl/NaCl flux below 700 °C exhibits much higher specific surface areas.

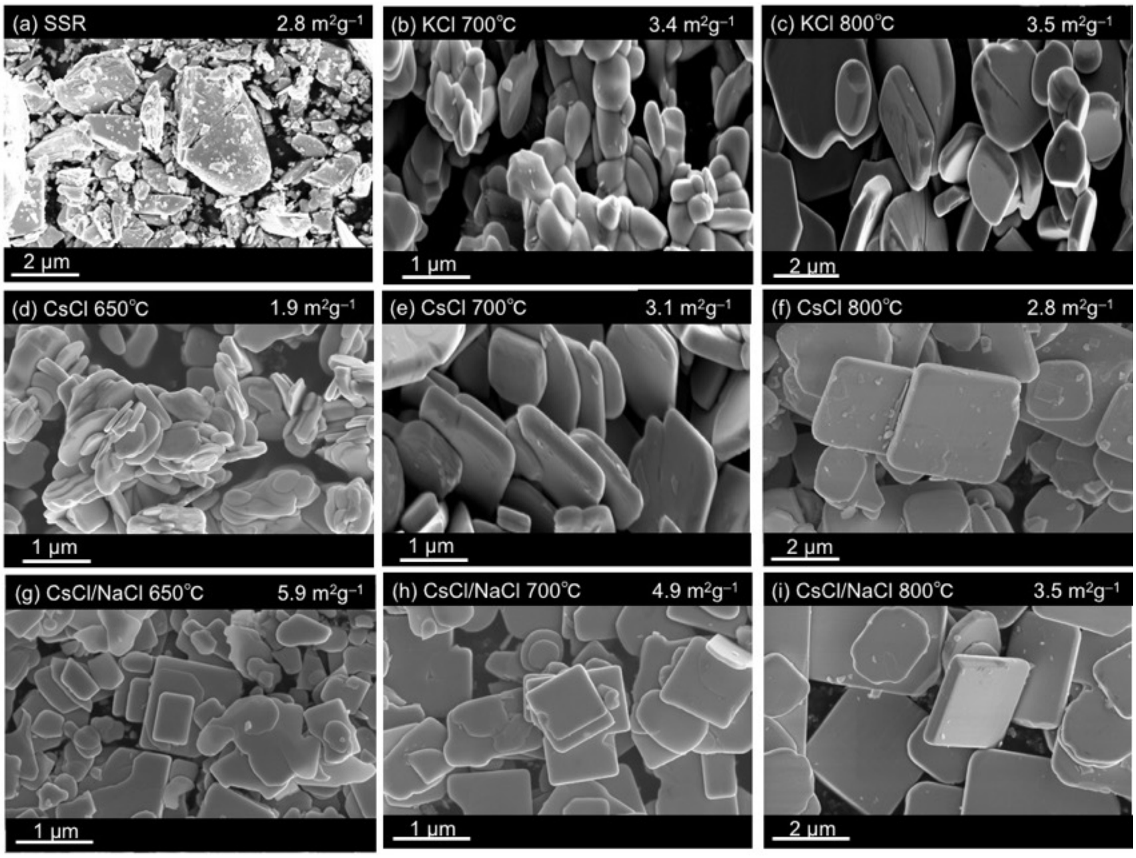

**Figure 3-3.** SEM images of $Bi_4NbO_8Cl$ prepared via (a) SSR or (b-i) flux method. (b,c) with KCl at 700 , 800 °C; (d-f) with CsCl at 650, 700, 800 °C; with (g-i) CsCl/NaCl at 650, 700, 800 °C.

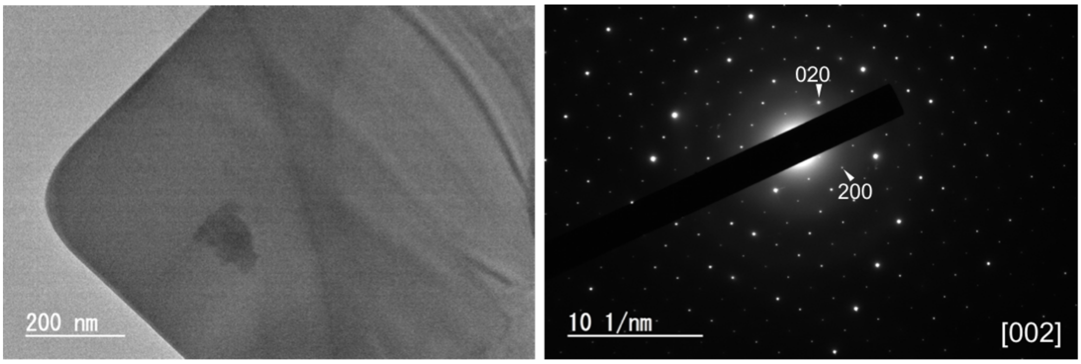

**Figure 3-4.** TEM image and electron diffraction patterns of $Bi_4NbO_8Cl$ prepared via the flux method (CsCl/NaCl flux at 650 °C).

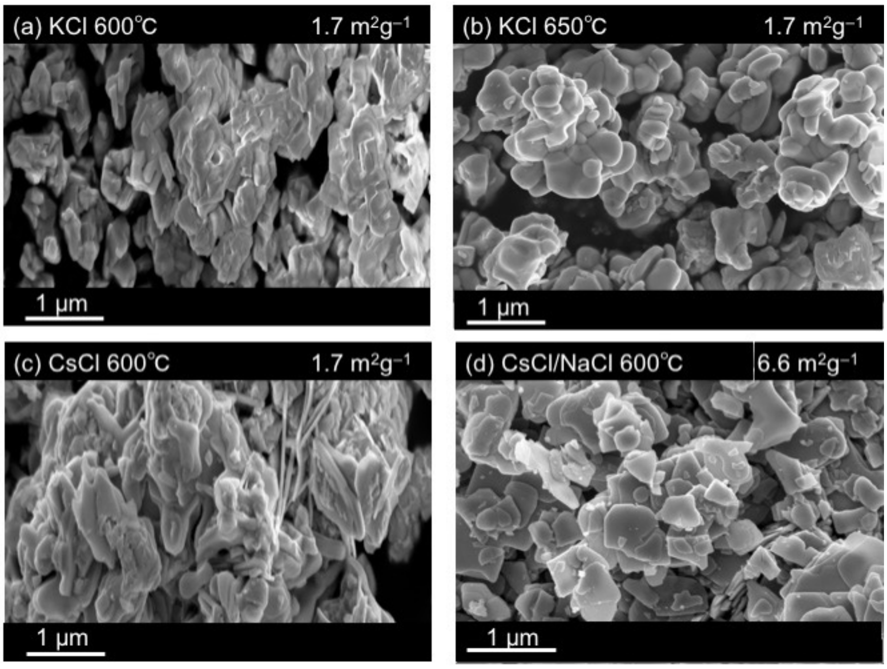

**Figure 3-5.** SEM images of $Bi_4NbO_8Cl$ prepared via the flux method (a,b) with KCl at 600 and 650 °C; (c) with CsCl at 600 °C; (d) with CsCl/NaCl at 600 °C.

Figure 3-6 shows the photocatalytic $O_2$ evolution on the $Bi_4NbO_8Cl$ samples. The reactions were performed in the presence of $Fe^{3+}$ as an electron acceptor under visible-light irradiation. Notably, higher activity was achieved for the samples prepared with CsCl/NaCl at low temperatures (600 °C and 650 °C). The rates of $O_2$ evolution for 650 °C is slightly better than 600 °C. The higher temperature treatments drastically deactivate the reactions, which is probably caused by the reduced surface area (see values shown in Figure 3-3) and/or the formation of Cl defects.[18] The sample using CsCl showed a similar trend, whereas for KCl the activity was moderate up to 700 °C above which it became negligibly low. The optimized activities with KCl or CsCl are lower than that obtained with CsCl/NaCl at 650 °C. This is likely due to the insufficient crystal growth at such low temperatures where neither the KCl nor CsCl salts melt completely. From these results, we conclude that using the eutectic mixture of CsCl/NaCl is effective for preparing fine $Bi_4NbO_8Cl$ particles with high photocatalytic activity.

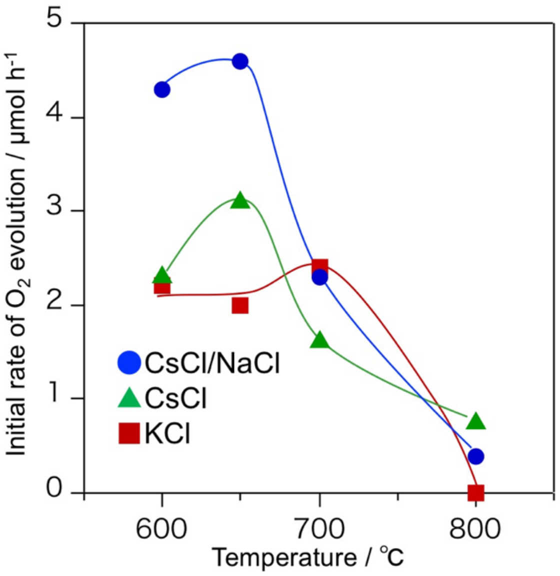

**Figure 3-6.** Initial rates of $O_2$ evolution over $Bi_4NbO_8Cl$ samples prepared with KCl, CsCl or CsCl/NaCl flux at various calcination temperatures in an aqueous $FeCl_3$ solution (8 mM, 100 mL) under visible light irradiation ($\lambda$ > 420 nm).

### Optimization of synthetic conditions with CsCl/NaCl eutectic mixture

As shown above, the $Bi_4NbO_8Cl$ samples prepared with CsCl/NaCl at 600 °C and 650 °C exhibit considerably higher activity, whereas the sample prepared at 600 °C appreciably contains an impurity phase. Although various conditions were applied to produce pure and highly active samples at 600 °C, they failed. Hence, we further optimized the conditions at 650 °C; the results are summarized in Table 3-1. Figures 7a and 7c show the XRD patterns and SEM images of the samples prepared at different solute concentrations (0.5, 1 and 5 mol%) at a fixed calcination time of 10 h. The particle size increased with increasing solute concentration, undoubtedly due to the increased frequency of the ionic collision in the flux. Consequently, the sample prepared with 1 mol% of solute exhibited the highest activity. With the fixed solute concentration of 1 mol%, the optimum calcination time was determined to be 10 h. The lower activity with shorter time (5 h) is likely due to the presence of a small fraction of impurity phases and/or the insufficient quality of crystals (see Figure 3-7b). Meanwhile, a longer time (20 h) resulted in excessive crystal growth (Figure 3-7d) accompanied by considerable decreased surface area (from 7.2 m$^2$ g$^{-1}$ to 3.6 m$^2$ g$^{-1}$), and most likely lowered the activity. Subsequently, the $Bi_4NbO_8Cl$ samples prepared by the calcination of 1 mol% of solute at 650 °C for 10 h were used following the investigations.

**Table 3-1.** Experimental condition for preparation of $Bi_4NbO_8Cl$ under CsCl/NaCl flux.$^a$

| Solute conc. / mol% | Calcination time / h | $O_2$ evolution rate / µmol h$^{-1}$ | BET surface area / m$^2$ g$^{-1}$ |
|---|---|---|---|
| 5 | 10 | 4.6 | 5.9 |
| 0.5 | 10 | 4.8 | 6.8 |
| 1 | 10 | 6.2 | 7.2 |
| 1 | 5 | 5.0 | 7.3 |
| 1 | 20 | 4.4 | 3.6 |

$^a$Calcination temperature was 650 °C.

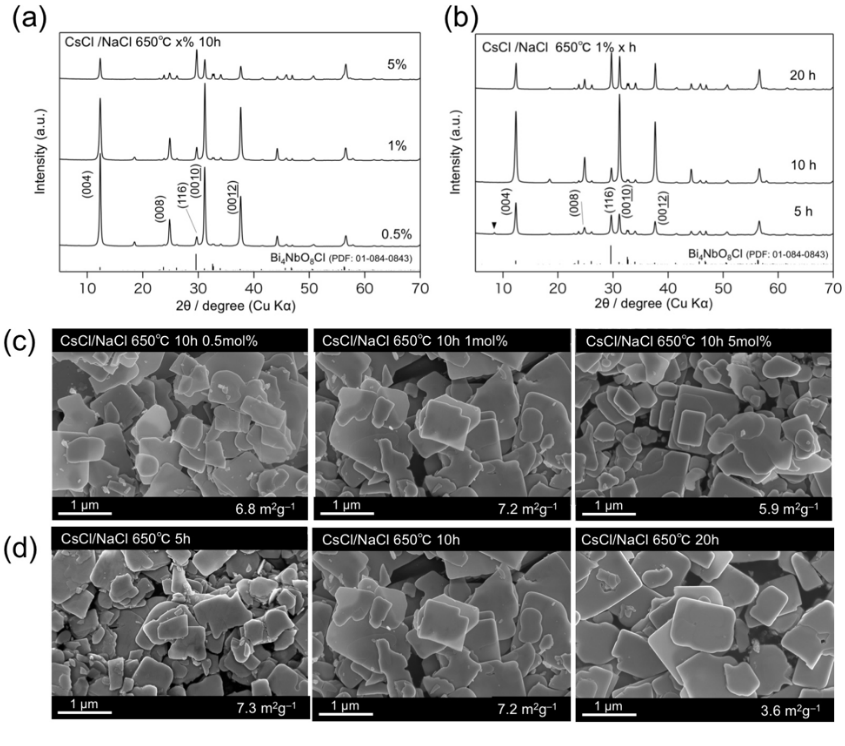

**Figure 3-7.** (a,b) XRD patterns and (c,d) SEM images of $Bi_4NbO_8Cl$ prepared with CsCl/NaCl flux at various solute concentrations and calcination times.

As shown in Figure 3-8, the $Bi_4NbO_8Cl$ sample prepared by the optimized condition exhibits approximately three times higher $O_2$ evolution rate than the sample prepared by the optimized SSR method (at 900 °C for 20 h, Figure 3-9). The AQE measured under a 420 nm monochromatic light have also improved from 0.5% to 0.8%, as shown in Table 3-2.

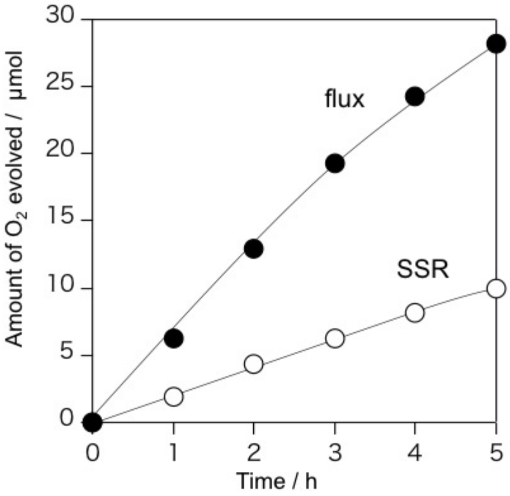

**Figure 3-8.** Time courses of $O_2$ evolution over $Bi_4NbO_8Cl$ samples prepared via flux method (CsCl/NaCl flux at 650 °C) and solid-state reaction method in an aqueous $FeCl_3$ solution (8 mM, 100 mL) under visible light irradiation ($\lambda > 420$ nm).

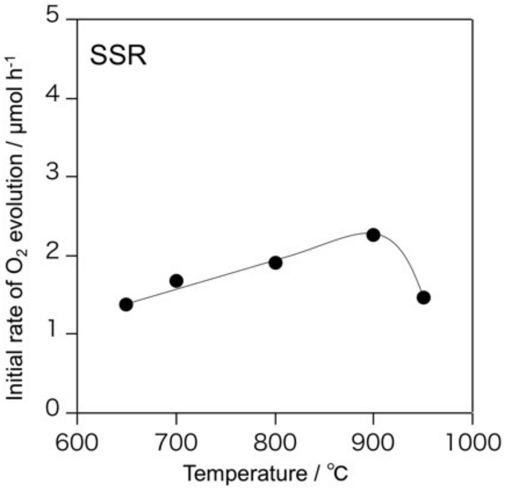

**Figure 3-9.** Initial rates of $O_2$ evolution over $Bi_4NbO_8Cl$ samples prepared at various temperature (650 ~ 950 °C) via the solid-state reaction method in an aqueous $FeCl_3$ solution (8 mM, 100 mL) under visible light irradiation ($\lambda > 400$ nm).

**Table 3-2.** Apparent quantum efficiencies of each sample.[a]

| | SSR | flux | $RuO_2$/SSR | $RuO_2$/flux | Pt/SSR | Pt/flux |
|---|---|---|---|---|---|---|
| AQE | 0.5 | 0.8 | 0.9 | 1.3 | 0.8 | 2.5 |

Recently, Sayama *et. al.* reported that the photocatalytic $O_2$ evolution activity of $WO_3$ was significantly improved by the surface Cs-modification.[25] In the present study, since CsCl was employed in the flux synthesis, such effect can be considered. Indeed, as shown in Figure 3-10, the cesium specie residue remained at the just surface of the flux (was not incorporated in the bulk). In order to investigate the effect of the surface Cs-modification on the $Bi_4NbO_8Cl$, we actually conducted the impregnation of CsCl on the SSR sample according to the literature. The Cs-modification had little effect on the $O_2$ evolution activity from $Fe^{3+}$ aqueous solution over $Bi_4NbO_8Cl$ (without treatment: 2.2 μmol $h^{-1}$, with Cs-modification: 2.5 μmol $h^{-1}$), indicating that the significant improvement of the photocatalytic activity by the flux method is not due to the surface Cs residue.

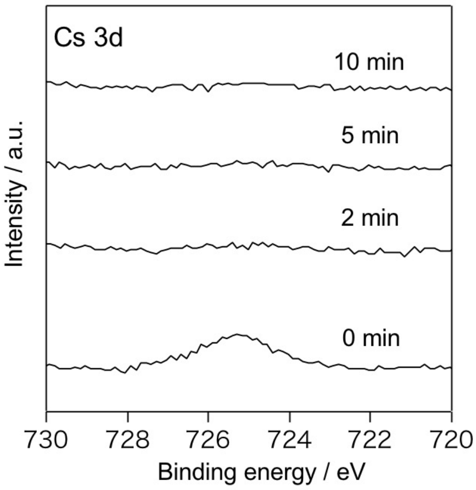

**Figure 3-10.** XP spectra of Cs 3d region of the flux sample before and after Ar sputtering (2, 5, 10 min). The binding energies were referenced to the Au $4f_{7/2}$ level of deposited Au metal.

### Carrier dynamics and surface adsorption property of $Bi_4NbO_8Cl$ samples prepared by two different methods

As demonstrated above, the present synthesis with CsCl/NaCl flux proved to be an effective method to prepare a highly active $Bi_4NbO_8Cl$ photocatalyst for water oxidation. One of the crucial factors for the higher activity likely be the higher surface area of the $Bi_4NbO_8Cl$ particles obtained by the CsCl/NaCl flux method, as confirmed by their SEM images and specific surface area measurement. In addition to the surface area, the amount of crystal defects (i.e., crystallinity) significantly affects the photocatalytic activity because such defects generally serve as the recombination sites of photogenerated electrons and holes.[26,27] To visualize the charge dynamics in the prepared $Bi_4NbO_8Cl$ samples, we employed TRMC, which has been reported as a powerful measurement to provide an access to the local mobility and lifetimes of photogenerated charge carriers without an electrode.[28] Figure 3-11 shows the transient $\phi\sum\mu$ of $Bi_4NbO_8Cl$ by 355 nm laser excitation ($I_0$ = $4.6 \times 10^{15}$ photons $cm^{-2}$), which is presumably attributed to photogenerated electrons, because of the well-known n-type nature.[16] Figure 3-12 shows the dependence of $\phi\sum\mu$ maximum ($\phi\sum\mu_{\mathrm{max}}$) on the incident laser intensity ($I_0$) of the flux sample, where the appearance of a convex curve is caused by a trap-filling effect that have been reported in $TiO_2$ nanoparticle.[29,30] The optimized flux sample exhibited ~4.8 times greater signal ($\phi\sum\mu_{\mathrm{max}} = 7.6 \times 10^{-6}$ $m^2 V^{-1}s^{-1}$) than the optimized SSR sample ($\phi\sum\mu_{\mathrm{max}} = 7.6 \times 10^{-6}$ $m^2 V^{-1}s^{-1}$) (0.1 μs after the laser excitation), indicating much improved carrier generation efficiency and/or mobility in the flux-synthesized one. This is certainly attributed to the high crystallinity and/or low defect density of the flux-synthesized samples. This property was achieved by employing the liquid-state reaction synthesis, where higher-quality crystals can be expected compared to using an SSR; the flux synthesis resulted in well-orientated plate-like crystals as confirmed in the SEM images (Figure 3-7). Moreover, in the present study, molten salts of chlorides were used as solvents, and possibly enabled the suppression of the $Cl^-$ defects in the bulk of the flux samples. This is supported by the UV-vis diffuse reflectance spectra of the flux and SSR samples, as shown in Figure 3-13. A broad absorption at $\lambda \geq 480$ nm was observed for the SSR samples; this absorption is often attributed to the presence of anion defects and/or the reduced species of cations.[31,32]

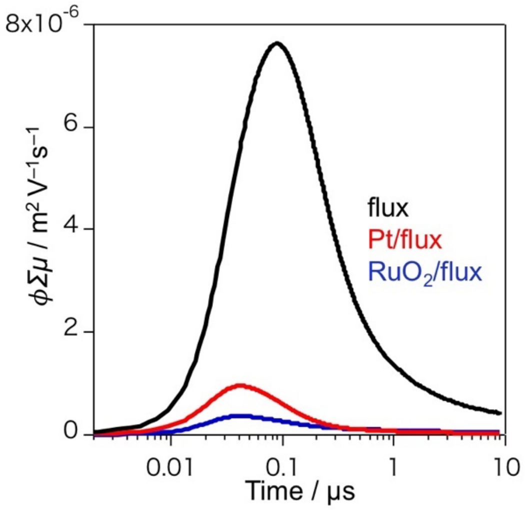

**Figure 3-11.** TRMC signals of $RuO_2$ or Pt-loaded $Bi_4NbO_8Cl$ samples prepared via flux method (CsCl/NaCl flux at 650 °C).

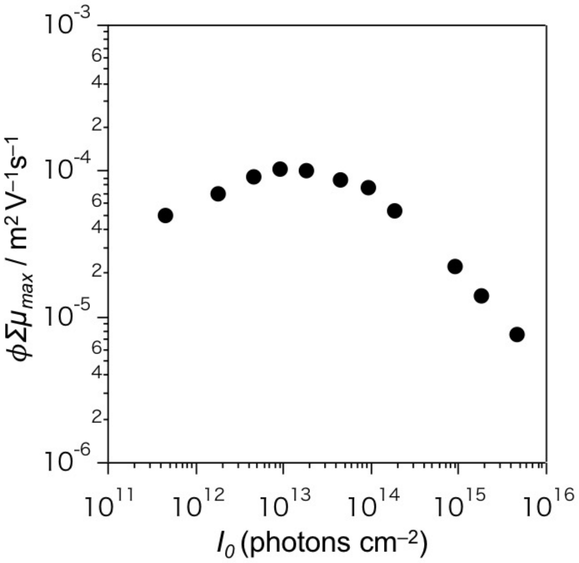

**Figure 3-12.** Dependence of $\phi\sum\mu_{\max}$ on the incident laser intensity ($I_0$) of the flux sample. The initial increase of $\phi\sum\mu_{\max}$ with increasing $I_0$ is due to a trap filling effect (an increase and saturation of $\sum\mu$), while the gradual decrease at high $I_0$ is rationalized by a high order deactivation process such as exciton−exciton annihilation, exciton−carrier annihilation, and charge recombination, which occur within the time resolution.[2,3]

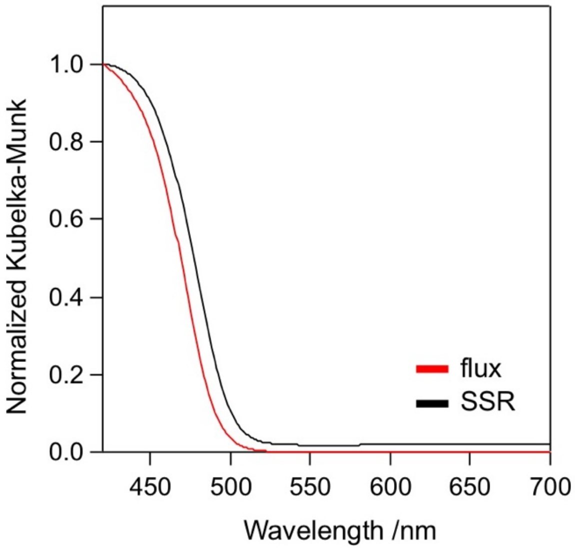

**Figure 3-13.** DRS of $Bi_4NbO_8Cl$ samples prepared via the flux method (CsCl/NaCl flux at 650 °C) and the solid-state reaction method.

Another important factor to consider is the adsorption capability of the surface to the redox mediator (i.e., $Fe^{3+}/Fe^{2+}$), which is sometimes associated with the facets exposed.[33] In the present reaction system, the photogenerated electrons reduce $Fe^{3+}$ while the photogenerated holes oxidize water. Therefore, a higher amount of $Fe^{3+}$ adsorbed on the surface of the photocatalyst is favorable to enhance the reaction of electrons and thereby increase the rate of water oxidation by holes. Additionally, a higher amount of $Fe^{2+}$ adsorbed certainly increases the probability of backward reactions (i.e., re-oxidation of $Fe^{2+}$ by holes) and thereby lower the efficiency of water oxidation (i.e., $O_2$ evolution). Figures 14a and 14b show the amount of $Fe^{3+}$ or $Fe^{2+}$ ions adsorbed on each sample in aqueous solutions with different concentrations of $FeCl_3$ or $FeCl_2$. No apparent difference is shown between the two samples, while the sample prepared via the flux method adsorbs a slightly higher amount of both $Fe^{3+}$ and $Fe^{2+}$. As shown in Figure 3-15, the initial rates of $O_2$ evolution on both samples were obviously and similarly lowered by the increased concentration of $Fe^{2+}$ ions with a fixed concentration of $Fe^{3+}$ (8 mM). These findings strongly suggest that the difference in the adsorption property is not the primary reason for the higher activity of the flux sample.

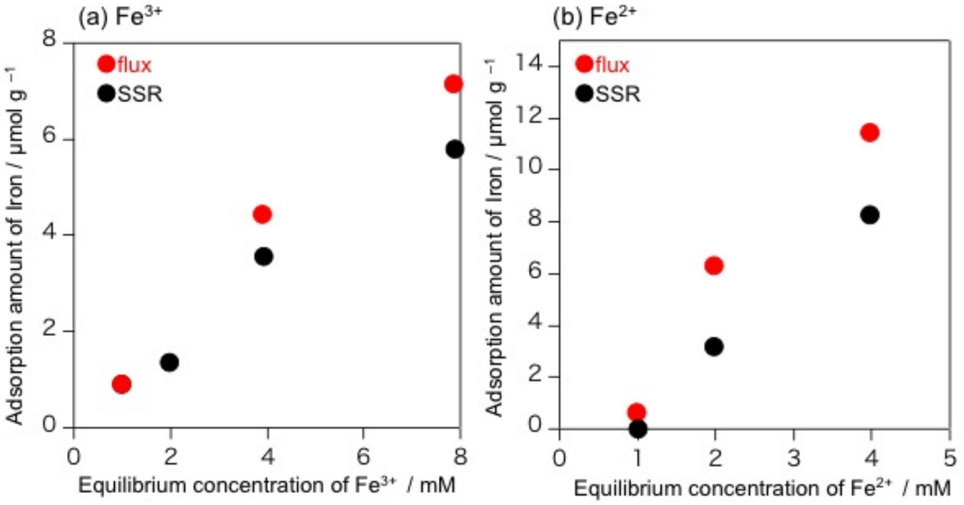

**Figure 3-14.** Adsorption properties of (a) Fe$^{3+}$ and (b) Fe$^{2+}$ ions on the $Bi_4NbO_8Cl$ samples prepared via the flux method (CsCl/NaCl flux at 650 °C) and the solid-state reaction method.

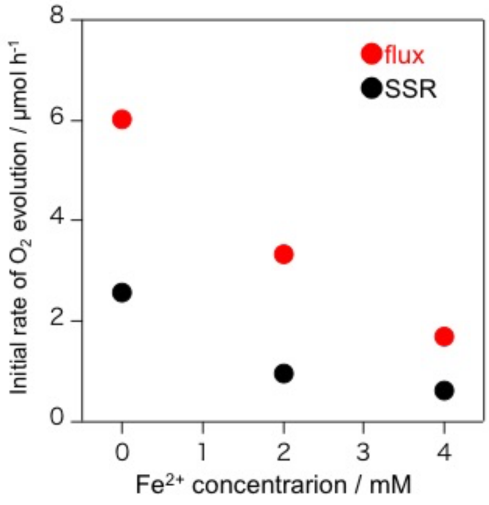

**Figure 3-15.** Initial rates of $O_2$ evolution over $Bi_4NbO_8Cl$ samples prepared via the flux method (CsCl/NaCl flux at 650 °C) and the solid-state reaction method in an solution containing different concentrations of Fe$^{2+}$ (0 ~ 4 mM) and a fixed concentration of Fe$^{3+}$ (8 mM, 100 mL) under visible light irradiation ($\lambda > 400$ nm).

From these results, we conclude that the higher activity of the flux sample is due to the favorable factors simultaneously obtained by the present flux synthesis at a lowered temperature with CsCl/NaCl flux, i.e., the lower defect density and the high surface area.

### Effect of Cocatalyst Loading on $O_2$-evolving Activity

Loading a cocatalyst onto photocatalyst particles is an effective way to improve the activities for various photocatalytic reactions such as the water-splitting reaction. In the present study, loadings of well-known Pt[34,35] and $RuO_2$[36–39] were attempted via the impregnation method to improve the activity of the $Bi_4NbO_8Cl$ photocatalyst for $O_2$ evolution with $Fe^{3+}$ electron acceptor. The cocatalyst loaded samples are hereafter denoted as Pt/flux which is an example of the $Bi_4NbO_8Cl$ sample synthesized by flux method with loading of Pt cocatalyst. The particle sizes of Pt and $RuO_2$ loaded were confirmed to be ~4 nm and 3 nm, respectively, regardless of the origin of the mother $Bi_4NbO_8Cl$ photocatalyst, as shown in Figure 3-16. Although the loading of these cocatalysts increased the rate of $O_2$ evolution on both the $Bi_4NbO_8Cl$ photocatalysts prepared via SSR and the flux methods, the enhancement in the flux sample is astonishingly higher compared to that of the SSR sample as seen in Figure 3-17.[40] The rates of $O_2$ evolution on the $RuO_2$/flux and Pt/flux were ~3.5 and 7 times higher than the unloaded one, respectively, along with distinct improvements in quantum efficiencies (see Table 3-2). As shown in Figure 3-18, $RuO_2$/flux showed the steady $O_2$ evolution over the $RuO_2$/flux without a notable decrease in the evolution rate, reaching complete consumption of the added electron acceptor ($Fe^{3+}$). Additionally, the XRD patterns of $RuO_2$/flux are almost identical before and after the reaction, indicating the sufficient stability of the $RuO_2$/flux sample.

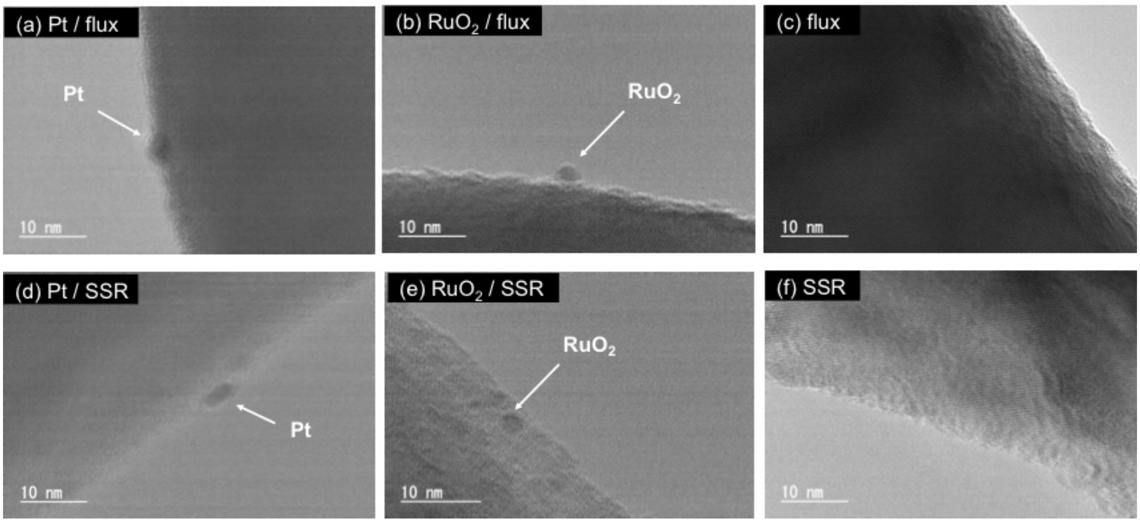

**Figure 3-16.** TEM images of (a,d) Pt- or (b,e) $RuO_2$-loaded $Bi_4NbO_8Cl$, along with (c,f) unmodified

ones. The $Bi_4NbO_8Cl$ samples prepared via (a-c) the flux method (CsCl/NaCl flux at 650 °C) and (d-f) the solid-state reaction method.

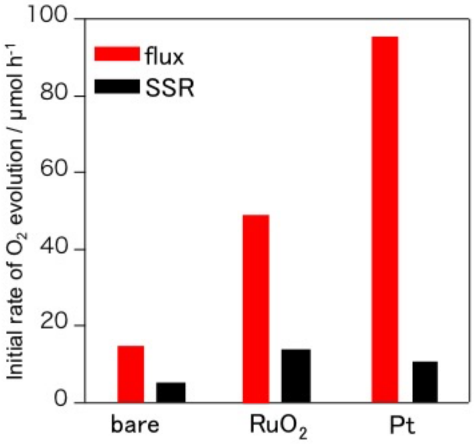

**Figure 3-17.** Initial rates of $O_2$ evolution over cocatalyst (Pt or $RuO_2$) loaded $Bi_4NbO_8Cl$ samples prepared via flux method (CsCl/NaCl flux at 650 °C) and solid-state reaction method in an aqueous $FeCl_3$ solution (8 mM, 100 mL) under visible light irradiation ($\lambda$ > 420 nm). Each cocatalyst was loaded via impregnation followed by heated under $H_2$ flow (20 mL $min^{-1}$) at 150 °C for Pt or Ar flow (20 mL $min^{-1}$) at 450 °C for $RuO_2$.

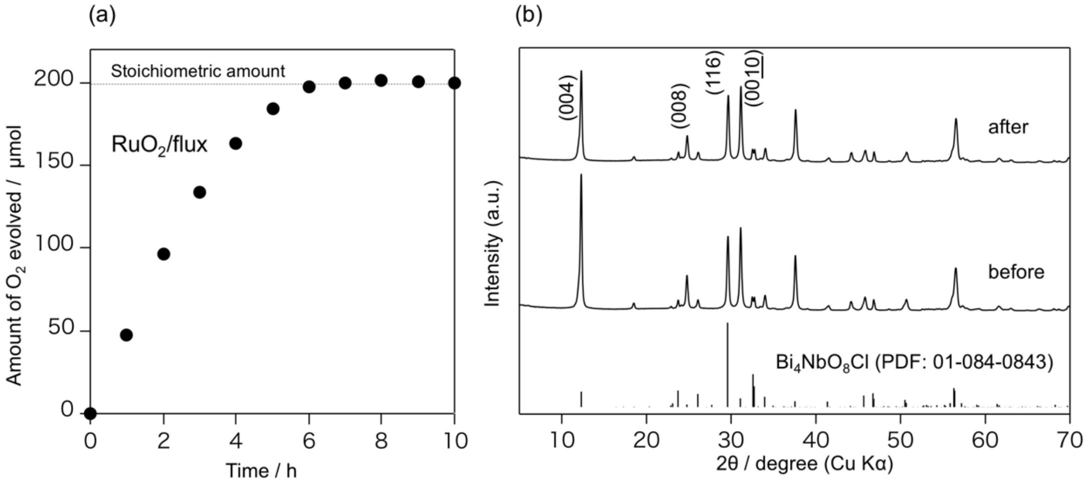

**Figure 3-18.** (a) Time course of $O_2$ evolution over a $RuO_2$-loaded $Bi_4NbO_8Cl$ sample prepared via the flux method (CsCl/NaCl flux at 650 °C) in an aqueous $FeCl_3$ solution (8 mM, 100 mL) under visible light irradiation ($\lambda > 400$ nm). (b) XRD patterns of the $RuO_2$-loaded $Bi_4NbO_8Cl$ before and after the photocatalytic reaction.

The primary role of such cocatalysts has been generally regarded as (1) enhancing the charge separation in the semiconductor particles, and (2) catalytically facilitating the surface chemical reactions by the carriers.[3] TRMC measurements were conducted to investigate the influence of the former (i.e., charge separation process). The peak intensity had drastically decreased by the loading of the cocatalyst as seen in Figure 3-19, indicating the decrease in density of the photoexcited electrons on the conduction band[41,42] of $Bi_4NbO_8Cl$. The results suggested that one of the roles of $RuO_2$ and Pt cocatalysts is the collectors of photogenerated electrons on the conduction band of $Bi_4NbO_8Cl$. As for the latter (i.e., catalytic activity), the electrochemical measurement on the Pt- or $RuO_2$-loaded FTO electrode confirmed their comparable activity for the reduction of $Fe^{3+}$, as shown in Figure 3-20. For the water oxidation, the $RuO_2$-loaded FTO exhibited a higher activity than the Pt-loaded one (i.e., lower overpotential and higher current), while a simple comparison is difficult due to the possible difference in other factors such as their morphologies.

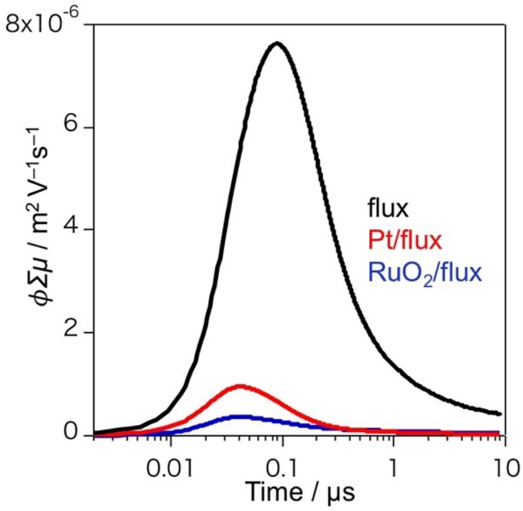

**Figure 3-19.** TRMC signals of $RuO_2$ or Pt-loaded $Bi_4NbO_8Cl$ samples prepared via flux method (CsCl/NaCl flux at 650 °C).

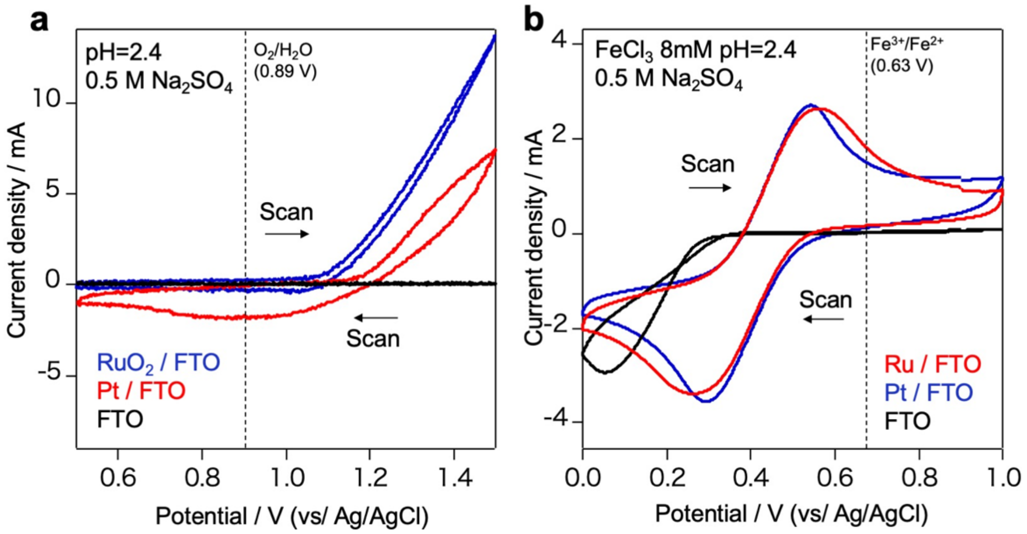

**Figure 3-20.** CV profiles of FTO substrates loaded with Pt or $RuO_2$ in 0.5 M aqueous $Na_2SO_4$ solution (a) in the absence and (b) presence of $Fe^{3+}$ (8 mM, pH 2.4).

These findings suggested that one of the key functions of both the $RuO_2$ and Pt cocatalysts is effective capturing the photoexcited electrons and catalyzed the reduction of $Fe^{3+}$ on the surface, providing significantly improved rate of $O_2$ evolution. However, one cannot exclude the possibility that the $RuO_2$ species accelerate the oxidation of water in part along with the reduction as reported previously.[35] More importantly, the effect of cocatalyst loading was much more prominent on the flux sample compared to that on the SSR sample. This is reasonable because the unmodified flux sample exhibited a much higher TRMC signal compared to the SSR sample (see Figure 3-11). Such higher signals generally indicate improved efficiency in carrier generation and/or mobility in the bulk, both of which will positively assist the capture of electrons by the cocatalysts.

### Overall Water Splitting with Two-step Visible-light Excitation

An overall water splitting was subsequently attempted using the optimized $Bi_4NbO_8Cl$ samples as $O_2$-evolving photocatalysts in the presence of $Fe^{3+}/Fe^{2+}$ redox. Strontium titanate doped with Rh cations (1 mol% to Ti) was used as the $H_2$-evolving photocatalyst after the loading of Ru-based cocatalyst (denoted as Ru/$SrTiO_3$:Rh).[23,24] Figure 3-21 shows the time courses of the gas evolution from the mixed suspension of Ru/$SrTiO_3$:Rh and $RuO_2$/$Bi_4NbO_8Cl$ samples under visible light. Clearly, the use of the $RuO_2$/flux resulted in higher rates of $H_2$ and $O_2$ evolutions compared to the case of $RuO_2$/SSR, reflecting their activities for the half reaction ($O_2$ evolution) as described above. The gas evolution with the stoichiometric ratio continued without a notable decrease in the evolution rates. The AQE for Z-scheme overall water splitting with the use of $RuO_2$/flux and $RuO_2$/SSR were determined to be 1.3% and 0.7% at 420 nm, respectively.

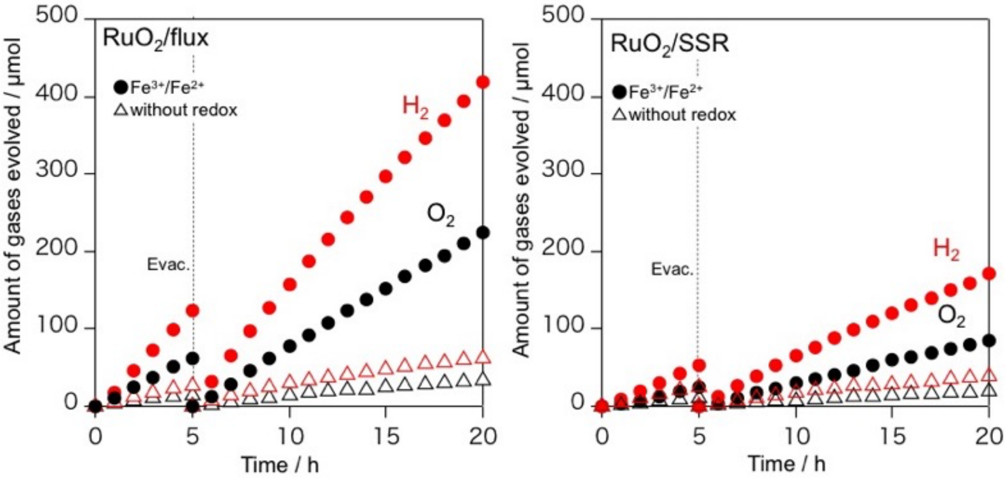

**Figure 3-21.** Time courses of $H_2$ and $O_2$ evolution over a mixture of $RuO_2/Bi_4NbO_8Cl$ samples prepared via flux method (CsCl/NaCl flux at 650 ℃) or solid-state reaction method (50 mg) and Ru/$SrTiO_3$:Rh (50 mg) in $FeCl_3$ aqueous solution (2 mM, 100 mL) at pH 2.4 under visible light irradiation ($\lambda > 420$ nm).

When the Pt/flux sample was used instead of the $RuO_2$/flux one, the rates of gas evolution in the steady sate were obviously lowered (see the second run of Pt/flux in Figure 3-22), despite the higher activity of the former in the half reaction (see Figure 3-17). Although the initial rate of the $O_2$ evolution in the first run with the Pt/flux is indeed higher, the rate drastically decreased after 2 h of irradiation. The suppressed gas evolution is undoubtedly due to the occurrence of a backward reaction over the Pt cocatalyst (i.e., catalytic water formation from $H_2$ and $O_2$). Indeed, the gas pressure of the mixture of $H_2$ and $O_2$ (2:1) in a closed system with the Pt/flux rapidly decreased due to the water formation, whereas it almost unchanged with the $RuO_2$/flux (Figure 3-23).

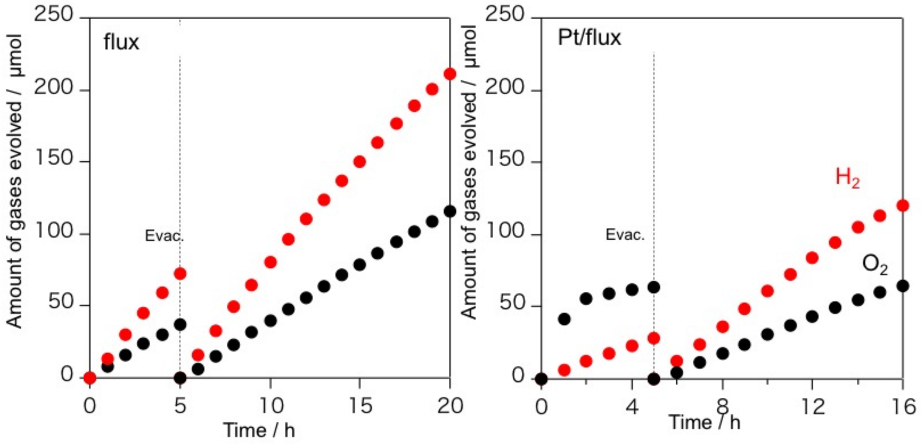

**Figure 3-22.** Time courses of $H_2$ and $O_2$ evolution over a mixture of bare or Pt-loaded $Bi_4NbO_8Cl$ samples prepared via the flux method (CsCl/NaCl flux at 650 °C) (50 mg) and Ru/$SrTiO_3$:Rh (50 mg) in $FeCl_3$ aqueous solution (2 mM, 100 mL) at pH 2.4 under visible light irradiation ($\lambda > 400$ nm).

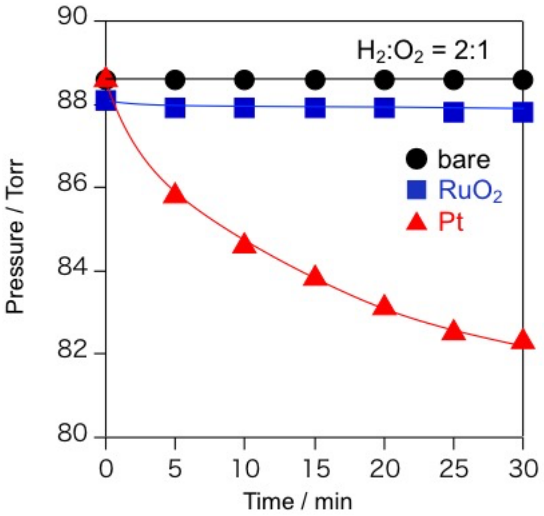

**Figure 3-23.** Water formation from $H_2$ and $O_2$ in the gas-phase reaction over Pt/flux, $RuO_2$/flux and flux. A mixture of $H_2$ and air gases ($H_2 : O_2 = 2 : 1$) was introduced into a gas-circulating system with a Pyrex glass cell containing 20 mg of photocatalyst powder without water.

In summary, we demonstrated that the combination of the highly active $Bi_4NbO_8Cl$ photocatalyst prepared via the appropriate flux and $RuO_2$ cocatalyst that facilitates the surface reaction but suppresses the backward water formation, thus enabling the improvement in the total efficiency in the Z-scheme water splitting using $Bi_4NbO_8Cl$ as an $O_2$-evolving photocatalyst with $Fe^{3+}/Fe^{2+}$ redox.

## 3.4. Conclusion

In summary, this study demonstrated that the liquid-state reaction, i.e., using the flux method with the appropriate molten salt is an effective method to improve the activity of the $Bi_4NbO_8Cl$ photocatalyst for water oxidation in the presence of the $Fe^{3+}$ electron acceptor under visible light irradiation. We found that the choice of molten salt, which is primarily associated with the melting point, is critical for producing a highly efficient $Bi_4NbO_8Cl$ photocatalyst because the higher temperature with flux had caused a reduced surface area and possibly increased the Cl defects. Thus, the CsCl/NaCl eutectic mixture was the best choice among the molten salts employed, thereby affording sufficiently high ionic diffusion and providing well-grown crystals even at low temperatures of 650 °C without superfluous crystal growth that decrease the surface area. As confirmed by the TRMC measurements, the sample prepared via the flux method possesses favorable bulk properties such as much improved carrier generation efficiency and/or mobility. Thus, the liquid-state synthesis with the appropriate flux can simultaneously satisfy a larger surface and higher crystal quality, both of which are strongly desired to improve the photocatalytic activity. Another important finding is that the positive effect by loading the cocatalyst was much more prominent in the flux sample compared to that on the SSR sample, certainly due to the improved efficiency in carrier generation and/or mobility in the bulk, both of which will positively assist the capture of electrons by the cocatalysts. The findings in the present study will offer useful insights into the preparation of highly active oxyhalide photocatalysts, not only $Bi_4NbO_8Cl$ but also a wide range of those with the Sillen−Aurivillius perovskite or related structure, and thereby provide the possibility of highly efficient water splitting under solar light based on such oxyhalide photocatalysts.

# Reference

(1) Kudo, A.; Miseki, Y. Heterogeneous Photocatalyst Materials for Water Splitting. *Chem. Soc. Rev.* **2009**, *38*, 253–278.

(2) Osterloh, F. E. Inorganic Nanostructures for Photoelectrochemical and Photocatalytic Water Splitting. *Chem. Soc. Rev.* **2013**, *42*, 2294–2320.

(3) Maeda, K. Photocatalytic Water Splitting Using Semiconductor Particles: History and Recent Developments. *J. Photochem. Photobiol. C Photochem. Rev.* **2011**, *12*, 237–268.

(4) Abe, R. Development of a New System for Photocatalytic Water Splitting into $H_2$ and $O_2$ under Visible Light Irradiation. *Bull. Chem. Soc. Jpn.* **2011**, *84*, 1000–1030.

(5) Inoue, Y. Photocatalytic Water Splitting by $RuO_2$-Loaded Metal Oxides and Nitrides with $d^0$- and $d^{10}$ -Related Electronic Configurations. *Energy Environ. Sci.* **2009**, *2*, 364–386.

(6) Kitano, M.; Hara, M. Heterogeneous Photocatalytic Cleavage of Water. *J. Mater. Chem* **2010**, *20*, 627–641.

(7) Abe, R. Recent Progress on Photocatalytic and Photoelectrochemical Water Splitting under Visible Light Irradiation. *J. Photochem. Photobiol. C Photochem. Rev.* **2010**, *11*, 179–209.

(8) Sayama, K.; Mukasa, K.; Abe, R.; Abe, Y.; Arakawa, H. Stoichiometric Water Splitting into $H_2$ and $O_2$ Using a Mixture of Two Different Photocatalysts and an $IO_3^-/I^-$ Shuttle Redox Mediator under Visible Light Irradiation. *Chem. Commun.* **2001**, 2416–2417.

(9) Abe, R.; Takata, T.; Sugihara, H.; Domen, K. Photocatalytic Overall Water Splitting under Visible Light by TaON and $WO_3$ with an $IO_3^-/I^-$ Shuttle Redox Mediator. *Chem. Commun.* **2005**, 3829–3831.

(10) Abe, R.; Shinmei, K.; Hara, K.; Ohtani, B. Robust Dye-Sensitized Overall Water Splitting System with Two-Step Photoexcitation of Coumarin Dyes and Metal Oxide Semiconductors. *Chem Commun* **2009**, 3577–3579.

(11) Kato, H.; Sasaki, Y.; Iwase, A.; Kudo, A. Role of Iron Ion Electron Mediator on Photocatalytic Overall Water Splitting under Visible Light Irradiation Using Z-Scheme Systems. *Bull. Chem. Soc. Jpn.* **2007**, *80*, 2457–2464.

(12) Kato, T.; Hakari, Y.; Ikeda, S.; Jia, Q.; Iwase, A.; Kudo, A. Utilization of Metal Sulfide Material of $(CuGa)_{1-x}Zn_{2x}S_2$ Solid Solution with Visible Light Response in Photocatalytic and Photoelectrochemical Solar Water Splitting Systems. *J. Phys. Chem. Lett.* **2015**, *6*, 1042–1047.

(13) Suzuki, H.; Tomita, O.; Higashi, M.; Abe, R. Tungstic Acids $H_2WO_4$ and $H_4WO_5$ as Stable Photocatalysts for Water Oxidation under Visible Light. *J. Mater. Chem. A* **2017**, *5*, 10280–10288.

(14) Fujito, H.; Kunioku, H.; Kato, D.; Suzuki, H.; Higashi, M.; Kageyama, H.; Abe, R. Layered Perovskite Oxychloride $Bi_4NbO_8Cl$: A Stable Visible Light Responsive Photocatalyst for Water Splitting. *J. Am. Chem. Soc.* **2016**, *138*, 2082–2085.

(15) Kusainova, A. M.; Zhou, W.; Irvine, J. T. S.; Lightfoot, P. Layered Intergrowth Phases $Bi_4MO_8X$ (X = Cl, M = Ta and X = Br, M = Ta or Nb): Structural and Electrophysical Characterization. *J. Solid State Chem.* **2002**, *166*, 148–157.

(16) Kunioku, H.; Higashi, M.; Tomita, O.; Yabuuchi, M.; Kato, D.; Fujito, H.; Kageyama, H.; Abe, R. Strong Hybridization between Bi-6s and O-2p Orbitals in Sillén–Aurivillius Perovskite $Bi_4MO_8X$ (M = Nb, Ta; X = Cl, Br), Visible Light Photocatalysts Enabling Stable Water Oxidation. *J. Mater. Chem. A* **2018**, *6*, 3100–3107.

(17) Kato, D.; Hongo, K.; Maezono, R.; Higashi, M.; Kunioku, H.; Yabuuchi, M.; Suzuki, H.; Okajima, H.; Zhong, C.; Nakano, K.; Abe, R.; Kageyama, H. Valence Band Engineering of Layered Bismuth Oxyhalides toward Stable Visible-Light Water Splitting: Madelung Site Potential Analysis. *J. Am. Chem. Soc.* **2017**, *139*, 18725–18731.

(18) Kunioku, H.; Nakada, A.; Higashi, M.; Tomita, O.; Kageyama, H.; Abe, R. Improved Water Oxidation under Visible Light on Oxyhalide $Bi_4MO_8X$ (M = Nb, Ta; X = Cl, Br) Photocatalysts Prepared Using Excess Halogen Precursors. *Sustain. Energy Fuels* **2018**, *2*, 1474-1480.

(19) Kato, H.; Kudo, A. Photocatalytic Decomposition of Pure Water into $H_2$ and $O_2$ over $SrTa_2O_6$ Prepared by a Flux Method. *Chem. Lett.* **1999**, 28, 1207–1208.

(20) Kato, H.; Kobayashi, M.; Hara, M.; Kakihana, M. Fabrication of $SrTiO_3$ Exposing Characteristic Facets Using Molten Salt Flux and Improvement of Photocatalytic Activity for Water Splitting. *Catal. Sci. Technol.* **2013**, *3*, 1733–1738

(21) Hojamberdiev, M.; Yubuta, K.; Vequizo, J. J. M.; Yamakata, A.; Oishi, S.; Domen, K.; Teshima, K. $NH_3$-Assisted Flux Growth of Cube-like $BaTaO_2N$ Submicron Crystals in a Completely Ionized Nonaqueous High-Temperature Solution and Their Water Splitting Activity. *Cryst. Growth Des.* **2015**, *15*, 4663–4671.

(22) Tao, X.; Zhao, Y.; Mu, L.; Wang, S.; Li, R.; Li, C. Bismuth Tantalum Oxyhalogen: A Promising Candidate Photocatalyst for Solar Water Splitting. *Adv. Energy Mater.* **2017**, 8, 1701392.

(23) Konta, R.; Ishii, T.; Kato, H.; Kudo, A. Photocatalytic Activities of Noble Metal Ion Doped $SrTiO_3$ under Visible Light Irradiation. *J. Phys. Chem. B* **2004**, *108*, 8992–8995.

(24) Sasaki, Y.; Iwase, A.; Kato, H.; Kudo, A. The Effect of Co-Catalyst for Z-Scheme Photocatalysis Systems with an $Fe^{3+}/Fe^{2+}$ Electron Mediator on Overall Water Splitting under Visible Light Irradiation. *J. Catal.* **2008**, *259*, 133–137.

(25) Miseki, Y.; Sayama, K. High-Efficiency Water Oxidation and Energy Storage Utilizing Various Reversible Redox Mediators under Visible Light over Surface-Modified $WO_3$. *RSC Adv.* **2014**, *4*, 8308–8316.

(26) Maeda, K.; Murakami, N.; Ohno, T. Dependence of Activity of Rutile titanium(IV) Oxide Powder for Photocatalytic Overall Water Splitting on Structural Properties. *J. Phys. Chem. C* **2014**, *118*, 9093–9100.

(27) Prieto-Mahaney, O.-O.; Murakami, N.; Abe, R.; Ohtani, B. Correlation between Photocatalytic Activities and Structural and Physical Properties of Titanium(IV) Oxide Powders. *Chem. Lett.* **2009**, *38*, 238–239.

(28) Saeki, A.; Yoshikawa, S.; Tsuji, M.; Koizumi, Y.; Ide, M.; Vijayakumar, C.; Seki, S. A Versatile Approach to Organic Photovoltaics Evaluation Using White Light Pulse and Microwave Conductivity. *J. Am. Chem. Soc.* **2012**, *134*, 19035–19042.

(29) Emilio, C. A.; Litter, M. I.; Kunst, M.; Bouchard, M.; Colbeau-Justin, C. Phenol Photodegradation on Platinized-$TiO_2$ Photocatalysts Related to Charge-Carrier Dynamics. *Langmuir* **2006**, *22*, 3606–3613.

(30) Saeki, A.; Yasutani, Y.; Oga, H.; Seki, S. Frequency-Modulated Gigahertz Complex Conductivity of TiO2 Nanoparticles: Interplay of Free and Shallowly Trapped Electrons. *J. Phys. Chem. C* **2014**, *118*, 22561–22572.

(31) Murakami, N.; Mahaney, O. O. P.; Abe, R.; Torimoto, T.; Ohtani, B. Double-Beam Photoacoustic Spectroscopic Studies on Transient Absorption of titanium(IV) Oxide Photocatalyst Powders. *J. Phys. Chem. C* **2007**, *111*, 11927–11935.

(32) Nakada, A.; Saeki, A.; Higashi, M.; Kageyama, H.; Abe, R. Two-Step Synthesis of Sill E ′ N – Aurivillius Type Oxychlorides to Enhance Their Photocatalytic Activity for Visible-Light-Induced Water Splitting. *J. Mater. Chem. A*, **2018**, *6*, 10909–10917.

(33) Tomita, O.; Nitta, S.; Matsuta, Y.; Hosokawa, S.; Higashi, M.; Abe, R. Improved Photocatalytic Water Oxidation with $Fe^{3+}/Fe^{2+}$ Redox on Rectangular-Shaped $WO_3$ Particles with Specifically Exposed Crystal Faces via Hydrothermal Synthesis. *Chem. Lett.* **2016**, *46*, 221–224.

(34) Abe, R.; Higashi, M.; Domen, K. Overall Water Splitting under Visible Light through a Two-Step Photoexcitation between TaON and $WO_3$ in the Presence of an Iodate–Iodide Shuttle Redox Mediator. *ChemSusChem* **2011**, *4*, 228–237.

(35) Tsuji, K.; Tomita, O.; Higashi, M.; Abe, R. Manganese-Substituted Polyoxometalate as an Effective Shuttle Redox Mediator in Z-Scheme Water Splitting under Visible Light. *ChemSusChem* **2016**, *9*, 2201–2208.

(36) Darwent, J. R.; Mills, A. Photo-Oxidation of Water Sensitized by $WO_3$ Powder. *J. Chem. Soc. Faraday Trans. 2* **1982**, *78*, 359–367.

(37) Nakada, A.; Nishioka, S.; Vequizo, J. J. M.; Muraoka, K.; Kanazawa, T.; Yamakata, A.; Nozawa, S.; Kumagai, H.; Adachi, S.; Ishitani, O.; Maeda, K. Solar-Driven Z-Scheme Water Splitting Using Tantalum/nitrogen Co-Doped Rutile Titania Nanorod as an Oxygen Evolution Photocatalyst. *J. Mater. Chem. A* **2017**, *5*, 11710–11719.

(38) Maeda, K.; Abe, R.; Domen, K. Role and Function of Ruthenium Species as Promoters with TaON-Based Photocatalysts for Oxygen Evolution in Two-Step Water Splitting under Visible Light. *J. Phys. Chem. C* **2011**, *115*, 3057–3064.

(39) Suzuki, H.; Nitta, S.; Tomita, O.; Higashi, M.; Abe, R. Highly Dispersed $RuO_2$ Hydrates Prepared via Simple Adsorption as Efficient Cocatalysts for Visible-Light-Driven Z-Scheme Water Splitting with an $IO_3^-/I^-$ Redox Mediator. *ACS Catal.* **2017**, *7*, 4336–4343.

(40) The $O_2$ evolution rate over the unloaded $Bi_4NbO_8Cl$ samples were different even by using same batch comparing the experiments before Figure 3-4 and after Figure 3-6 because a different photon flux of the light source was used due to changing the lot of Xe lamp.

(41) Pichat, P.; Enriquez, R.; Mietton, E. Investigations of Photo-Excited $TiO_2$ Based on Time Resolved Microwave Conductivity and Oxygen Isotopic Exchange. *Solid State Phenom.* **2010**, *162*, 41–48.

(42) Subramanian, V.; Wolf, E. E.; Kamat, P. V. Catalysis with $TiO_2$/Gold Nanocomposites. Effect of Metal Particle Size on the Fermi Level Equilibration. *J. Am. Chem. Soc.* **2004**, *126*, 4943–4950.

# Chapter 4

## Manipulation of charge carrier flow in $Bi_4NbO_8Cl$ nanoplate photocatalyst with metal loading

## 4.1. Introduction

Semiconductor photocatalysis is a promising solar energy conversion method. Therein, photogenerated charge carriers migrate from the bulk to the surface to induce redox reactions–water splitting being the primary target.[1–3] For practical solar-to-hydrogen conversion system via photocatalytic water splitting, both the effective absorption of photons in visible light region and the efficient charge separation of photoexcited charge carriers (electrons, holes) are crucial. Thus, semiconductor materials with narrow band gaps such as non-oxides and mixed-anion materials have increasingly been investigated as photocatalysts.[4–9] Although an extraordinarily high quantum efficiency of nearly 100 % has recently been demonstrated under UV light on Al-doped $SrTiO_3$ particulate photocatalyst,[3] such highly efficient charge separation has not yet achieved on visible-light-responsive photocatalysts with narrow bandgaps. Recent efforts, including the above mentioned Al-$SrTiO_3$ and some visible-responsive materials (e.g., $BiVO_4$, $BaTaO_2N$), have focused on facet engineering to expose crystal faces suitable for redox reactions,[3,10–13] where the energy level of each facet determines the charge separation. However, it is not always possible to expose a desired facet of the targeted semiconductors. Moreover, this strategy relies on the intrinsic characteristics of photocatalysts' facets and does not answer the fundamental question of how charge separation is achieved in the bulk of photocatalysts; the carrier flow inside the photocatalyst particle is still not fully understood.

Layered semiconductors such as UV-responsive $K_4Nb_6O_{17}$ have shown promise in photocatalysis[4,14,15] with a couple of advantages, including their controllability of the chemical composition through ion exchange[16–18] and large surface-to-volume ratios.[19] However, from the viewpoint of efficient charge separation inside the photocatalysts, two-dimensional crystal structures may be unfavorable because both photoexcited electrons and holes travel mainly along the in-plane direction, as observed theoretically[20–23] and experimentally.[24–26] Such parallel carrier flows based on the crystal and band structure make it difficult to separate the oxidation and reduction reaction sites in the photocatalyst particles, often resulting in charge recombination. Although the reduction and oxidation sites on several layered photocatalysts such as $BaLa_4Ti_4O_{15}$ were separated,[13,27] the underlying carrier flows in the bulk of the photocatalysts remain elusive.

We have recently reported that $Bi_4NbO_8Cl$ with a layered Sillén-Aurivillius structure comprising [$Bi_2O_2$], [$NbO_4$], and [Cl] modules (Figure 4-1a), exhibits the highest activity among layered compounds, as an $O_2$ evolution photocatalyst in visible-light Z-scheme water-splitting.[28] When prepared by a flux method, $Bi_4NbO_8Cl$ yields nanoplates with good crystallinity.[29] However, despite its band positions suitable for both $H_2$ and $O_2$ production from water, the $H_2$ evolution activity of $Bi_4NbO_8Cl$ was negligible, and surprisingly, the situation did not change when Pt, an established $H_2$ evolution cocatalyst,[4] was introduced.[30,31] This result suggests that charge carriers are not effectively separated in $Bi_4NbO_8Cl$.

Here, we demonstrate an efficient spatial charge separation in $Bi_4NbO_8Cl$ nanoplates by controlling the direction of carrier flows with Rh loading. In the absence of a cocatalyst, both photoexcited electrons and holes travel along the in-plane direction based on the band dispersions, resulting in recombination at the edge of the nanoplate. However, site-selective Rh deposition at the edge allows the electrons to migrate in the in-plane direction and to be captured by the cocatalyst, while the holes hop along the out-of-plane direction. The resultant spatial charge separation significantly improves the $H_2$ evolution activity. Based on experimental and theoretical investigations, we discuss the carrier flow dynamics and the associated photocatalytic properties of Rh-loaded $Bi_4NbO_6Cl$ nanoplates in comparison to unloaded- and Pt-loaded ones.

## 4.2. Experimental

### Materials.

CsCl (99.0%), NaCl (99.5%), $Bi_2O_3$ (99.99%), BiOCl (99.5%), $Nb_2O_5$ (99.9%), $H_2PtCl_6$ (99.9%), $CH_3OH$ (99.8%), $Pb(NO_3)_2$ (99.9%), and $MnSO_4$•$5H_2O$ (99.9%) were purchased from FUJIFILM Wako Pure Chemical Corporation. $Rh(NO_3)_3$ and $Na_3RhCl_6$ were purchased from Kanto Chemical Corporation. Sodium 2-Sulfonate-1,3,5,7-tetramethyl-8-(3,4-dinitrophenyl)-4,4-difluoro-4-bora-3a,4a-diaza-s-indacene (MS-DN-BODIPY) was synthesized according to literature. Water was purified using a Milli-Q purification system (Direct-Q UV S.).

### Preparation of $Bi_4NbO_8Cl$ Nanoplates.

$Bi_4NbO_8Cl$ nanoplates were synthesized via flux method according to our previous report.[29] An eutectic mixture (65:35) of CsCl and NaCl was used as a flux. The flux was mixed with a stoichiometric mixture of $Bi_2O_3$, BiOCl, and $Nb_2O_5$ at a solute concentration of 1 mol %. The total mass was set to be 25 g. The mixture was placed in an alumina crucible with a capacity of 30 $cm^3$, and then heated at a rate of 50 °C $h^{-1}$ to 650 °C, being held at the final temperature for 10 h. After the natural cooling under ambient conditions, the product was washed thoroughly with deionized water, collected by filtration, and air-dried.

**Cocatalyst Loading.**

Rh and Pt and other cocatalysts (Ru, Ir, and Pd) were loaded on $Bi_4NbO_8Cl$ by photo-deposition (PD) and impregnation. In the PD process, metal cations in precursors are reduced by photogenerated electrons and deposited on photocatalysts. The following precursors were employed: $H_2PtCl_6$, $RuCl_3$, $Na_3IrCl_6$, $H_2PdCl_4$ and $Na_3RhCl_6$. In a typical procedure of photo-deposition, 0.2 g of $Bi_4NbO_8Cl$ powder and a calculated amount of metal precursor (0.5–20 wt% for Pt and Rh, 0.5 wt% for others) were mixed in 250 mL of 20 vol% MeOH aqueous solution. The suspension was then irradiated with visible light ($\lambda > 400$ nm) for 5–12 h through a cutoff filter from a 300-W Xe-arc lamp with continuous stirring in a Pyrex reaction vessel connected to a closed circulation system under Ar atmosphere at around 298 K.

On the other hand, in the impregnation method, the deposition process is initiated by the “forced” adsorption of metal cations onto photocatalyst surfaces by solvent evaporation, followed by thermal reduction[5]. First, 0.2 of $Bi_4NbO_8Cl$ powder was immersed in an aqueous solution containing each precursor (0.5 wt%). In the case of 5 wt% of Rh deposition by the impregnation method, $Rh(NO_3)_3$ was used. The suspension was evaporated under constant stirring until complete dryness was reached, followed by heating under an $H_2$ flow at 200 °C for 30 min.

**Characterization.**

Scanning electron microscopy (SEM) images were taken using a Zeiss Nvision 40 microscope. High-angle annular dark-field scanning transmission electron microscopy

(HAADF-STEM) and annular bright-field scanning transmission electron microscopy (ABF-STEM) images were collected using a JEM-ARM200CF (JEOL Ltd., Tokyo, Japan) operating at an accelerating voltage of 200 kV and equipped with a cold field emission gun and a Cs corrector to observe atomic columns of $Bi_4NbO_8Cl$. Elemental analysis was carried out using JEM-ARM200CF equipped with energy dispersive X-ray spectroscopy (EDX). The samples were prepared by grinding the material and depositing a few drops of the suspension onto a holey copper grid covered with a thin carbon film. Transmission electron microscopy (TEM) was carried out using a JEOL JEM-2100F microscope. X-ray photoelectron spectroscopy (XPS) measurements were performed with an ULVAC-PHI 5500MT system.

### Photocatalytic Reaction.

Photocatalytic reactions were performed in a gas closed-circulation system. Photocatalyst powder (0.1 g) was dispersed in a methanol aqueous solution (20 vol%, 100 mL) in a Pyrex top-window cell. The photocatalyst was irradiated with UV and visible light ($\lambda > 300$ nm) or visible light ($\lambda > 400$ nm) through a cutoff filter from a 300-W Xe-arc lamp. The quantity of the evolved gas was determined using an online gas chromatograph (thermal conductivity detector; molecular sieve 5 Å column packing; Ar carrier gas). The apparent quantum efficiency (AQE) was evaluated using a 405 nm monochromatic LED light source (ASAHI SPECTRA, CL-1501).

### Single-molecule Fluorescence Imaging.

To obtain isolated $Bi_4NbO_8Cl$ particles, a well-dispersed methanol suspension of $Bi_4NbO_8Cl$ in low concentration was spin-coated onto a cleaned cover glass. The particle-coated cover glass was annealed at 363 K for 30 min to immobilize the particles on the glass surface, and then placed in a chamber filled with an Ar-saturated aqueous methanol solution of MS-DN-BODIPY (1 μM). A 488-nm CW laser (OBIS 488LX, Coherent; 10 mW $cm^{-2}$) passing through an objective lens (CFI Plan Apo λ100×H, Nikon; NA 1.45) after reflection by a dichroic mirror (Di02-R488, Semrock) was reflected completely at the cover glass-solution interface to generate an evanescent field, which made it possible to detect the fluorescent products selectively on the bottom surface of the crystal. The emission from the sample was collected by the same objective lens, after which it was magnified by a 1.5× built-in magnification changer, and passed through a band-pass filter (FF01-535/50, Semrock) to remove undesired scattered light. The emission images were recorded using an electron-multiplying charge-coupled device (EMCCD) camera (Evolve 512, Roper Scientific) using Micro-Manager (https://www.micro-manager.org/). All experimental data were obtained at room temperature.

**Single-particle PL Imaging.**

PL microscopy measurement was also conducted based on a Nikon Ti-E inverted fluorescence microscope. For wide-field microscopy, the 405 nm CW laser (OBIS 405LX, Coherent; 30 mW $cm^{-2}$) was used to excite the $Bi_4NbO_8Cl$. The emission images were recorded on an EMCCD at a rate of 30 frames $s^{-1}$. A suitable dichroic mirror (Di02-R488, Semrock) and a long-pass filter (BLP01-488R, Semrock) were used to improve the signal-to-noise ratio. For confocal microscopy, the 405-nm pulsed diode laser (Advanced Laser Diode System, PiL040X; 45-ps FWHM, 1 MHz repetition rate) was used to excite the samples. The emitted photons were passed through a 100-μm pinhole and then directed onto a single-photon avalanche diode (Micro Photon Devices, SPD-050). The signals from the detector were sent to a time-correlated single photon counting module (Becker & Hickl, SPC-130EM) for further analysis. A dichroic mirror (Semrock, Di02-R405) and a longpass filter (Semrock, BLP01-458R) were used to remove the scattering from excitation light. PL spectra were obtained by directing the emission into an imaging spectrograph (SOL instruments, MS3504i) equipped with a CCD camera (Andor, DU416A-LDC-DD) through a slit. All experimental data were obtained at room temperature under air. The data were analyzed using the open source image software ImageJ (http://rsb.info.nih.gov/ij/) and Origin 2015 (Origin-Lab).

**Photocatalytic Deposition of $PbO_2$ and $MnO_2$.**

Photo-deposition of $PbO_2$ or $MnO_2$ was conducted with $Pb(NO_3)_2$ or $MnSO_4$. Photocatalyst powders (20 mg) were dispersed in 10 mL of an aqueous $Pb(NO_3)_2$ or $MnSO_4$ solution (5 wt% as Pb or Mn) in a test tube. After the suspension was purged with $O_2$ gas for 30 min, visible light ($\lambda > 400$ nm) was irradiated by a 300-W Xe-arc lamp.

After the 3 h irradiation, the suspension was filtered, washed with deionized water and dried at room temperature.

### TRMC Measurements.

X-band microwave (~9.1 GHz) and third harmonic generation (THG; 355 nm) of a Nd:YAG laser (Continuum Inc., Surelite II, 5−8 ns pulse duration, 10 Hz) were used as the probe and band-gap excitation ($4.6 \times 10^{15}$ photons $cm^{-2}$ $pulse^{-1}$), respectively. A powdery $Bi_4NbO_8Cl$ sample was fixed onto a quartz substrate using optically clear adhesive tape that does not interfere with any TRMC signal. The photoconductivity $\Delta\sigma$ was calculated using the following formula: $\Delta\sigma = \Delta P_r/(AP_r)$, where $\Delta P_r$, $A$, and $P_r$ are the transient power change of the reflected microwave, the sensitivity factor, and the power of reflected microwave, respectively. The obtained $\Delta\sigma$ values were then converted into the product of the quantum yield ($\varphi$) and the sum of the carrier mobilities ($\sum\mu = \mu_+ + \mu_-$) using the following formula: $\varphi\sum\mu = \Delta\sigma(eI_0F_{\mathrm{light}})^{-1}$, in which $e$ and $F_{\mathrm{light}}$ are the unit charge of a single electron and a correction (or filling) factor, respectively. All TRMC measurements were performed under an ambient atmosphere at 25 °C.

### TRAS Measurements.

A set of custom-built TRAS spectrometers was employed as described previously.[32] In the femtosecond to nanosecond regions, experiments were performed using a conventional pump−probe method based on a Ti:sapphire laser system (Spectra Physics, Solstice & TOPAS Prime; duration, 90 fs; repetition rate, 1 kHz). In this experiment, a 355 nm laser pulse was used as the pump pulse. The experiments were performed in air to prevent heating of the sample and to minimize the accumulation of electrons in the photocatalyst due to the high-frequency pump pulse irradiation (500 Hz). In the microsecond to seconds region, transient absorption spectra were measured from 25,000 to 1,000 $cm^{-1}$. 355 nm light (Continuum, Surelite-II, 6 ns, 355 nm, repetition rate of 5−0.01 Hz) was used as the pump pulse. The spectra were obtained at intervals of 200 $cm^{-1}$ and averaged over 300 scans per spectrum. The measurements were performed under vacuum at room temperature. The powder photocatalyst was fixed on a $CaF_2$ plate with a density of ∼1 mg $cm^{-2}$, and the sample plate obtained was placed in a stainless steel cell. For fair comparison with **PD-Rh-$Bi_4NbO_8Cl$** and **PD-Pt-$Bi_4NbO_8Cl$**, **Bare-$Bi_4NbO_8Cl$** was irradiated by visible light for 5 h in a MeOH solution prior to use.

**Density Functional Theory Calculation.**

The band structure calculation of $Bi_4NbO_8Cl$ was performed within the framework of Density Functional Theory (DFT) using a plane-wave pseudopotential method as implemented in the Cambridge Serial Total Energy Package (CASTEP) code of BIOVIA's Material Studio 2019.[33] The interaction between the ionic core and valence electrons was treated with the OTFG ultra-soft pseudopotential using the scalar relativistic Kolling-Harmon approximation. The non-scalar relativistic effects and spin–orbital coupling (SOC) were not considered. The Perdew-Burke-Ernzerhof (PBE) function of generalized gradient approximation (GGA) was employed as the exchange-correlation functional. A plane wave basis set with an energy cut off of 630 eV and the Monkhorst-Pack 3 × 3 × 1 *k*-point mesh was used. The minimization algorithm of Broyden–Fletcher–Goldfarb–Shanno (BFGS) was employed for geometry optimizations with total an energy convergence tolerance of $10^{-6}$ eV per atom. The separation between k-points in the band structure calculations was adopted by 0.001 Å. Other convergence parameters are as follows: a self-consistent field tolerance of $1 \times 10^{-5}$ eV per atom, a maximum stress of 0.05 GPa, and the maximum ionic displacement of $1 \times 10^{-3}$ Å.

Effective mass $m^*$ was calculated according to the obtained band structure. m* is defined by the following equation:

$$\frac{m_0}{m^*} = \frac{m_0}{\hbar^2}\frac{d^2\varepsilon}{dk^2} \tag{6}$$

where m0 is the free electron mass, $k$ is the reciprocal lattice vector in the direction of interest, and $d^2\varepsilon/dk^2$ is the curvature of band at a maximum or a minimum, respectively. Assuming the band around their minima/maxima to be parabolic, we estimate the curvature of the band using the finite differences approximation:

$$\frac{d^2\varepsilon}{dk^2} \approx \frac{2[\varepsilon(k+\Delta k)-\varepsilon(k)]}{\Delta k^2} \tag{7}$$

where Δk = 0.05 Å.

## 4.3. Results and Discussion

### Improvement of $Bi_4NbO_8Cl$ Photocatalytic $H_2$ Evolution Activity

As stated above, the $H_2$ evolution activity of bare $Bi_4NbO_8Cl$ (hereafter denoted as **Bare-$Bi_4NbO_8Cl$**) is low even though it has a conduction band (CB) potential sufficient for $H^+$ reduction,[30] and little improvement is seen when the Pt cocatalyst (5 wt%) is loaded by a photodeposition (PD) method (**Pt-$Bi_4NbO_8Cl$**; Figure 4-1b). In contrast, Rh loading (5 wt%) via PD significantly enhances photocatalytic $H_2$ production, as displayed in the time course of $H_2$ evolution (**Rh-$Bi_4NbO_8Cl$**; Figure 4-1b). We additionally investigated $H_2$ production activities for samples with various metal cocatalysts (Pt, Ru, Ir, Pd, Au, Rh) deposited by PD and impregnation methods, the most frequently used methods for particulate photocatalysts. The results highlight the superiority of **Rh-$Bi_4NbO_8Cl$** (Figure 4-2). $H_2$ evolution is observed at a remarkably high rate under visible-light irradiation ($\lambda$ > 400 nm) on **Rh-$Bi_4NbO_8Cl$** (Figure 4-3). This result confirms that visible-light water splitting is possible and that photocatalytic $H_2$ evolution is based on the bandgap excitation of $Bi_4NbO_8Cl$ (Figure 4-4). Although the activity decreased during long-term irradiation due to physical detachment of the cocatalyst (Figure 4-5), the stability will be improved further by elaborated loading procedures.

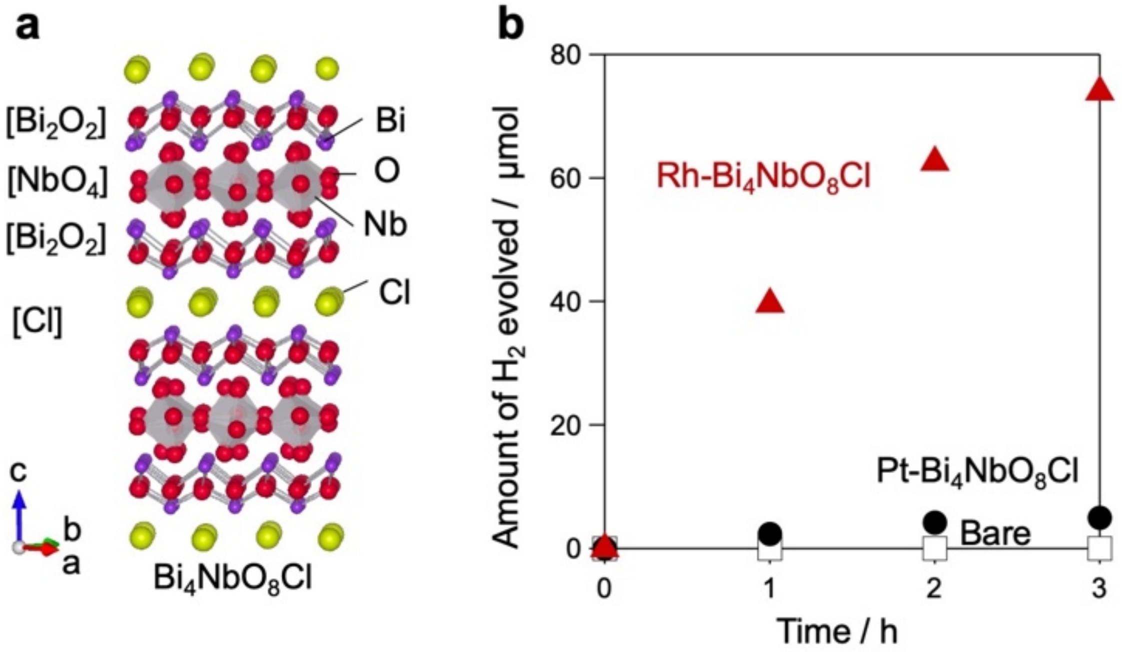

**Figure 4-1. a**, Crystal Structure of layered perovskite oxyhalide $Bi_4NbO_8Cl$. **b**, Time courses of $H_2$ evolution over **Bare-$Bi_4NbO_8Cl$** (squares), and **Rh-$Bi_4NbO_8Cl$** (triangles) and **Pt-$Bi_4NbO_8Cl$**

(circles) in a methanol aqueous solution (20vol%) under photoirradiation ($\lambda$ > 300 nm).

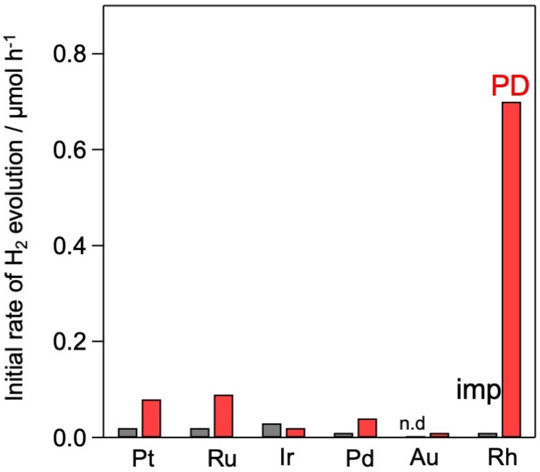

**Figure 4-2.** Various metal cocatalysts (0.5 wt% calculated as metal) were loaded by the photodeposition (PD) or impregnation (imp) method.

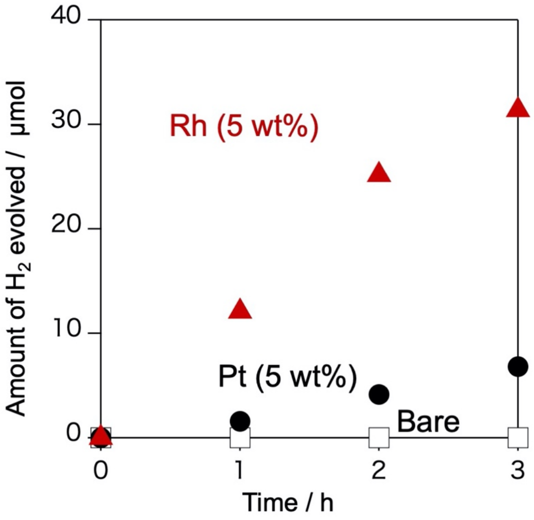

**Figure 4-3.** Time courses of $H_2$ evolution over Bare-$Bi_4NbO_8Cl$ (squares), Rh-$Bi_4NbO_8Cl$ (triangles) and Pt-$Bi_4NbO_8Cl$ (circles) in a methanol aqueous solution (20 vol%) under visible-light irradiation ($\lambda$ > 400 nm).

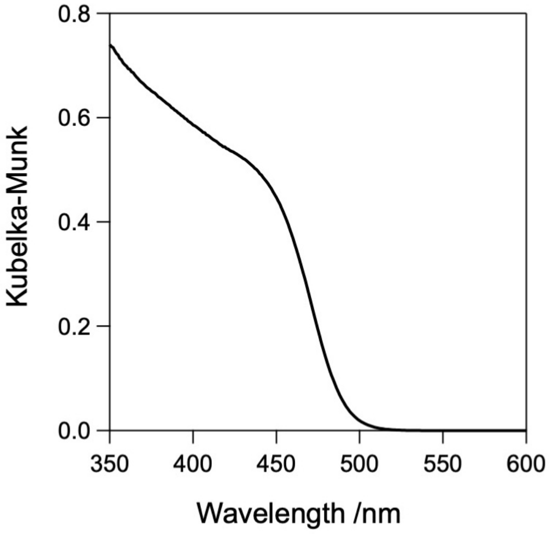

**Figure 4-4.** Diffuse reflectance spectra of $Bi_4NbO_8Cl$.

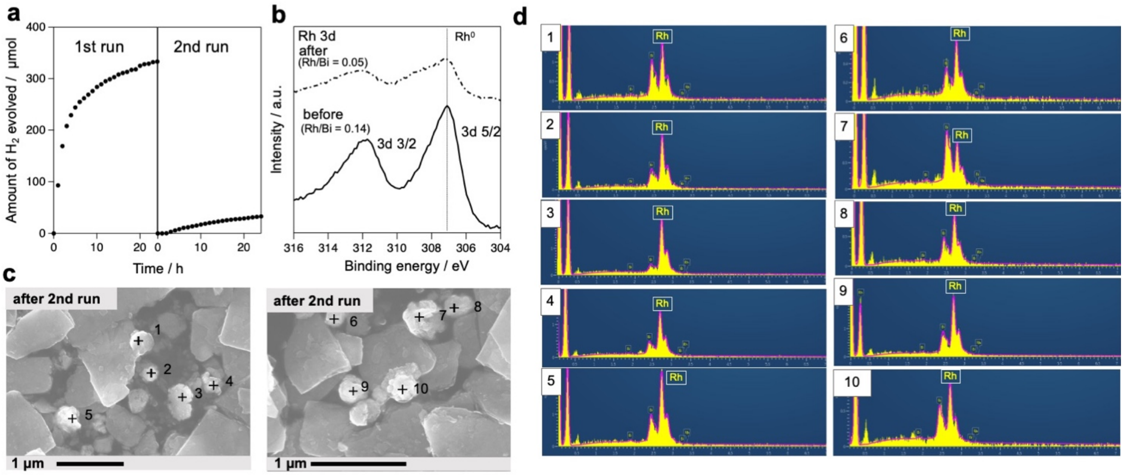

**Figure 4-5. a,** Repeatability test for photocatalytic $H_2$ evolution using **Rh-$Bi_4NbO_8Cl$** (20 wt% Rh) in a methanol aqueous solution (20 vol%) under visible light irradiation ($\lambda > 400$ nm). **b,** XP spectra of Rh 3d regions of **Rh-$Bi_4NbO_8Cl$** before and after the catalytic reaction in **a**. **c, d,** SEM images and EDX analysis for **Rh-$Bi_4NbO_8Cl$** after the photocatalytic $H_2$ evolution reaction. The $H_2$ evolution activity of **Rh-$Bi_4NbO_8Cl$** was deteriorated after 24 h operation. This is due to the detachment of Rh from the photocatalyst during the catalytic process, where the photocatalyst suspension was illuminated upon continuous stirring. After the photocatalytic reaction, XPS showed a decrease in the relative intensity of Rh with respect to Bi. Herein, the photocatalytic particles were collected by filtration with a PTFE membrane filter having 0.2 µm pore size (Omnipore). Therefore, the detached Rh nanoparticles smaller than 0.2 µm were not be collected, which resulted in the decreased intensity of Rh with respect to Bi after the reaction. Some of the Rh particles peeled off from the $Bi_4NbO_8Cl$ nanoplate were observed also in SEM images. Note that such cocatalyst detachment is often problematic in various photocatalytic systems.[1–3] In the present case, the Rh cocatalyst is aggregated largely, which could promote the mechanical detachment upon stirring.

### Site-selective Deposition of Metal Cocatalyst

We conducted detailed investigations using mainly electron microscopic tools (Figure 4-6) to understand why **Rh-$Bi_4NbO_8Cl$** showed excellent $H_2$ evolution activity. Figure 4-6a and 4-7 represents a typical SEM image of **Bare-$Bi_4NbO_8Cl$** synthesized by the flux method, which has nanoplate morphology with large aspect ratios; typical lateral length and thickness are approximately 1 μm and 50 nm, respectively.[29] The TEM/SAED pattern (Figure 4-8) indicated that the dominant facet is the (001) plane. HAADF-STEM images recorded along the [110] and [100] directions are shown in Figures 4-6f, g and Figure 4-9, consistent with the reported crystal structure.[34] Notably, the STEM/EDX line scan analysis and elemental maps suggest that the outermost layer is the [$Bi_2O_2$] layer (Figures 4-6h-l and Figure 4-9).

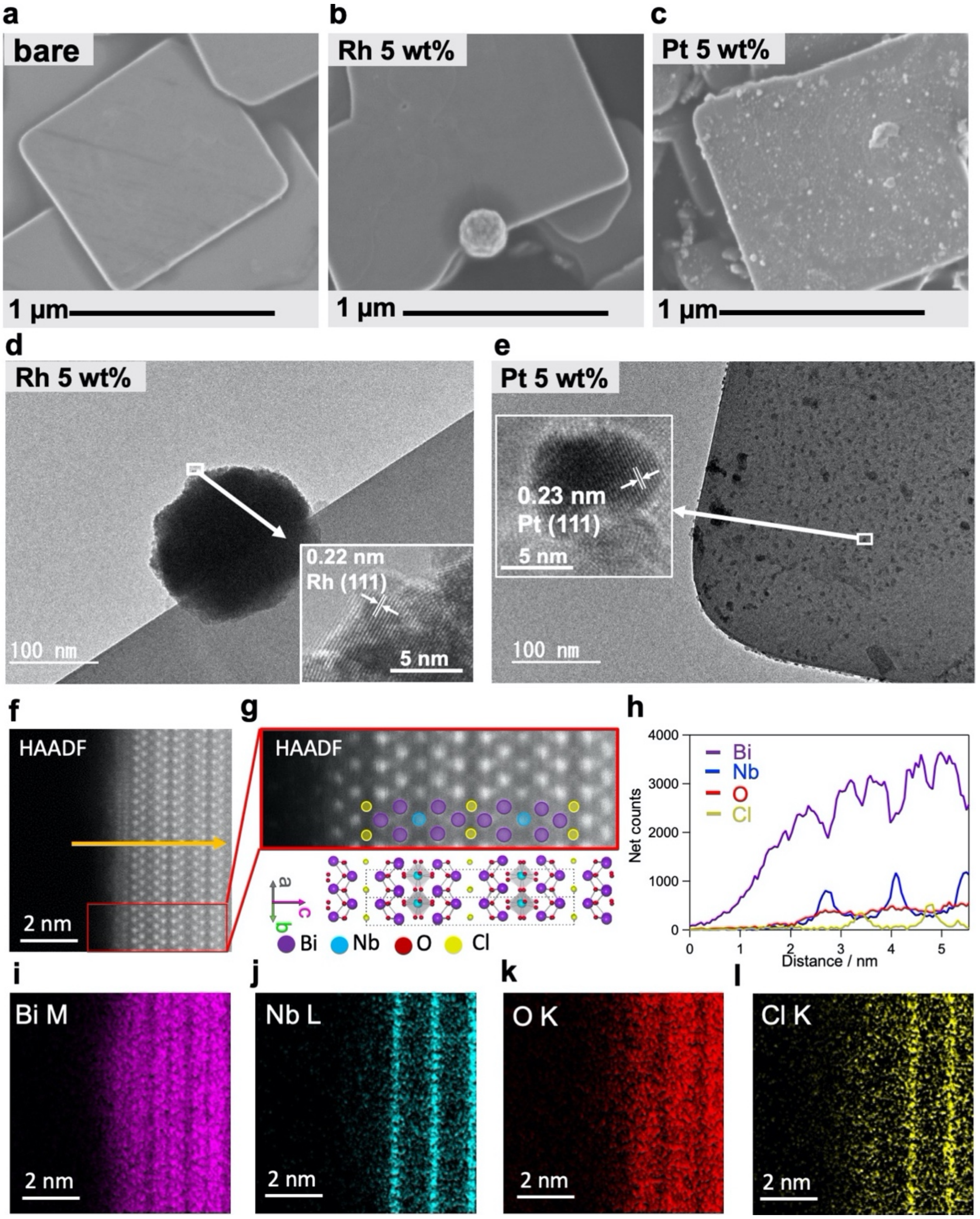

**Figure 4-6. a-c**, SEM images of **Bare-$Bi_4NbO_8Cl$** (**a**), **Rh-$Bi_4NbO_8Cl$** (**b**), and **Pt-$Bi_4NbO_8Cl$** (**c**). **d**, **e**, Bright-field TEM images of **Rh-$Bi_4NbO_8Cl$** (**d**) and **Pt-$Bi_4NbO_8Cl$** (**e**). The insets show HRTEM images of the cocatalysts. **f**, HAADF-STEM image of a **Bare-$Bi_4NbO_8Cl$** nanoplate along the [110] direction. **g**, Close-up in the red rectangle in **f**, together with the $Bi_4NbO_8Cl$ crystal structure. **h-l**, STEM-EDX line scan analysis (**h**) along the yellow arrow in **f** and atomic resolution elemental maps (**i-l**) for Bi (**i**), Nb (**j**), O (**k**), Cl (**l**).

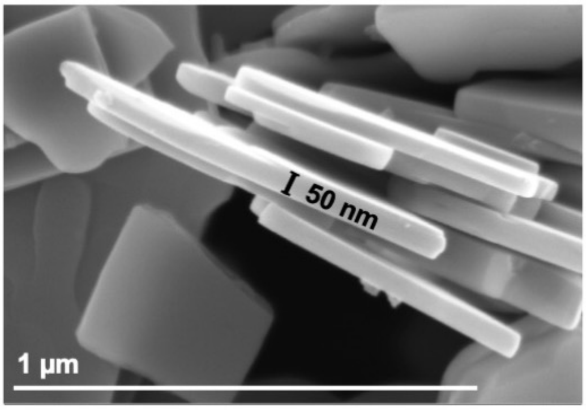

**Figure 4-7.** SEM images of Bare-$Bi_4NbO_8Cl$

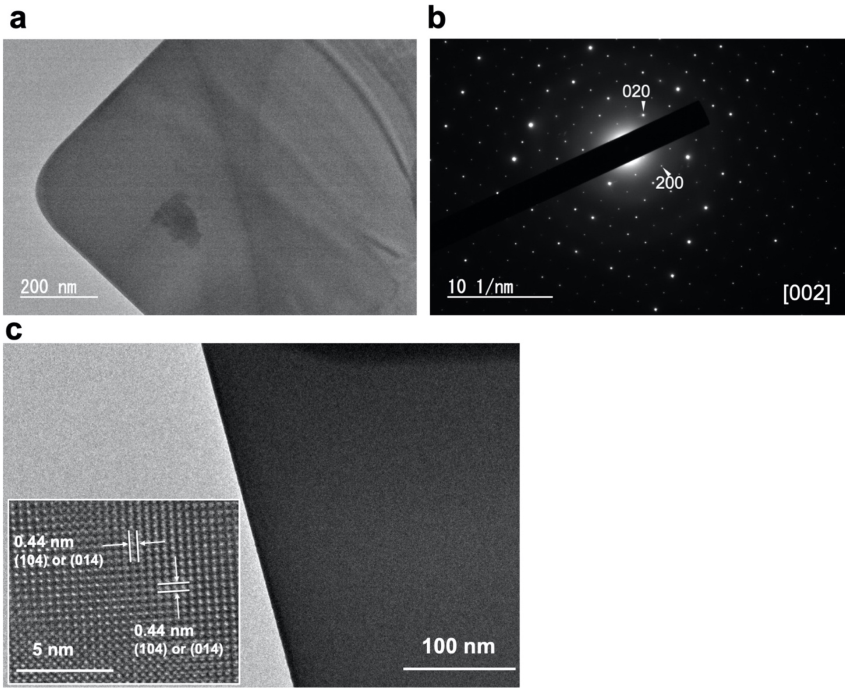

**Figure 4-8.** Bright-field TEM images (**a, c**) and TEM/SAED (**b**) for the $Bi_4NbO_8Cl$ nanoplate.

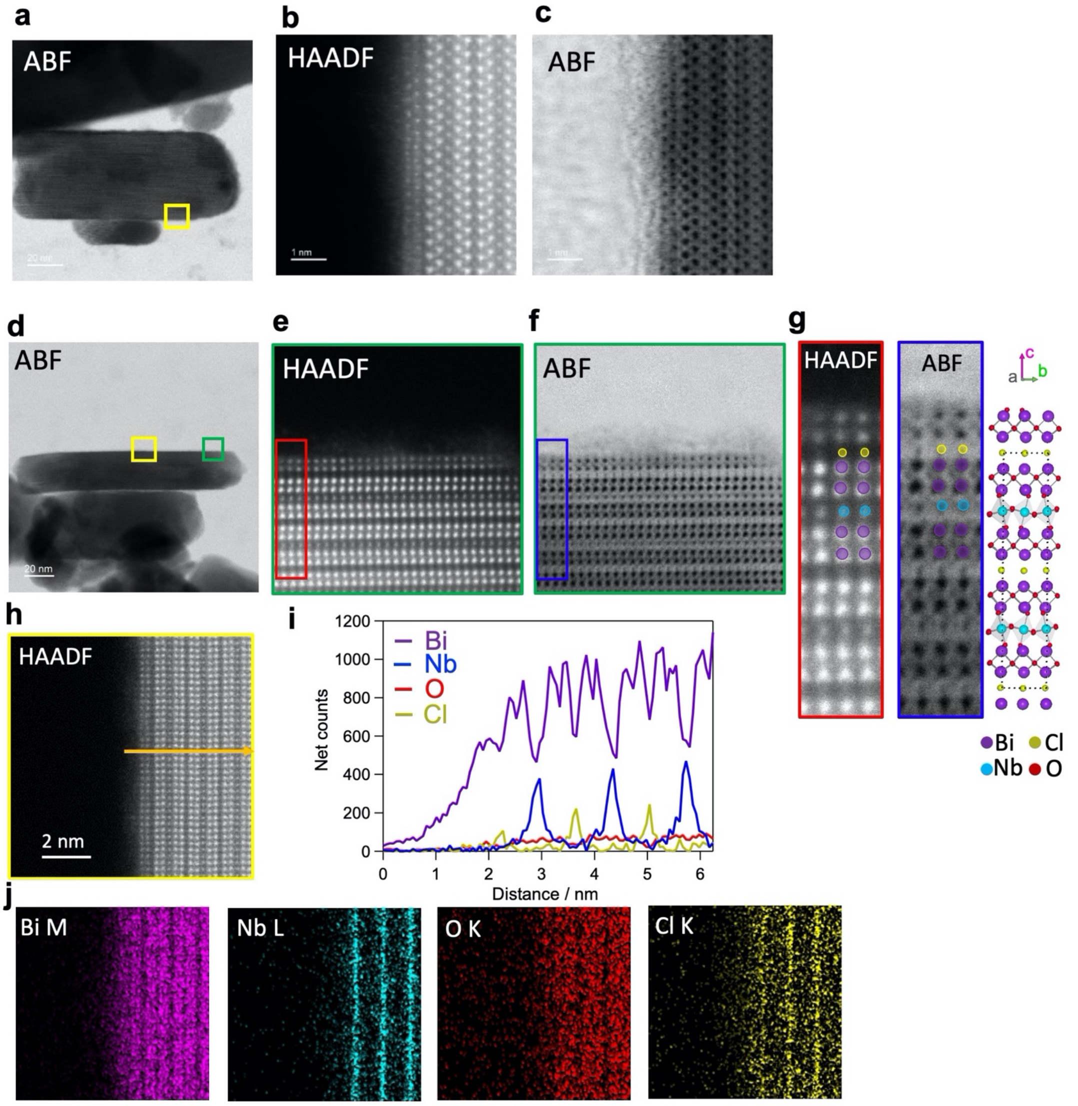

**Figure 4-9. a-c,** HAADF (b) and ABF (**a, c**) STEM images for the same $Bi_4NbO_8Cl$ particle shown in Figure 4-2a. **b, c** Zoomed view of the yellow box in **a**. **d,** ABF-STEM image of another $Bi_4NbO_8Cl$ nanoplate along the [100] direction. **e, f,** Zoomed view of the green box in **d**. **g,** Close-up in the red (HAADF) and blue (ABF) rectangles in **e** and **f**, respectively, along with the corresponding $Bi_4NbO_8Cl$ crystal structure. **h,** Zoomed view of the yellow box in d. **i, j,** Atomic resolution STEM-EDX line analysis (**i**) along the yellow arrow in **h** and elemental maps (j). These results are consistent with the chemical composition and crystal structure of $Bi_4NbO_8Cl$ and also show that the outermost layer comprises of the $[Bi_2O_2]$ layer.

A major difference between **Rh-$Bi_4NbO_8Cl$** and **Pt-$Bi_4NbO_8Cl$** is the location of the cocatalyst, as seen in SEM and HRTEM images; Rh cocatalyst, deposited as agglomerations, was found only at the edges of the $Bi_4NbO_8Cl$ nanoplate (Figures 4-5b,d), whereas Pt cocatalyst was observed as nanoparticulate dispersed mainly on the (001) facet (Figures 4-6c,e). Absorption spectroscopy (Figure 4-10) ensured that precursors for the Rh and Pt cocatalysts, $RhCl_6^{3-}$ and $PtCl_4^{2-}$, were fully consumed during the PD process. The analysis of HRTEM (Figures 4-6d, e) and XPS (Figure 4-11) confirmed that the Rh and Pt species were reduced to zero-valence by photogenerated electrons. The crystal phase and the valance state of $Bi_4NbO_8Cl$ were not changed by the cocatalyst loading (Figure 4-12). For **Rh-$Bi_4NbO_8Cl$**, no Rh species were observed on the (001) facet (Figure 4-13), showing selective deposition at the edges. Direct photoreduction of $Rh^{3+}$ was ruled out by a control experiment (Figure 4-14). We also verified that the p/n type, doping level, and Zeta potentials were not affected by the Pt and Rh loading (Figure 4-15). The $H_2$ evolution rate of **Rh-$Bi_4NbO_8Cl$** reached 222.4 μmol $h^{-1}$ at 20 wt% loading (Figure 4-16), showing an apparent quantum efficiency (AQE) value of 2.6 % at 405 nm (Table 4-1); note that there is room for improvement as the Rh particles grew into aggregates (Figures 4-17d–f, 18c,d).

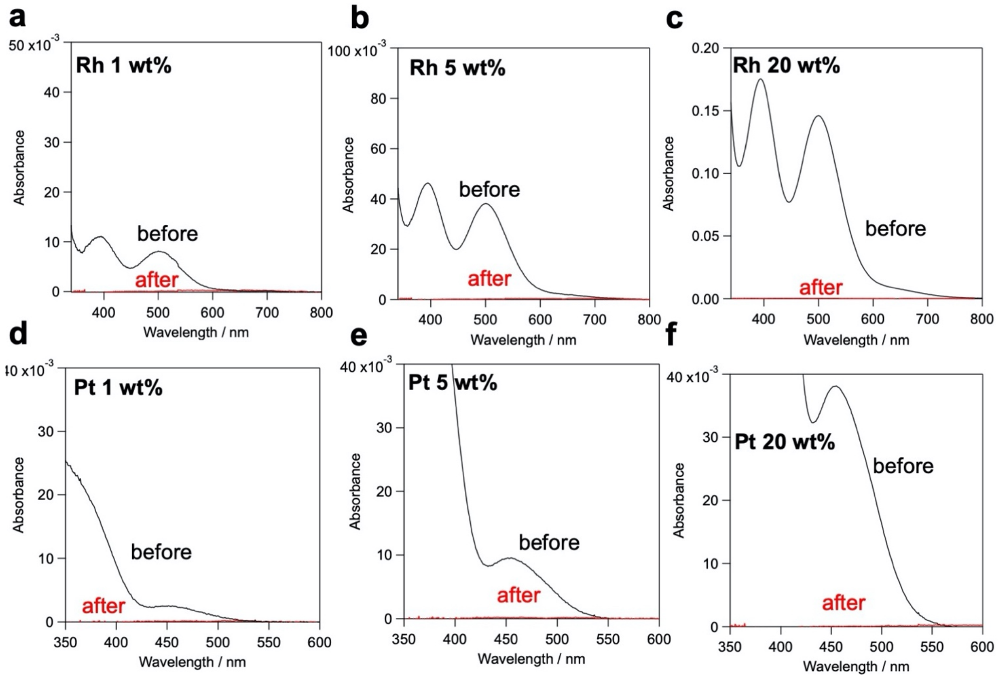

**Figure 4-10.** Absorption spectra of precursors for cocatalysts ($RhCl_6^{3-}$ (**a-c**) and $PtCl_4^{2-}$ (**d-f**)) in the solutions before and after the PD process onto $Bi_4NbO_8Cl$ (feed amount: 1–20 wt%).

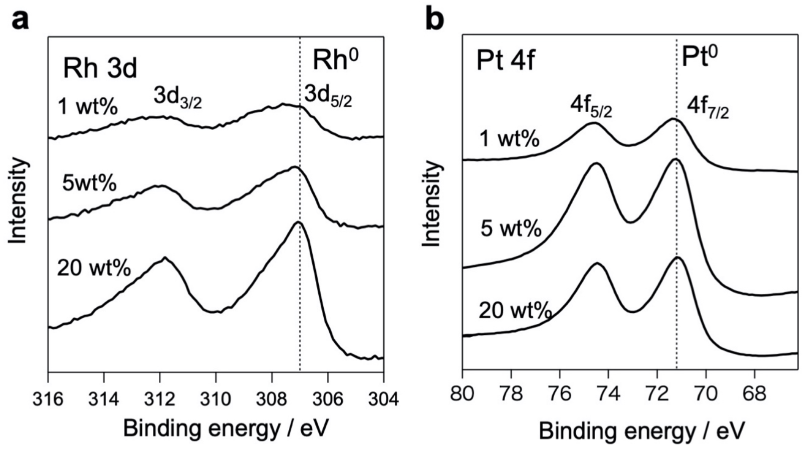

**Figure 4-11.** XPS spectra of Rh-$Bi_4NbO_8Cl$ and Pt-$Bi_4NbO_8Cl$ in the Rh 3d (**a**) and Pt 4f (**b**) regions. The binding energies of elemental Rh and Pt were referred to from a reference handbook.[35]

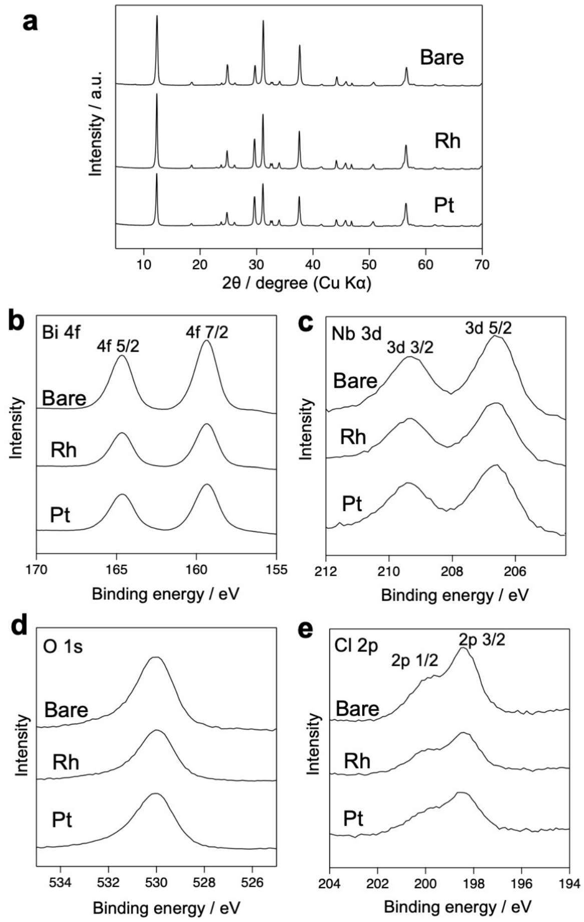

**Figure 4-12. a**, XRD patterns of Bare-, Rh-, and Pt-$Bi_4NbO_8Cl$. b-e, XPS spectra of Bare-, Rh-, and Pt-$Bi_4NbO_8Cl$ in the Bi 4f (**b**), Nb 3d (**c**), O 1s (**d**), and Cl 2p (**e**) regions.

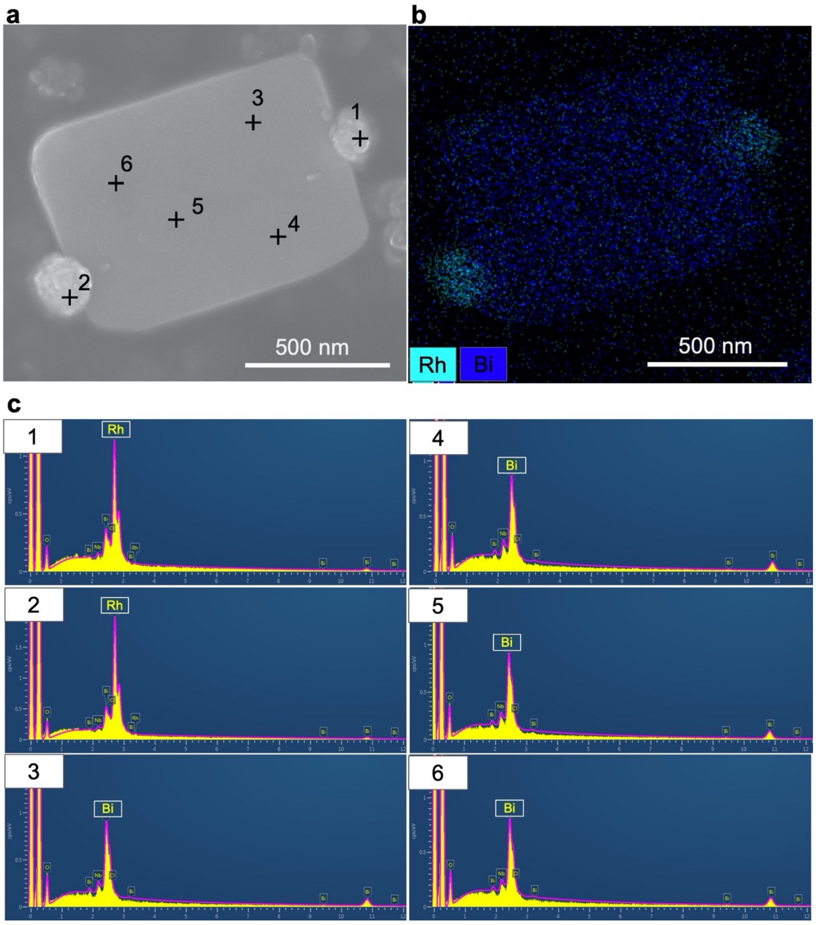

**Figure 4-13.** SEM image (**a**), SEM/EDX mapping (**b**), and SEM/EDX point analysis (**c**) for Rh-$Bi_4NbO_8Cl$.

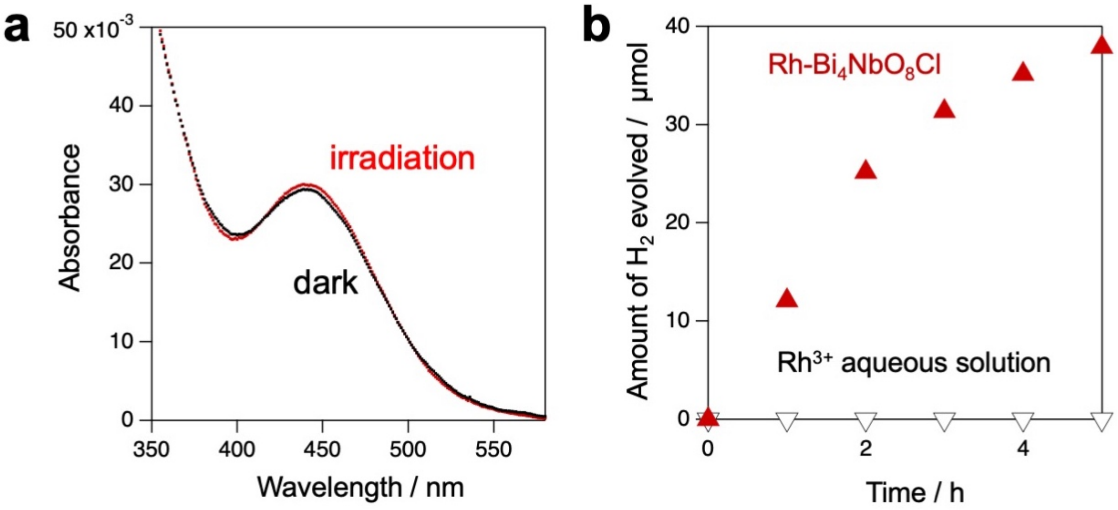

**Figure 4-14. a,** Absorption spectra of a solution containing the $Rh^{3+}$ precursor ($Na_3RhCl_6$) after 5 h stirring with or without photoirradiation ($\lambda$ > 400 nm). **b,** Time courses of $H_2$ evolution under light irradiation ($\lambda$ > 400 nm) from a $Na_3RhCl_6$ methanol aqueous solution (hollow downward triangle) and **Rh-$Bi_4NbO_8Cl$** in a methanol aqueous solution (red upward triangles).

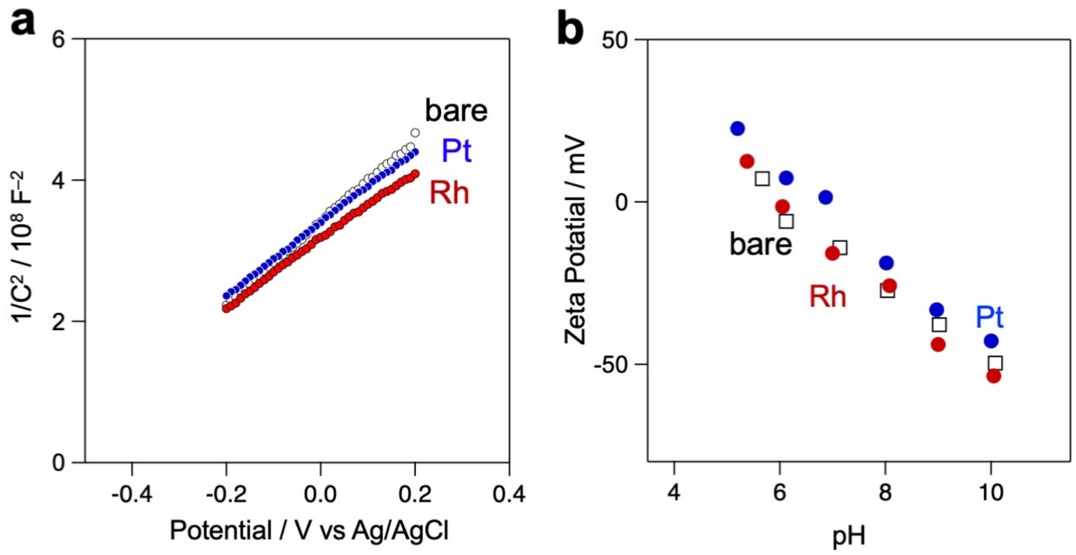

**Figure 4-15.** **a**, Mott–Schottky plots in a 0.1 M phosphate buffer solution (pH = 6). **b**, Zeta potentials-pH plots for **Bare-Bi$_4$NbO$_8$Cl**, **Pt-Bi$_4$NbO$_8$Cl**, and **Rh-Bi$_4$NbO$_8$Cl**.

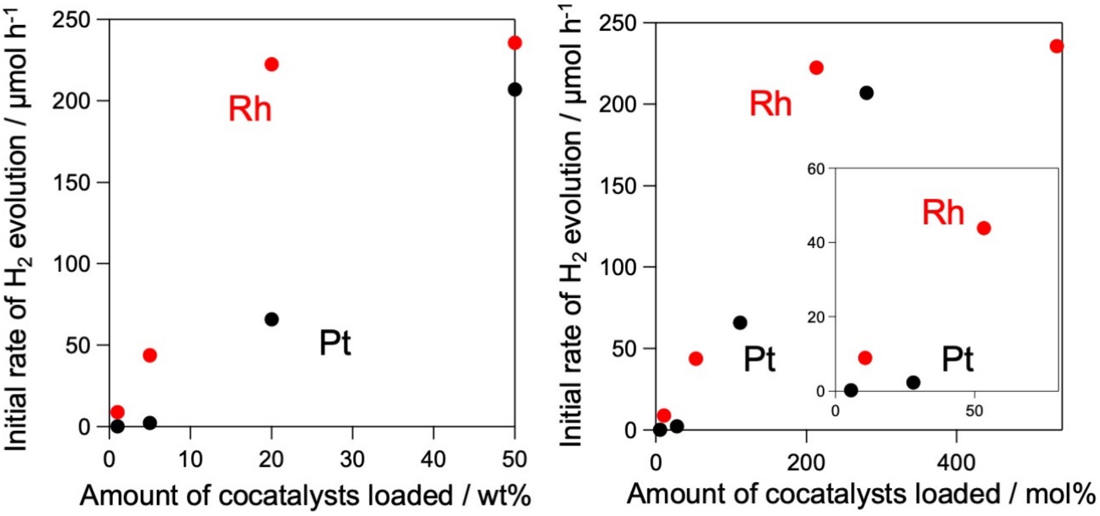

**Figure 4-16.** Initial H$_2$ evolution rate over **Rh-Bi$_4$NbO$_8$Cl** and **Pt-Bi$_4$NbO$_8$Cl** is plotted versus the loading amount (in wt% (**a**), mol% (**b**)) of Rh and Pt. Light source, 300 W xenon lamp ($\lambda > 300$ nm); Medium, 100 mL of a methanol aqueous solution (20 vol%). In both plots, **Rh-Bi$_4$NbO$_8$Cl** clearly shows much higher H$_2$ evolution activity than **Pt-Bi$_4$NbO$_8$Cl** at a low loading amount, where Rh is selectively deposited on the edge while Pt is scattered on (001) of the Bi$_4$NbO$_8$Cl nanoparticle (Figure 4-17). At high mol%, where Pt comes to be deposited on both edge and (001) surface, the H$_2$ evolution activity looks similar in Pt and Rh despite better catalytic activity for HER of Pt than Rh.[36] This result indicates that Pt on (001), acting as a recombination site, affords a negative contribution to the H$_2$ evolution, while Pt of the edge provides a positive contribution to the H$_2$ evolution, showing the importance the deposition site of the cocatalyst for efficient H$_2$ evolution.

**Table 4-1**. AQE values for sacrificial hydrogen evolution reactions on semiconductor photocatalysts.

| Photocatalyst | BG / eV | | $H_2$ evolution | |
|---|---|---|---|---|
| | | | Activity / µmol $h^{-1}$ | AQE / % |
| $SrTiO_3$:Rh[37] | 2.3 | MeOH | 117 | 5.2 (420nm) |
| TaON[38] | 2.5 | MeOH | 120 | 0.8 (420–500nm) |
| $Ta_3N_5$[39] | 2.1 | MeOH | 10 | 0.1 (420-600 nm) |
| $LaTiO_2N$[40] | 2.1 | MeOH | 30 | 0.15 (420 nm < λ < 600 nm) |
| $Sm_2Ti_2O_5S_2$[41] | 2 | MeOH | 22 | 0.3 (440 nm < λ < 650 nm) |
| La–In oxysulfide[42] | 2.6 | MeOH | 10 | 0.2 (420 nm < λ < 600 nm) |
| $Bi_4NbO_8Cl$ (This work) | 2.4 | MeOH | 93 | 2.6 (405 nm) |

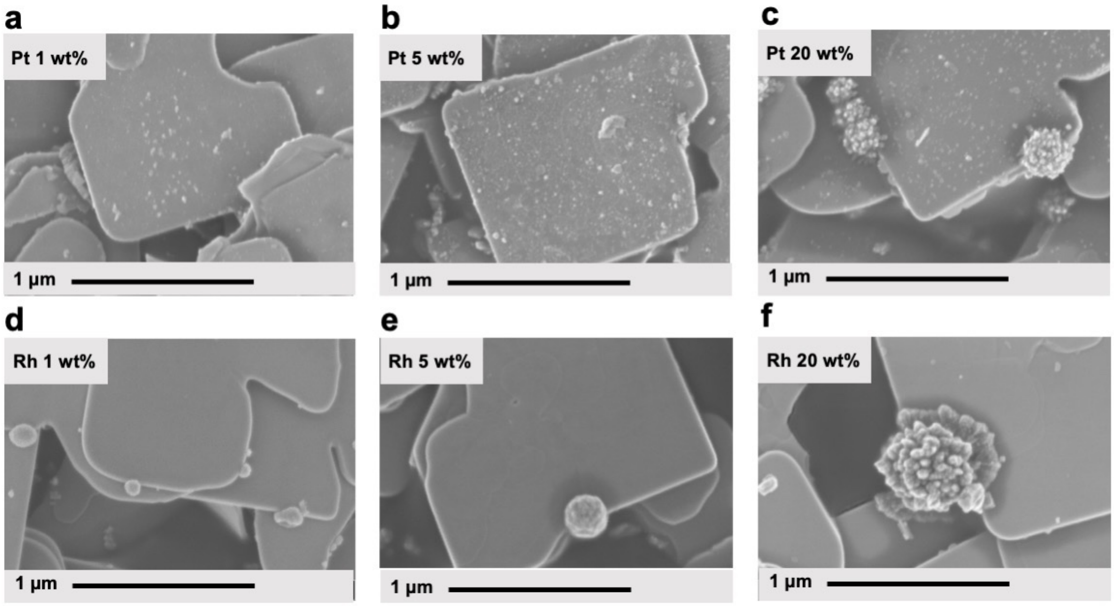

**Figure 4-17.** SEM images Pt-$Bi_4NbO_8Cl$ (**a-c**) and Rh-$Bi_4NbO_8Cl$ (**d-f**) with various loading proportions (1–20 wt%).

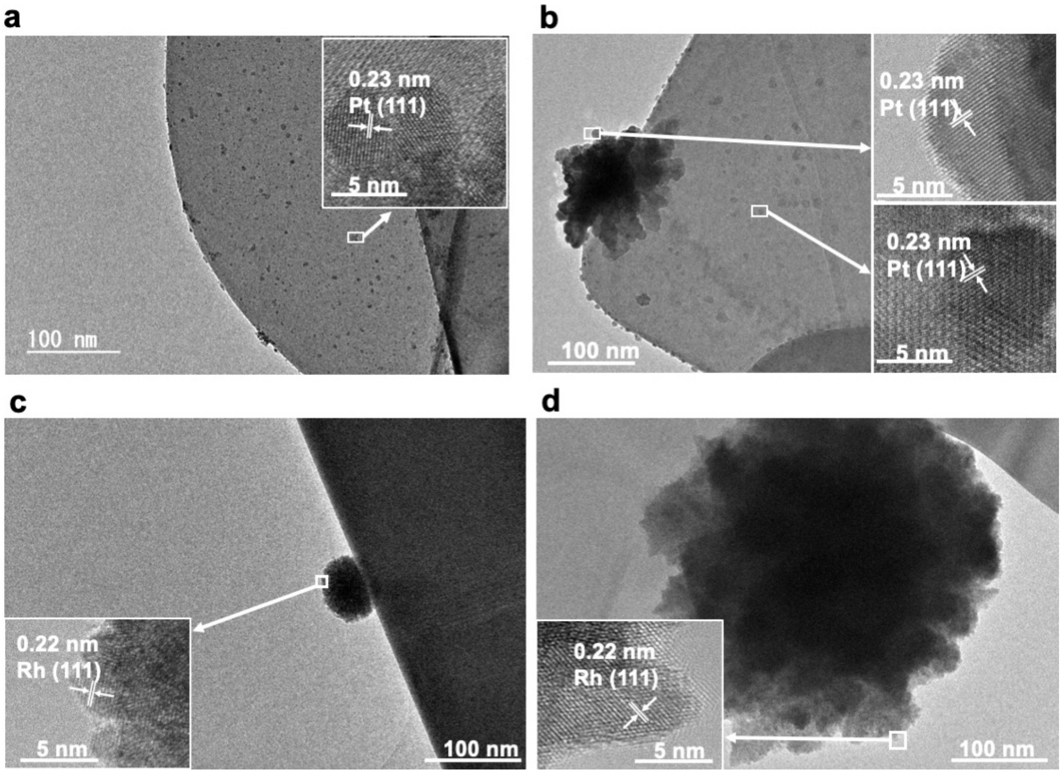

**Figure 4-18. a**, **b**, HRTEM images of **Pt-Bi$_4$NbO$_8$Cl** with 1 wt% (**a**) and 20 wt% (**b**) of Pt loading. **c**, **d**, HRTEM images of **Rh-Bi$_4$NbO$_8$Cl** with 1 wt% (**c**) and 20 wt% (**d**) of Rh loading.

As in the case of Rh and Pt, photoreduction of Au$^{3+}$ and Ag$^{+}$ resulted in preferential deposition as elemental metals on the edges and dominant facet, respectively (Figure 4-19). Note that although Au was deposited at the edge as Rh, the Au-loaded Bi$_4$NbO$_8$Cl showed a negligible activity (Figure 4-2), due to the much inferior HER catalytic activity of Au to Rh.[28] The observed variation in metal deposition sites is unaccountable by the known facet-dependent redox mechanism in which reductive cocatalyst deposition should take place at fixed sites suitable for reduction, regardless of the metal species.[11] A possible mechanism for the variation in the metal deposition site is described in Figure 4-20, where reduction rate of each metal may be a key.

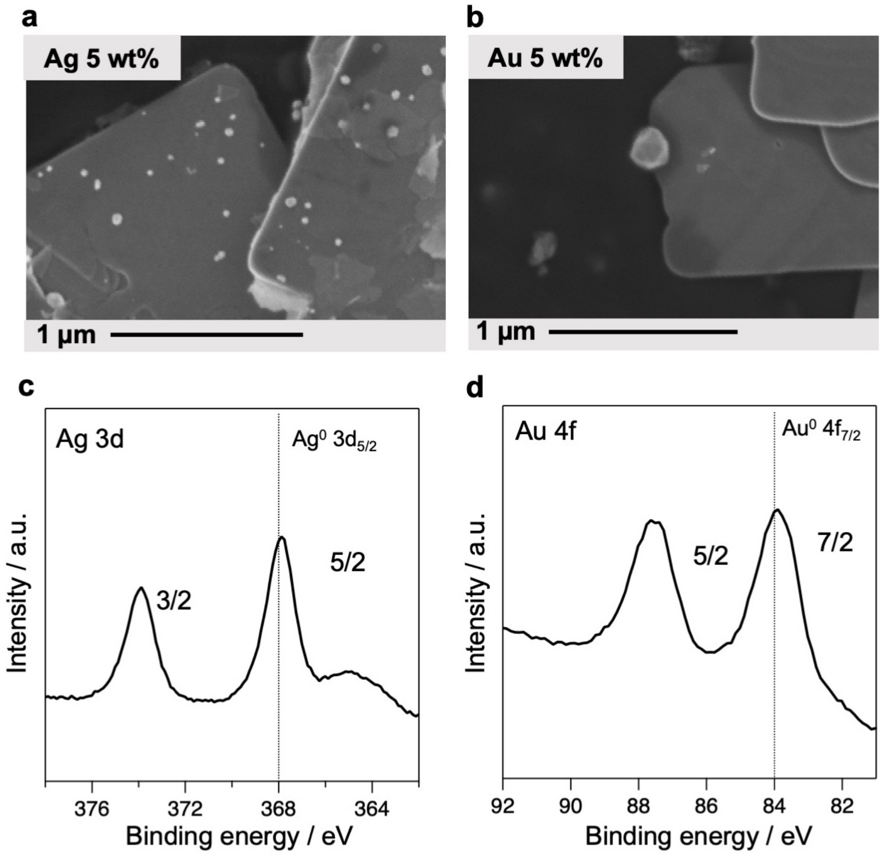

**Figure 4-19.** **a**, **b,** SEM images of $Bi_4NbO_8Cl$ nanoplates loaded with Ag- (**a**) or Au- (**b**) via PD. 5 wt% of Ag and Au were loaded with $AgNO_3$ and $HAuCl_4$ as precursors, respectively. **c**, **d,** XPS spectra for Ag- and Au-loaded $Bi_4NbO_8Cl$ nanoplates focusing on the Ag 3d (**c**) and Au 4f (**d**) region. The binding energies of $Ag^0$ and $Au^0$ were referred to from a reference hand book.[35] These results indicate a selectivity of deposition site depending on metal species. Although Au was deposited at the edge as Rh, the Au-loaded $Bi_4NbO_8Cl$ showed a negligible activity (less than 0.01 μmol $h^{-1}$, Figure 4-2), which is accounted for by the fact that the HER activity of Au is inferior to that of Rh.[36]

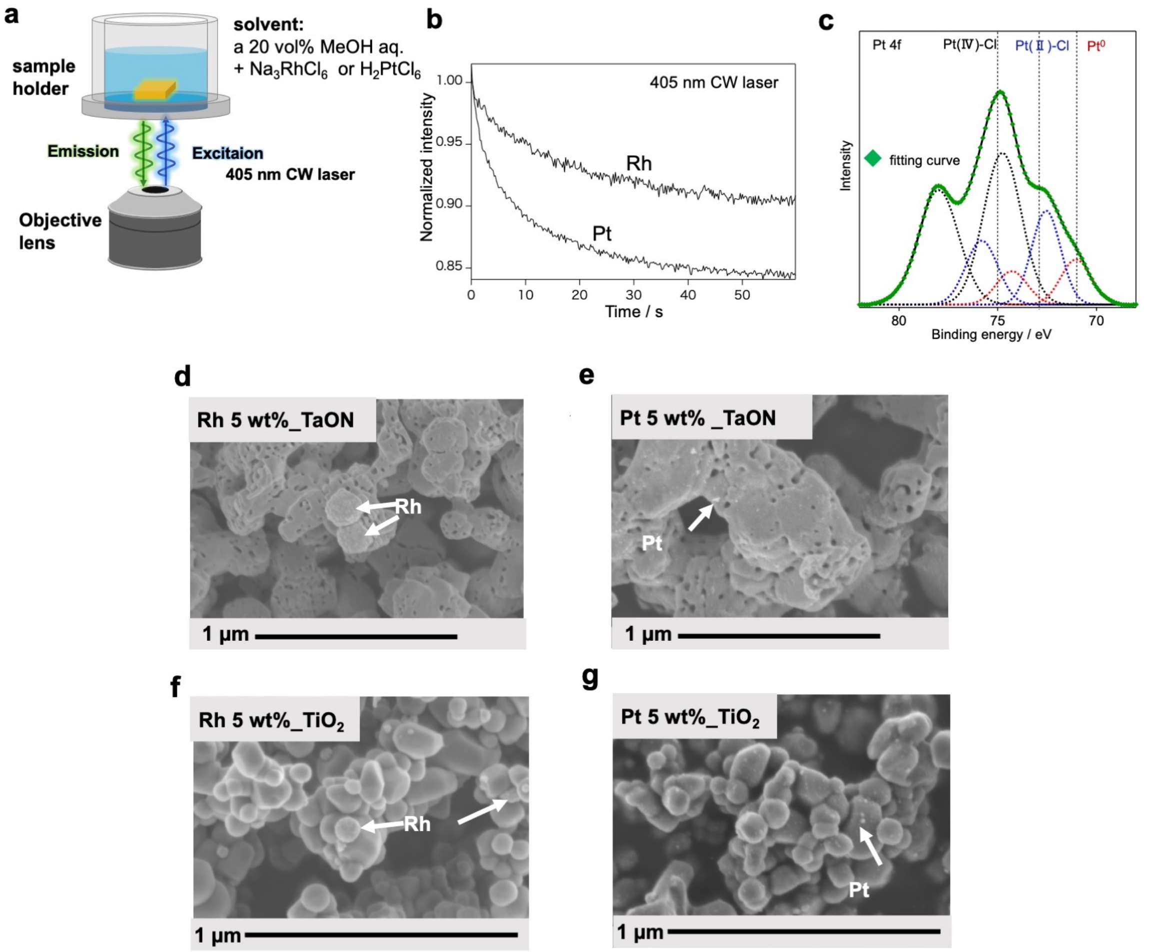

**Figure 4-20. a**, Experimental setup to acquire time-course PL decays by the metal deposition on $Bi_4NbO_8Cl$. **b**, Decay in the PL intensity of $Bi_4NbO_8Cl$ in the presence of $Pt^{4+}$ or $Rh^{3+}$ under 405 nm laser irradiation. **c**, XP spectrum focusing on the Pt 4f region for $Bi_4NbO_8Cl$ after 5 min in the Pt photo-deposition process ($\lambda > 400$ nm, 300 W Xe-lamp). The binding energies of the Pt species were referred to a previous literature.[43] **e-g**, SEM images Rh- and Pt-TaON (**d**,**e**) and Rh- and Pt-$TiO_2$ (**f**,**g**).

The PL intensity decay in **b** was much faster in the presence of $Pt^{4+}$. This indicates that $Pt^{4+}$ is reduced faster, which should lead to the lesser selectivity in the deposition site. As a result, especially at low Pt-loading wt%, Pt is deposited preferentially on the (001) facet with an area much greater than the edge (Figure 4-14a, b). A greater reduction rate is reported to produce smaller particles,[44] which is consistent with the present case. In contrast, $Rh^{3+}$ is reduced at a slower rate, which allows the Rh to be selectively deposited on the edge where electrons accumulate. The Rh deposited via the impregnation method are not selectively on the edge of the particle, indicating that the specific absorption property of Rh may not determine the deposition site as shown in Figure 4-21. In addition, we have conducted Pt and Rh photo-deposition on TaON and $TiO_2$, both of which are often-used photocatalyst. As shown in **d–g**, Rh was deposited aggregately, while Pt were highly dispersive on TaON and $TiO_2$. These results indicate that the reactivity of the $Pt^{4+}$ and $Rh^{3+}$ itself affects the photoreduction process and reduction sites.

Although further investigation is required to draw a concrete conclusion, the number of electrons participating in the reduction of metal ions might be associated with the reduction rates. The numbers of electrons to be required for the each reduction step of a metal ion, are greater for Rh and Au than for Pt and Ag: $[Rh^{III}Cl_6]^{3-} + 3e^- \rightarrow Rh + 6Cl^-$; $[Au^{III}Cl_4]^- + 3e^- \rightarrow Au + 4Cl^-$; $[Pt^{IV}Cl_6]^{2-} + 2e^- \rightarrow [Pt^{II}Cl_4]^{2-} + 2Cl$ and $[Pt^{II}Cl_4]^{2-} + 2e^- \rightarrow Pt + 4Cl^-$; $Ag^+ + e^- \rightarrow Ag$. Note that $Pt^{II}$ was the genuine intermediate for the photodeposition process of $Pt^{IV}$, which was clarified by the XP spectrum measured for a $Bi_4NbO_8Cl$ sample in the early stage of the photodeposition (**c**).

In general, dispersed nanoparticles with small overpotentials for target reactions are preferable as cocatalysts and can often enhance photocatalytic reactions.[45–47] However, the contrasting $H_2$ evolution activities of **Pt-$Bi_4NbO_8Cl$** and **Rh-$Bi_4NbO_8Cl$** suggest that the effect of the deposition site is pivotal, rather than the intrinsic catalytic capability of the cocatalyst, which is supported by the following four additional observations:
(1) The impregnation method produced Rh particles mainly dispersed on the (001) facet (with a minor fraction on the edge), which did not serve as an effective $H_2$ evolution cocatalyst (Figure 4-21). (2) Pt cocatalyst enhanced $H_2$ evolution when loaded on the edges of $Bi_4NbO_8Cl$ nanoplates. With increased loading (20 wt%), some Pt nanoparticles appeared on the edges of **Pt-$Bi_4NbO_8Cl$** (Figures 4-17a-c, 18a,b). The **Pt-$Bi_4NbO_8Cl$** sample with 20 wt% Pt exhibited a rate of $H_2$ evolution of 65.9 μmol $h^{-1}$ (Figure 4-16), which was greater than those of the samples with 1 wt% and 5 wt% Pt mainly on the (001) facet (0.3 and 2.4 μmol $h^{-1}$). (3) When Pt were deposited on not only (001) surface but also the edge at high loading amount, the $H_2$ evolution activity of Pt-$Bi_4NbO_8Cl$ were not higher than that of Rh-$Bi_4NbO_8Cl$, regardless whether the activity is plotted versus the loading amount in wt% or mol% (Figure 4-16), despite better catalytic activity for HER of Pt than Rh. This result indicates that Pt on (001) affords a negative contribution to the $H_2$ evolution. (4) When additional Pt (1 wt%) was deposited on the (001) facet of **Rh-$Bi_4NbO_8Cl$** with 5 wt% Rh, the photocatalytic activity deteriorated substantially (from 39.5 to 8.5 μmol $h^{-1}$, Figure 4-22). (5) **Rh-$Bi_4NbO_8Cl$** showed a higher photocatalytic activity for not only water reduction but also water oxidation than **Pt-$Bi_4NbO_8Cl$** (Figure 4-23a), although the catalytic activity for $IO_3^-$ reduction of Rh is inferior to that of Pt (Figure 4-23b, c). These results clearly show that the deposition site, rather than the metal species, of the cocatalyst significantly affects the photocatalytic activity.

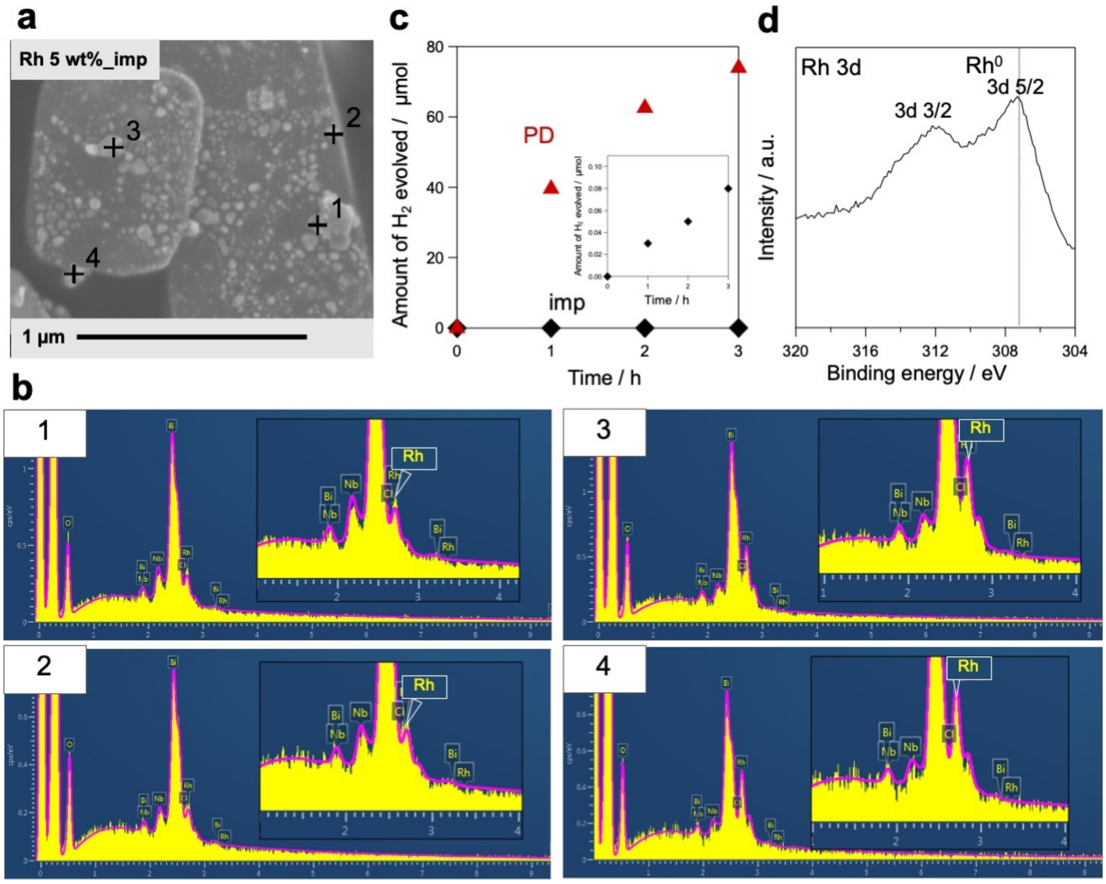

**Figure 4-21.** SEM images (**a**) and SEM/EDX point analysis (**b**) of a Rh-loaded $Bi_4NbO_8Cl$ sample (5 wt%) by the impregnation method. **c,** Time courses of $H_2$ evolution in a methanol aqueous solution (20 vol%) under visible light irradiation (λ > 400 nm). **d,** XPS spectrum for a Rh-loaded $Bi_4NbO_8Cl$ sample by the impregnation method in the Rh 3d region. Note that the impregnation method often affords random depositions, because this process is initiated by the "forced" adsorption of metal cations onto photocatalyst surfaces by solvent evaporation, followed by thermal reduction[8].

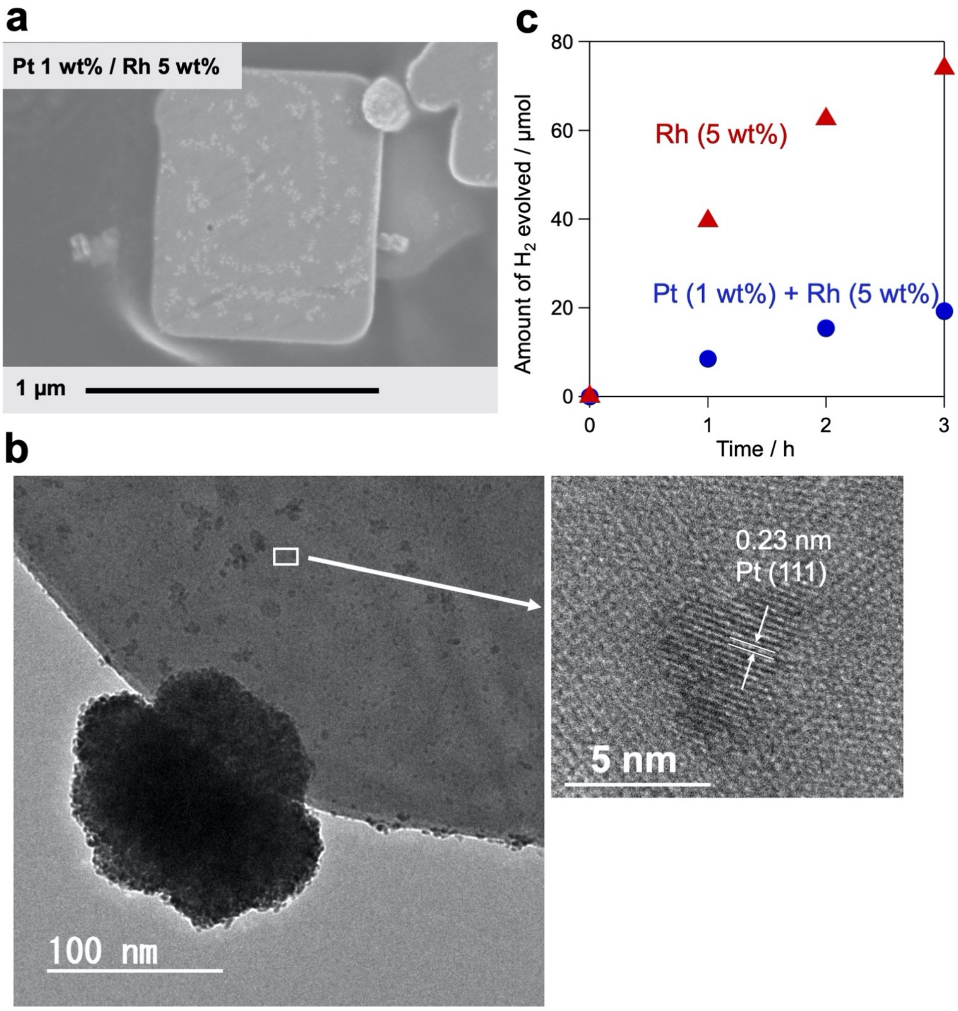

**Figure 4-22.** SEM (**a**) and HRTEM (**b**) images of Pt (1 wt%)-loaded Rh-$Bi_4NbO_8Cl$ (5 wt% Rh). **c,** Time courses of $H_2$ evolution over Pt (1 wt%)-loaded Rh-$Bi_4NbO_8Cl$ (5 wt% Rh) in a methanol aqueous solution (20 vol%) under light irradiation (λ > 300 nm).

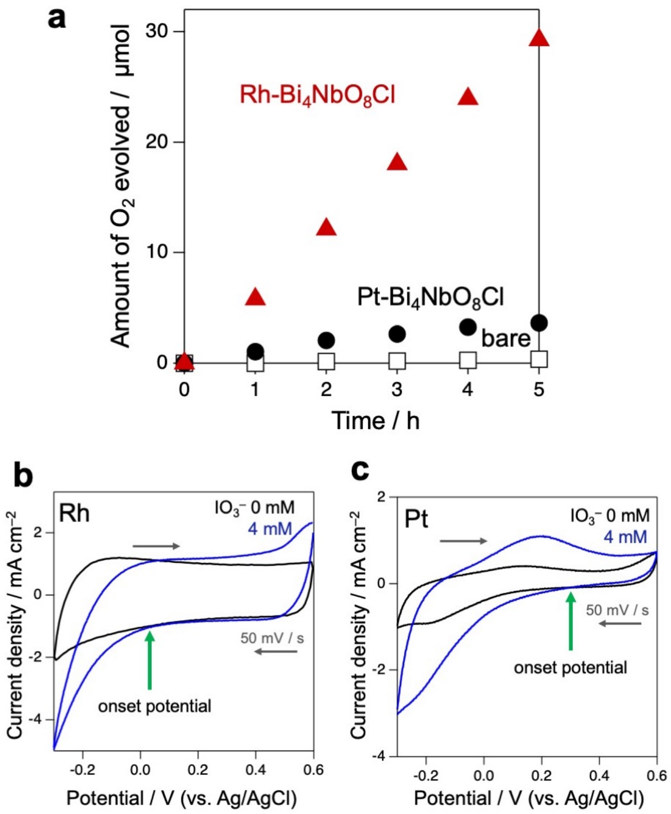

**Figure 4-23.** **a**, Time courses of $O_2$ evolution over Bare-$Bi_4NbO_8Cl$ (squares), Rh-$Bi_4NbO_8Cl$ (triangles) and Pt-$Bi_4NbO_8Cl$ (circles) in in aqueous $NaIO_3$ solution (4 mM) under visible-light ($\lambda >$ 400 nm) irradiation. **b**, **c**, Cyclic voltammogram of FTO substrates loaded with Rh (b) or Pt (c) in 0.5 M aqueous $Na_2SO_4$ solution with or without 4 mM $IO_3^-$, at a scan rate of 50 $mVs^{-1}$. The Pt and Rh electrodes ware prepared via the drop-casting method on a fluorine-doped tin oxide (FTO) glass electrode. A small amount of $H_2PtCl_6$ or $Na_3RhCl_6$ aqueous solution was spread on an FTO substrate. The substrate was dried in air at room temperature and subsequently calcined under an $H_2$ flow (20 mL $min^{-1}$) at 473 K for 30 min. Electrochemical measurements were performed using a potentiostat (VersaSTAT4, Princeton Applied Research Co., Ltd.) and a cell consisting of a prepared electrode, Pt wire, and Ag/AgCl electrode as the working electrode, counter electrode, and the reference electrode, respectively.

### Carrier Flows in Bare-$Bi_4NbO_8Cl$

We hereafter elucidate the dynamics of photoexcited carriers in $Bi_4NbO_8Cl$. Let us first discuss the results of time-resolved microwave conductivity (TRMC),[48,49] which provides direct insight into the carrier flow in **Bare-$Bi_4NbO_8Cl$**. Of note, we adopted two measurement configurations (Figure 4-24a) taking advantage of the morphology of $Bi_4NbO_8Cl$ nanoplates; the anisotropy of carrier mobilities perpendicular and parallel to the (001) plane was evaluated by changing the direction of the incident microwave with respect to the nanoplates fixed to a substrate (Figure 4-25). The conductivity transients for the two settings are displayed in Figure 4-24b, indicating an intense signal for the in-plane direction, with a maximum value of photoconductivity $\varphi\sum\mu$ being 17 times higher. Provided that $\varphi$ is constant (supported by the fact that the photoexcitation for carrier generation is fixed throughout the experiment), the TRMC results indicate that the $Bi_4NbO_8Cl$ nanoplate exhibits a large anisotropy in the charge carrier flow, with greater mobility along the in-plane direction.

Theoretical investigations further support the anisotropic nature of the carrier flow in $Bi_4NbO_8Cl$. Figure 4-24c depicts orbital distribution estimated by DFT calculations, indicating that Bi-6p orbitals in the [$Bi_2O_2$] layer mainly contributes to the bottom of the conduction band (CB, blue) and O-2p orbitals in the [$NbO_4$] layer to the top of the valence band (VB, orange). The band structure of $Bi_4NbO_8Cl$ (Figures 4-24d, 26) shows that both the CB and VB have greater dispersion along the in-plane directions (Γ-X and Γ-Y) than the out-of-plane direction (Γ-Z), in common with layered materials (e.g., $PbBiO_2Cl$[23] and $Sr_2TaO_3N$[50]). However, a closer look reveals that the CB is more dispersive than the VB, and the effective mass of electrons (0.25 $m_0$) is smaller than that of holes (1.4 $m_0$). Thus, electrons have in-plane mobility much higher than holes.

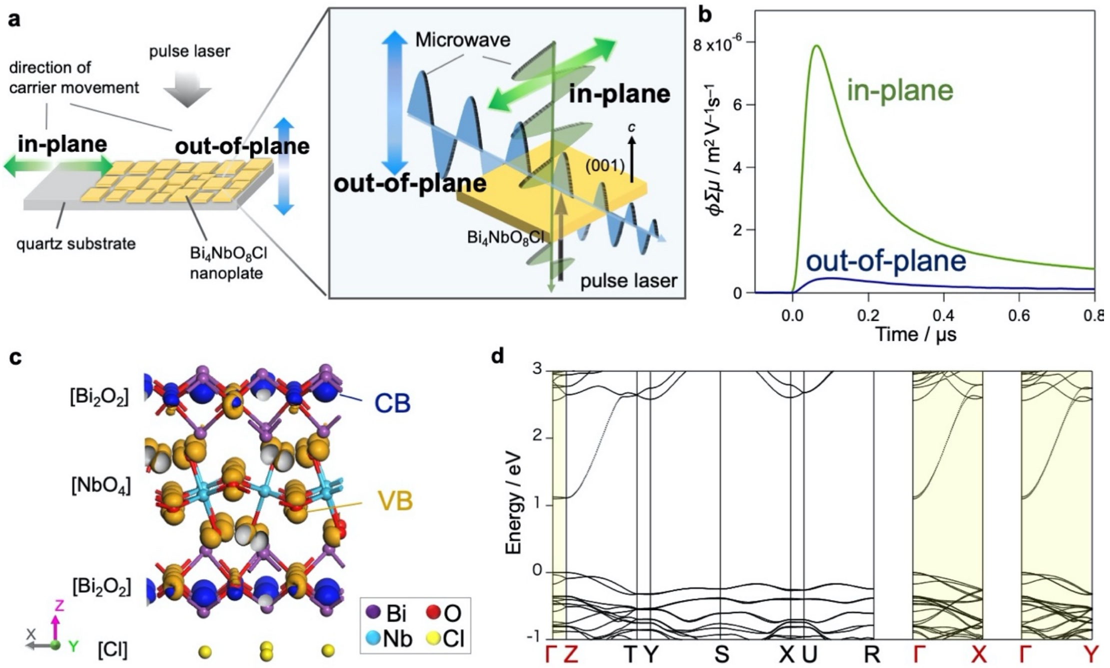

**Figure 4-24. a,** Schematic illustration of the experimental setup for the anisotropic TRMC measurement. **b**, Conductivity transients for **Bare-$Bi_4NbO_8Cl$**. Blue and green profiles are those observed along the in-plane and out-of-plane direction against the (001) plane corresponding to the blue and green arrows in **a**, respectively. A signal intensity is photoconductivity $\varphi\sum\mu$, where $\varphi$ and $\sum\mu$ are the quantum efficiency of the charge carrier photogeneration and sum of the carrier mobilities, respectively. **c,** Orbital distribution of the lower parts of the conduction band (blue) and the upper parts of the valence band (orange) of $Bi_4NbO_8Cl$ estimated by DFT calculation. **d,** Band structure of $Bi_4NbO_8Cl$, where both CB minimum and VB maximum are located at the Γ point.

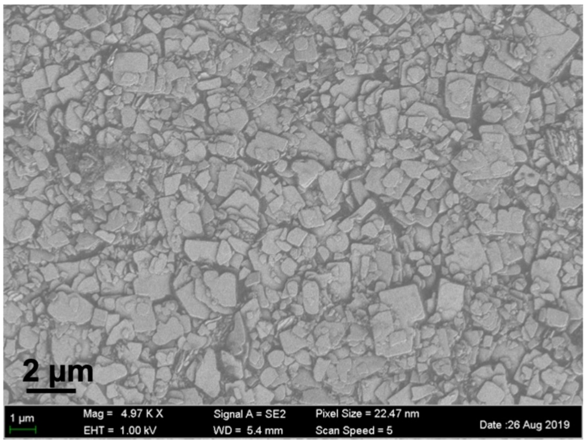

**Figure 4-25.** SEM image of the $Bi_4NbO_8Cl$ sample deposited on a quartz substrate. Simple deposition of $Bi_4NbO_8Cl$ sheets onto a quartz substrate resulted in a fixed, face-to-face orientation against the substrate, which allowed us to evaluate the anisotropy of carrier mobility in directions perpendicular and parallel to the (001) plane.

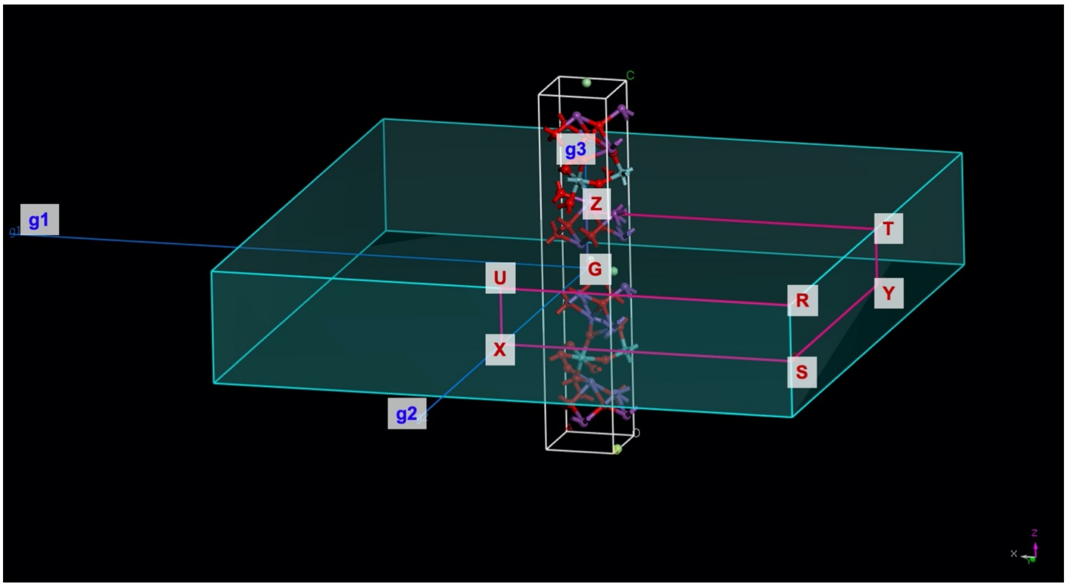

**Figure 4-26.** First Brillouin zone of $Bi_4NbO_8Cl$. The magenta line corresponds to the path of the band structure diagram, and g1, g2, and g3 denote the reciprocal vectors.

### Fate of the Carriers

The fate of photogenerated carriers in $Bi_4NbO_8Cl$ was visualized by single-particle photoluminescence (PL) imaging,[51] using recombination of the electron and hole, or redox reaction products as probes. The PL image of a single **Bare-$Bi_4NbO_8Cl$** nanoplate excited by a 405 nm pulse laser (Figure 4-27a and Figure 4-28) shows strong emission on the edges of the nanoplate when referring to a concurrent optical transmission image of the nanoplate (Figure 4-27b). Herein we conclude that the optical waveguide effect does not play a chief role in the strong emission on the edge, because PL from the bulk and that from the edge possess lifetimes different with each other, and the waveguide effect is negligible when the particle is irradiated with a 532 nm laser $Bi_4NbO_8Cl$ does not absorb (Table 4-2 and Figure 4-28). Combined with the TRMC results, this single-particle PL imaging result of **Bare-$Bi_4NbO_8Cl$** indicates that both photogenerated carriers move in the in-plane direction, leading to recombination at the nanoplate edges.

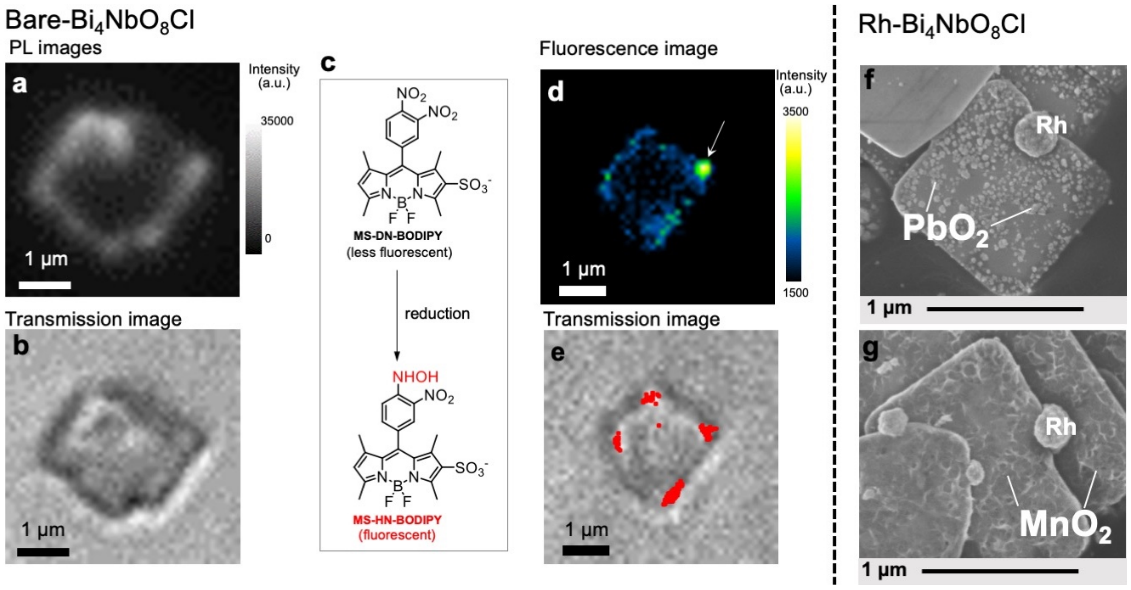

**Figure 4-27.** **a**,**b**, PL (**a**) and transmission images (**b**) of a single **Bare-$Bi_4NbO_8Cl$** nanoplate immobilized on a cover glass in air under 405 nm laser irradiation. The PL intensity was integrated over all monitored wavelengths. **c,** Reductive turn-on conversion of the fluorescent molecular probe used in single-molecule fluorescence imaging. **d**, **e**, Fluorescence (**d**) and transmission (**e**) images of a single **Bare-$Bi_4NbO_8Cl$** nanoplate immobilized on a cover glass in an Ar-saturated aqueous methanol solution containing MS-DN-BODIPY (0.3 μM). For **d**, the image was taken under 488 nm laser irradiation. The red dots in **e** represent fluorescence bursts observed during 180 s irradiation. **f**, **g**, SEM images of **Rh-$Bi_4NbO_8Cl$** after the photocatalytic deposition of $PbO_2$ (**f**) and $MnO_2$ (**g**).

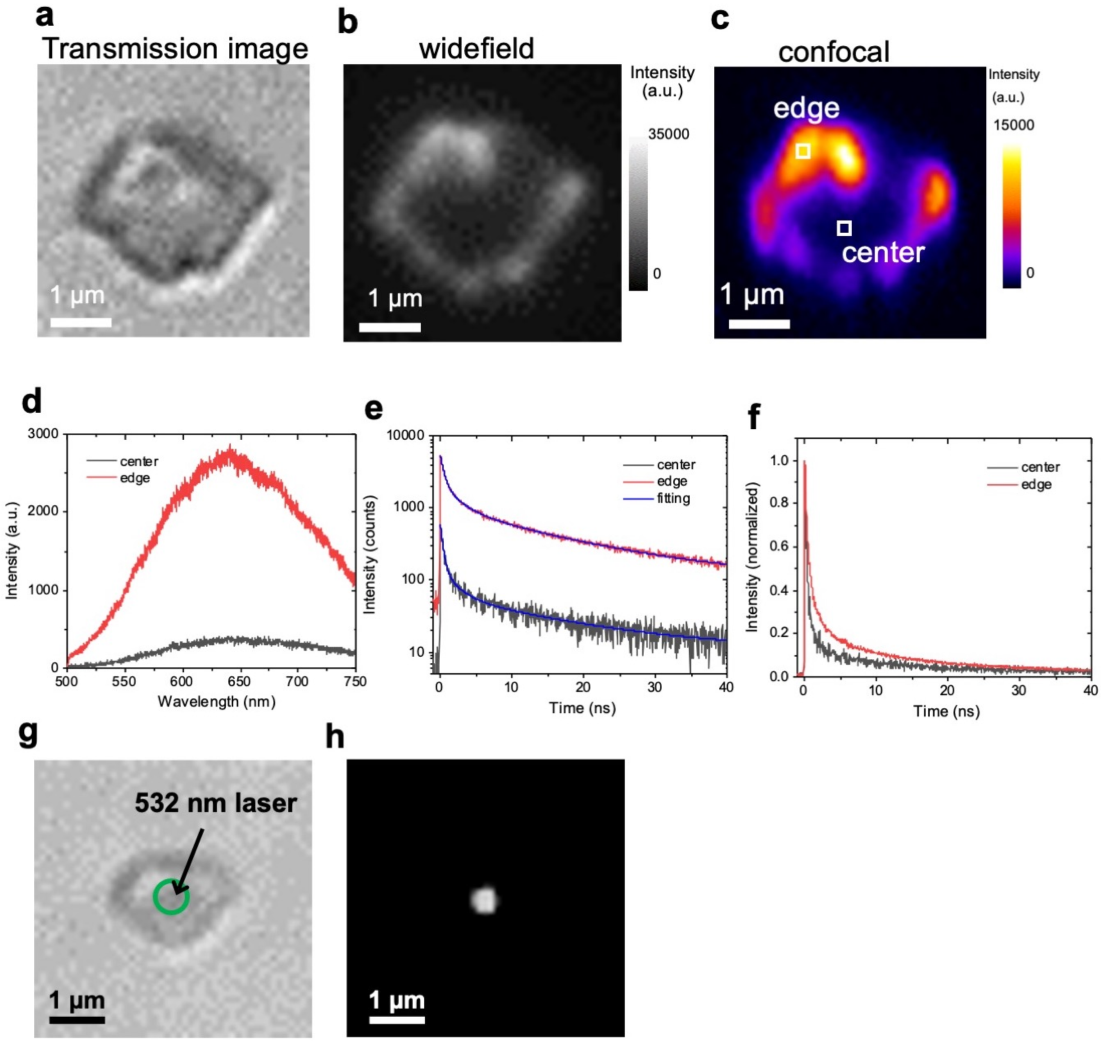

**Figure 4-28.** Transmission (**a**) and PL images (**b, c**) of a single **Bare-Bi$_4$NbO$_8$Cl** nanoplate immobilized on a cover glass in air under 405 nm laser irradiation. The PL intensity was integrated over all monitored wavelengths (> 500 nm). **d-f**, PL spectra (**d**) and decays (**e**, **f**) from the edge and center of the nanoplate monitored in the white boxes in **c**. **g**, A transmission image of a single **Bare-Bi$_4$NbO$_8$Cl** nanoplate immobilized on a cover glass in air. The illuminated region by a 532 nm laser in **h** is shown by the green circle. **h,** Another image of the same region taken in the dark except for the illumination by a focused 532 nm laser. The full width at half maximum (FWHM) of the bright spot on the crystal is approximately 570 nm, which was determined by Gaussian fitting.

The PL image shown in Figure 4-23a is a wide-field image in which the entire particle was photoexcited at once. On the other hand, here we employed confocal microscopy technique, where the luminescence was recorded point-by-point (100.7 nm intervals) under localized laser excitation. The PL intensity was much greater at the edge than at the basal plane. Moreover, decay profiles and lifetimes are different between luminescence at the edge and that from the center of the (001) plane.

In addition, when only the center of a $Bi_4NbO_8Cl$ nanoplate was irradiated by a focused 532 nm CW laser, at which wavelength $Bi_4NbO_8Cl$ has a negligible absorption (Figure 4-4), the incident light did not propagate to the edges of the nanoplate (**h**). From these experimental facts, we have concluded the PL observed at the edge originates from the edge itself, and there is a minor contribution from luminescence transmitted from the bulk part of $Bi_4NbO_8Cl$ through the optical waveguide mode.

**Table 4-2.** Fitting parameters for the PL decays.

| | $a_1$ | $\tau_1$ (ns) | $a_2$ | $\tau_2$ (ns) | $a_3$ | $\tau_3$ (ns) | **<$\tau$> (ns)**[a] |
|---|---|---|---|---|---|---|---|
| center | 1697 | 0.38 | 109 | 2.0 | 53 | 15.4 | 7.9 |
| edge | 4971 | 0.52 | 1354 | 2.3 | 923 | 14.6 | 10.7 |

[a] $\langle\tau\rangle = (a_1\tau_1^2 + a_2\tau_2^2 + a_3\tau_3^2)/(a_1\tau_1 + a_2\tau_2 + a_3\tau_3)$

We then performed two measurements in the presence of reactants to study the dynamics of either carrier, using single-molecule fluorescence imaging technique for electrons[52,53] and oxidative PD of metal oxides for holes. Figure 4-27d shows the fluorescence image of a single **Bare-$Bi_4NbO_8Cl$** nanoplate excited at 488 nm in an Ar-saturated aqueous methanol solution containing MS-DN-BODYPY molecular probe for electrons (Figure 4-27c), wherein methanol served as a hole scavenger. Green and yellow spots showing intense fluorescence were observed mostly at the edge of the $Bi_4NbO_8Cl$ nanoplate. These spots arose from luminescent MS-HN-BODIPY converted from non-luminescent MS-DN-BODYPY upon reduction by photogenerated electrons,[54] as supported by the time evolution of fluorescence mapping (Figure 4-29). Several fluorescence bursts were detected during 180 s of photoirradiation, which are displayed in Figure 4-27e as red spots overlaid with a concurrent optical transmission image of the nanoplate, with the reproducibility checked on other nanoplates (Figure 4-30). Overall, the single-molecule fluorescence experiments show that photoexcited electrons predominantly move along the in-plane direction and accumulate at the nanoplate edge.

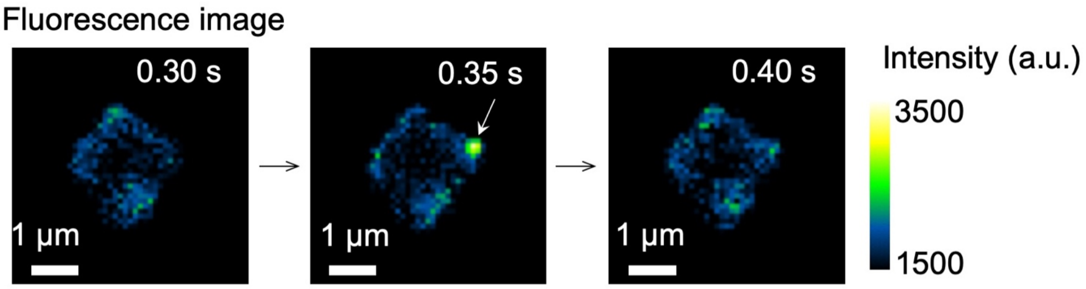

**Figure 4-29.** The green fluorescence from individual product molecules appeared as burst-like signals due to dissociation from the surface into the bulk solution[15].

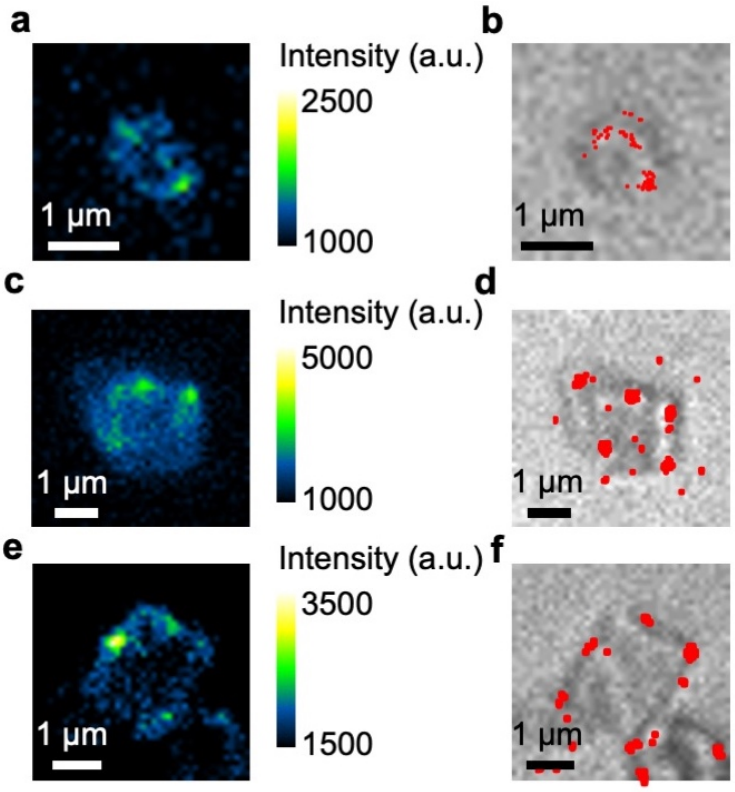

**Figure 4-30. a, c, e,** The fluorescence images were taken under 488 nm laser irradiation. **b, d, f,** The red dots represent fluorescence bursts observed during 180 s irradiation.

Turning to the holes, we conducted photocatalytic oxidation of $Pb^{2+}$ and $Mn^{2+}$ in oxygen-saturated aqueous solution. Here, the metal ions are oxidized by photogenerated holes to the corresponding metal oxides ($PbO_2$ and $MnO_2$) deposited on the photocatalyst surface, thereby acting as probes for the oxidation sites of photocatalysts.[11] On the other hand, photoexcited electrons are trapped by electron acceptors ($O_2$ and/or $H_2O$). For

**Bare-$Bi_4NbO_8Cl$** nanoplate, negligible metal oxide deposition was observed under visible light irradiation ($\lambda$ > 400 nm) (Figure 4-31), which suggests that holes recombine with electrons before participating in oxidation. In contrast, **Rh-$Bi_4NbO_8Cl$** experienced $PbO_2$ and $MnO_2$ deposition (Figures 4-32-35); a number of particles and sponge-like deposits, in the cases of $Pb^{2+}$ and $Mn^{2+}$, respectively, were scattered on the (001) facet (Figures 4-27f, g). The result for **Rh-$Bi_4NbO_8Cl$** is particularly important as it indicates that photogenerated holes are allowed to migrate along the out-of-plane direction and reach the (001) surface, despite the dispersionless VB structure along this direction. Together with the hydrogen evolution experiments (Figure 4-1b), we conclude that the carrier dynamics of **Rh-$Bi_4NbO_8Cl$** is characterized by a unique charge separation, where electrons and holes are spatially separated and migrate, respectively, toward Rh at the nanoplate edge and toward the basal plane, triggering their respective redox reactions.

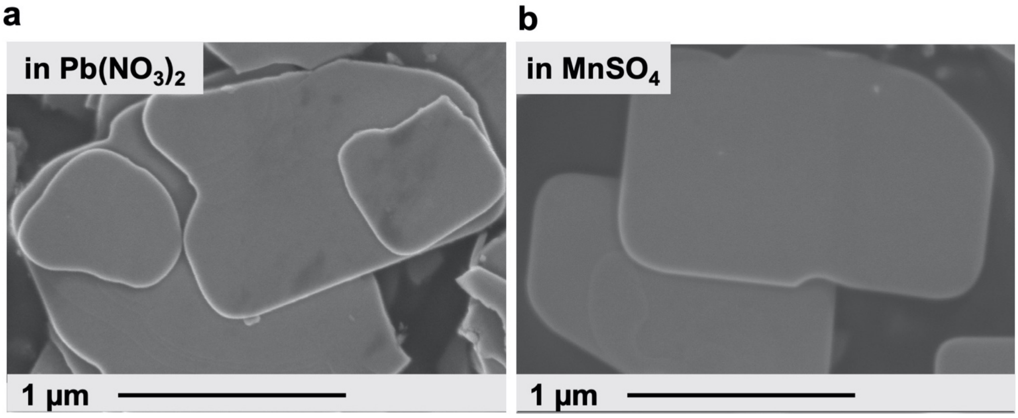

**Figure 4-31.** SEM images of the **Bare-$Bi_4NbO_8Cl$** after visible light irradiation in $Pb(NO_3)_2$ (**a**) and $MnSO_4$ (**b**) solutions with $O_2$ bubbling.

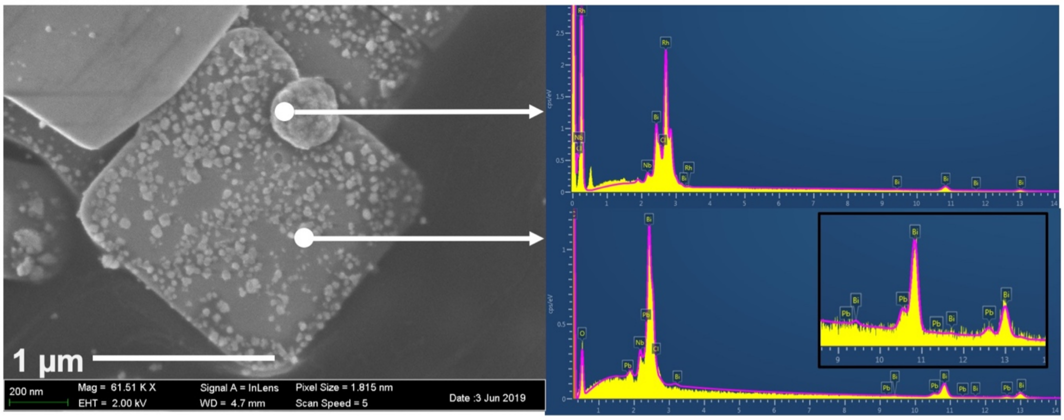

**Figure 4-32.** SEM image and SEM/EDX analysis for Rh-$Bi_4NbO_8Cl$ after the photocatalytic deposition of $PbO_2$.

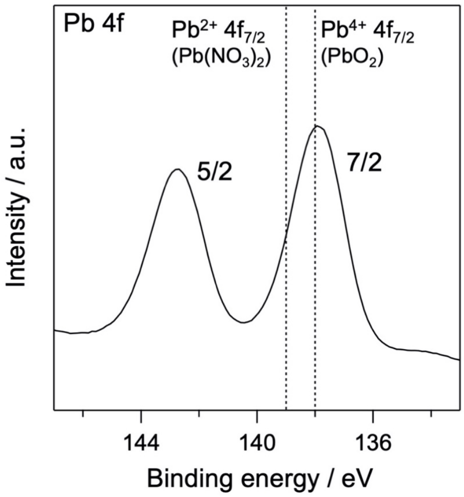

**Figure 4-33.** XPS spectra of **Rh-$Bi_4NbO_8Cl$** after the photocatalytic deposition of $PbO_2$ in the Pb 4f region. The binding energies of $Pb^{2+}$ and $Pb^{4+}$ were referred to from a reference hand book.[35]

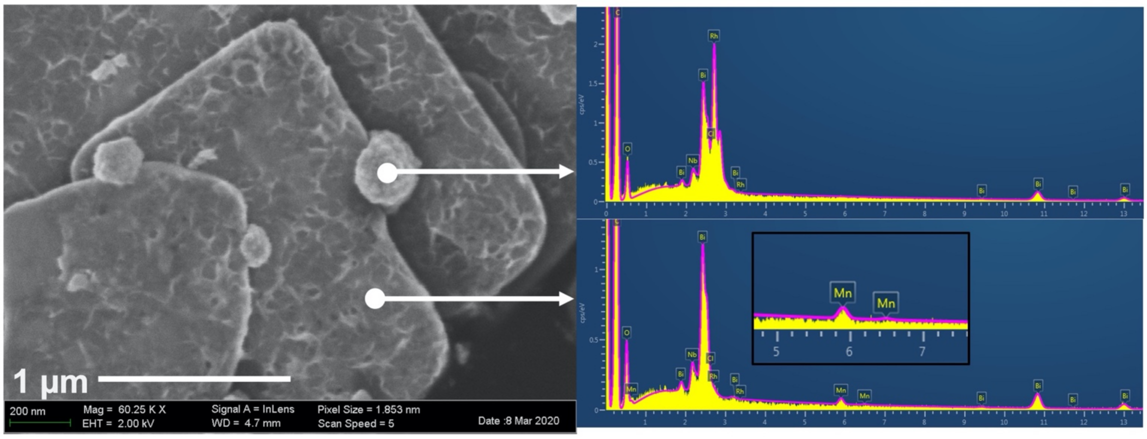

**Figure 4-34.** SEM image and SEM/EDX analysis for Rh-$Bi_4NbO_8Cl$ after the photocatalytic deposition of $MnO_2$.

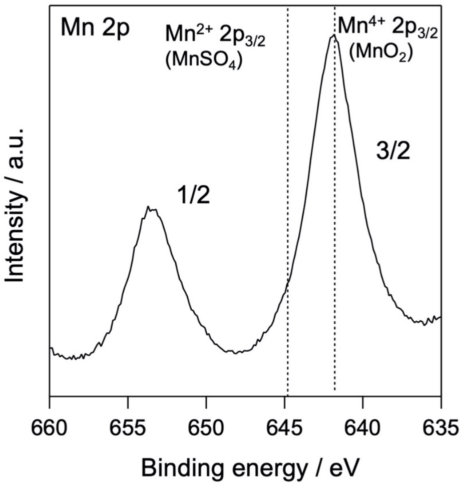

**Figure 4-35.** XPS spectra of **Rh-$Bi_4NbO_8Cl$** after the photocatalytic deposition of $MnO_2$ in the Mn 2p region. The binding energies of $Mn^{2+}$ and $Mn^{4+}$ were referred to from a reference hand book.[35]

### Carrier decay dynamics

We further compared the charge carrier decay profiles using time-resolved absorption spectroscopy (TRAS), as used for semiconductor photocatalysts.[32,55] A microsecond transient spectrum for **Bare-$Bi_4NbO_8Cl$,** when excited by a 355 nm laser pulse (Figure 4-36a), shows three characteristic absorption peaks at 2,000 $cm^{-1}$, 13,000 $cm^{-1}$, and 20,600 $cm^{-1}$. Referring to previous results (e.g., $TiO_2$,[56–58] α-$Fe_2O_3$[59] and $LaTiO_2N$[32]), the first absorption is attributed to photogenerated free (or shallowly trapped) electrons in the CB,[60,61] the second one to the excitation of trapped electrons from the mid-gap state to the CB[55] (derived from halogen defects, see Figure 4-37), and the third one to the photogenerated holes. The initial decay profiles after photoexcitation were examined using femtosecond TARS, focusing on the absorbance changes at 2,000 and 20,600 $cm^{-1}$ (Figures 4-36b-e). The decay of free electrons at 2,000 $cm^{-1}$ was accelerated by the loading of Rh or Pt compared to **Bare-$Bi_4NbO_8Cl$** (Figures 4-36b,c); especially **Pt-$Bi_4NbO_8Cl$** decayed more rapidly than **Rh-$Bi_4NbO_8Cl$**. Regarding hole absorption at 20,600 $cm^{-1}$ (Figures 4-36d, e), the Pt cocatalyst accelerated a decline in the absorption peak, while the decay acceleration was less prominent in **Rh-$Bi_4NbO_8Cl$**. These observations suggest that Pt on the (001) facet traps both electrons and holes, while Rh at the edge captures only electrons, leaving holes in the bulk of $Bi_4NbO_8Cl$ on picosecond timescales.

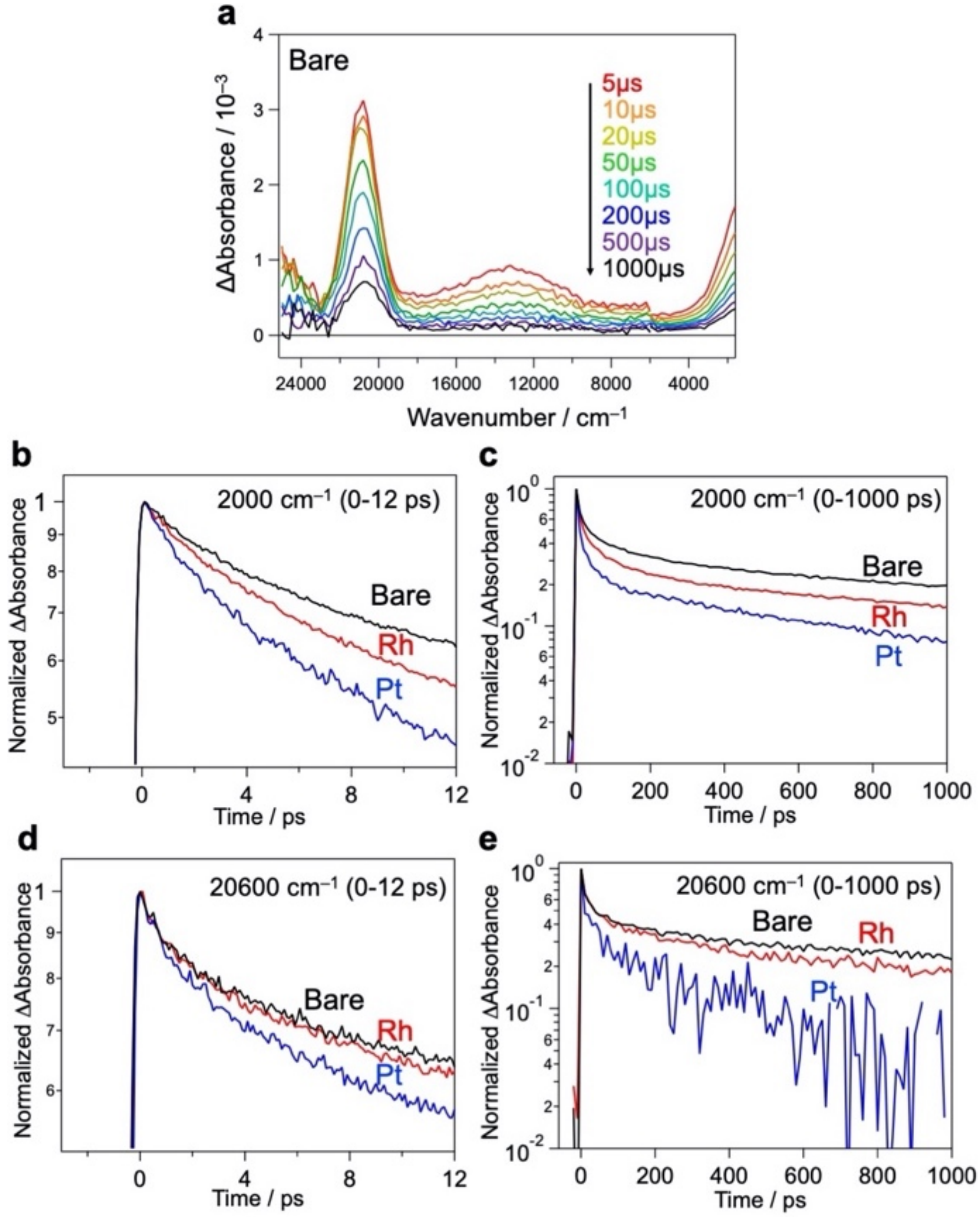

**Figure 4-36. a**, Microsecond TRAS of **Bare-Bi$_4$NbO$_8$Cl** measured in the vacuum. The sample was excited by 355 nm laser pulses (6 ns duration, 0.5 mJ, 5 Hz). **b-e**, Femtosecond decay profiles of transient absorptions at 2,000 cm$^{-1}$ (**b**, **c**) and 20,600 cm$^{-1}$ (**d**, **e**) for **Bare-Bi$_4$NbO$_8$Cl**, **Rh-Bi$_4$NbO$_8$Cl**, and **Pt-Bi$_4$NbO$_8$Cl**. The samples were excited by 355 nm laser pulses (90 fs duration, 6 μJ, 500 Hz) in air for the several pico-second (ps) region.

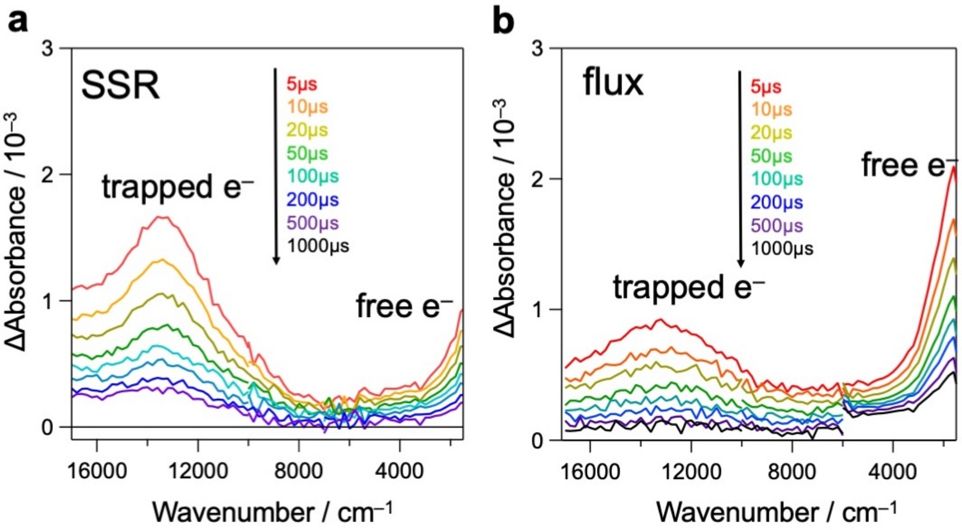

**Figure 4-37.** Time-resolved absorption spectra of $Bi_4NbO_8Cl$ prepared via the conventional solid-state reaction (SSR) and flux synthesis. The samples were excited at 355 nm (6 ns duration, 0.5 mJ, 5 Hz). We previously reported that $Bi_4NbO_8Cl$ prepared by a high temperature solid-state-reaction (SSR) method suffered from Cl defects.[62] In the present study, the $Bi_4NbO_8Cl$ samples prepared via the flux method, where Cl defects are relatively suppressed, were used.[29] In fact, as shown in Figure 4-6a, f-l, and Figure 4-8, the flux-prepared sample feature high quality of crystals. The signal intensities originating from the trapped electrons (at the mid-gap state) and free ones are, respectively, greater and smaller in SSR-prepared $Bi_4NbO_8Cl$ than flux-prepared one. The TRAS result indicates the mid-gap state should stem from the Cl defects.

### Carrier Flow Engineering

Figure 4-38 illustrates the suggested carrier flow dynamics and charge separation of the three $Bi_4NbO_8Cl$ nanoplate samples. The thorough and systematic study described above allows us to reveal how the deposition site of the cocatalyst affects the direction of the carrier flow in the bulk and influences the $H_2$ evolution photocatalytic activity. Hereafter, the carrier flow in each material is discussed from the viewpoints of solid-state chemistry, solid state physics, semiconductor engineering, and catalysis science.

In **Bare-$Bi_4NbO_8Cl$**, photogenerated carriers (both electrons and holes) are likely to travel in-plane, as expected from the layered crystal structure and band dispersion. More precisely, the in-plane dispersion of the conduction band is greater than that of the valence band (Figure 4-24d), suggesting that electrons are lighter than the holes and can migrate faster along this direction. However, since the bare surface of $Bi_4NbO_8Cl$ has no catalytic site for $H^+$ reduction, the lighter electrons cannot flow out of the nanoplate. As a result, the electrons are trapped by the holes that subsequently reach the nanoplate edges, causing recombination, as confirmed by PL imaging (Figure 4-27).

Once Rh is loaded on the nanoplate edges (**Rh-$Bi_4NbO_8Cl$**), the situation changes drastically. Herein, the "light" electrons, which arrive at the edge first, can be extracted from the nanoplate by Rh and then used in the reduction of $H^+/H_2O$, instead of recombining with the holes, as demonstrated by TRAS (Figure 4-36). With the electrons being consumed, the photo-generated "heavy" holes must move to the surface of the nanoplate to react with methanol in order to satisfy charge neutrality in the bulk $Bi_4NbO_8Cl$. Of importance here is that our $Bi_4NbO_8Cl$ crystals are in the form of nanoplates with a thickness of about 50 nm, and this forces the holes to hop towards the nearest (001) facet (Figure 4-38c) against the dispersionless out-of-plane VB. The resultant *orthogonal* carrier flow realizes the spatial separation of photoexcited electrons and holes, greatly enhancing photocatalytic activity.

In **Pt-$Bi_4NbO_8Cl$**, Pt captures both electrons and holes, contrary to what the band dispersion of $Bi_4NbO_8Cl$ tells us (Figure 4-38b). Here, changes in the flows of both carriers are accounted for by band bending. In general, when novel metals such as Pt are brought into contact with an n-type semiconductor, upward band bending and Schottky barrier are formed in the space charge layer.[63] In fact, such upward band bending was reported to allow photogenerated holes to migrate from n-type photocatalysts to Pt.[64–66] In **Pt-$Bi_4NbO_8Cl$**, Pt nanoparticles are highly dispersed on the basal plane (i.e., (001) facet) of the nanoplate (Figure 4-6c). Considering the fact that the typical thickness of the space charge layer is a few tens of nanometers,[67] the thickness of about 50 nm in the present nanoplates means that the scattered Pt and n-type $Bi_4NbO_8Cl$ junctions give effective upward band bending over the entire crystal, allowing the photogenerated holes to move into Pt. On the other hand, the photogenerated electrons are prone to move in the in-plane direction toward the edge of $Bi_4NbO_8Cl$ due to the high mobility along the in-plane direction. However, in **Pt-$Bi_4NbO_8Cl$**, they cannot be consumed at the edge, because of the inertness to $H^+$ reduction in the absence of a cocatalyst there. As a result, electrons are eventually captured by Pt on the (001) plane, followed by recombination with holes therein, as shown by TRAS (Figure 4-36). The electron transfer mechanism from $Bi_4NbO_8Cl$ to Pt might be tunneling through the Schottky barrier,[68–70] where the high dispersity of Pt on the (001) facet should increase the probability of electron transfer to Pt via tunneling. Note that the preceding hole transfer from $Bi_4NbO_8Cl$ to Pt reduces the band bending and barrier height, which may make the subsequent electron transfer easier. In addition, the requirement for charge neutrality in the bulk $Bi_4NbO_8Cl$ after the hole transfer to Pt may also be at play in the electron transfer to Pt and subsequent recombination with the holes. Other possible case is that, at the edge, electrons are recombined with holes that are not captured by Pt as in **Bare-$Bi_4NbO_8Cl$**.

Recall that previous studies on photocatalytic systems relied on facet engineering for efficient charge separation; in $TiO_2$,[10] $BiVO_4$,[11] $SrTiO_3$[12] and $Bi_2MoO_6$,[13] where the photooxidation and reduction sites are separated inherently on different facets. For example, in $BiVO_4$,[11] photo-oxidation and photo-reduction take place preferentially on the (110) and (010) facets, respectively, which is associated with the VBM/CBM levels and the energy of each facet surface. This means that the direction of the carrier flow is determined by the inherent properties of photocatalysts themselves. The choice of the facet plane is a parameter to control. However, there are difficulties and uncertainties in exposing the desired facet experimentally. The present study proposes another strategy for the efficient charge separation: site-specific metal loading manipulates the carrier flow of layered $Bi_4NbO_8Cl$; the intrinsic but unfavorable parallel carrier flow was changed into the orthogonal one.

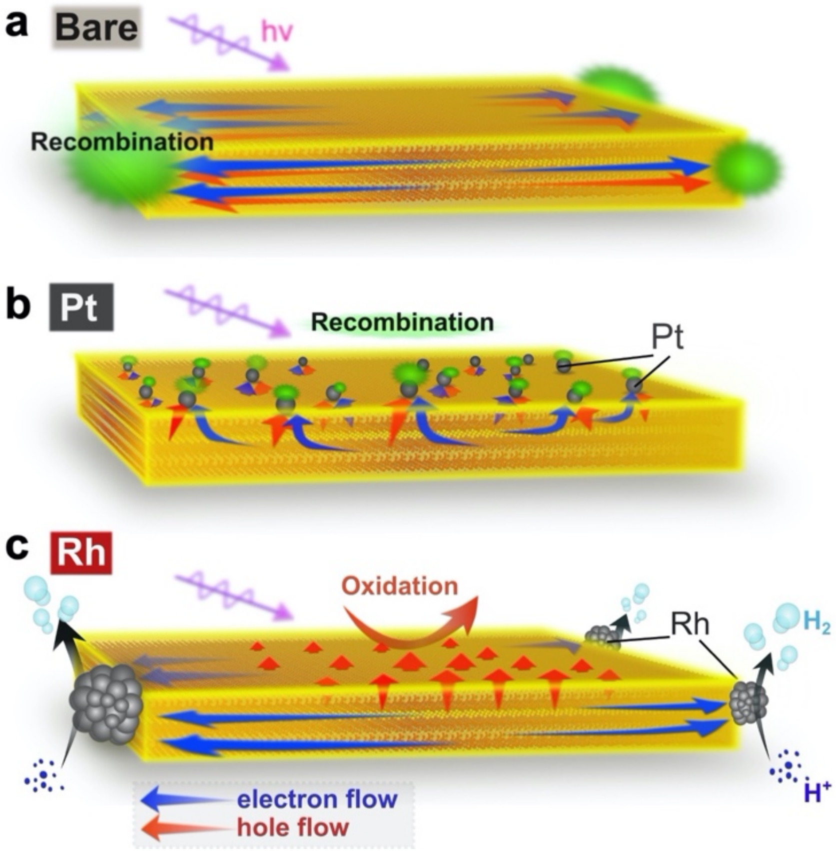

**Figure 4-38. a-c**, Suggested major carrier flow in **Bare-$Bi_4NbO_8Cl$** (**a**), **Pt-$Bi_4NbO_8Cl$** (**b**) and **Rh-$Bi_4NbO_8Cl$** (**c**). In **Bare-$Bi_4NbO_8Cl$**, both electrons and holes are prone to move in the in-plane direction according to their band dispersions, resulting in recombination at the nanoplate edges. In **Pt-$Bi_4NbO_8Cl$**, both carriers are collected by the Pt cocatalyst based on the band bending mechanism, leading again to recombination (Figure 4-37b). However, the edge-deposited Rh cocatalyst in **Rh-$Bi_4NbO_8Cl$** can collect photogenerated "light" electrons predominantly, while "heavy" holes left in the photocatalyst hop towards the (001) facet thanks to the anisotropic crystalline shape (approximately 50 nm in thickness). The orthogonal carrier flow leads to the high photocatalytic hydrogen activity.

## 4.4. Conclusion

In summary, we successfully manipulated the carrier flow in a layered $Bi_4NbO_8Cl$ nanoplate suffering from charge recombination by Rh deposition at the edge, which leads to the spatial charge separation and significantly improves the photocatalytic activity. In conjunction with differences in the in-plane dispersion between the conduction and valence bands, the site-selective deposition allows the Rh cocatalyst to extract photoexcited light electrons efficiently from the photocatalyst, which then forces the remaining heavy holes to hop perpendicular to the plane with the aid of anisotropic crystal geometry. We believe the present strategy is applicable not only to other Sillén-(Aurivillius) layered oxyhalide series,[30,71,72] but also to a variety of semiconductor photocatalysts including mixed-anion compounds with narrow band gaps;[57–59] above all, those considered to be useless or inefficient as photocatalysts can be transformed into effective ones by metal-species deposition on appropriate sites using knowledge on band structures. The present work provides a deeper understanding on, and a new insight for charge separation in semiconductor photocatalysts.

# Reference

(1) Chen, S.; Takata, T.; Domen, K. Particulate Photocatalysts for Overall Water Splitting. *Nat Rev Mater* **2017**, *2* (10), 17050.

(2) Wang, Q.; Hisatomi, T.; Jia, Q.; Tokudome, H.; Zhong, M.; Wang, C.; Pan, Z.; Takata, T.; Nakabayashi, M.; Shibata, N.; Li, Y.; Sharp, I. D.; Kudo, A.; Yamada, T.; Domen, K. Scalable Water Splitting on Particulate Photocatalyst Sheets with a Solar-to-Hydrogen Energy Conversion Efficiency Exceeding 1%. *Nature Mater* **2016**, *15* (6), 611–615.

(3) Takata, T.; Jiang, J.; Sakata, Y.; Nakabayashi, M.; Shibata, N.; Nandal, V.; Seki, K.; Hisatomi, T.; Domen, K. Photocatalytic Water Splitting with a Quantum Efficiency of Almost Unity. *Nature* **2020**, *581* (7809), 411–414.

(4) Kudo, A.; Miseki, Y. Heterogeneous Photocatalyst Materials for Water Splitting. *Chem. Soc. Rev.* **2009**, *38* (1), 253–278.

(5) Kageyama, H.; Hayashi, K.; Maeda, K.; Attfield, J. P.; Hiroi, Z.; Rondinelli, J. M.; Poeppelmeier, K. R. Expanding Frontiers in Materials Chemistry and Physics with Multiple Anions. *Nat Commun* **2018**, *9* (1), 772.

(6) Wang, Z.; Inoue, Y.; Hisatomi, T.; Ishikawa, R.; Wang, Q.; Takata, T.; Chen, S.; Shibata, N.; Ikuhara, Y.; Domen, K. Overall Water Splitting by $Ta_3N_5$ Nanorod Single Crystals Grown on the Edges of $KTaO_3$ Particles. *Nat Catal* **2018**, *1* (10), 756–763.

(7) Cui, J.; Li, C.; Zhang, F. Development of Mixed-Anion Photocatalysts with Wide Visible-Light Absorption Bands for Solar Water Splitting. *ChemSusChem* **2019**, *12* (9), 1872–1888.

(8) Lin, L.; Yu, Z.; Wang, X. Crystalline Carbon Nitride Semiconductors for Photocatalytic Water Splitting. *Angew. Chem. Int. Ed.* **2019**, *58* (19), 6164–6175.

(9) Wang, Q.; Nakabayashi, M.; Hisatomi, T.; Sun, S.; Akiyama, S.; Wang, Z.; Pan, Z.; Xiao, X.; Watanabe, T.; Yamada, T.; Shibata, N.; Takata, T.; Domen, K. Oxysulfide Photocatalyst for Visible-Light-Driven Overall Water Splitting. *Nat. Mater.* **2019**, *18*, 827–832.

(10) Ohno, T.; Sarukawa, K.; Matsumura, M. Crystal Faces of Rutile and Anatase $TiO_2$ Particles and Their Roles in Photocatalytic Reactions. *New J. Chem.* **2002**, *26* (9), 1167–1170.

(11) Li, R.; Zhang, F.; Wang, D.; Yang, J.; Li, M.; Zhu, J.; Zhou, X.; Han, H.; Li, C. Spatial Separation of Photogenerated Electrons and Holes among {010} and {110} Crystal Facets of $BiVO_4$. *Nat Commun* **2013**, *4* (1), 1432.

(12) Mu, L.; Zhao, Y.; Li, A.; Wang, S.; Wang, Z.; Yang, J.; Wang, Y.; Liu, T.; Chen, R.; Zhu, J.; Fan, F.; Li, R.; Li, C. Enhancing Charge Separation on High Symmetry $SrTiO_3$ Exposed with Anisotropic Facets for Photocatalytic Water Splitting. *Energy Environ. Sci.* **2016**, *9* (7), 2463–2469.

(13) Wu, X.; Hart, J. N.; Wen, X.; Wang, L.; Du, Y.; Dou, S. X.; Ng, Y. H.; Amal, R.; Scott,

J. Improving the Photo-Oxidative Performance of $Bi_2MoO_6$ by Harnessing the Synergy between Spatial Charge Separation and Rational Co-Catalyst Deposition. *ACS Appl. Mater. Interfaces* **2018**, *10* (11), 9342–9352.

(14) Osterloh, F. E. Inorganic Nanostructures for Photoelectrochemical and Photocatalytic Water Splitting. *Chem. Soc. Rev.* **2013**, *42* (6), 2294–2320.

(15) Wang, X.; Maeda, K.; Thomas, A.; Takanabe, K.; Xin, G.; Carlsson, J. M.; Domen, K.; Antonietti, M. A Metal-Free Polymeric Photocatalyst for Hydrogen Production from Water under Visible Light. *Nature Mater* **2009**, *8* (1), 76–80.

(16) Sayama, K.; Tanaka, A.; Domen, K.; Maruya, K.; Onishi, T. Photocatalytic Decomposition of Water over Platinum-Intercalated Potassium Niobate ($K_4Nb_6O_{17}$). *J. Phys. Chem.* **1991**, *95* (3), 1345–1348.

(17) Ebina, Y.; Sakai, N.; Sasaki, T. Photocatalyst of Lamellar Aggregates of $RuO_x$-Loaded Perovskite Nanosheets for Overall Water Splitting. *J. Phys. Chem. B* **2005**, *109* (36), 17212–17216.

(18) Oshima, T.; Lu, D.; Ishitani, O.; Maeda, K. Intercalation of Highly Dispersed Metal Nanoclusters into a Layered Metal Oxide for Photocatalytic Overall Water Splitting. *Angew. Chem. Int. Ed.* **2015**, *54* (9), 2698–2702.

(19) Compton, O. C.; Carroll, E. C.; Kim, J. Y.; Larsen, D. S.; Osterloh, F. E. Calcium Niobate Semiconductor Nanosheets as Catalysts for Photochemical Hydrogen Evolution from Water. *J. Phys. Chem. C* **2007**, *111* (40), 14589–14592.

(20) Le Bahers, T.; Haller, S.; Le Mercier, T.; Barboux, P. Assessing the Use of BiCuOS for Photovoltaic Application: From DFT to Macroscopic Simulation. *J. Phys. Chem. C* **2015**, *119* (31), 17585–17595.

(21) Stoumpos, C. C.; Cao, D. H.; Clark, D. J.; Young, J.; Rondinelli, J. M.; Jang, J. I.; Hupp, J. T.; Kanatzidis, M. G. Ruddlesden–Popper Hybrid Lead Iodide Perovskite 2D Homologous Semiconductors. *Chem. Mater.* **2016**, *28* (8), 2852–2867.

(22) Wang, Z.; Ganose, A. M.; Niu, C.; Scanlon, D. O. First-Principles Insights into Tin-Based Two-Dimensional Hybrid Halide Perovskites for Photovoltaics. *J. Mater. Chem. A* **2018**, *6* (14), 5652–5660.

(23) Suzuki, H.; Kanno, S.; Hada, M.; Abe, R.; Saeki, A. Exploring the Relationship between Effective Mass, Transient Photoconductivity, and Photocatalytic Activity of $Sr_xPb_{1-x}BiO_2Cl$($x$ = 0–1) Oxyhalides. *Chem. Mater.* **2020**, *32* (10), 4166–4173.

(24) Cheng, B.; Li, T.-Y.; Wei, P.-C.; Yin, J.; Ho, K.-T.; Retamal, J. R. D.; Mohammed, O. F.; He, J.-H. Layer-Edge Device of Two-Dimensional Hybrid Perovskites. *Nat Commun* **2018**, *9* (1), 5196.

(25) Tsai, H.; Nie, W.; Blancon, J.-C.; Stoumpos, C. C.; Asadpour, R.; Harutyunyan, B.;

Neukirch, A. J.; Verduzco, R.; Crochet, J. J.; Tretiak, S.; Pedesseau, L.; Even, J.; Alam, M. A.; Gupta, G.; Lou, J.; Ajayan, P. M.; Bedzyk, M. J.; Kanatzidis, M. G.; Mohite, A. D. High-Efficiency Two-Dimensional Ruddlesden–Popper Perovskite Solar Cells. *Nature* **2016**, *536* (7616), 312–316.

(26) Li, J.; Cai, L.; Shang, J.; Yu, Y.; Zhang, L. Giant Enhancement of Internal Electric Field Boosting Bulk Charge Separation for Photocatalysis. *Adv. Mater.* **2016**, *28* (21), 4059–4064.

(27) Iizuka, K.; Wato, T.; Miseki, Y.; Saito, K.; Kudo, A. Photocatalytic Reduction of Carbon Dioxide over Ag Cocatalyst-Loaded $ALa_4Ti_4O_{15}$ (A = Ca, Sr, and Ba) Using Water as a Reducing Reagent. *J. Am. Chem. Soc.* **2011**, *133* (51), 20863–20868.

(28) Ng, B.; Putri, L. K.; Kong, X. Y.; Teh, Y. W.; Pasbakhsh, P.; Chai, S. Z-scheme Photocatalytic Systems for Solar Water Splitting. *Adv. Sci.* **2020**, *7* (7), 1903171.

(29) Ogawa, K.; Nakada, A.; Suzuki, H.; Tomita, O.; Higashi, M.; Saeki, A.; Kageyama, H.; Abe, R. Flux Synthesis of Layered Oxyhalide $Bi_4NbO_8Cl$ Photocatalyst for Efficient *Z* -Scheme Water Splitting under Visible Light. *ACS Appl. Mater. Interfaces* **2019**, *11* (6), 5642–5650.

(30) Fujito, H.; Kunioku, H.; Kato, D.; Suzuki, H.; Higashi, M.; Kageyama, H.; Abe, R. Layered Perovskite Oxychloride $Bi_4NbO_8Cl$: A Stable Visible Light Responsive Photocatalyst for Water Splitting. *J. Am. Chem. Soc.* **2016**, *138* (7), 2082–2085.

(31) Nakada, A.; Higashi, M.; Kimura, T.; Suzuki, H.; Kato, D.; Okajima, H.; Yamamoto, T.; Saeki, A.; Kageyama, H.; Abe, R. Band Engineering of Double-Layered Sillén–Aurivillius Perovskite Oxychlorides for Visible-Light-Driven Water Splitting. *Chem. Mater.* **2019**, *31* (9), 3419–3429.

(32) Yamakata, A.; Kawaguchi, M.; Nishimura, N.; Minegishi, T.; Kubota, J.; Domen, K. Behavior and Energy States of Photogenerated Charge Carriers on Pt- or $CoO_x$-Loaded $LaTiO_2N$ Photocatalysts: Time-Resolved Visible to Mid-Infrared Absorption Study. *J. Phys. Chem. C* **2014**, *118* (41), 23897–23906.

(33) Clark, S. J.; Segall, M. D.; Pickard, C. J.; Hasnip, P. J.; Probert, M. I. J.; Refson, K.; Payne, M. C. First Principles Methods Using CASTEP. *Z. Kristallogr.* **2005**, *220* (5/6), 567–570.

(34) Kusainova, A. M.; Zhou, W.; Irvine, J. T. S.; Lightfoot, P. Layered Intergrowth Phases $Bi_4MO_8X$ (X=Cl, M=Ta and X=Br, M=Ta or Nb): Structural and Electrophysical Characterization. *Journal of Solid State Chemistry* **2002**, *166* (1), 148–157.

(35) Moulder, J. F.; Stickle, W. F.; Sobol, P. E.; Bomben, K. D. *Handbook of X-Rays Photoelectron Spectroscopy*; Chastain, J., Ed.; Perkin-Elmer Corporation: Minnesota, 1992.

(36) Trasatti, S. Work Function, Electronegativity, and Electrochemical Behaviour of Metals. *Journal of Electroanalytical Chemistry and Interfacial Electrochemistry* **1972**, *39* (1), 163–184.

(37) Konta, R.; Ishii, T.; Kato, H.; Kudo, A. Photocatalytic Activities of Noble Metal Ion Doped $SrTiO_3$ under Visible Light Irradiation. *J. Phys. Chem. B* **2004**, *108* (26), 8992–8995.

(38) Hara, M.; Nunoshige, J.; Takata, T.; Kondo, J. N.; Domen, K. Unusual Enhancement of $H_2$ Evolution by Ru on TaON Photocatalyst under Visible Light Irradiation. *Chem. Commun.* **2003**, *24*, 3000–3001.

(39) Hitoki, G.; Ishikawa, A.; Takata, T.; Kondo, J. N.; Hara, M.; Domen, K. $Ta_3N_5$ as a Novel Visible Light-Driven Photocatalyst ($\lambda < 600$ Nm). *Chem. Lett.* **2002**, *31* (7), 736–737.

(40) Kasahara, A.; Nukumizu, K.; Hitoki, G.; Takata, T.; Kondo, J. N.; Hara, M.; Kobayashi, H.; Domen, K. Photoreactions on $LaTiO_2N$ under Visible Light Irradiation. *J. Phys. Chem. A,* **2002**, *106*, 6750–6753.

(41) Ishikawa, A.; Takata, T.; Kondo, J. N.; Hara, M.; Kobayashi, H.; Domen, K. Oxysulfide $Sm_2Ti_2S_2O_5$ as a Stable Photocatalyst for Water Oxidation and Reduction under Visible Light Irradiation ($\lambda \leq 650$ Nm). *J. Am. Chem. Soc.* **2002**, *124* (45), 13547–13553.

(42) Ogisu, K.; Ishikawa, A.; Teramura, K.; Toda, K.; Hara, M.; Domen, K. Lanthanum–Indium Oxysulfide as a Visible Light Driven Photocatalyst for Water Splitting. *Chem. Lett.* **2007**, *36* (7), 854–855.

(43) Romanchenko, A.; Likhatski, M.; Mikhlin, Y. X-Ray Photoelectron Spectroscopy (XPS) Study of the Products Formed on Sulfide Minerals upon the Interaction with Aqueous Platinum (IV) Chloride Complexes. *Minerals* **2018**, *8* (12), 578.

(44) Tossi, C.; Hällström, L.; Selin, J.; Vaelma, M.; See, E.; Lahtinen, J.; Tittonen, I. Size- and Density-Controlled Photodeposition of Metallic Platinum Nanoparticles on Titanium Dioxide for Photocatalytic Applications. *J. Mater. Chem. A* **2019**, *7* (24), 14519–14525.

(45) Sakamoto, N.; Ohtsuka, H.; Ikeda, T.; Maeda, K.; Lu, D.; Kanehara, M.; Teramura, K.; Teranishi, T.; Domen, K. Highly Dispersed Noble-Metal/Chromia (Core/Shell) Nanoparticles as Efficient Hydrogen Evolution Promoters for Photocatalytic Overall Water Splitting under Visible Light. *Nanoscale* **2009**, *1* (1), 106.

(46) Zhang, F.; Maeda, K.; Takata, T.; Hisatomi, T.; Domen, K. Investigation of Cocatalysts on Silver-Modified $Sm_2Ti_2S_2O_5$ Photocatalyst for Water Reduction and Oxidation under Visible Light Irradiation. *Catalysis Today* **2012**, *185* (1), 253–258.

(47) Gujral, S. S.; Simonov, A. N.; Higashi, M.; Fang, X.-Y.; Abe, R.; Spiccia, L. Highly Dispersed Cobalt Oxide on TaON as Efficient Photoanodes for Long-Term Solar Water Splitting. *ACS Catal.* **2016**, *6* (5), 3404–3417.

(48) Saeki, A.; Yoshikawa, S.; Tsuji, M.; Koizumi, Y.; Ide, M.; Vijayakumar, C.; Seki, S. A Versatile Approach to Organic Photovoltaics Evaluation Using White Light Pulse and Microwave Conductivity. *J. Am. Chem. Soc.* **2012**, *134* (46), 19035–19042.

(49) Suzuki, H.; Higashi, M.; Kunioku, H.; Abe, R.; Saeki, A. Photoconductivity–Lifetime Product Correlates Well with the Photocatalytic Activity of Oxyhalides $Bi_4TaO_8Cl$ and $PbBiO_2Cl$: An Approach to Boost Their $O_2$ Evolution Rates. *ACS Energy Lett.* **2019**, *4* (7), 1572–1578.

(50) Bouri, M.; Aschauer, U. Bulk and Surface Properties of the Ruddlesden–Popper Oxynitride $Sr_2TaO_3N$. *Phys. Chem. Chem. Phys.* **2018**, *20* (4), 2771–2776.

(51) Tachikawa, T.; Ochi, T.; Kobori, Y. Crystal-Face-Dependent Charge Dynamics on a $BiVO_4$ Photocatalyst Revealed by Single-Particle Spectroelectrochemistry. *ACS Catal.* **2016**, *6* (4), 2250–2256.

(52) Tachikawa, T.; Majima, T. Single-Molecule, Single-Particle Fluorescence Imaging of $TiO_2$-Based Photocatalytic Reactions. *Chem. Soc. Rev.* **2010**, *39* (12), 4802.

(53) Tachikawa, T.; Yamashita, S.; Majima, T. Evidence for Crystal-Face-Dependent $TiO_2$ Photocatalysis from Single-Molecule Imaging and Kinetic Analysis. *J. Am. Chem. Soc.* **2011**, *133* (18), 7197–7204.

(54) Tachikawa, T.; Yonezawa, T.; Majima, T. Super-Resolution Mapping of Reactive Sites on Titania-Based Nanoparticles with Water-Soluble Fluorogenic Probes. *ACS Nano* **2013**, *7* (1), 263–275.

(55) Tang, J.; Durrant, J. R.; Klug, D. R. Mechanism of Photocatalytic Water Splitting in $TiO_2$. Reaction of Water with Photoholes, Importance of Charge Carrier Dynamics, and Evidence for Four-Hole Chemistry. *J. Am. Chem. Soc.* **2008**, *130* (42), 13885–13891.

(56) Bahnemann, D. W.; Hilgendorff, M.; Memming, R. Charge Carrier Dynamics at $TiO_2$ Particles: Reactivity of Free and Trapped Holes. *J. Phys. Chem. B* **1997**, *101* (21), 4265–4275.

(57) Yoshihara, T.; Katoh, R.; Furube, A.; Tamaki, Y.; Murai, M.; Hara, K.; Murata, S.; Arakawa, H.; Tachiya, M. Identification of Reactive Species in Photoexcited Nanocrystalline $TiO_2$ Films by Wide-Wavelength-Range (400−2500 Nm) Transient Absorption Spectroscopy. *J. Phys. Chem. B* **2004**, *108* (12), 3817–3823.

(58) Tamaki, Y.; Furube, A.; Murai, M.; Hara, K.; Katoh, R.; Tachiya, M. Direct Observation of Reactive Trapped Holes in $TiO_2$ Undergoing Photocatalytic Oxidation of Adsorbed Alcohols: Evaluation of the Reaction Rates and Yields. *J. Am. Chem. Soc.* **2006**, *128* (2), 416–417.

(59) Barroso, M.; Mesa, C. A.; Pendlebury, S. R.; Cowan, A. J.; Hisatomi, T.; Sivula, K.; Grätzel, M.; Klug, D. R.; Durrant, J. R. Dynamics of Photogenerated Holes in Surface Modified $\alpha$-$Fe_2O_3$ Photoanodes for Solar Water Splitting. *PNAS* **2012**, *109* (39), 15640–15645.

(60) Pankove, J. I. *Optical Processes in Semiconductors*; New York: Dover Publication, 1975.

(61) Basu, P. K. *Theory of Optical Processes in Semiconductors*; Oxford University Press: New York, 1997.

(62) Kunioku, H.; Nakada, A.; Higashi, M.; Tomita, O.; Kageyama, H.; Abe, R. ≈. *Sustainable Energy Fuels* **2018**, *2* (7), 1474–1480.

(63) Curran, J. S.; Lamouche, D. Transport and Kinetics in Photoelectrolysis by Semiconductor Particles in Suspension. *J. Phys. Chem.* **1983**, *87* (26), 5405–5411.

(64) Yoshida, M.; Yamakata, A.; Takanabe, K.; Kubota, J.; Osawa, M.; Domen, K. ATR-SEIRAS Investigation of the Fermi Level of Pt Cocatalyst on a GaN Photocatalyst for Hydrogen Evolution under Irradiation. *J. Am. Chem. Soc.* **2009**, *131* (37), 13218–13219.

(65) Schäfer, S.; Wyrzgol, S. A.; Caterino, R.; Jentys, A.; Schoell, S. J.; Hävecker, M.; Knop-Gericke, A.; Lercher, J. A.; Sharp, I. D.; Stutzmann, M. Platinum Nanoparticles on Gallium Nitride Surfaces: Effect of Semiconductor Doping on Nanoparticle Reactivity. *J. Am. Chem. Soc.* **2012**, *134* (30), 12528–12535.

(66) Yan, F.; Wang, Y.; Zhang, J.; Lin, Z.; Zheng, J.; Huang, F. Schottky or Ohmic Metal-Semiconductor Contact: Influence on Photocatalytic Efficiency of Ag/ZnO and Pt/ZnO Model Systems. *ChemSusChem* **2014**, *7* (1), 101–104.

(67) Li, L.; Salvador, P. A.; Rohrer, G. S. Photocatalysts with Internal Electric Fields. *Nanoscale* **2014**, *6* (1), 24–42.

(68) Kwon, S.; Lee, S. J.; Kim, S. M.; Lee, Y.; Song, H.; Park, J. Y. Probing the Nanoscale Schottky Barrier of Metal/Semiconductor Interfaces of Pt/CdSe/Pt Nanodumbbells by Conductive-Probe Atomic Force Microscopy. *Nanoscale* **2015**, *7* (29), 12297–12301.

(69) Parker, G. H.; Mead, C. A. Tunneling in CdTe Schottky Barriers. *Phys. Rev.* **1969**, *184* (3), 780–787.

(70) Anderson, B.; Anderson, R. *Fundamentals of SEMICONDUCTOR DEVICES*, Second Edition.; McGraw-Hill Education, 2017.

(71) Nakada, A.; Kato, D.; Nelson, R.; Takahira, H.; Yabuuchi, M.; Higashi, M.; Suzuki, H.; Kirsanova, M.; Kakudou, N.; Tassel, C.; Yamamoto, T.; Brown, C. M.; Dronskowski, R.; Saeki, A.; Abakumov, A.; Kageyama, H.; Abe, R. Conduction Band Control of Oxyhalides with a Triple-Fluorite Layer for Visible Light Photocatalysis. *J. Am. Chem. Soc.* **2021**, *143* (6), 2491–2499.

(72) Ogawa, K.; Suzuki, H.; Zhong, C.; Sakamoto, R.; Tomita, O.; Saeki, A.; Kageyama, H.; Abe, R. Layered Perovskite Oxyiodide with Narrow Band Gap and Long Lifetime Carriers for Water Splitting Photocatalysis. *J. Am. Chem. Soc.* **2021**, *143* (22), 8446–8453.

# Chapter 5

## $CrO_x$ layer promoting electron transfer from photocatalyst to noble-metal cocatalysts for efficient charge separation and $H_2$ evolution

## 5.1. Introduction

Photocatalytic water splitting employing semiconductor materials is of great attractive because of the potential for clean $H_2$ production by harvesting abundant solar light.[1–4] Therein, cocatalysts loaded on semiconductor photocatalysts are essential for highly efficient photocatalytic water splitting. They have mainly two roles: (1) to capture photoexcited carriers (electrons or holes) and (2) to reduce the activation energy of surface reactions as "catalysts".[5] Owing to the low activation energy for water reduction (i.e., excellent abilities as HER catalysts), noble metals (Pt, Rh, etc.) are often used as cocatalysts for $H_2$ evolution photocatalysis.[6] However, the former role, how they capture photoexcited carriers, remains not fully understood because the nanoscale metal-semiconductor interface is highly complex process.[7,8] Some reports show that Pt captures photoexcited holes as well as electrons in some cases, which results in undesirable recombination.[9–11] Thus, there should be sufficient room for the elaboration of co-catalysts based on their carrier capturing abilities.

Herein, we focus on chromium oxide ($CrO_x$). $CrO_x$/Rh cocatalyst, where Rh core is encapsulated by $CrO_x$ shell, is one of the most commonly used cocatalysts for photocatalytic water splitting,[12,13,4] owing to its excellent resistance to backward reactions such as water formation (from $H_2$ and $O_2$) and $O_2$ reduction, which are problematic in bare-noble metals like Pt and Rh.[5] The role of the $CrO_x$ layer is known to shield Rh from $O_2$; the $CrO_x$ layer is permeable to $H^+$ but not to $O_2$, preventing $O_2$ molecules from reaching the Rh surface.[14] However, we have noticed that some previous results cannot be explained only by the suppression of back reactions caused by $O_2$. For example, co-loading of $CrO_x$ with Rh enhanced the activity of the $H_2$ evolution half-reaction from a sacrificial agent,[14,15] where $O_2$ did not evolve and the suppression of back reactions with $O_2$ cannot be the origin of the enhancement. This result motivated us to investigate the unrevealed function of $CrO_x$. As the $CrO_x$ does not catalyze $H^+$ reduction,[16,17] we have focused on effect of the $CrO_x$ on the carrier transfer process from photocatalysts to noble metal reaction sites.

In the present study, we propose a favorable role of $CrO_x$ in electron transfer from photocatalysts to a noble metal (i.e., reduction site); $CrO_x$ functions as an electron transport layer. The $CrO_x$ layer loaded on the pre-loaded Rh improves photocatalytic $H_2$

evolution activity under visible light over the $Bi_4NbO_8Cl$. The $H_2$ evolution is further improved by encapsulation of Rh nanoparticles in amorphous $CrO_x$, which is achieved by newly developed deposition method where Rh and Cr species are simultaneously loaded on the photocatalyst by using $Cr^{3+}$ as a precursor. Time-resolved spectroscopy reveal that the loaded $CrO_x$ functions as an electron transport layer between the $Bi_4NbO_8Cl$ photocatalyst and the Rh, where an appropriate band alignment between them is an essential factor.

## 5.2. Experimental

### Material

$Bi_2O_3$ (99.99 %), BiOCl (95.0 %), $Nb_2O_5$ (99.9 %), NaCl (99.5 %), CsCl, methanol (99.8 %), $Rh_2O_3$, $K_2CrO_4$ (99.0 %), and BN were purchased from FUJIFILM Wako Pure Chemical Corporation. $Na_3RhCl_6 \cdot nH_2O$ (80.0 %), $Cr(NO_3)_3 \cdot 9H_2O$ (98.0 %), and $Cr_2O_3$ (98.5 %) were purchased from Kanto Chemical Corporation.

Synthesis of $Bi_4NbO_8Cl$ by the flux method

$Bi_4NbO_8Cl$ was synthesized by the flux method as reported in our previous work.[18] Briefly, a stoichiometric mixture of $Bi_2O_3$, BiOCl, and $Nb_2O_5$ was mixed with flux (NaCl and CsCl in a molar ratio of 35:65) at 1 mol%. The mixture (25 g) placed in a 30 mL alumina crucible was heated at a rate of 50 °C $h^{-1}$ to 650 °C and held at the final temperature for 10 h. The product was naturally cooled to room temperature, thoroughly washed with distilled water, filtered, and dried in the air.

### Loading of co-catalyst

Prepared $Bi_4NbO_8Cl$ (0.2 g) was dispersed in an aqueous methanol solution (20 vol%, 250 mL). Depending on the preparation conditions, Rh precursor ($Na_3RhCl_6 \cdot nH_2O$) and/or Cr precursor ($Cr(NO_3)_3 \cdot 9H_2O$ or $K_2CrO_4$) were added to the solution. The amount of precursor added was 1.0 wt% for Rh and 1.5 wt% for Cr as a metal cation. After degassing, the solution was irradiated with visible light ($\lambda$ > 400 nm) for 5 h at room temperature with continuous stirring. The irradiation was conducted using a 300 W Xe lamp equipped with a CM1 cold mirror and an L-42 cutoff filter. The product was filtered, washed thoroughly with distilled water, and dried in the air.

### Characterization

The prepared samples were studied by powder X-ray diffraction (XRD), X-ray absorption fine structure (XAFS) spectroscopy, X-ray photoelectron spectroscopy (XPS), transmission electron microscopy (TEM), and scanning electron microscopy (SEM). The XRD measurement was carried out with MiniFlex II (Rigaku) using Cu-Kα as an X-ray source. The XAFS measurement was carried out at the AR-NW10A and BL12C beamline of Photon Factory (High Energy Accelerator Research Organization, Tsukuba, Japan). The X-ray energy was varied using a Si(111) double-crystal monochromator. Reference samples (Rh foil, $Rh_2O_3$, $Cr(NO_3)_3$, $Cr_2O_3$, $Cr(OH)_3$, and $K_2CrO_4$) were measured in the transmission mode. $Cr(OH)_3$ was obtained from the precipitate formed by adding NaOH to $Cr(NO_3)_3$ solution. $Rh_2O_3$, $Cr(NO_3)_3$, $Cr_2O_3$, $Cr(OH)_3$, and $K_2CrO_4$ were diluted in boron nitride and compressed to form pellets. The prepared various $Bi_4NbO_8Cl$ samples were measured in fluorescence mode using a multichannel solid-state detector. The XPS measurements were carried out with 5500MT (ULVAC-PHI) using Mg-Kα as an X-ray source. The spectra were calibrated with a $4f_{7/2}$ peak (84.0 eV) of Au deposited on the sample surface using a magnetron sputtering device (MSP-1S). TEM and SEM observations were conducted using JEM-2100F (JEOL) and Nvision 40 (Zeiss), respectively.

### Photocatalytic reaction

Photocatalytic reactions were performed in a closed circulation system. A sample (0.1 g) was dispersed in an aqueous methanol solution (20 vol%, 250 mL) in a Pyrex reaction vessel. After degassing, the solution was irradiated from a 300 W Xe lamp at room temperature with continuous stirring. In the case of $Bi_4NbO_8Cl$, the visible light ($\lambda > 400$ nm) was irradiated using a CM1 cold mirror and an L-42 cutoff filter. Evolved gases were analyzed using a thermal conductivity detector (TCD) gas chromatograph (GC-8A, SHIMADZU) using Ar as a carrier gas.

### Transient absorption measurement

The transient absorption (TA) measurements were performed using a custom-built spectrometer as described previously. Briefly, for microsecond measurements, samples fixed on a $CaF_2$ plate were excited by a 355 nm laser pulse (0.5 mJ pulse energy, 0.5–1 Hz repetition rate). As a probe light, the visible to near-IR light (25,000–6,000 $cm^{-1}$) was irradiated from a halogen lamp and the mid-IR light (6,000–1,000 $cm^{-1}$) was irradiated from the $MoSi_2$ coil. The transmitted or diffuse reflected probe light monochromated by a spectrometer was detected by Si, InGaAs, and MCT detectors for the visible, near-IR, and mid-IR regions, respectively. The picosecond measurements were performed by using a Ti:sapphire laser system (Spectra-Physics, Solstice & TOPAS Prime; 90 fs duration; 500 Hz repetition rate). To excite the samples, 355 nm pulses (6 μJ pulse energy) were used. The probe 20,800 $cm^{-1}$ and 2,000 $cm^{-1}$ pulses were detected by a photomultiplier and MCT detector, respectively. All TA measurements were performed in $N_2$ (20 torr). The bare sample was irradiated with visible light in an aqueous methanol solution in advance to make the conditions the same as other photodeposited samples.

## 5.3. Results and Discussion

### Characterization of Rh and $CrO_x$ loaded on $Bi_4NbO_8Cl$

We employed $Bi_4NbO_8Cl$, a promising visible-light water-splitting photocatalyst,[19] synthesized by the flux method.[18] Cocatalysts were loaded using $Na_3RhCl_6$, $CrNO_3 \cdot 9H_2O$ ($Cr^{III}$), and $K_2CrO_4$ ($Cr^{VI}$) as precursors. When a photocatalyst is irradiated in an aqueous $Cr(NO_3)_3$ solution, $Cr^{3+}$ precipitates as $CrO_x$ on the photocatalysts via the reaction with $OH^-$ produced in the reduction of $NO_3^-$ by the photogenerated electrons ($NO_3^- + H_2O + 2e^- \rightarrow NO_2^- + 2OH^-$).[20] In the case of $K_2CrO_4$, $Cr_2O_3$ is deposited on photocatalysts via the photoreduction of $Cr^{VI}$ to $Cr^{III}$.[21]

Herein, we employed two different deposition procedures: stepwise[21,22] and simultaneous deposition.[23] In the stepwise deposition process, after Rh is deposited on the photocatalyst via photo-reduction ($Rh^{3+} + 3e^- \rightarrow Rh$), $CrO_x$ is coated on it, which is denoted as $Cr^{III}$/Rh or $Cr^{VI}$/Rh depending on the precursor used. In the simultaneous deposition, the photocatalyst is irradiated in the solution containing both Rh and Cr precursor (denoted as Rh+$Cr^{III}$ or Rh+$Cr^{VI}$). To our knowledge, the simultaneous deposition using $Cr^{III}$ as a precursor has not been investigated so far. A sample loaded with only Rh was also prepared.

Figure 5-1 shows the Rh-K and Cr-K edge X-ray absorption near edge structure (XANES) spectra of the prepared samples. Rh was loaded as a metal, except for Rh+Cr$^{VI}$ where Rh was loaded as a trivalent oxide (Figure 5-1a). The Cr-K spectra of all prepared samples were in good agreement with that of $Cr_2O_3 \cdot nH_2O$ (Figure 5-1b) and $CrO_x$ species loaded on GaN:ZnN,[14,22] which is supported by the XPS analysis (Figure 5-2).

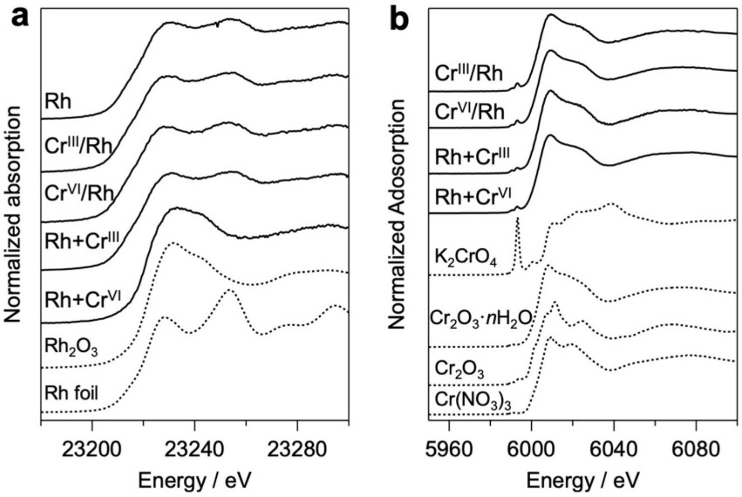

**Figure 5-1.** (a) Rh-K and (b) Cr-K edge XANES spectra of $Bi_4NbO_8Cl$ loaded with Rh and Cr prepared in various methods. The Rh-K edge spectra of Rh foil and $Rh_2O_3$ and Cr-K edge spectra of $Cr(NO_3)_3$, $Cr_2O_3$, $Cr_2O_3 \cdot nH_2O)_3$, $K_2CrO_4$ are shown as a reference. $Cr_2O_3 \cdot nH_2O$ was obtained from the precipitate formed by adding NaOH to $Cr(NO_3)_3$ solution.

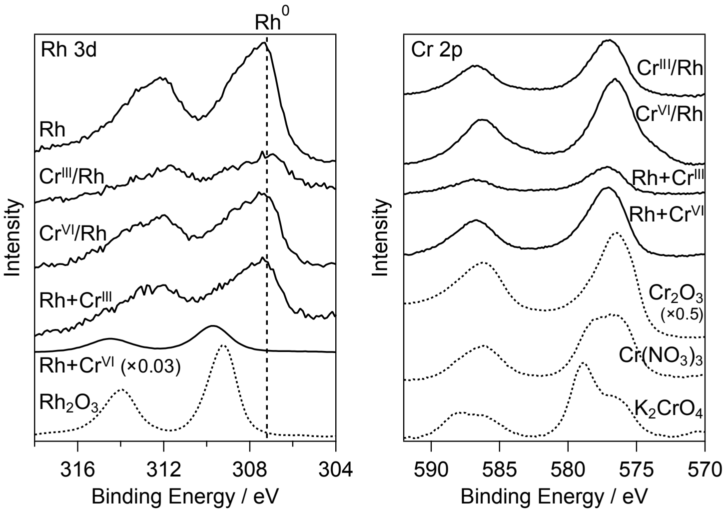

**Figure 5-2.** Rh 3d and Cr 2p XPS results of $Bi_4NbO_8Cl$ loaded with Rh and Cr prepared in various methods. The Rh 3d spectrum of $Rh_2O_3$ and the Cr 2p spectra of $Cr_2O_3$, $Cr(NO_3)_3$, and $K_2CrO_4$ are shown as references.

When only Rh was loaded on $Bi_4NbO_8Cl$, Rh was deposited as agglomerates with a size of approximately 40–50 nm (Figures 5-3a and 4); the lattice fringes in the transmission electron microscopy (TEM) image ensured the zero-valent state of the Rh. After $CrO_x$ deposition on the Rh-loaded sample ($Cr^{III}$/Rh and $Cr^{VI}$/Rh), Rh was coated with the amorphous $CrO_x$ layer (Figure 5-3b, c), while the morphology and size of Rh itself remain unchanged. In Rh+$Cr^{III}$, the highly dispersed small particles were observed, where Rh with a size of a few nanometers is fully enclosed by an amorphous $CrO_x$ shell (Figure 5-3d). Although some large particles were also observed (Figure 5-5), their number is quite small (less than 5.2% in the observed 200 particles). On the other hand, in Rh+$Cr^{VI}$, only an amorphous particle was deposited, which may be $Rh^{III}$-$Cr^{III}$ mixed-oxide by referring to literature[24,23] and the observed trivalency of the Rh in this sample (Figure 5-1a).

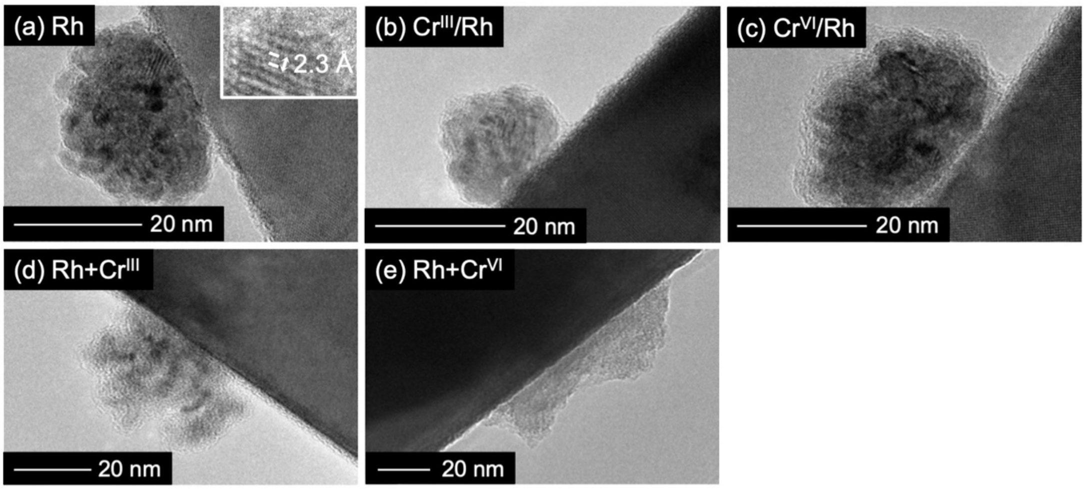

**Figure 5-3.** HR-TEM images of (a) Rh, (b) $Cr^{III}$/Rh, (c) $Cr^{VI}$/Rh, (d,e) Rh+$Cr^{III}$, and (f) Rh+$Cr^{VI}$ loaded $Bi_4NbO_8Cl$.

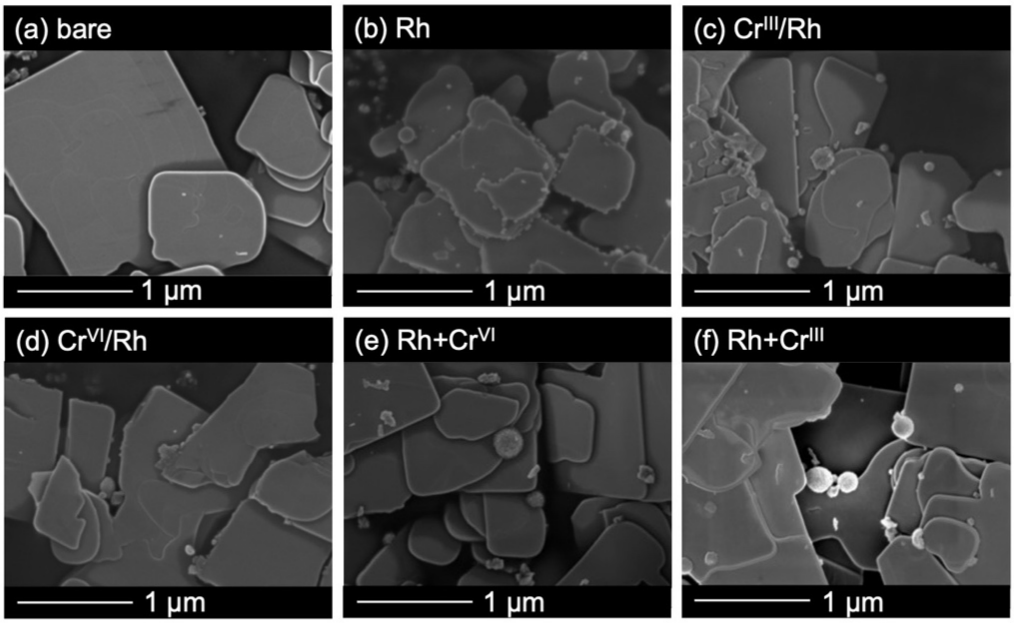

**Figure 5-4.** SEM images of (a) bare and (b) Rh, (c) $Cr^{III}$/Rh, (d) $Cr^{VI}$/Rh, (e) Rh+$Cr^{VI}$, and (f) Rh+$Cr^{III}$ loaded $Bi_4NbO_8Cl$.

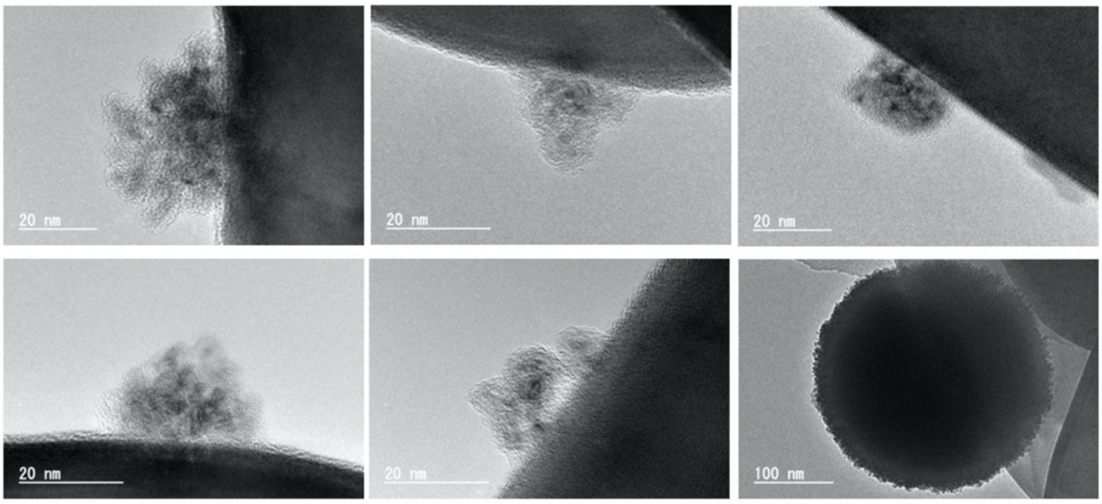

**Figure 5-5.** TEM images of Rh+Cr$^{III}$ loaded $Bi_4NbO_8Cl$.

### Photocatalytic activity

The $H_2$ evolution activity of the prepared samples was evaluated in a sacrificial aqueous methanol solution under visible irradiation ($\lambda > 400$ nm) (Figure 5-6). The co-deposition of $CrO_x$ with Rh improved the photocatalytic activity (except for Rh+Cr$^{VI}$). Especially, Rh+Cr$^{III}$ showed over 10 times higher activity than the case with only Rh. The stepwise deposition of $CrO_x$ on Rh (Cr$^{III}$/Rh and Cr$^{VI}$/Rh) also enhanced the activity. On the other hand, the activity of Rh+Cr$^{VI}$ was negligible probably because Rh species is not the zerovalent state, and thus, we excluded Rh+Cr$^{VI}$ hereafter. As described in the introduction, these results clearly show another favorable role of $CrO_x$ for efficient $H_2$ evolution other than the shielding effect of $O_2$ molecules from Rh.

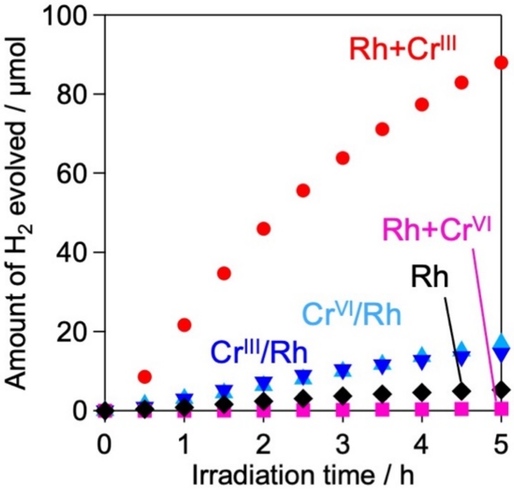

**Figure 5-6.** Time courses of $H_2$ evolution of $Bi_4NbO_8Cl$ loaded with Rh and Cr prepared in various methods. The reactions were conducted in an aqueous methanol solution (20 vol%, 250 mL) under visible light irradiation ($\lambda$ > 400 nm).

### Effect of $CrO_x$ on the carrier dynamic

Based on the two main roles of cocatalysts, the $CrO_x$ may affect the charge transfer process from the photocatalyst to Rh as it has been reported that the $CrO_x$ does not promote catalytical HER.[16,17] The effect of the $CrO_x$ on the carrier dynamics in the $Bi_4NbO_8Cl$ was verified using transient absorption (TA) spectroscopy, a powerful technique to study carrier dynamics in particulate photocatalysts.[25,26] Figure 5-7a shows the TA spectra of bare $Bi_4NbO_8Cl$, where the bandgap excitation induces two absorption increases in the infrared (IR) (2,000 $cm^{-1}$) and the visible (20,800 $cm^{-1}$) regions. The IR features have been attributed to photogenerated free electrons in the conduction band (CB) and/or shallowly trapped electrons,[27,28] while the visible features have been associated with the photogenerated holes.[26,29] Figure 5-7b and c show the IR (2,000 $cm^{-1}$) and visible (20,800 $cm^{-1}$) TA kinetics, reflecting the population of the photoexcited carriers, of the bare and the $CrO_x$ loaded $Bi_4NbO_8Cl$. The $CrO_x$ loading decreases the IR signal but increases the visible signal, where the intensity changes caused by $CrO_x$ appear at the rise of signal due to instrumental limit. This result suggests that the loaded $CrO_x$ affects the initial process of the carrier dynamics in $Bi_4NbO_8Cl$, resulting the decrease and increase of the population at μs region of the photoexcited electrons and holes, respectively, in $Bi_4NbO_8Cl$. The initial process of the charge transfer was further studies using femtosecond TA. Figures 5-7d, e show decays of the IR and visible signals, respectively, in picosecond region. The $CrO_x$ loading accelerated the decay of the electron (IR) but deaccelerated that of holes (visible), which suggests that the $CrO_x$ captures the photoexcited electrons from $Bi_4NbO_8Cl$, prolonging the hole lifetime by promoting spatial separation of electrons and holes. The carrier transfer from semiconductors to cocatalysts generally takes place on the pico-to-nanosecond time scale,[8,25,30] as is the present case with $CrO_x$. These results suggest that the loaded $CrO_x$ selectively captures photoexcited electrons from the photocatalyst but not holes.

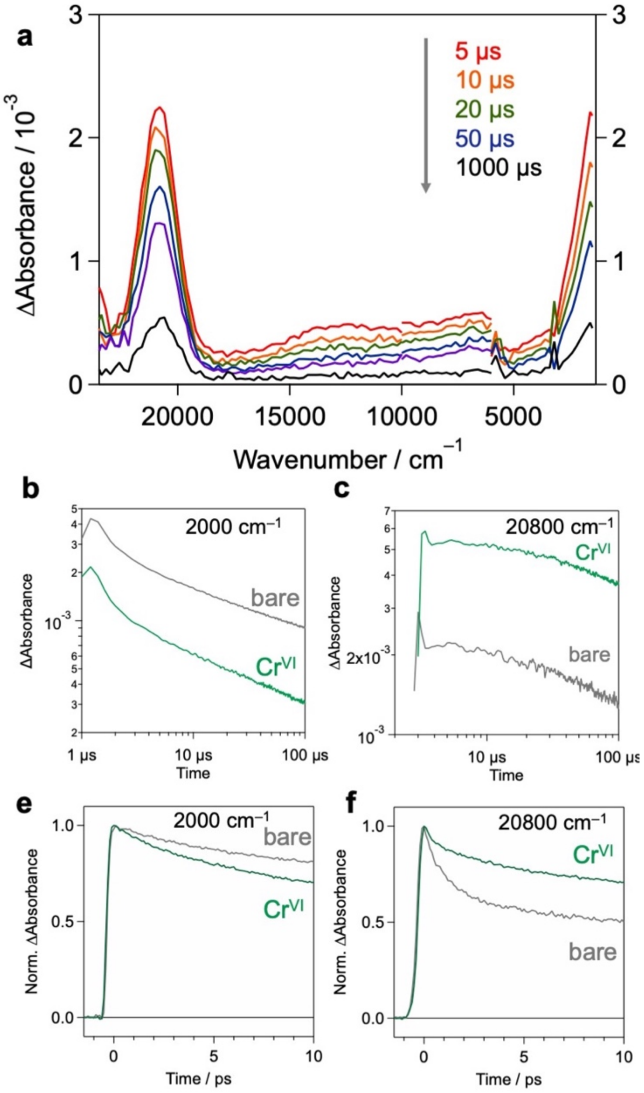

**Figure 5-7. a,** Time-resolved absorption spectra of bare $Bi_4NbO_8Cl$ exited by UV laser pulses (355 nm, 0.5 mJ $cm^{-2}$) in a vacuum. **b-f**, Decay kinetics of the transient absorption in the (b,c) microsecond and (e,f) picosecond regions measured at (a,e) 2000 $cm^{-1}$ and (b,f) 20800 $cm^{-1}$ in $N_2$ (20 Torr). The samples were excited by UV laser pulses (355 nm).

### Carrier dynamic in $CrO_x$ and Rh coloaded $Bi_4NbO_8Cl$

The function of $CrO_x$ as an electron transporting layer was observed also in case of the co-loading of $CrO_x$ with Rh on $Bi_4NbO_8Cl$. As shown in Figures 5-8a and 8b, Rh deposition decreased the signal intensity of electron but increased hole absorptions, which suggests that Rh captures photoexcited electrons as discussed in Chapter 4. The stepwise deposition of $CrO_x$ on Rh ($Cr^{III}$/Rh and $Cr^{VI}$/Rh) decreased the electron signal but had little effect on the hole signal, which indicates that the loaded $CrO_x$ facilitates the photoexcited electron transfer from the photocatalyst to Rh. More importantly, in Rh+$Cr^{III}$, showing the highest photocatalytic activity, the signal of holes was further increased as compared with the sample loaded by only Rh, while the electron signal was decreased as is the case of $Cr^{III}$/Rh and $Cr^{VI}$/Rh, which indicates that the selective electron transfer from the photocatalyst to Rh was further enhanced in Rh+$Cr^{III}$ sample as compared to the Rh-loaded sample.

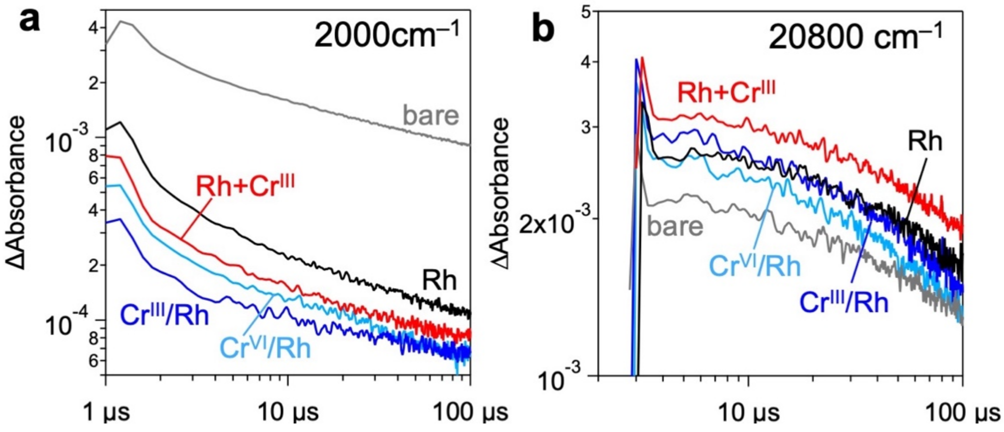

**Figure 5-8.** Decay kinetics of the transient absorption in the picosecond regions measured at (a) 2000 $cm^{-1}$ and (b) 20800 $cm^{-1}$ in $N_2$ (20 Torr). The samples were excited by UV laser pulses (355

From these results, we concluded that the $CrO_x$ serves as an electron transport layer between the photocatalyst and the reaction site (Rh) and enhances the charge-separation and thus photocatalytic activity. Figure 5-9a illustrates the suggested carrier flow dynamics and charge separation in the $Cr^{III}$/Rh (or $Cr^{VI}$/Rh) and Rh+$Cr^{III}$ samples. In $Cr^{III}$/Rh and $Cr^{VI}$/Rh, $CrO_x$ layer is loaded on the pre-loaded Rh (Figure 5-3). The $CrO_x$ species capture the photoexcited electrons from the $Bi_4NbO_8Cl$, as revealed by TA study (Figures 5-7 and 8). Therefore, we concluded that the $CrO_x$ layer serves as an electron path between $Bi_4NbO_8Cl$ and Rh, facilitating electron transfer to Rh and increasing the number of electrons participating $H^+$ reduction on Rh (Figure 5-9a).

Notably, in Rh+$Cr^{III}$ showing the highest activity, the highly dispersed small particles were observed and Rh nanoparticles are almost fully enclosed by an amorphous $CrO_x$ shell. Therein, the electron transfer to Rh was promoted despite the reduced interface between Rh and $Bi_4NbO_8Cl$, while the undesirable hole transfer to Rh was further suppressed. Given the results of $Cr^{III}$/Rh and $Cr^{VI}$/Rh showing that the $CrO_x$ layer serves as an electron path, we concluded that $CrO_x$ intermediating between $Bi_4NbO_8Cl$ and Rh in Rh+$Cr^{III}$ selectively pass electrons, suppressing the undesirable hole transfer to Rh (Figure 5-9b), which can be problematic when the photocatalyst is directly in contact with Rh. Although some large particles without $CrO_x$ were also observed in this sample as stated above, they may not be responsible for the photocatalytic activity and the observed TA kinetics, given the small ratio of the large particles (about 5%).

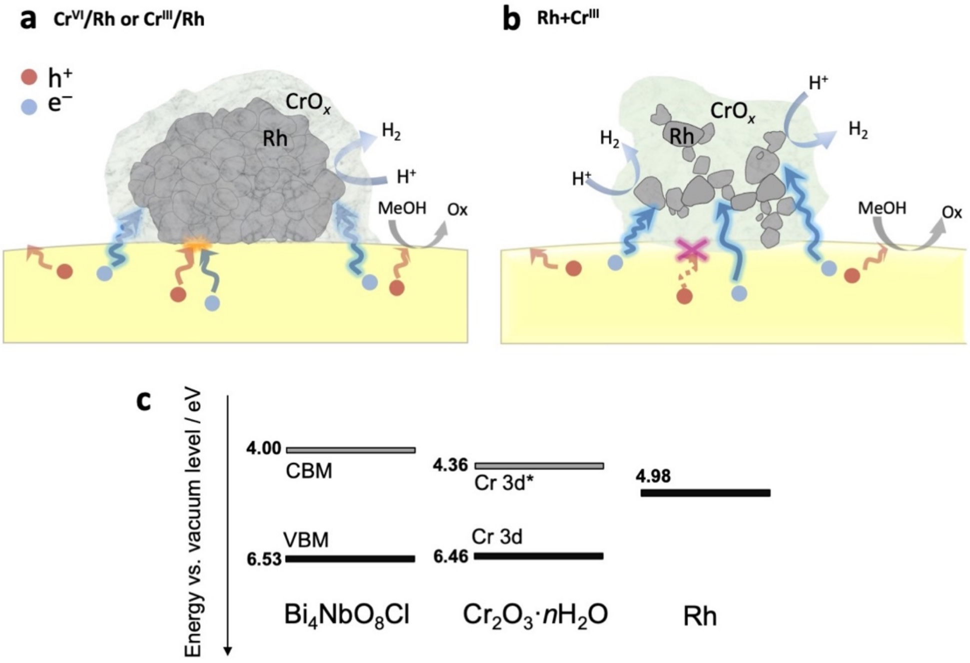

**Figure 5-9. a,b** Schematic illustration of the role of $CrO_x$ in the carrier transfer process from semiconductor to Rh in (a) $Cr^{III}$/Rh ( or $Cr^{VI}$/Rh) and (b) Rh+$Cr^{III}$. **c**, Energy level diagram for $Bi_4NbO_8Cl$, $Cr_2O_3\cdot nH_2O$, and Rh.

### The origin of the function of $CrO_x$ as an electron transport layer

By analogy with the "electron transport layer" employed in solar-cells,[31] the unveiled role of the $CrO_x$, promoting electron transfer between semiconductor and noble-metal reaction site, should stems from the band alignment between them. Cr-oxide species have actually been reported to work as electron transport layer between a photo-absorber layer consisted of a semiconductor (e.g., lead-halide perovskite solar cells) and an electrode (e.g., a fluorine-doped tin oxide (FTO) and Ag substrates).[32,33]

The band alignment between $Bi_4NbO_8Cl$ and $CrO_x$ was estimated by diffuse reflectance spectroscopy (DRS) and photoelectron yield spectroscopy (PYS), as shown in Figure 5-10. The $Cr_2O_3 \cdot nH_2O$ particles were prepared via precipitation method where $OH^-$ was added to the solution containing $Cr^{3+}$ ions to imitate the photo-deposition process of $CrO_x$ from $Cr^{3+}$ on $Bi_4NbO_8Cl$. The Cr-K edge XANES of the prepared $Cr_2O_3 \cdot nH_2O$ particles are almost same as that of the $CrO_x$ species loaded on $Bi_4NbO_8Cl$ (Figure 5-1). Figure 5-9c shows the estimated band alignment between $Bi_4NbO_8Cl$ and $Cr_2O_3 \cdot nH_2O$. The CBM (Cr 3d*)[34] position of the $Cr_2O_3 \cdot nH_2O$ is favorable for electrons transfer from the CBM of $Bi_4NbO_8Cl$ to $Cr_2O_3 \cdot nH_2O$. On the other hand, the difference between the VBM (Cr 3d) position[35] of $Cr_2O_3 \cdot nH_2O$ and $Bi_4NbO_8Cl$ is less than that of the CBMs, which may be the reason for the hole transfer from the VBM of the $Bi_4NbO_8Cl$ to $Cr_2O_3 \cdot nH_2O$ being slower than the electron transfer.

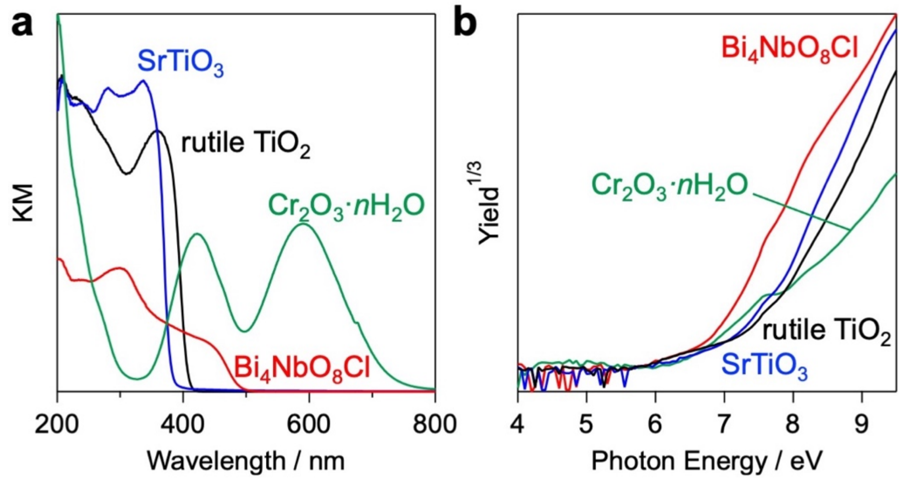

**Figure 5-10.** (a) Diffuse reflection spectra and (b) photoemission yield spectra of $Bi_4NbO_8Cl$, $Cr_2O_3 \cdot nH_2O$, $SrTiO_3$, and $TiO_2$.

We also confirmed that the role of the $CrO_x$ as electron transport layer is not specific to Rh. As discussed in Chapter 4, Pt does not function as an effective cocatalyst on $Bi_4NbO_8Cl$ because the Pt captures both electrons and holes, being the recombination center. We expected that if the $CrO_x$ selectively transfer electrons from $Bi_4NbO_8Cl$ to Pt, Pt should work as HER cocatalyst by selectively capturing the electrons. As shown in Figure 5-13, the subsequent deposition of $CrO_x$ layer on Pt (Figure 5-11, 12) did not enhance the photocatalytic activity, which is in contrast to $Cr^{III}$/Rh and $Cr^{VI}$/Rh. This is because, when Pt and $Bi_4NbO_8Cl$ are in contact, Pt serves as a recombination center by capturing holes and electrons more considerably than Rh (Chapter 4), and thus $CrO_x$ layer on Pt exerts little influence on the charge separation between Pt and $Bi_4NbO_8Cl$. On the other hand, when Pt and Cr species were simultaneously loaded on $Bi_4NbO_8Cl$ (Pt+$Cr^{III}$), Pt was encapsulated by amorphous $CrO_x$ (Figure 5-11, 21) as with the case of Rh+$Cr^{III}$, which results in the significant improvement of the photocatalytic activity (Figure 5-13). The $CrO_x$ layer intermediates between Pt and $Bi_4NbO_8Cl$ to some extent in Pt+$Cr^{III}$, suppressing the undesirable hole transfer to Pt and enabling selective electron transfer from the photocatalyst to the noble metal, which was revealed by TA measurement (Figure 5-14).

From these results, we conclude that the $CrO_x$ functioning as an electron transport layer promotes charge separation between the photocatalyst and noble metal reaction site, which results in significant improvement of the photocatalytic activity.

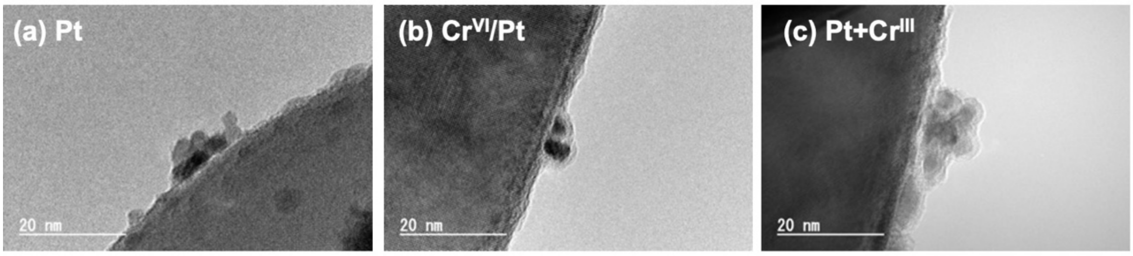

**Figure 5-11.** TEM images of (a-b) Pt, (c-d) $Cr^{VI}$/Pt, and (e-f) Pt+$Cr^{III}$ loaded $Bi_4NbO_8Cl$.

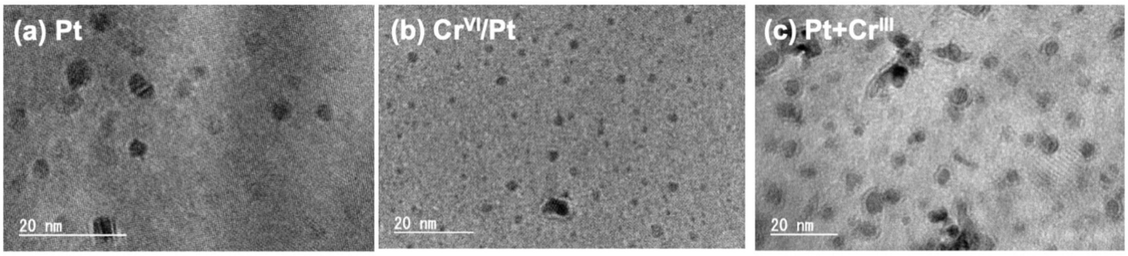

**Figure 5-12.** TEM images of (a-b) Pt, (c-d) $Cr^{VI}$/Pt, and (e-f) Pt+$Cr^{III}$ loaded on the dominant facet ((001)) of $Bi_4NbO_8Cl$.

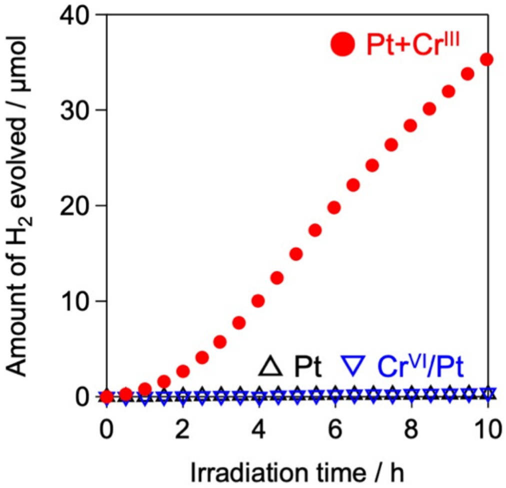

**Figure 5-13.** Time courses of $H_2$ evolution of Pt and/or Cr loaded $Bi_4NbO_8Cl$ samples. The reactions were conducted in an aqueous methanol solution (20 vol%, 250 mL) under visible light irradiation ($\lambda > 400$ nm).

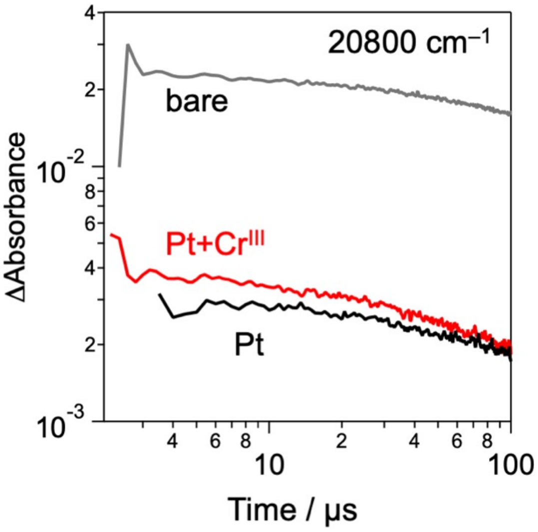

**Figure 5-14.** Decay kinetics of the transient absorption in the picosecond regions measured at 20800 $cm^{-1}$ in $N_2$ (20 Torr) of Pt and/or Cr loaded $Bi_4NbO_8Cl$ samples. The samples were excited by UV laser pulses (355 nm).

**Applicability to other photocatalysts**

As shown in Figure 5-15a, the effectivity of the co-loading of $CrO_x$ and Rh on the $H_2$ evolution reaction depends on the semiconductor photocatalysts employed. The simultaneous photodeposition of Cr and Rh on $SrTiO_3$ (Rh+$Cr^{III}$) shows higher activity than the Rh loaded $SrTiO_3$, although the enhancement was moderate as compared to the case with $Bi_4NbO_8Cl$. The valence band of $SrTiO_3$ is more positive than that of $Bi_4NbO_8Cl$ (Figure 5-15b), which may result in the holes transfer to $CrO_x$ easier than the case of $Bi_4NbO_8Cl$, and thus the low improvement rate. The deposited Rh and $CrO_x$/Rh particles on $SrTiO_3$ have similar morphology to those on $Bi_4NbO_8Cl$ (Figure 5-16). In contrast to $Bi_4NbO_8Cl$ and $SrTiO_3$, co-deposition of $CrO_x$ lowered the photocatalytic activity of Rh loaded $TiO_2$ probably because the inappropriate band alignment between $TiO_2$ and $CrO_x$[36] where the driving force of the electron transfer from the CB of $TiO_2$ to that of $CrO_x$ was lower than the case with $Bi_4NbO_8Cl$ and $SrTiO_3$ (Figure 5-15b). Although the amorphous $CrO_x$ was not clearly observed on Rh (Figure 5-17b), XPS confirms the loading of $CrO_x$ via simultaneous photodeposition (Figure 5-17c).

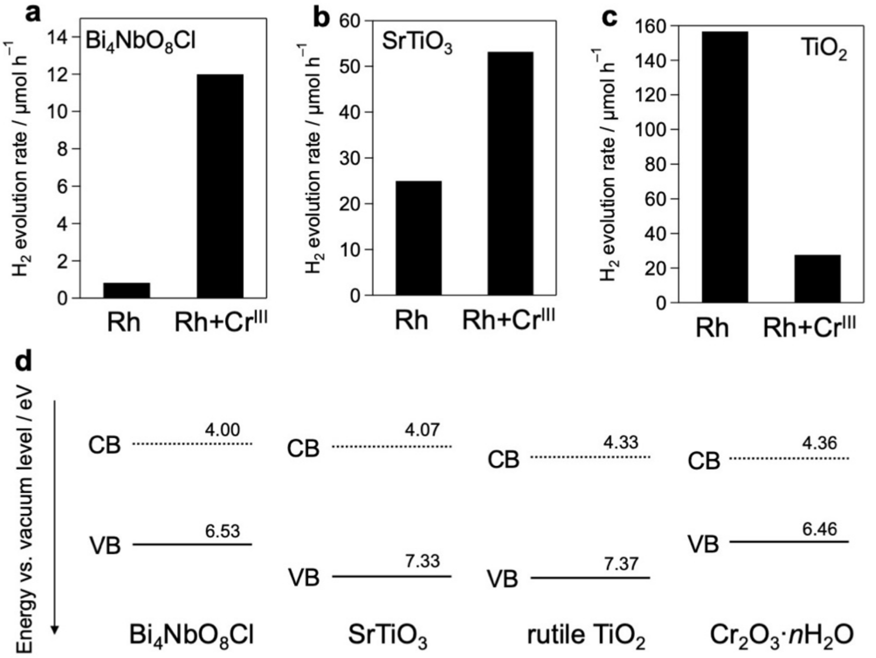

**Figure 5-15. a-b,** Effect of $CrO_x$ co-deposited with Rh on the photocatalytioc activity over (a) $Bi_4NbO_8Cl$ ($\lambda > 400$ nm), (b) $SrTiO_3$ ($\lambda > 300$ nm), and $TiO_2$ ($\lambda > 300$ nm). **d**, Energy level diagram for $Bi_4NbO_8Cl$, $SrTiO_3$, $TiO_2$, and $Cr_2O_3 \cdot nH_2O$.

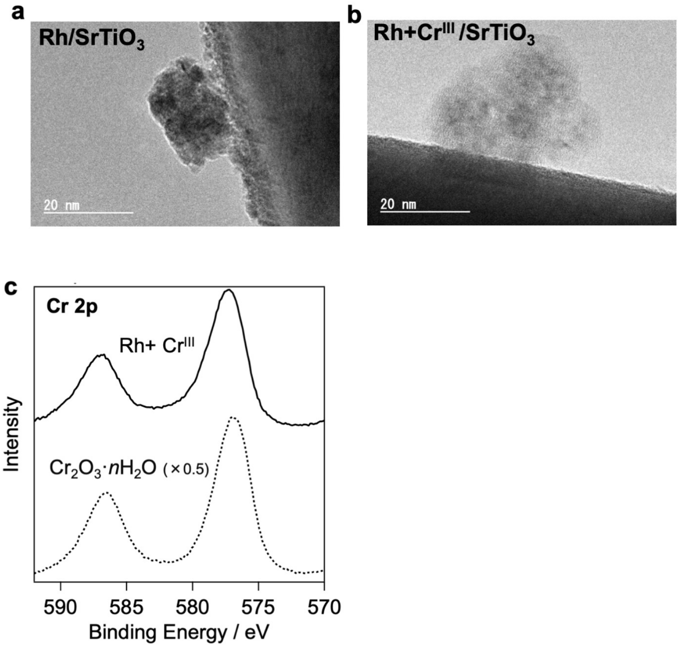

**Figure 5-16.** TEM images of (a) Rh, (b) Rh+Cr$^{III}$/SrTiO$_3$. c, XPS spectra for Rh+Cr$^{III}$/SrTiO$_3$ focusing on the Cr 2p region.

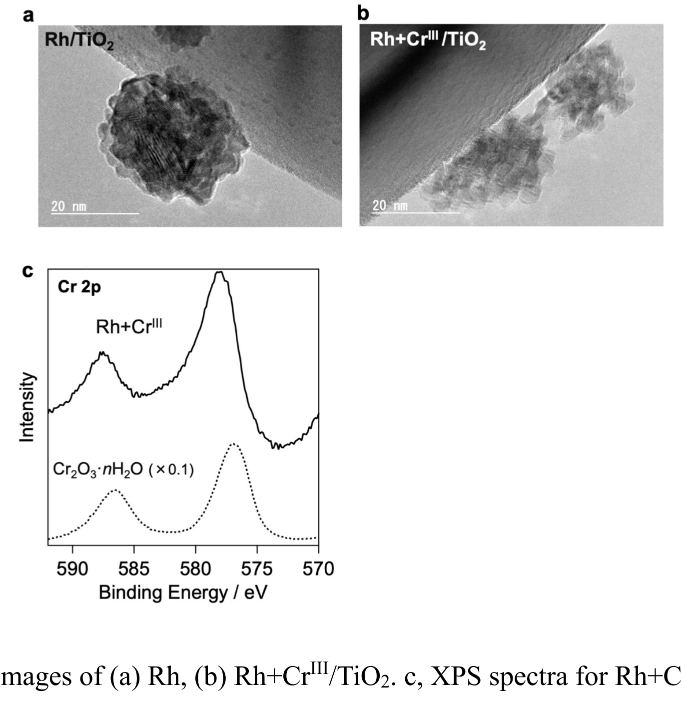

**Figure 5-17.** TEM images of (a) Rh, (b) Rh+Cr$^{III}$/TiO$_2$. c, XPS spectra for Rh+Cr$^{III}$/TiO$_2$ focusing on the Cr 2p region.

## Suppression of the backward reactions in overall water splitting

In the present study, we revealed that the simultaneous deposition method using $Cr^{3+}$ precursor ($Rh+Cr^{III}$), which had not been investigated so far, can be an effective deposition method of $CrO_x/Rh$ cocatalyst, from the viewpoint of the carrier transfer process (Figure 5-9b). As noted in the introduction, the $CrO_x$ layer has been employed as a resistance to backward reactions such as water formation (from $H_2$ and $O_2$) and $O_2$ reduction on noble metal cocatalyst. To investigate the suppression of the backward reaction by $CrO_x$ in $Rh+Cr^{III}$, we conducted the overall water splitting using $SrTiO_3$ under UV and visible light irradiation. Notably, $Bi_4NbO_8Cl$ does not successfully split water even when $CrO_x$ was deposited via the conventional ($Cr^{VI}/Rh$) or the present ($Rh+Cr^{III}$) method, which is our future work.

As shown in Figure 5-18, the Rh-loaded $SrTiO_3$ without $CrO_x$ does not show stoichiometric water splitting due to the undesirable reaction with $O_2$ molecule on the exposed Rh.[5] On the other hand, the $CrO_x$ deposition ($Rh+Cr^{III}$ or $Cr^{VI}/Rh$) enables stoichiometric water splitting, showing the resistance to backward reactions. Moreover, the $SrTiO_3$ with Rh and $CrO_x$ loaded via the present method ($Rh+Cr^{III}$) shows slightly higher photocatalytic activity than the $SrTiO_3$ with Rh and $CrO_x$ loaded via the conventional method ($Cr^{VI}/Rh$). From these results, the $CrO_x$ layer deposited via the present method ($Rh+Cr^{III}$) has resistance to the backward reaction as in the case of the conventional method.

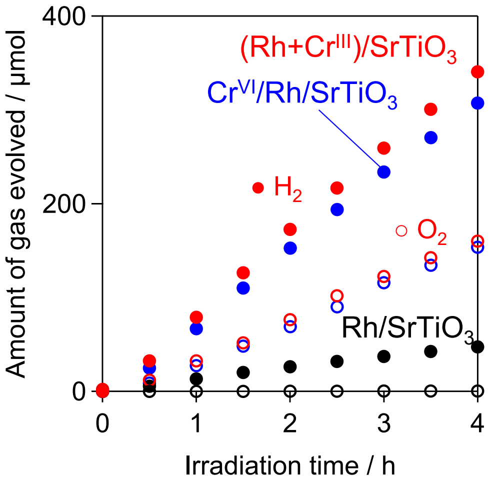

**Figure 5-18.** Time courses of overall water splitting of Rh and Cr loaded $SrTiO_3$. Every reaction was conducted with 0.1 g of the sample in pure water (250 mL) under UV irradiation ($\lambda > 300$ nm).

## 5.4. Conclusion

In summary, we demonstrate that $CrO_x$ helps the photoexcited electrons to transfer from a photocatalyst to a noble-metal reaction site. The $CrO_x$ layer on the pre-loaded Rh serves as an electron path, facilitating electron transfer from $Bi_4NbO_8Cl$ photocatalyst to Rh, which results in improved $H_2$ evolution activity under visible light. Notably, when Rh and $CrO_x$ are loaded simultaneously via the photodeposition method using $Cr^{3+}$ precursor, Rh nanoparticles fully enclosed by amorphous $CrO_x$ are produced. Therein, the $CrO_x$ layer passes only electrons to Rh, suppressing the undesirable hole transfer to Rh, which affords further improvement on the activity. Thus far, facilitation of surface reactions (e.g., HER, OER) have mainly been investigated as functions of cocatalysts. On the other hand, we revealed the crucial role of $CrO_x$ on the carrier transfer process from the photocatalyst to the catalyst (reaction site). We believe that the precise control of the physicochemical property of Cr species by, for example, doping,[37] making solid solutions with other transition metal compounds,[34] employing other ligands (anions),[38,39] enable us to reveals the more detailed carrier dynamics during the carrier transporting to noble metal for suppressing the undesirable charge recombination more effectively. The present study offers a new approach to design cocatalysts based on their carrier capturing abilities.

## Reference

(1) Abe, R. Development of a New System for Photocatalytic Water Splitting into $H_2$ and $O_2$ under Visible Light Irradiation. *BCSJ* **2011**, *84*, 1000–1030.

(2) Shaner, M. R.; Atwater, H. A.; Lewis, N. S.; McFarland, E. W. A Comparative Technoeconomic Analysis of Renewable Hydrogen Production Using Solar Energy. *Energy Environ. Sci.* **2016**, *9*, 2354–2371.

(3) Bala Chandran, R.; Breen, S.; Shao, Y.; Ardo, S.; Weber, A. Z. Evaluating Particle-Suspension Reactor Designs for Z-Scheme Solar Water Splitting *via* Transport and Kinetic Modeling. *Energy Environ. Sci.* **2018**, *11*, 115–135.

(4) Takata, T.; Jiang, J.; Sakata, Y.; Nakabayashi, M.; Shibata, N.; Nandal, V.; Seki, K.; Hisatomi, T.; Domen, K. Photocatalytic Water Splitting with a Quantum Efficiency of Almost Unity. *Nature* **2020**, *581*, 411–414.

(5) Maeda, K.; Domen, K. Development of Novel Photocatalyst and Cocatalyst Materials for Water Splitting under Visible Light. *BCSJ* **2016**, *89*, 627–648.

(6) Kudo, A.; Miseki, Y. Heterogeneous Photocatalyst Materials for Water Splitting. *Chem. Soc. Rev.* **2009**, *38*, 253–278.

(7) Subramanian, V.; Wolf, E. E.; Kamat, P. V. Catalysis with $TiO_2$/Gold Nanocomposites. Effect of Metal Particle Size on the Fermi Level Equilibration. *J. Am. Chem. Soc.* **2004**, *126*, 4943–4950.

(8) Wu, K.; Zhu, H.; Liu, Z.; Rodríguez-Córdoba, W.; Lian, T. Ultrafast Charge Separation and Long-Lived Charge Separated State in Photocatalytic CdS–Pt Nanorod Heterostructures. *J. Am. Chem. Soc.* **2012**, *134*, 10337–10340.

(9) Yoshida, M.; Yamakata, A.; Takanabe, K.; Kubota, J.; Osawa, M.; Domen, K. ATR-SEIRAS Investigation of the Fermi Level of Pt Cocatalyst on a GaN Photocatalyst for Hydrogen Evolution under Irradiation. *J. Am. Chem. Soc.* **2009**, *131*, 13218–13219.

(10) Schäfer, S.; Wyrzgol, S. A.; Caterino, R.; Jentys, A.; Schoell, S. J.; Hävecker, M.; Knop-Gericke, A.; Lercher, J. A.; Sharp, I. D.; Stutzmann, M. Platinum Nanoparticles on Gallium Nitride Surfaces: Effect of Semiconductor Doping on Nanoparticle Reactivity. *J. Am. Chem. Soc.* **2012**, *134*, 12528–12535.

(11) Yan, F.; Wang, Y.; Zhang, J.; Lin, Z.; Zheng, J.; Huang, F. Schottky or Ohmic Metal-Semiconductor Contact: Influence on Photocatalytic Efficiency of Ag/ZnO and Pt/ZnO Model Systems. *ChemSusChem* **2014**, *7*, 101–104.

(12) Wang, Z.; Inoue, Y.; Hisatomi, T.; Ishikawa, R.; Wang, Q.; Takata, T.; Chen, S.; Shibata, N.; Ikuhara, Y.; Domen, K. Overall Water Splitting by $Ta_3N_5$ Nanorod Single Crystals Grown on the Edges of $KTaO_3$ Particles. *Nat Catal* **2018**, *1*, 756–763.

(13) Wang, Q.; Nakabayashi, M.; Hisatomi, T.; Sun, S.; Akiyama, S.; Wang, Z.; Pan, Z.; Xiao, X.; Watanabe, T.; Yamada, T.; Shibata, N.; Takata, T.; Domen, K. Oxysulfide Photocatalyst for Visible-Light-Driven Overall Water Splitting. *Nat. Mater.* **2019**, *18*, 827–832.

(14) Maeda, K.; Teramura, K.; Lu, D.; Saito, N.; Inoue, Y.; Domen, K. Roles of $Rh/Cr_2O_3$ (Core/Shell) Nanoparticles Photodeposited on Visible-Light-Responsive $(Ga_{1x}Zn_x)(N_{1-x}O_x)$ Solid Solutions in Photocatalytic Overall Water Splitting. *J. Phys. Chem. C* **2007**, *111*, 7554–7560.

(15) Cho, Y.-J.; Moon, G.; Kanazawa, T.; Maeda, K.; Choi, W. Selective Dual-Purpose Photocatalysis for Simultaneous $H_2$ Evolution and Mineralization of Organic Compounds Enabled by a $Cr_2O_3$ Barrier Layer Coated on $Rh/SrTiO_3$. *Chem. Commun.* **2016**, *52*, 9636–9639.

(16) Qureshi, M.; Shinagawa, T.; Tsiapis, N.; Takanabe, K. Exclusive Hydrogen Generation by Electrocatalysts Coated with an Amorphous Chromium-Based Layer Achieving Efficient Overall Water Splitting. *ACS Sustainable Chem. Eng.* **2017**, *5*, 8079–8088.

(17) Yoshida, M.; Takanabe, K.; Maeda, K.; Ishikawa, A.; Kubota, J.; Sakata, Y.; Ikezawa, Y.; Domen, K. Role and Function of Noble-Metal/Cr-Layer Core/Shell Structure Cocatalysts for Photocatalytic Overall Water Splitting Studied by Model Electrodes. *J. Phys. Chem. C* **2009**, *113*, 10151–10157.

(18) Ogawa, K.; Nakada, A.; Suzuki, H.; Tomita, O.; Higashi, M.; Saeki, A.; Kageyama, H.;

Abe, R. Flux Synthesis of Layered Oxyhalide $Bi_4NbO_8Cl$ Photocatalyst for Efficient *Z* -Scheme Water Splitting under Visible Light. *ACS Appl. Mater. Interfaces* **2019**, *11*, 5642–5650.

(19) Fujito, H.; Kunioku, H.; Kato, D.; Suzuki, H.; Higashi, M.; Kageyama, H.; Abe, R. Layered Perovskite Oxychloride $Bi_4NbO_8Cl$: A Stable Visible Light Responsive Photocatalyst for Water Splitting. *J. Am. Chem. Soc.* **2016**, *138*, 2082–2085.

(20) Chu, S.; Rashid, R. T.; Liu, X.; Mi, Z. Photodeposition of a Conformal Metal Oxide Nanocoating. *Chem. Commun.* **2019**, *55*, 6305–6308.

(21) Maeda, K.; Teramura, K.; Lu, D.; Saito, N.; Inoue, Y.; Domen, K. Noble-Metal/$Cr_2O_3$ Core/Shell Nanoparticles as a Cocatalyst for Photocatalytic Overall Water Splitting. *Angew. Chem. Int. Ed.* **2006**, *45*, 7806–7809.

(22) Maeda, K.; Sakamoto, N.; Ikeda, T.; Ohtsuka, H.; Xiong, A.; Lu, D.; Kanehara, M.; Teranishi, T.; Domen, K. Preparation of Core-Shell-Structured Nanoparticles (with a Noble-Metal or Metal Oxide Core and a Chromia Shell) and Their Application in Water Splitting by Means of Visible Light. *Chem. Eur. J.* **2010**, *16*, 7750–7759.

(23) Maeda, K.; Lu, D.; Teramura, K.; Domen, K. Simultaneous Photodeposition of Rhodium–Chromium Nanoparticles on a Semiconductor Powder: Structural Characterization and Application to Photocatalytic Overall Water Splitting. *Energy Environ. Sci.* **2010**, *3*, 471–478.

(24) Maeda, K.; Lu, D.; Teramura, K.; Domen, K. Direct Deposition of Nanoparticulate Rhodium–Chromium Mixed-Oxides on a Semiconductor Powder by Band-Gap Irradiation. *J. Mater. Chem.* **2008**, *18*, 3539.

(25) Yamakata, A.; Kawaguchi, M.; Nishimura, N.; Minegishi, T.; Kubota, J.; Domen, K. Behavior and Energy States of Photogenerated Charge Carriers on Pt- or $CoO_x$-Loaded $LaTiO_2N$ Photocatalysts: Time-Resolved Visible to Mid-Infrared Absorption Study. *J. Phys. Chem. C* **2014**, *118*, 23897–23906.

(26) Tang, J.; Durrant, J. R.; Klug, D. R. Mechanism of Photocatalytic Water Splitting in $TiO_2$. Reaction of Water with Photoholes, Importance of Charge Carrier Dynamics, and Evidence for Four-Hole Chemistry. *J. Am. Chem. Soc.* **2008**, *130*, 13885–13891.

(27) Pankove, J. I. *Optical Processes in Semiconductors*; New York: Dover Publication, 1975.

(28) Basu, P. K. *Theory of Optical Processes in Semiconductors*; Oxford University Press: New York, 1997.

(29) Murofushi, K.; Ogawa, K.; Suzuki, H.; Sakamoto, R.; Tomita, O.; Kato, K.; Yamakata, A.; Saeki, A.; Abe, R. Earth-Abundant Iron(III) Species Serves as a Cocatalyst Boosting the Multielectron Reduction of $IO_3^-/I^-$ Redox Shuttle in Z-Scheme Photocatalytic Water Splitting. *J. Mater. Chem. A* **2021**, *9*, 11718–11725.

(30) Li, Q.; Zhao, F.; Qu, C.; Shang, Q.; Xu, Z.; Yu, L.; McBride, J. R.; Lian, T. Two-

Dimensional Morphology Enhances Light-Driven $H_2$ Generation Efficiency in CdS Nanoplatelet-Pt Heterostructures. *J. Am. Chem. Soc.* **2018**, *140*, 11726–11734.

(31) Wang, K.; Olthof, S.; Subhani, W. S.; Jiang, X.; Cao, Y.; Duan, L.; Wang, H.; Du, M.; Liu, S. (Frank). Novel Inorganic Electron Transport Layers for Planar Perovskite Solar Cells: Progress and Prospective. *Nano Energy* **2020**, *68*, 104289.

(32) Zheng, S.; Li, W.; Su, T.; Xie, F.; Chen, J.; Yang, Z.; Zhang, Y.; Liu, S.; Aldred, M. P.; Wong, K. Y.; Xu, J.; Chi, Z. Metal Oxide $CrO_x$ as a Promising Bilayer Electron Transport Material for Enhancing the Performance Stability of Planar Perovskite Solar Cells. *Sol. RRL* **2018**, *2*, 1700245.

(33) Dong, J.; Wu, J.; Jia, J.; He, X.; Lan, Z.; Fan, L.; Lin, J.; Huang, M. Annealing-Free $Cr_2O_3$ Electron-Selective Layer for Efficient Hybrid Perovskite Solar Cells. *ChemSusChem* **2018**, *11*, 619–628.

(34) Wang, Y.; Lopata, K.; Chambers, S. A.; Govind, N.; Sushko, P. V. Optical Absorption and Band Gap Reduction in $(Fe_{1-x}Cr_x)_2O_3$ Solid Solutions: A First-Principles Study. *J. Phys. Chem. C* **2013**, *117*, 25504–25512.

(35) Cakra Wardhana, A.; Yamaguchi, A.; Shoji, S.; Liu, M.; Fujita, T.; Hitosugi, T.; Miyauchi, M. Visible-Light-Driven Photocatalysis via Reductant-to-Band Charge Transfer in Cr(III) Nanocluster-Loaded $SrTiO_3$ System. *Applied Catalysis B: Environmental* **2020**, *270*, 118883.

(36) Sekizawa, K.; Oh-ishi, K.; Morikawa, T. Photoelectrochemical Water-Splitting over a Surface Modified p-Type $Cr_2O_3$ Photocathode. *Dalton Trans.* **2020**, *49*, 659–666.

(37) Arca, E.; Kehoe, A. B.; Veal, T. D.; Shmeliov, A.; Scanlon, D. O.; Downing, C.; Daly, D.; Mullarkey, D.; Shvets, I. V.; Nicolosi, V.; Watson, G. W. Valence Band Modification of $Cr_2O_3$ by Ni-Doping: Creating a High Figure 5-of Merit p-Type TCO. *J. Mater. Chem. C* **2017**, *5*, 12610–12618.

(38) Ohkoshi, S.; Nakagawa, K.; Tomono, K.; Imoto, K.; Tsunobuchi, Y.; Tokoro, H. High Proton Conductivity in Prussian Blue Analogues and the Interference Effect by Magnetic Ordering. *J. Am. Chem. Soc.* **2010**, *132*, 6620–6621.

(39) Lin, L.; Lin, Z.; Zhang, J.; Cai, X.; Lin, W.; Yu, Z.; Wang, X. Molecular-Level Insights on the Reactive Facet of Carbon Nitride Single Crystals Photocatalysing Overall Water Splitting. *Nat Catal* **2020**, *3*, 649–655.

# *Chapter 6*

## ***Earth-abundant iron(III) species serves as a cocatalyst boosting the multi-electron reduction of $IO_3^-/I^-$ redox shuttle in Z-scheme photocatalytic water splitting***

## 2.2. Introduction

Water splitting based on semiconductor photocatalysts is regarded as a promising strategy to achieve clean hydrogen production from solar energy.[1–4] While several semiconductors, such as $SrTiO_3$, split water with high efficiencies under ultraviolet (UV) illumination,[4] visible light utilization is crucial for practical applications as nearly half of the solar energy incident on the earth lies in the visible light region. Z-scheme water splitting facilitates visible light utilization by allocating the Gibbs free energy for water splitting between two photocatalysts that are responsible for $O_2$ and $H_2$ evolution. Therefore, the two photocatalysts are tethered electrically by a redox shuttle couple (e.g., $Fe^{3+}/Fe^{2+}$, $IO_3^-/I^-$), which transports electrons between them.[1,5]

The $IO_3^-/I^-$ couple has been employed as a redox shuttle in various Z-scheme systems,[5] enjoying an advantage that $IO_3^-/I^-$ may work in mild pH conditions of 5 – 9, where most photocatalysts do not suffer from deactivation (e.g., dissolution). [6] However, its multi-electron reduction ($IO_3^- + 6H^+ + 6e^- \rightleftarrows I^- + 3H_2O$; 1.09 V vs. RHE) suffers from a small reaction rate on the $O_2$ evolution photocatalyst surface, which deteriorates the overall water splitting efficiency. Although facilitating this process should be crucial, cocatalysts for redox shuttles have attracted less attention than those for oxygen and hydrogen evolution reactions.[7] Thus far, the example of redox cocatalysts for $IO_3^-$ is limited to noble metal species, such as Pt, Ru, and Ir,[6–11] leaving sufficient room for investigation, especially from the perspective of resources.

In this study, we demonstrate that earth-abundant iron oxide ($FeO_x$) functions as an effective cocatalyst for the 6-electron reduction of $IO_3^-$, allowing the $Bi_4TaO_8Cl$ photocatalyst to evolve $O_2$ from water containing $IO_3^-$. A series of experimental investigations have argued that the $Fe^{III}/Fe^{II}$ redox couple in $FeO_x$ is responsible for the acceleration of electron capture from $Bi_4TaO_8Cl$ and reduction of $IO_3^-$. $FeO_x$ also serves as a redox cocatalyst for other photocatalysts and redox mediators. We also demonstrate that $FeO_x$-loaded $Bi_4TaO_8Cl$ applies to a visible-light Z-scheme system with an $IO_3^-/I^-$ redox shuttle.

## 2.2. Experimental

### Synthesis

$Bi_4TaO_8Cl$ was prepared by a two-step synthesis via the polymerized complex (PC) method according to the literature.[12] The particulate $Bi_3TaO_7$ sample was initially prepared by the PC method as follows: $Bi(NO_3)_3•5H_2O$ (9 mmol, FUJIFILM Wako Pure Chemical Corporation) and $TaCl_5$ (3 mmol, Kojundo Chemical Laboratory Co., Ltd.)

were mixed in methanol (20 mL) followed by addition of citric acid (0.13 mol, FUJIFILM Wako Pure Chemical Corporation). The mixture was stirred at 423 K to obtain a transparent solution. After the addition of ethylene glycol (32 mL, FUJIFILM Wako Pure Chemical Corporation), the solution was heated at 593 K on a hot stirrer with stirring. The obtained brown gel was further heated at 623 K using a mantle heater to produce a black solid mass. Finally, the black solid mass was calcinated at 773 K for 2 h in air. The produced $Bi_3TaO_7$ (6.7 mmol) was then mixed with BiOCl (FUJIFILM Wako Pure Chemical Corporation, 7.0 mmol), followed by heating in an evacuated silica tube at 973 K for 20 h.

$SrTiO_3$:Rh was prepared by solid-state reaction.[13] A mixture of $TiO_2$, $SrCO_3$ and $Rh_2O_3$ (Ti : Sr : Rh = 1 : 1.07 : 0.01) was calcined in air at 1073 K for 1 h and subsequently at 1273 K for 10 h. A Pt cocatalyst (0.5 wt% calculated as metal) was loaded onto $SrTiO_3$:Rh by the impregnation method using $H_2PtCl_6·6H_2O$ (FUJIFILM Wako Pure Chemical Corporation) as a precursor by calcination at 473 K for 1 h in $H_2$ flow (20 $mLmin^{-1}$). $BiVO_4$ was prepared according to literature via a room temperature aqueous process.[14] A commercially available $WO_3$ (Kojundo Chemical Laboratory Co., Ltd., consisting mainly of monoclinic as well as a portion of triclinic phase) was used after the removal of the fine particles with triclinic phase by several cycles of an ultrasonic dispersion into Milli-Q water followed by centrifugation at 1000 rpm for 10 min.[15] A commercially available $TiO_2$ (Merck, Anatase) was used. $\beta$-FeOOH was also synthesized according to the literature[16] for a reference sample in the X-ray absorption experiments.

### Deposition of $FeO_x$

The Fe species were loaded using the impregnation method. The $Bi_4TaO_8Cl$ powder (0.3 g) was dispersed in an aqueous solution containing $FeCl_3$ (12.75 mM, 2.0 mL) followed by evaporation of the solvent in a water bath, and heat treatment at 573 K for 1 h in an Ar flow (20 $mLmin^{-1}$). The loading amount of Fe species was set to 10 mol% for the $Bi_4TaO_8Cl$.

### Characterization

Powder XRD (MiniFlex II, Rigaku, X-ray source: Cu Kα), UV-visible diffuse reflectance spectroscopy (V-650, JASCO), SEM-EDX (NVision 40, Carl Zeiss-SIINT) were used to characterize the samples. Transmission electron microscopy (TEM) was performed using a JEOL JEM-2100F microscope. Fe K-edge X-ray absorption fine structure (XAFS) measurements were performed at the BL01B1 beamline of SPring-8. The X-ray absorption spectra were measured in transmission or fluorescence mode at room temperature using a Si(111) two-crystal monochromator.

### Photocatalytic reaction

Photocatalytic reactions were performed using a gas closed-circulation system. Photocatalyst powders (0.2 g) were dispersed in an aqueous $NaIO_3$ solution (4 mM, 250 mL) in a Pyrex cell. The photocatalysts were irradiated with visible light ($\lambda > 400$ nm) through a cutoff filter (HOYA; L42) from a 300-W Xe-arc lamp (PerkinElmer; Cermax-PE300BF). In the case of $TiO_2$, UV and visible light were irradiated without the cutoff filter ($\lambda > 300$ nm). The quantity of the evolved gases was determined using an online gas chromatograph (thermal conductivity detector; molecular sieve 5 Å column packing; Ar carrier gas). The apparent quantum efficiency (AQE) for $O_2$ evolution was measured using a Xe lamp (MAX-302, Asahi Spectra Co. Ltd.) attached with a bandpass filter (central wavelength: 420 nm).

The Z-scheme water-splitting reaction was conducted using $FeO_x$-loaded $Bi_4TaO_8Cl$ (50 mg) and Pt-loaded $SrTiO_3$:Rh (100 mg) as $O_2$- and $H_2$-evolving photocatalysts, respectively. They were suspended in NaI (0.98 mM) and $NaIO_3$ (0.02 mM) aqueous solution (250 mL) at pH 5. The suspension was irradiated with visible light ($\lambda > 400$ nm).

### Electrochemical experiment

The $FeO_x$ electrode was prepared by the drop-casting method on a fluorine-doped tin oxide (FTO) glass electrode. A small amount (50 μL) of $FeCl_3$ MeOH solution (12.5 mM) was spread on an FTO substrate. The substrate was dried in air at room temperature and subsequently calcined under an Ar flow (20 mL $min^{-1}$) at 573 K for 1 h. Electrochemical measurements were performed using a potentiostat (VersaSTAT4, Princeton Applied Research Co., Ltd.) and a cell consisting of a prepared electrode, Pt wire, and Ag/AgCl electrode as the working electrode, counter electrode, and the reference electrode, respectively.

Mott–Schottky measurements were conducted to evaluate the flat-band potential of semiconductors as follows: The sample was mixed with a small amount of water, and the obtained paste was coated on a fluorine-doped tin oxide (FTO) conductive substrate via a squeezing method and dried in air at 80 °C. The Mott–Schottky plots were recorded using electrochemical analyzer (PARSTAT2263, Princeton Applied Research). Electrochemical measurements were performed in a three-electrode cell and a $Na_2SO_4$ solution (0.5 M, pH 5.0 adjusted by HCl) with 10 mV amplitude and a frequency of 1 kHz. The flat-band potentials are assumed to be CBMs owing to the n-type nature of the samples.

### Reaction between $Fe(OH)_2$ and $IO_3^-$

All the experiments were conducted under Ar bubbling to prevent the oxidation of $Fe^{II}$ by $O_2$ in air. $Fe(OH)_2$ colloidal solution (0.2 M as Fe, greenish-white) was prepared as described in the literature.[36] First, $FeCl_2$•$4H_2O$ (10 mmol) was dissolved in Milli-Q water (30 mL). Then, the $FeCl_2$ aq. (0.33 M, 30 mL) was mixed with aqueous NaOH (1 M, 20 mL) with vigorous stirring. 2 mL of this colloidal solution was added to the aqueous solution with or without $NaIO_3$ (4 mM, 100 mL, adjusted to pH5 using HCl aq.) with stirring.

After stirring the mixed solutions, 500 μL of each solution was sampled and immediately added to aqueous HCl (1 M, 4.5 mL). The obtained solution (50 μL), 2 M acetate buffer solution (2.1 mL), and $9.6\times10^{-4}$ M TPTZ solution (0.7 mL) were mixed, and the amount of $Fe^{2+}$ was determined based on the absorbance at 596.5 nm using UV-vis spectroscopy (UV-1800, Shimadzu).

For quantification of $IO_3^-$ and $I^-$, 500 μL of this mixed solution was sampled and added to Milli-Q water (4.5 mL). Then, $IO_3^-$ and $I^-$ in the solution were quantified by ion chromatography (CDD-10ASP, Shim-pack, IC-SA2, Shimadzu).

### TRMC Measurement

An X-band microwave (~9.1 GHz) was used as the probe. The third harmonic generation (THG; 355 nm) of a Nd:YAG laser (Continuum Inc., Surelite II, 5−8 ns pulse duration, 10 Hz) as the excitation source ($4.6 \times 10^{15}$ photons $cm^{-2}$ $pulse^{-1}$) The powdered samples were fixed to quartz substrates using optically clear adhesive tape (the tape does not interfere with any TRMC signal). The photoconductivity $\Delta\sigma$ was calculated using the following formula: $\Delta\sigma = \Delta P_r/(AP_r)$, where $\Delta P_r$, $A$, and $P_r$ are the transient power change of the reflected microwave, the sensitivity factor, and the power of microwave reflected, respectively. The obtained $\Delta\sigma$ values were then converted to the product of the quantum yield ($\varphi$) and the sum of the charge carrier mobilities ($\sum\mu = \mu_+ + \mu_-$) using the following formula: $\varphi\sum\mu = \Delta\sigma(eI_0F_{light})^{-1}$, where $e$ and $F_{light}$ are the unit charge of a single electron and a correction (or filling) factor, respectively. All TRMC measurements were performed in an ambient atmosphere at room temperature (25°C).

## TRAS measurement

A set of custom-built TRAS spectrometers was employed as described previously.[17] In the femtosecond to nanosecond regions, experiments were performed using a conventional pump–probe method based on a Ti:sapphire laser system (Spectra Physics, Solstice & TOPAS Prime; duration, 90 fs; repetition rate, 1 kHz). In this experiment, a 355 nm laser pulse was used as the pump pulse. The experiments were performed in air to prevent heating of the sample and to minimize the accumulation of electrons in the photocatalyst due to the high-frequency pump pulse irradiation (500 Hz). In the microsecond to second region, the transient absorption spectra were measured from 25,000 to 1,000 $cm^{-1}$. A 355 nm light (Continuum, Surelite-II, 6 ns, 355 nm, repetition rate of 5−0.01 Hz) was used as the pump pulse. The spectra were obtained at intervals of 200 $cm^{-1}$ and averaged over 300 scans per spectrum. The measurements were performed under vacuum at room temperature. The powder photocatalyst was fixed on a $CaF_2$ plate with a density of ∼1 mg $cm^{-2}$, and the obtained sample plate was placed in a stainless steel cell.

## Density Functional Theory Calculation

The band structure calculation of $Bi_4TaO_8Cl$ was performed within the framework of density functional theory (DFT) using a plane-wave pseudopotential method as implemented in the Cambridge Serial Total Energy Package (CASTEP) code of BIOVIA’s Material Studio 2020.[18] The Perdew-Burke-Ernzerhof (PBE) function of the generalized gradient approximation (GGA) was employed as the exchange-correlation functional. A plane wave basis set with an energy cut-off of 630 eV and the Monkhorst-Pack 3 × 3 × 1 k-point mesh was used. The minimization algorithm of Broyden–Fletcher–Goldfarb–Shanno (BFGS) was employed for geometry optimizations with a total energy convergence tolerance of $10^{-6}$ eV per atom. The separation between the k-points in the band structure calculations was 0.001 Å. Other convergence parameters are as follows: a self-consistent field tolerance of $1 \times 10^{-5}$ eV per atom, a maximum stress of 0.05 GPa, and the maximum ionic displacement of $1 \times 10^{-3}$ Å.

The effective mass m* was calculated based on the obtained band structure. m* is defined as follows.

$$\frac{m_0}{m^*} = \frac{m_0}{\hbar^2}\frac{d^2\varepsilon}{dk^2} \qquad (2)$$

where $m_0$ is the free electron mass, k is the reciprocal lattice vector in the direction of interest, and $d^2\varepsilon/dk^2$ is the curvature of the band at a maximum or minimum, respectively.

Assuming the band around their minima/maxima to be parabolic, we estimate the curvature of the band using the finite difference approximation:

$$\frac{d^2\varepsilon}{dk^2} \approx \frac{2[\varepsilon(k+\Delta k)-\varepsilon(k)]}{\Delta k^2} \qquad (3)$$

where Δk = 0.05 Å.

## 2.3. Results and Discussion

### Characterization of Fe species loaded on $Bi_4TaO_8Cl$

The $FeO_x$ cocatalyst was loaded onto $Bi_4TaO_8Cl$ via the impregnation method. The loading amount of the Fe species was set to be 10 mol% against $Bi_4TaO_8Cl$ (approximately 0.5 wt% as Fe), unless otherwise stated. Negligible differences were observed in the XRD pattern and the band edge positions of $Bi_4TaO_8Cl$ before and after the loading of $FeO_x$ (Figures 6-1 and 2).

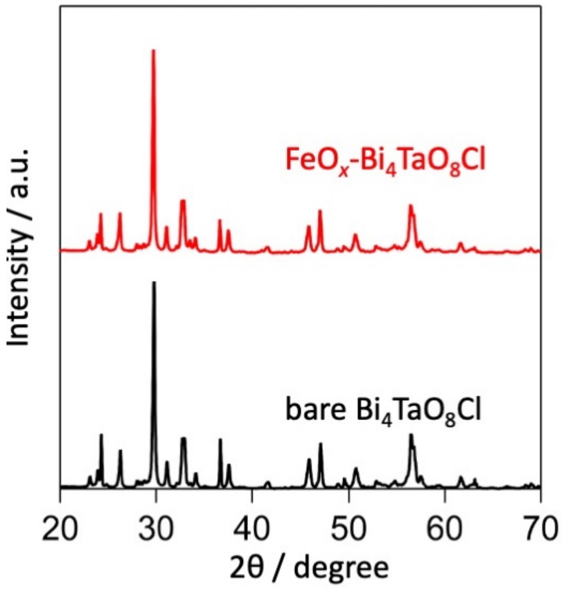

**Figure 6-1.** XRD pattern of bare and $FeO_x$-$Bi_4TaO_8Cl$ samples.

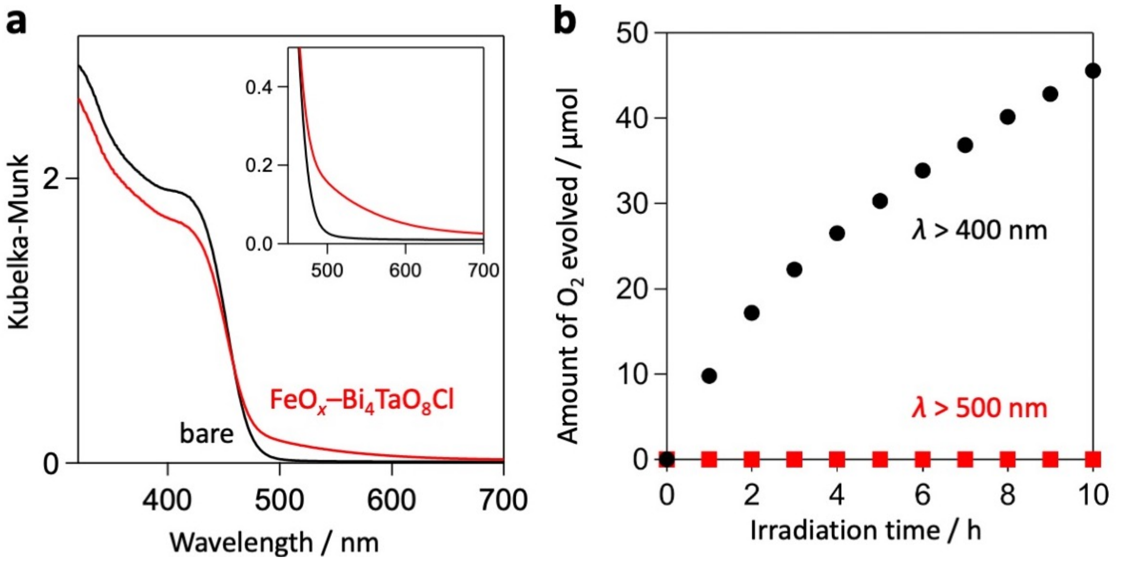

**Figure 6-2.** a, DRS of bare and FeO$_x$- Bi$_4$TaO$_8$Cl. b, Time courses of $O_2$ evolution over FeO$_x$-Bi$_4$TaO$_8$Cl in aqueous NaIO$_3$ solution (4 mM) under visible-light (λ > 400 or > 500 nm) irradiation. FeO$_x$-Bi$_4$TaO$_8$Cl shows an absorption shoulder at 480-620 nm. However, upon excitation with 500 nm, negligible $O_2$ evolution was observed. We then assign the absorption shoulder to light scattering by the FeO$_x$ particles, rather than the direct interfacial charge transfer.

The FeO$_x$ cocatalyst was identified by K-edge X-ray absorption near edge structure (XANES) spectroscopy (Figure 6-3a). $\beta$-FeOOH, Fe$_2$O$_3$, FeCl$_3$, and FeO were used as the reference samples. FeCl$_3$ is the precursor for FeO$_x$ loading. The FeO$_x$ cocatalyst on Bi$_4$TaO$_8$Cl shows a spectrum similar to that of $\beta$-FeOOH and Fe$_2$O$_3$, while it exhibits a difference from that of FeO. This result demonstrates the trivalency of the loaded Fe species. As shown in Figure 6-3b, we also acquired Fe K-edge Fourier-transformed extended X-ray absorption fine structure (EXAFS) spectra. $\beta$-FeOOH, Fe$_2$O$_3$, and FeCl$_3$ were used as the Fe (III) references. The FeO$_x$ cocatalyst sample features a nearest neighbor distance similar to those for $\beta$-FeOOH and Fe$_2$O$_3$ while that for FeCl$_3$ is greater. Therefore, the nearest neighboring atom for Fe in the FeO$_x$ cocatalyst is oxygen. From the XANES and EXAFS results, we conclude that the identity of FeO$_x$ is trivalent oxides/oxyhydroxides. Transmission electron microscopy (TEM) revealed the amorphous nature of the FeO$_x$ cocatalyst (Figure 6-3c), which is highly dispersed on the photocatalyst (Figure 6-4).

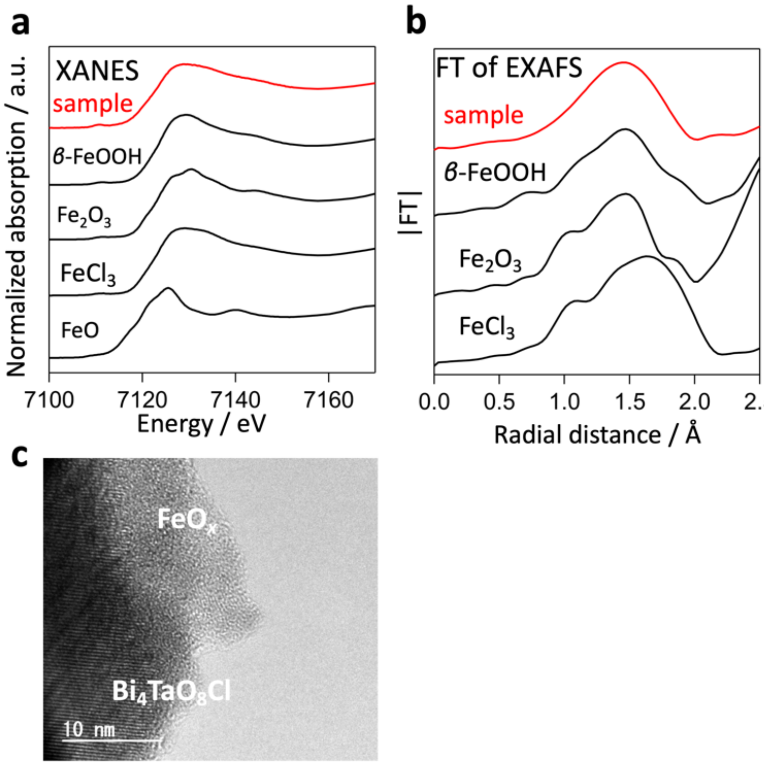

**Figure 6-3.** Fe K-edge XANES (a) Fourier transforms of EXAFS (b) spectra for $FeO_x$-$Bi_4TaO_8Cl$. c, TEM image of $FeO_x$-$Bi_4TaO_8Cl$.

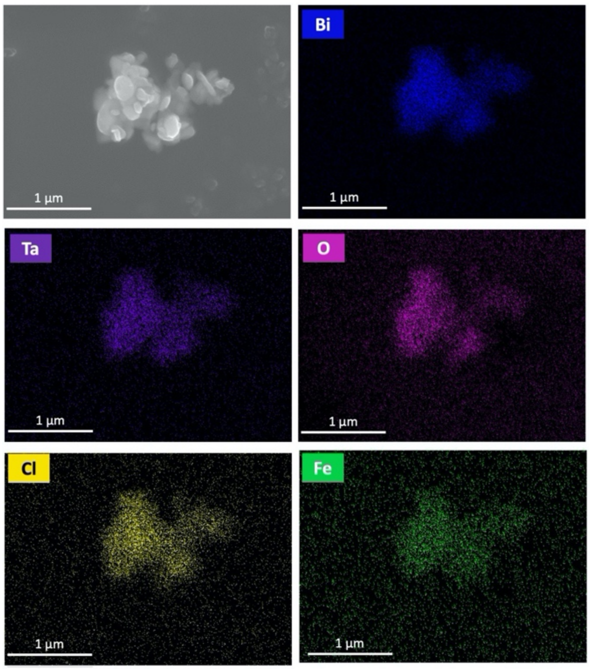

**Figure 6-4.** SEM image and SEM-EDS elemental mapping of $FeO_x$-$Bi_4TaO_8Cl$.

## Activation of photocatalytic $O_2$ evolution by $FeO_x$

The photocatalytic activity of bare and $FeO_x$-loaded $Bi_4TaO_8Cl$ for $O_2$ evolution was evaluated in the presence of $IO_3^-$ as an electron acceptor. As shown in Figure 6-5, bare $Bi_4TaO_8Cl$ exhibited negligible $O_2$ evolution under visible-light irradiation ($\lambda > 400$ nm). Note that bare $Bi_4TaO_8Cl$ is capable of oxidizing water into $O_2$ in the presence of one-electron acceptors ($Ag^+ + e^- \rightarrow Ag$; $Fe^{3+} + e^- \rightarrow Fe^{2+}$).[12,19] Therefore, the negligible activity of the bare sample should stem from the absence of active sites for the multielectron reduction of $IO_3^-$. In contrast, $FeO_x$-loaded $Bi_4TaO_8Cl$ showed $O_2$ evolution at a relatively high and steady rate. The amount of evolved $O_2$ in 10 h was 65.6 µmol, which was much greater than the $O_2$ provided the stoichiometric oxidation of $H_2O$ proceeded by loaded-$FeO_x$ (17 µmol / 4 $e^-$ = 4.2 µmol). Note that the loading amount and calcination temperature for $FeO_x$ loading were optimized for the $O_2$ evolution reaction (Figure 6-6) and the apparent quantum efficiency (AQE) at 420 nm was 1.4 %. The $O_2$ evolution of bare $Bi_4TaO_8Cl$ was not improved by the addition of $Fe^{3+}$ in the aqueous medium (Figure 6-7), indicating that $FeO_x$ loaded on the surface of the photocatalyst is essential for boosting $O_2$ evolution. The possibility of direct interfacial charge transfer[20] from the valence band maximum of $Bi_4TaO_8Cl$ to $Fe^{III}$ was ruled out by the negligible $O_2$ evolution under light irradiation below the band gap of $Bi_4TaO_8Cl$ (Figure 6-2b). $FeO_x$-loaded and bare $Bi_4TaO_8Cl$ did not show a significant difference in the pH-dependent zeta potentials (Figure 6-8).

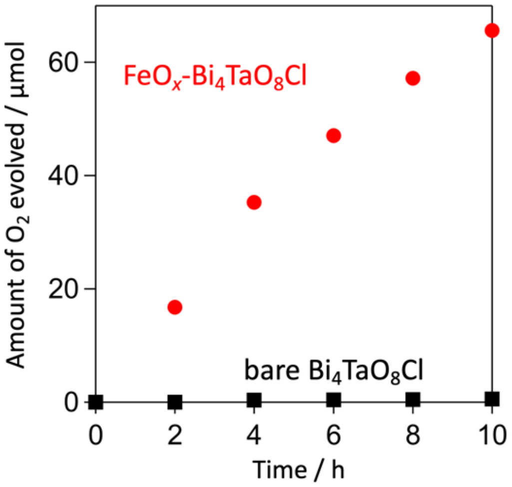

**Figure 6-5.** Time courses of $O_2$ evolution over $FeO_x$-$Bi_4TaO_8Cl$ (red circle) or bare $Bi_4TaO_8Cl$ (black square) in aqueous $NaIO_3$ solution (4 mM) under visible-light ($\lambda > 400$ nm) irradiation.

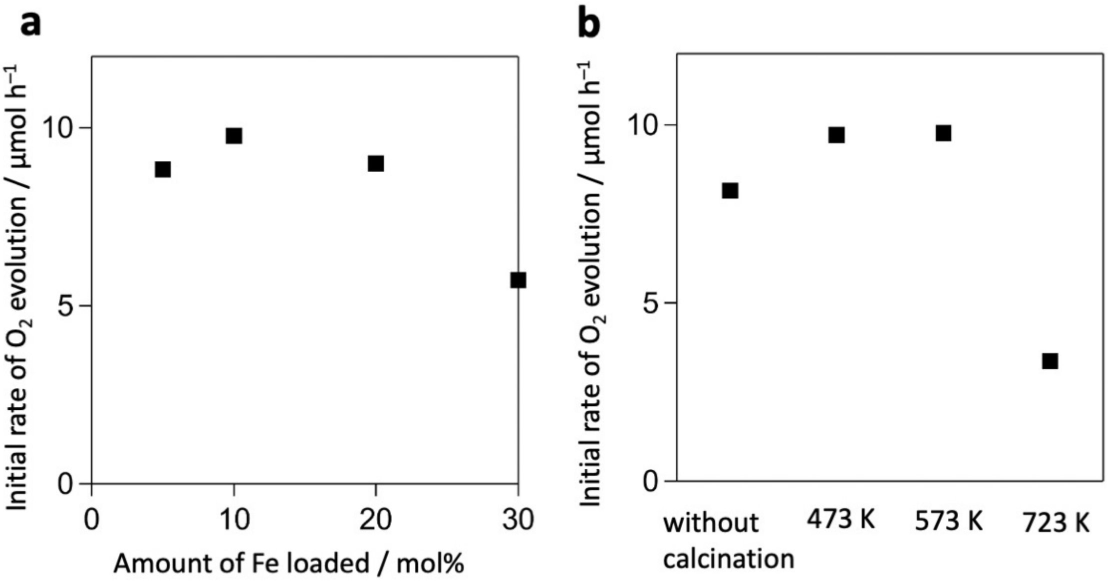

**Figure 6-6.** The effect of the loading amount (a) and the calcination temperature (b) for $FeO_x$-loading on photocatalytic activity.

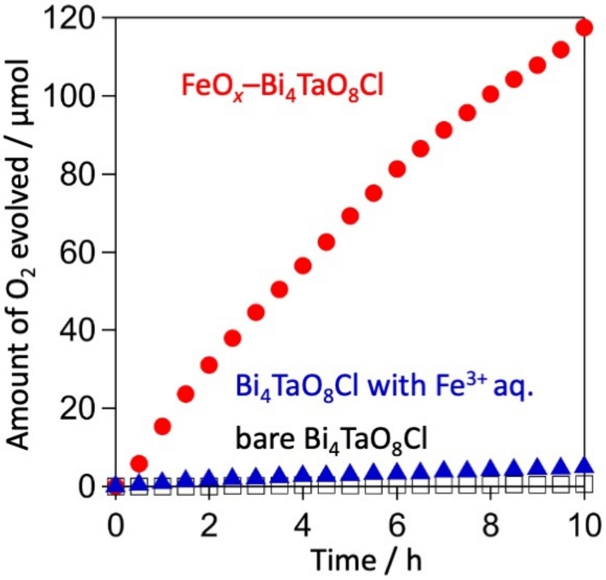

**Figure 6-7.** The effect of the adding of the $Fe^{3+}$ cation of same amount as the loaded $FeO_x$ (17 µmol) into the reaction solution ($NaIO_3$ solution (4 mM), pH = 2.5) on $O_2$ evolution under visible-light ($\lambda >$ 400 nm) irradiation. Mere adding of $Fe^{3+}$ to the reaction solution (blue triangle) show much lower $O_2$ evolution activity than the $FeO_x$-$Bi_4TaO_8Cl$. The small amount of $O_2$ on bare $Bi_4TaO_8Cl$ sample by the addition of $Fe^{3+}$ was probably generated through the reduction of $Fe^{3+}$ to $Fe^{2+}$ by photoexcited electrons.

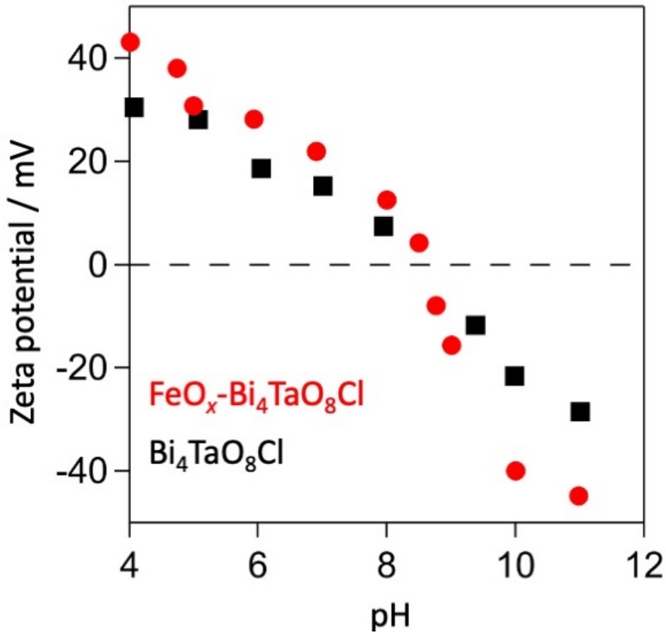

**Figure 6-8.** The pH dependence of Zeta potentials of bare and $FeO_x$-$Bi_4TaO_8Cl$.

From these results, we concluded that $FeO_x$ on $Bi_4TaO_8Cl$ acts as a redox cocatalyst for the multielectron reduction of the $IO_3^-$ electron acceptor. To the best of our knowledge, this is the first earth-abundant cocatalyst to promote $IO_3^-$ reduction.

**Photogenerated electron capture by $FeO_x$**

The role of a cocatalyst is to capture photogenerated carriers from the semiconductor photocatalyst and promote the catalytic reaction.[21] To clarify the electron capture ability of $FeO_x$, we employed time-resolved microwave conductivity (TRMC) measurement, which is known as a useful tool to investigate carrier dynamics in powdery photocatalysts.[22–24] Note that, based on the facts that the effective mass of electron is much smaller than that of holes in $Bi_4TaO_8Cl$ (Figure 6-9) and that the $Bi_4TaO_8Cl$ is a n-type semiconductor, electrons mainly contribute to the TRMC signal of $Bi_4TaO_8Cl$. As shown in Figure 6-10, $FeO_x$ loading lowered the transient photoconductivity, which suggests efficient electron capture by $FeO_x$.

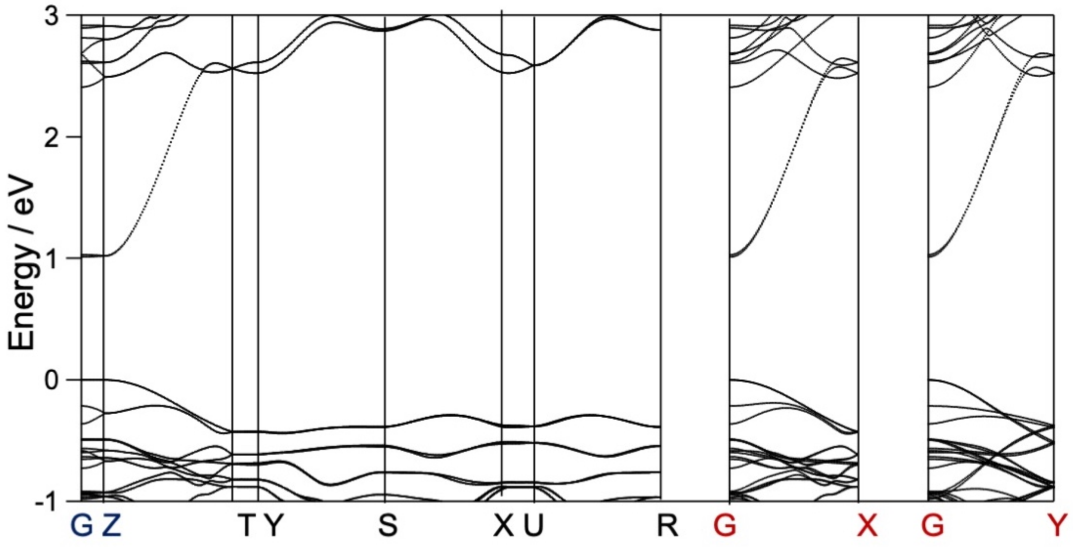

**Figure 6-9.** Band structure of $Bi_4TaO_8Cl$. Effective masses were estimated from the DFT results. The mean of the relative effective masses in the in-plane (Γ-X and Γ-Y) directions are 0.25 $m_0$ and 1.4 $m_0$ for electrons and holes, respectively.

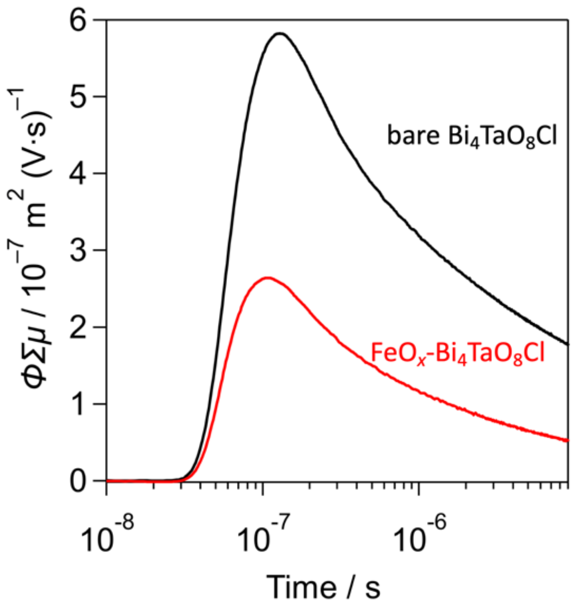

**Figure 6-10.** TRMC transients of $FeO_x$ loaded (red) or bare (black) $Bi_4TaO_8Cl$ samples ($\lambda_{ex} = 355$ nm, $I_0 = 4.6 \times 10^{15}$ photons $cm^{-2}$ $pulse^{-1}$).

This assignment was further supported by time-resolved absorption spectroscopy (TRAS), another useful tool for examining carrier dynamics in semiconductor photocatalysts.[17] Figure 6-11 shows microsecond transient absorption spectra for bare $Bi_4TaO_8Cl$, where the band gap excitation induces three absorption increases at 2,000

$cm^{-1}$, 13,800 $cm^{-1}$, and 21,400 $cm^{-1}$ (Figure 6-11a). Referring to previous results on $TiO_2$[25–29] and $LaTiO_2N$,[17] the first is attributed to photogenerated free electrons in the conduction band (CB) and/or shallowly trapped electrons,[30,31] the second is attributed to the excitation of trapped electrons from the mid-gap state to the CB,[17] and the third to holes. We then acquired the initial decay profiles using femtosecond TRAS, focusing on 2,000 $cm^{-1}$ and 21,400 $cm^{-1}$. Figure 6-11b and c show the decay curves of the bare $Bi_4TaO_8Cl$ and $FeO_x$-$Bi_4TaO_8Cl$. The loading of $FeO_x$ accelerated the decay of free electrons (Figure 6-11b) while the influence on the hole decay was found to be negligible (Figure 6-11c). These results indicate that $FeO_x$ selectively captured electrons from $Bi_4TaO_8Cl$

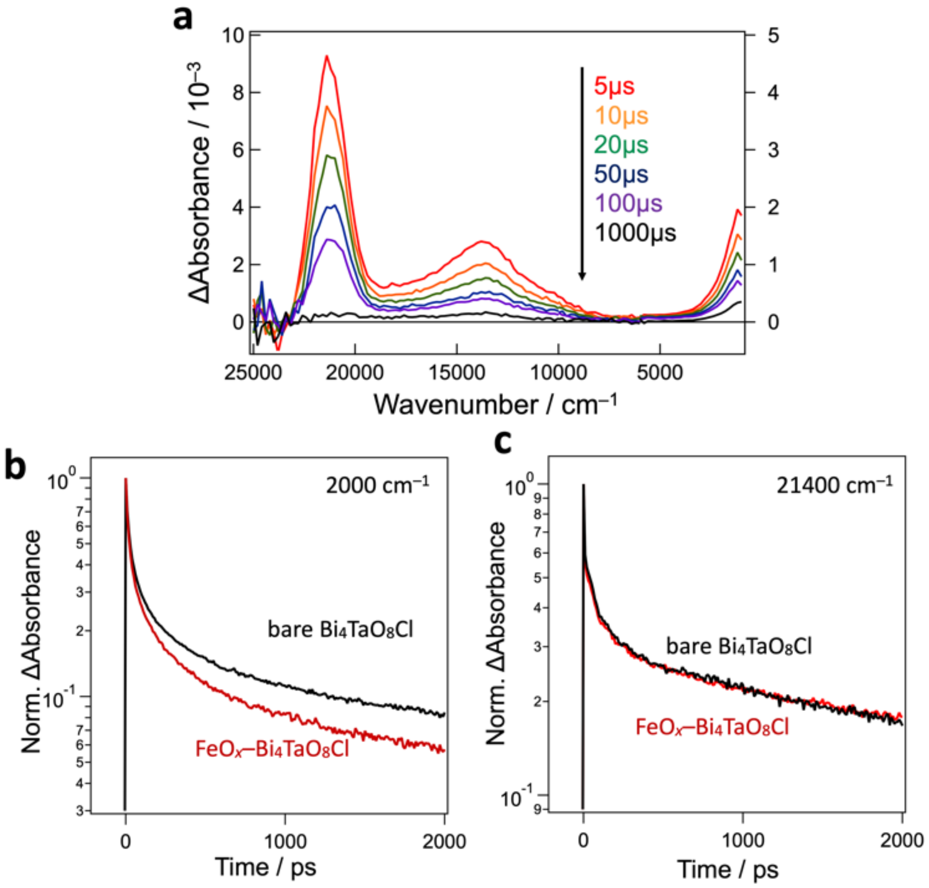

**Figure 6-11.** a, Microsecond TRAS of bare $Bi_4TaO_8Cl$ measured in the vacuum. The sample was excited by 355 nm laser pulses (6 ns duration, 0.5 mJ, 5 Hz). b, c, Femtosecond decay profiles of transient absorptions at 2,000 $cm^{-1}$ (b) and 21,400 $cm^{-1}$ (c) for bare $Bi_4TaO_8Cl$, $FeO_x$-$Bi_4TaO_8Cl$. The samples were excited by 355 nm laser pulses (90 fs duration, 6 μJ, 500 Hz) under air for the several pico-second (ps) region.

### The catalytic property of $FeO_x$ for $IO_3^-$ reduction

To verify the catalytic activity of $FeO_x$ for the reduction of $IO_3^-$, an $FeO_x$-decorated electrode was prepared on a fluorine-doped tin oxide (FTO) glass plate. Figure 6-12 shows the cyclic voltammograms obtained using bare FTO and the $FeO_x$/FTO electrodes. In the absence of the $IO_3^-$, the $FeO_x$/FTO electrode exhibited a small cathodic current at approximately −0.0 ~ −0.3 V vs. Ag/AgCl; through referral to a previous report on a FeOOH electrode,[32] this was attributed to the reduction of $Fe^{III}$ to $Fe^{II}$. The presence of $IO_3^-$ did not affect the onset potential of cathodic current from $Fe^{III}$ reduction (observed from about 0.0 V), which was followed by intense cathodic currents with an onset potential of approximately −0.4 V. The second cathodic current may stem from the catalytic reduction of $IO_3^-$ by the produced $Fe^{II}$ species, because, in the absence of $FeO_x$ (bare-FTO), the cathodic current was much lower. In addition, the anodic current from $Fe^{II}$ oxidation (observed from approximately −0.7 to −0.2 V) was suppressed by the increased $IO_3^-$ concentration. This result also suggests that the produced $Fe^{II}$ species during the cathodic sweep were consumed for $IO_3^-$ reduction.

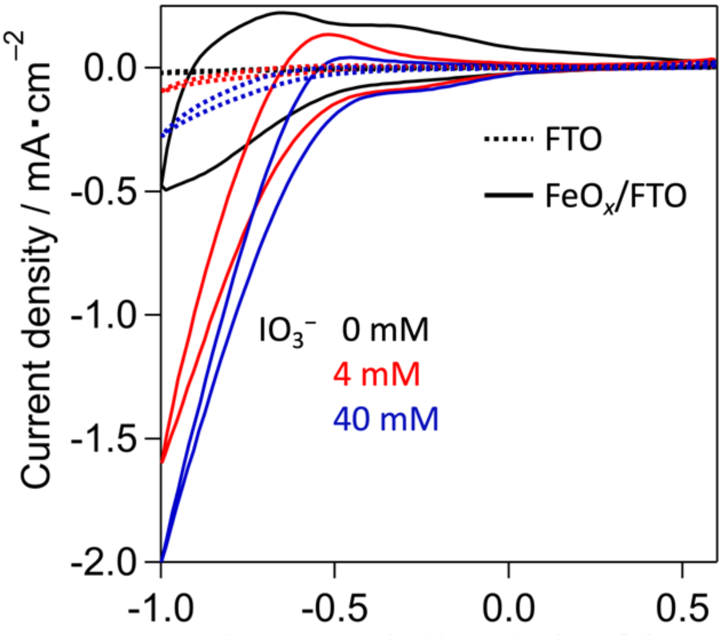

**Figure 6-12.** Cyclic voltammogram of a $FeO_x$/FTO and FTO electrode in 0.1 M $Na_2SO_4$ solution containing 0–40 mM $IO_3^-$ (pH 5), at a scan rate of 50 $mVs^{-1}$

### The working mechanism of $FeO_x$ cocatalyst

Based on the above-mentioned results, the role of $FeO_x$ as a cocatalyst for $IO_3^-$ reduction is illustrated in Figure 6-13. After photoexcitation of the $Bi_4TaO_8Cl$ photocatalyst, photogenerated electrons in the conduction band are captured by $FeO_x$ (step 1). As a result, $Fe^{III}$ is reduced to $Fe^{II}$ (step 2), which allows $FeO_x$ to accumulate electrons. Then, $Fe^{II}$ ions reduce $IO_3^-$ to $I^-$ while $Fe^{II}$ is re-oxidized to $Fe^{III}$ (step 3). Through the catalytic cycle (steps 1 – 3), $FeO_x$ can facilitate both carrier capture from the photocatalyst and reduction of the redox mediator, functioning as a cocatalyst. Step 1 was confirmed by time-resolved spectroscopy (Figures 6-10 and 11). Step 3 was proposed using electrochemical measurements (Figure 6-12).

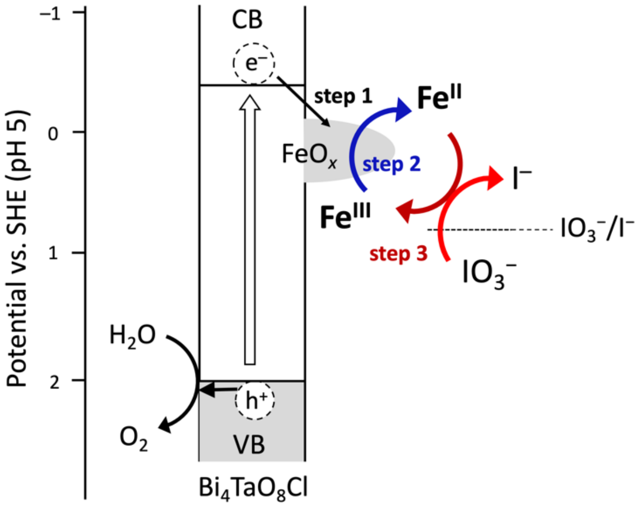

**Figure 6-13.** Schematic illustration of the role of $FeO_x$ deposited on the photocatalyst to promote reduction of $IO_3^-$.

Although we have not yet achieved direct observation of the $Fe^{II}$ species generated in $FeO_x$ (step 2) (Figure 6-14), the generation of $Fe^{II}$ was indirectly confirmed. Based on the Pourbaix diagram,[33] $Fe^{II}$ species should dissolve in the aqueous solution as $Fe^{2+}$ when the pH is approximately 5. Actually, visible light irradiation (10 h) on $FeO_x$-$Bi_4TaO_8Cl$ in an aqueous solution without $IO_3^-$ produced $Fe^{2+}$ in the aqueous phase, as detected by a colorimetric method (Figure 6-15). The amount of the produced $Fe^{2+}$ (6.1 µmol) was approximately 36 % of the initial $Fe^{III}$ species (17 µmol) within the loaded $FeO_x$. The production of $Fe^{2+}$ should be accompanied by $O_2$ evolution, but the produced amount of the $O_2$ (2.1 µmol) was about 38% more than the estimated amount (1.5 µmol) from the $Fe^{2+}$ detected in the aqueous solution (6.1 µmol), which in turn implies that a part of produced $Fe^{II}$ remains in the $FeO_x$ without dissolving in water. In sharp contrast, the presence of $IO_3^-$ suppressed the dissolution of $FeO_x$ during the $O_2$ evolution reaction (Figure 6-15), which suggests that the $Fe^{II}$ species produced in $FeO_x$ were promptly re-oxidized to insoluble $Fe^{III}$ in the photocatalytic reaction by $IO_3^-$. Despite the persistency of the $Fe^{II}$ species on $Bi_4TaO_8Cl$ in the presence of $IO_3^-$, the stability of the $O_2$ evolution has still large room to improve, which results from, for example, the aggregation and surface passivation of $FeO_x$ on $Bi_4TaO_8Cl$ (Figure 6-16).

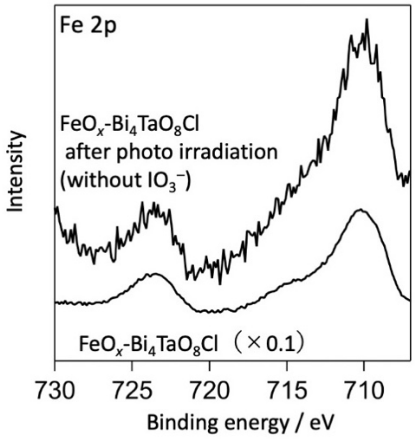

**Figure 6-14.** XP spectra focusing on Fe 2p region for $FeO_x$-$Bi_4TaO_8Cl$ before and after photoirradiation (10 h) in the absence of $IO_3^-$. The $FeO_x$ species should underwent facile oxidation by the ambient $O_2$.

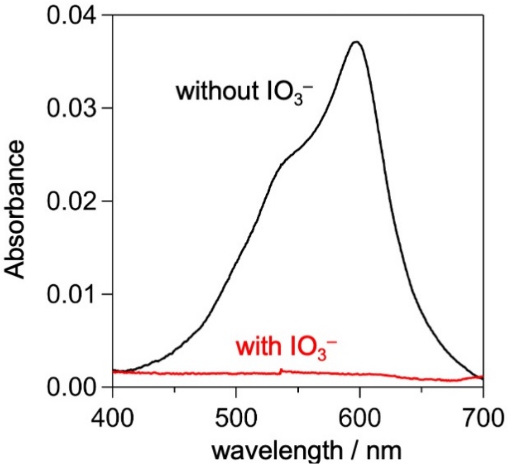

**Figure 6-15.** Absorption spectra of $Fe^{2+}$ produced in the reaction solution after the photo-irradiation on $FeO_x$-$Bi_4TaO_8Cl$ with or without $IO_3^-$ in the reaction solution.

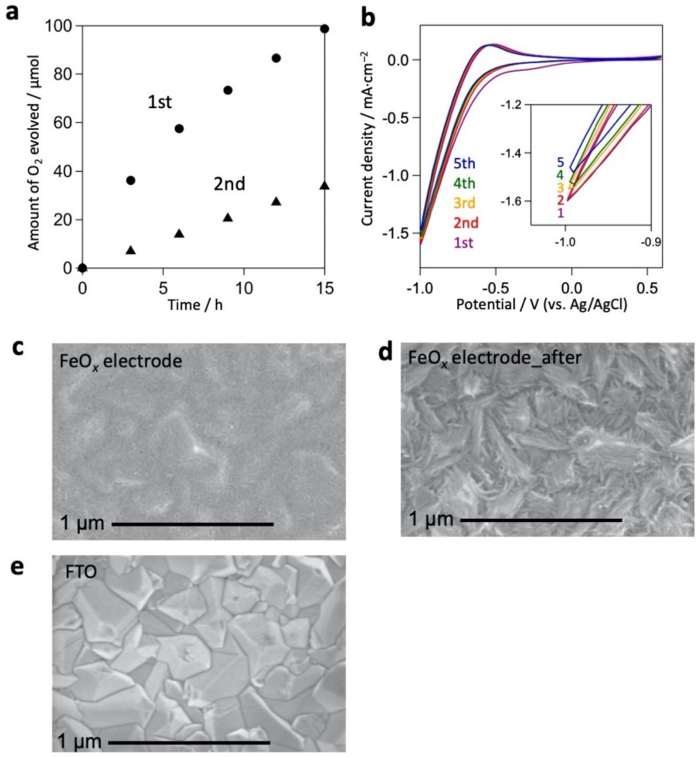

**Figure 6-16.** a, Repeatability test for the photocatalytic $O_2$ evolution over $FeO_x$-$Bi_4TaO_8Cl$ in $NaIO_3$ aqueous solution (4 mM) under visible light irradiation ($\lambda > 400$ nm). b, Cyclic voltammogram for a $FeO_x$/FTO working electrode in 0.1 M $Na_2SO_4$ solution containing 4 mM $NaIO_3$. c,d, SEM images of the $FeO_x$/FTO working electrode before and after the electrochemical operation. e, SEM image of bare FTO. In the cyclic voltammetry, the catalytic current for the reduction of $IO_3^-$ decreased by repeating the cycle. The morphology of $FeO_x$/FTO changed after the electrochemical operation, where the aggregation of $FeO_x$ proceeded in SEM.

Steps 2 and 3 were further verified by a complementary experiment, in which the spontaneous reduction of $IO_3^-$ by $Fe^{II}$ (Eq. (1)) were tested (Figure 6-17).

$$IO_3^- + 6Fe^{II} + 6H^+ \rightarrow I^- + 6Fe^{III} + 3H_2O \qquad (1)$$

An $Fe(OH)_2$ colloidal solution (greenish-white, as shown in Figure 6-17a) was added to an aqueous solution of $NaIO_3$. After mixing, the color of the solution changed immediately to brown, indicating the formation of $Fe(OH)_3$ (Figure 6-17d). In contrast, the addition of $Fe(OH)_2$ to pure water resulted in no color change (Figure 6-17e). Figure 6-18 shows the time courses of the $Fe^{II}$ amounts in each mixture, which were quantified by colorimeter analysis (see the details in the experimental section). $Fe^{II}$ was rapidly consumed to reduce $IO_3^-$. Another important finding was the almost complete (i.e., via 6-electrons) reduction of $IO_3^-$ to $I^-$, without leaving other intermediates, such as $I_2$ (or $I_3^-$);

this was confirmed by the quantification of $IO_3^-$ and $I^-$ through ion chromatography. As summarized in Table 6-1, the amounts of $Fe^{II}$, $IO_3^-$, and $I^-$ were roughly in accordance with the theoretical amount from Eq. (1).

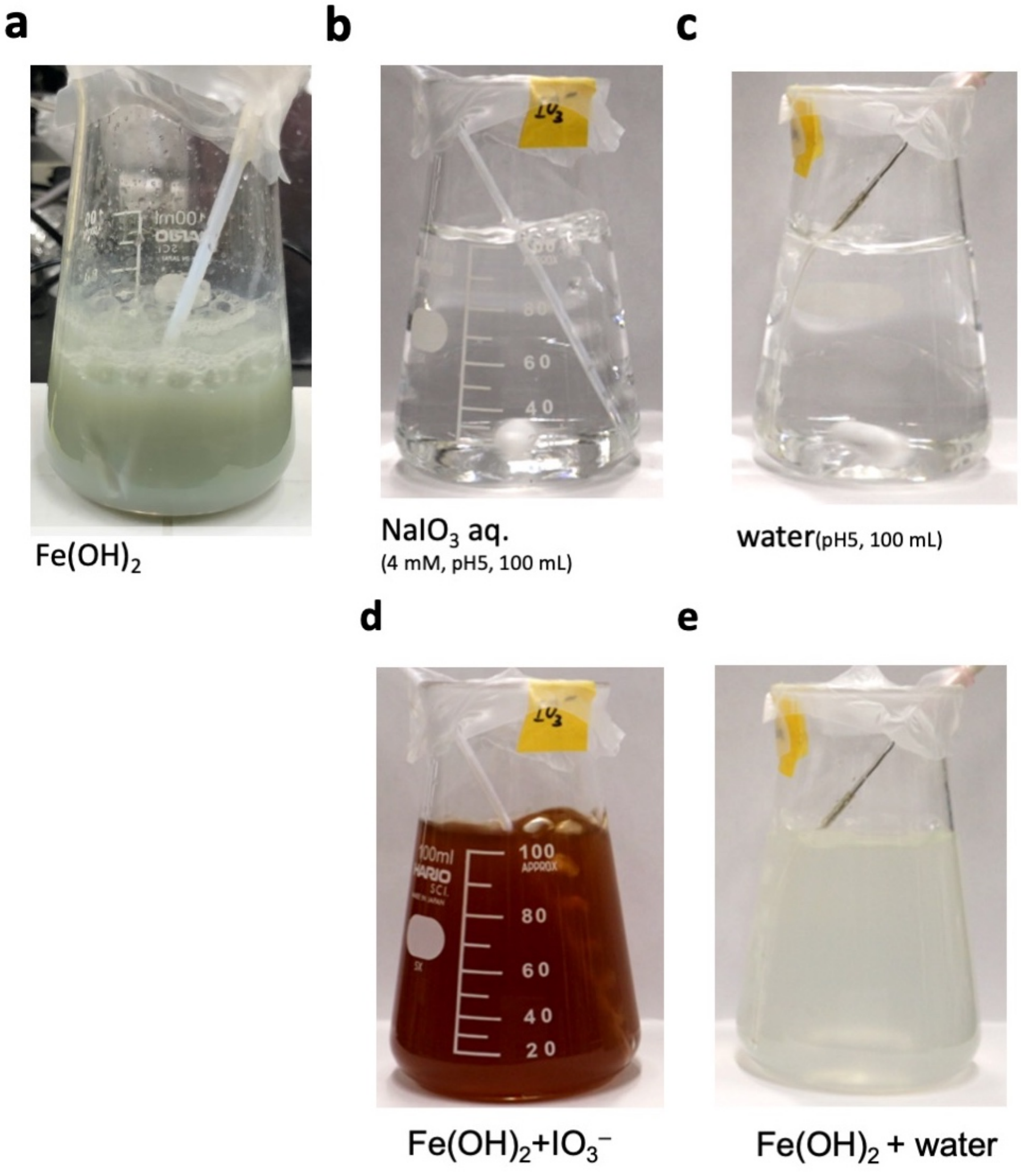

**Figure 6-17.** Pictures of as-prepared $Fe(OH)_2$ colloidal solution (a), $NaIO_3$ aqueous solution (b), water (c). $Fe(OH)_2$ colloidal solution (0.4 mmol as Fe) after adding to $IO_3^-$ aqueous solution (4 mM, 100 mL ) (d) and water (e).

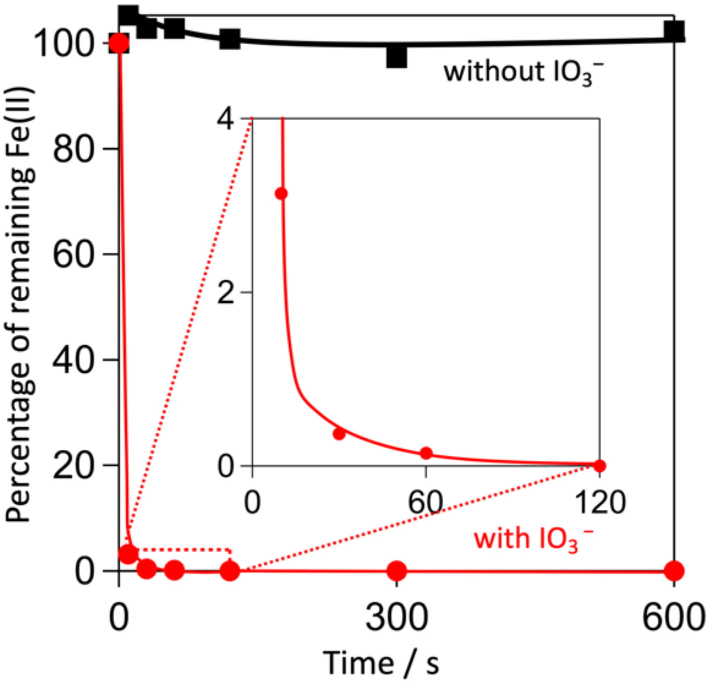

**Figure 6-18.** Time course of the Fe(II) amount after the adding of $Fe(OH)_2$ colloidal solution to $IO_3^-$ aqueous solution (red) and water (black).

**Table 6-1** The amount (μmol) of reactants in the $IO_3^-$ solution after adding the $Fe(OH)_2$ colloidal solution

| | before | After 10 min | Estimated amount from Eq. (1). |
|---|---|---|---|
| $IO_3^-$ | 400 μmol | 355 | 333 |
| $I^-$ | 0 | 61 | 67 |
| Fe(II) | 400 | n.d. | 0 |

The above results and discussion emphasize the proposed role of $FeO_x$ as a cocatalyst to boost $O_2$ evolution on the $Bi_4TaO_8Cl$ photocatalyst with an $IO_3^-$ electron acceptor (Figure 6-13). Although the actual redox potential of $Fe^{III}/Fe^{II}$ in $FeO_x$ remains elusive, based on the redox potentials of Fe species (e.g., $Fe(OH)_3/Fe(OH)_2$: −0.02 V; $Fe(OH)_3/Fe^{2+}$: +0.17 V vs. SHE at pH 5) and $IO_3^-$ ($IO_3^-/I^-$: +0.79 V vs. SHE at pH 5), $Fe^{II}$ can thermodynamically reduce $IO_3^-$. Further application of the present $FeO_x$ cocatalyst to various semiconductors may shed light on the redox potential, as will be discussed in the next section.

### Applicability to other photocatalysts and redox

We investigated the utility of $FeO_x$ in other photocatalysts and redox shuttles. $FeO_x$ was found to be effective for other photocatalysts, improving the $O_2$ evolution activity of $BiVO_4$ and anatase-$TiO_2$ in the presence of the $IO_3^-$ electron acceptor (Table 6-2). In contrast, it did not work for $WO_3$. The effect of $FeO_x$ reliant on photocatalysts is in stark contrast to previous cocatalysts for $IO_3^-$ reduction (e.g., Pt is effective for both $BiVO_4$ and $WO_3$),[1] providing a hint on the redox potential of $Fe^{III}/Fe^{II}$ in $FeO_x$. It is widely recognized that the conduction band minimum of $WO_3$ is more positive than that of $BiVO_4$.[34] We also measured the flatband potentials of $BiVO_4$ and $WO_3$ as −0.10 and +0.04 V (vs. SHE at pH 5), respectively (Figure 6-19). Thus, the lack of enhancement of $WO_3$ by $FeO_x$ strongly suggests the insufficient reduction power of photoexcited electrons in $WO_3$ for $Fe^{III}/Fe^{II}$ in $FeO_x$.

**Table 6-2** The effect of $FeO_x$ loading on $O_2$ evolution reaction

| Photocatalyst | Electron Acceptor | $O_2$ evolution in 3h / μmol | |
|---|---|---|---|
| | | bare | with $FeO_x$ |
| $BiVO_4$ | $IO_3^-$ | 12.7 | 28.5 |
| $TiO_2$ | $IO_3^-$ | 7.3 | 28.3 |
| $WO_3$ | $IO_3^-$ | n.d. | <0.2 |
| $Bi_4TaO_8Cl$ | $Co^{III}(bpy)_3^{3+}$ | 5.1 | 70.3 |
| $Bi_4TaO_8Cl$ | $Fe(CN)_6^{3-}$ | n.d. | 57.4 |

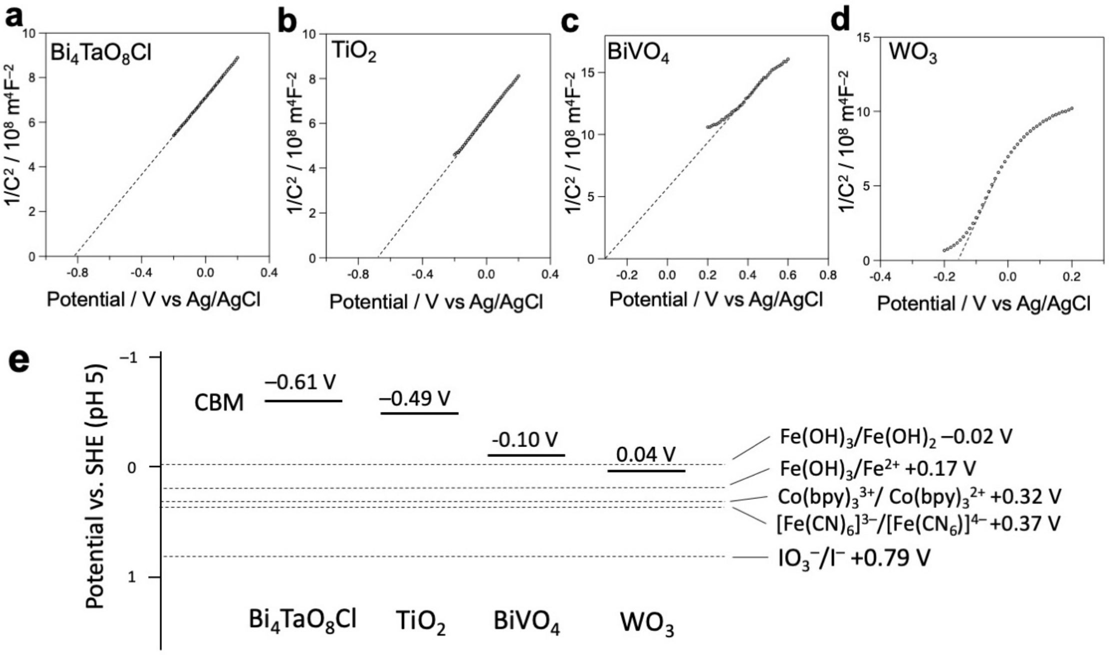

**Figure 6-19.** a-d, Mott–Schottky plots for $Bi_4TaO_8Cl$ (a), $TiO_2$ (b), $BiVO_4$ (c), $WO_3$ (d) in 0.5 M $Na_2SO_4$ solution (pH = 5). e, CBM positions of these samples estimated from the Mott-Schottky plots along with redox potentials of $Fe^{III}/Fe^{II}$, $IO_3^-/I^-$, $Co(bpy)_3^{3+}$/ $Co(bpy)_3^{2+}$, $[Fe(CN)_6]^{3-}/[Fe(CN_6)]^{4-}$.

It is noteworthy that $FeO_x$ loading on $Bi_4TaO_8Cl$ is also effective for other redox mediators (not only multi-electron acceptors), such as $Co^{III}(bpy)_3^{3+}$ or $Fe(CN)_6^{3-}$ (Table 6-2). In each case, the evolved $O_2$ is more significant than the estimated $O_2$ evolution, accompanied by the reduction in all the loaded-$FeO_x$ ($Fe^{III}$) to $Fe^{II}$ (4.2 μmol). These results also indicate that the redox potential of $Fe^{III}/Fe^{II}$ in $FeO_x$ is more negative than those of $Co^{III}(bpy)_3^{3+}$ (+0.32 V) and $Fe(CN)_6^{3-}$ (+0.37 V). Given the above, the redox potential of $Fe^{III}/Fe^{II}$ in $FeO_x$ seems to be located between −0.10 and +0.32 V (vs. SHE at pH 5).

The Pourbaix diagram for Fe species[27] provides us the redox of $Fe(OH)_3/Fe^{2+}$ (+0.17 V) when pH is 5. However, this potential should not directly apply to the present situation where $Fe^{II}$ is in $FeO_x$ not in the solution. We may estimate the redox potential of $Fe^{III}/Fe^{II}$ in $FeO_x$ from another related redox: $Fe(OH)_3/Fe(OH)_2$ existing only above pH 9 from the Pourbaix diagram. Assuming that $Fe^{II}$ does not dissolve into water even at pH 5, and that the redox of $Fe(OH)_3/Fe(OH)_2$ follows a Nernst slope, the redox potential might be approximately −0.02 V (vs. SHE at pH 5). This hypothetical value falls within the above-mentioned value (−0.10 ~ +0.32 V) and might justify the $Fe^{III}/Fe^{II}$ redox cycles with hydroxide forms in $FeO_x$ (Figure 6-13). Although further studies are necessary, these results suggest that $FeO_x$ loading can apply to other redox-based photocatalytic $O_2$ evolution systems if the potential relationship is appropriate (i.e., conduction band < $Fe^{III}/Fe^{II}$ < electron acceptor).

### Z-scheme water splitting

Finally, we applied $FeO_x$-loaded $Bi_4TaO_8Cl$ to a Z-scheme water splitting system as an $O_2$ evolution photocatalyst. Herein, the $IO_3^-/I^-$ couple as a redox mediator and Pt-loaded strontium titanate doped with Rh cations[35] (Pt/$SrTiO_3$:Rh) as a $H_2$-evolving photocatalyst were employed. As shown in Figure 6-20, $H_2$ and $O_2$ evolved stoichiometrically upon illumination with λ > 400 nm light, demonstrating visible-light Z-scheme water splitting.

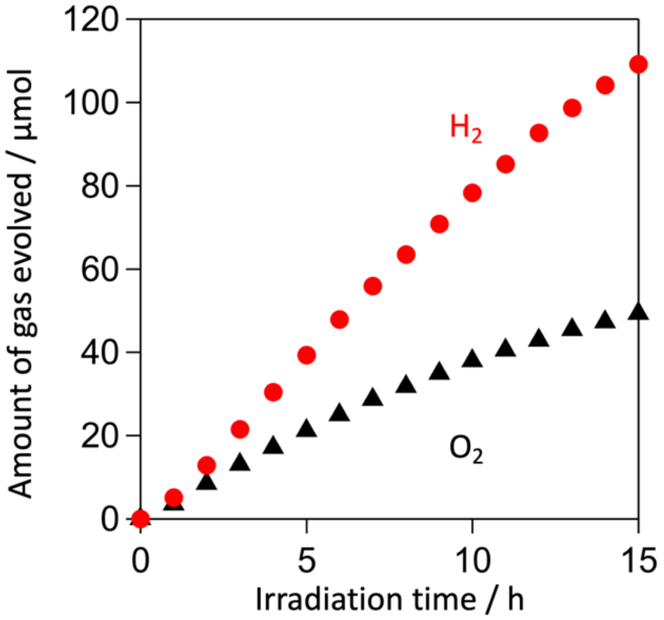

**Figure 6-20.** Time course of $H_2$ and $O_2$ evolution over a mixture of $FeO_x$-$Bi_4TaO_8Cl$ sample (50 mg) and Pt/$SrTiO_3$:Rh (100 mg) in NaI (0.98 mM) and $NaIO_3$ (0.02 mM) aqueous solution (250 mL) at pH 5 under visible light irradiation (λ > 400 nm)

## 2.4. Conclusion

In this study, we demonstrated that $FeO_x$ catalyzes the reduction of multi-electron $IO_3^-$ on the surface of photocatalysts. Based on experimental investigations, such as time-resolved spectroscopy, we elucidated the mechanism of the $IO_3^-$ reduction by $FeO_x$. The redox cycle of ($Fe^{III}/Fe^{II}$) in the loaded $FeO_x$ facilitates both the carrier capture from the photocatalyst and the reduction of the redox mediator. In addition, the loading of $FeO_x$ was effective for other photocatalysts and redox mediators. We believe that the present strategy, modification by $FeO_x$ promoting photocatalytic reactions via its redox cycle ($Fe^{III}/Fe^{II}$), can be widely applied to other photocatalytic systems and other transition metal species. Moreover, various materials containing transition metal cations with tunable redox potentials, such as hexacyanoferrate-based materials[36] and metal-organic frameworks,[37] are potential candidates for such cocatalysts. The present study marks the dawn of earth-abundant cocatalysts applicable to various redox mediators, paving the way for the future of visible-light water splitting.

## 2.5. Reference

(1) Abe, R. Development of a New System for Photocatalytic Water Splitting into $H_2$ and $O_2$ under Visible Light Irradiation. *BCSJ* **2011**, *84*, 1000–1030.

(2) Shaner, M. R.; Atwater, H. A.; Lewis, N. S.; McFarland, E. W. A Comparative Technoeconomic Analysis of Renewable Hydrogen Production Using Solar Energy. *Energy Environ. Sci.* **2016**, *9*, 2354–2371.

(3) Bala Chandran, R.; Breen, S.; Shao, Y.; Ardo, S.; Weber, A. Z. Evaluating Particle-Suspension Reactor Designs for Z-Scheme Solar Water Splitting *via* Transport and Kinetic Modeling. *Energy Environ. Sci.* **2018**, *11*, 115–135.

(4) Takata, T.; Jiang, J.; Sakata, Y.; Nakabayashi, M.; Shibata, N.; Nandal, V.; Seki, K.; Hisatomi, T.; Domen, K. Photocatalytic Water Splitting with a Quantum Efficiency of Almost Unity. *Nature* **2020**, *581*, 411–414.

(5) Ng, B.; Putri, L. K.; Kong, X. Y.; Teh, Y. W.; Pasbakhsh, P.; Chai, S. Z-scheme Photocatalytic Systems for Solar Water Splitting. *Adv. Sci.* **2020**, *7*, 1903171.

(6) Miseki, Y.; Fujiyoshi, S.; Gunji, T.; Sayama, K. Photocatalytic Water Splitting under Visible Light Utilizing $I_3^-/I^-$ and $IO_3^-/I^-$ Redox Mediators by Z-Scheme System Using Surface Treated PtOx/$WO_3$ as $O_2$ Evolution Photocatalyst. *Catal. Sci. Technol.* **2013**, *3*, 1750.

(7) Iwase, Y.; Tomita, O.; Higashi, M.; Nakada, A.; Abe, R. Effective Strategy for Enhancing Z-Scheme Water Splitting with the $IO_3^-/I^-$ Redox Mediator by Using a Visible Light Responsive TaON Photocatalyst Co-Loaded with Independently Optimized Two Different Cocatalysts. *Sustainable Energy Fuels* **2019**, *3*, 1501–1508.

(8) Suzuki, H.; Nitta, S.; Tomita, O.; Higashi, M.; Abe, R. Highly Dispersed $RuO_2$ Hydrates Prepared via Simple Adsorption as Efficient Cocatalysts for Visible-Light-Driven Z-Scheme Water Splitting with an $IO_3^-/I^-$ Redox Mediator. *ACS Catal.* **2017**, *7*, 4336–4343.

(9) Tabata, M.; Maeda, K.; Higashi, M.; Lu, D.; Takata, T.; Abe, R.; Domen, K. Modified $Ta_3N_5$ Powder as a Photocatalyst for $O_2$ Evolution in a Two-Step Water Splitting System with an Iodate/Iodide Shuttle Redox Mediator under Visible Light. *Langmuir* **2010**, *26*, 9161–9165.

(10) Maeda, K.; Abe, R.; Domen, K. Role and Function of Ruthenium Species as Promoters with TaON-Based Photocatalysts for Oxygen Evolution in Two-Step Water Splitting under Visible Light. *J. Phys. Chem. C* **2011**, *115*, 3057–3064.

(11) Higashi, M.; Abe, R.; Ishikawa, A.; Takata, T.; Ohtani, B.; Domen, K. Z-Scheme Overall Water Splitting on Modified-TaON Photocatalysts under Visible Light (Λ<500 Nm). *Chem. Lett.* **2008**, *37*, 138–139.

(12) Nakada, A.; Saeki, A.; Higashi, M.; Kageyama, H.; Abe, R. Two-Step Synthesis of Sillén–Aurivillius Type Oxychlorides to Enhance Their Photocatalytic Activity for Visible-Light-Induced Water Splitting. *J. Mater. Chem. A* **2018**, *6*, 10909–10917.

(13) Konta, R.; Ishii, T.; Kato, H.; Kudo, A. Photocatalytic Activities of Noble Metal Ion Doped $SrTiO_3$ under Visible Light Irradiation. *J. Phys. Chem. B* **2004**, *108*, 8992–8995.

(14) Kudo, A.; Omori, K.; Kato, H. A Novel Aqueous Process for Preparation of Crystal Form-Controlled and Highly Crystalline $BiVO_4$ Powder from Layered Vanadates at Room Temperature and Its Photocatalytic and Photophysical Properties. *J. Am. Chem. Soc.* **1999**, *121*, 11459–11467.

(15) Ogawa, K.; Tomita, O.; Takagi, K.; Nakada, A.; Higashi, M.; Abe, R. Improved Activity of Hydrothermally-Prepared $WO_3$ Photocatalysts by Sodium Salt Additives. *Chem. Lett.* **2018**, *47*, 985–988.

(16) Chen, K.; Chen, X.; Xue, D. Hydrothermal Route to Crystallization of FeOOH Nanorods via $FeCl_3 \cdot 6H_2O$: Effect of $Fe^3$ Concentration on Pseudocapacitance of Iron-Based Materials. *CrystEngComm* **2015**, *17*, 1906–1910.

(17) Yamakata, A.; Kawaguchi, M.; Nishimura, N.; Minegishi, T.; Kubota, J.; Domen, K. Behavior and Energy States of Photogenerated Charge Carriers on Pt- or $CoO_x$-Loaded $LaTiO_2N$ Photocatalysts: Time-Resolved Visible to Mid-Infrared Absorption Study. *J. Phys. Chem. C* **2014**, *118*, 23897–23906.

(18) Clark, S. J.; Segall, M. D.; Pickard, C. J.; Hasnip, P. J.; Probert, M. I. J.; Refson, K.; Payne, M. C. First Principles Methods Using CASTEP. *Z. Kristallogr.* **2005**, *220*, 567–570.

(19) Kunioku, H.; Nakada, A.; Higashi, M.; Tomita, O.; Kageyama, H.; Abe, R. ≈. *Sustainable Energy Fuels* **2018**, *2*, 1474–1480.

(20) Yu, H.; Irie, H.; Shimodaira, Y.; Hosogi, Y.; Kuroda, Y.; Miyauchi, M.; Hashimoto, K.

An Efficient Visible-Light-Sensitive Fe(III)-Grafted $TiO_2$ Photocatalyst. *J. Phys. Chem. C* **2010**, *114*, 16481–16487.

(21) Maeda, K.; Domen, K. Development of Novel Photocatalyst and Cocatalyst Materials for Water Splitting under Visible Light. *BCSJ* **2016**, *89*, 627–648.

(22) Ogawa, K.; Nakada, A.; Suzuki, H.; Tomita, O.; Higashi, M.; Saeki, A.; Kageyama, H.; Abe, R. Flux Synthesis of Layered Oxyhalide $Bi_4NbO_8Cl$ Photocatalyst for Efficient *Z* -Scheme Water Splitting under Visible Light. *ACS Appl. Mater. Interfaces* **2019**, *11*, 5642–5650.

(23) Saeki, A.; Yoshikawa, S.; Tsuji, M.; Koizumi, Y.; Ide, M.; Vijayakumar, C.; Seki, S. A Versatile Approach to Organic Photovoltaics Evaluation Using White Light Pulse and Microwave Conductivity. *J. Am. Chem. Soc.* **2012**, *134*, 19035–19042.

(24) Suzuki, H.; Kanno, S.; Hada, M.; Abe, R.; Saeki, A. Exploring the Relationship between Effective Mass, Transient Photoconductivity, and Photocatalytic Activity of $Sr_xPb_{1-x}BiO_2Cl$($x$ = 0–1) Oxyhalides. *Chem. Mater.* **2020**, *32*, 4166–4173.

(25) Meekins, B. H.; Kamat, P. V. Role of Water Oxidation Catalyst $IrO_2$ in Shuttling Photogenerated Holes across $TiO_2$ Interface. *J. Phys. Chem. Lett.* **2011**, *2*, 2304–2310.

(26) Bahnemann, D.; Henglein, A.; Lilie, J.; Spanhel, L. Flash Photolysis Observation of the Absorption Spectra of Trapped Positive Holes and Electrons in Colloidal Titanium Dioxide. *J. Phys. Chem.* **1984**, *88*, 709–711.

(27) Bahnemann, D. W.; Hilgendorff, M.; Memming, R. Charge Carrier Dynamics at $TiO_2$ Particles: Reactivity of Free and Trapped Holes. *J. Phys. Chem. B* **1997**, *101*, 4265–4275.

(28) Yoshihara, T.; Katoh, R.; Furube, A.; Tamaki, Y.; Murai, M.; Hara, K.; Murata, S.; Arakawa, H.; Tachiya, M. Identification of Reactive Species in Photoexcited Nanocrystalline $TiO_2$ Films by Wide-Wavelength-Range (400−2500 Nm) Transient Absorption Spectroscopy. *J. Phys. Chem. B* **2004**, *108*, 3817–3823.

(29) Tamaki, Y.; Furube, A.; Murai, M.; Hara, K.; Katoh, R.; Tachiya, M. Direct Observation of Reactive Trapped Holes in $TiO_2$ Undergoing Photocatalytic Oxidation of Adsorbed Alcohols: Evaluation of the Reaction Rates and Yields. *J. Am. Chem. Soc.* **2006**, *128*, 416–417.

(30) Pankove, J. I. *Optical Processes in Semiconductors*; New York: Dover Publication, 1975.

(31) Basu, P. K. *Theory of Optical Processes in Semiconductors*; Oxford University Press: New York, 1997.

(32) Fracchia, M.; Visibile, A.; Ahlberg, E.; Vertova, A.; Minguzzi, A.; Ghigna, P.; Rondinini, S. α- and γ-FeOOH: Stability, Reversibility, and Nature of the Active Phase under Hydrogen Evolution. *ACS Appl. Energy Mater.* **2018**, *1*, 1716–1725.

(33) Pourbaix, M. *Atlas of Electrochemical Equilibria in Aqueous Solutions*; National Association of Corrosion Engineers: Houston, Texas, USA, 1974.

(34) Hong, S. J.; Lee, S.; Jang, J. S.; Lee, J. S. Heterojunction $BiVO_4/WO_3$ Electrodes for Enhanced Photoactivity of Water Oxidation. *Energy Environ. Sci.* **2011**, *4*, 1781.

(35) Sasaki, Y.; Iwase, A.; Kato, H.; Kudo, A. The Effect of Co-Catalyst for Z-Scheme Photocatalysis Systems with an $Fe^{3+}/Fe^{2+}$ Electron Mediator on Overall Water Splitting under Visible Light Irradiation. *Journal of Catalysis* **2008**, *259*, 133–137.

(36) Paolella, A.; Faure, C.; Timoshevskii, V.; Marras, S.; Bertoni, G.; Guerfi, A.; Vijh, A.; Armand, M.; Zaghib, K. A Review on Hexacyanoferrate-Based Materials for Energy Storage and Smart Windows: Challenges and Perspectives. *J. Mater. Chem. A* **2017**, *5*, 18919–18932.

(37) Calbo, J.; Golomb, M. J.; Walsh, A. Redox-Active Metal–Organic Frameworks for Energy Conversion and Storage. *J. Mater. Chem. A* **2019**, *7*, 16571–16597.

# *General Conclusion*

In the present thesis, the Sillén–Aurivillius oxyhalide photocatalysts were designed, especially focusing on the exploitation of the wide range of visible-light and efficient utilization of the charge carrier generated in a particulate photocatalyst.

In Chapter 1, the Sillén–Aurivillius oxyioide photocatalyst with a narrow band gap and long lifetime carriers was developed. Although iodine-based semiconductors had been regarded to be unstable under the photocatalytic water splitting condition, the Sillén–Aurivillius oxyioide functions as a photocatalyst for water oxidation. The highly polarizable iodide causes the electrostatic destabilization of O 2p orbitals in perovskite layer and successfully increases the VBM composed of O-2p band without sacrifice of the stability under photoirradiation. The introduction of iodide to the Sillén–Aurivillius oxyhalide with a double-perovskite layer ($n = 2$) also provides longer carrier lifetime, leading to significantly higher quantum efficiency and photocatalytic activity as compared to the Cl/Br counterparts. Chapter 1 demonstrates that the iodine introduction enables both the exploitation of the wide range of visible-light and efficient utilization of the photoexcited carrier of Sillén–Aurivillius oxyhalide.

In Chapter 2, novel three Sillén–Aurivillius oxyiodides were successfully synthesized. These oxyiodides have narrower band gaps and show higher photocatalytic water oxidation activities than their chloride counterparts. In contrast to the case with $n = 2$ in Chapter 1, their CBMs, as well as VBMs, are negatively shifted as compared to the chloride counterparts, enabling the negative shift of the CBM without sacrifice of visible light absorbability and photocatalytic activity of Sillén–Aurivillius oxyhalides. Although, in the previous study, the CBM up shifting of the bismuth based layered oxychloride has been achieved by changing the “intra”-layer interaction of Bi and O, this up shift is accompanied by the breaking the Bi–O bonds, the decreasing photoconductivity, and the widening the band bap, where the photocatalytic activity is significantly deteriorated. In the present case, the change of the “inter”-layer Bi-Bi interaction by iodine introduction was shown to be the origin of the negative shift of the CBM. Chapter 2 not only developed novel three Sillén–Aurivillius oxyiodides photocatalysts but also demonstrated that the interlayer Bi-Bi interaction, which can be changed by replacing chlorine by iodine, is a controlling factor of the electronic structures of Sillén–Aurivillius oxyhalides.

In Chapter 3, the flux synthetic method of a Sillén–Aurivillius oxychloride, $Bi_4NbO_8Cl$, particles is developed. The obtained particles with nanoplate morphology have a larger surface and higher crystal quality than those prepared via the conventional solid-state reaction. The flux synthesis much improves the photoconductivity and thus the photocatalytic activity of $Bi_4NbO_8Cl$. Herein, the elaborated synthesis enables the efficient utilization of the photoexcited carriers in the oxyhalide.

In Chapter 4, the carrier dynamics in the $Bi_4NbO_8Cl$ nanoplate is unveiled and successfully modified to achieve efficient charge separation in a particle. In the pristine $Bi_4NbO_8Cl$, the parallel flow of the electrons and holes, which is typical for layered materials, end in the recombination at the edge of the nanoplate. Depositing Rh cocatalyst at the edges of nanoplates manipulates the carrier flow of layered $Bi_4NbO_8Cl$. The Rh cocatalyst extracts photoexcited light electrons efficiently from the photocatalyst, which then forces the remaining heavy holes to hop perpendicular to the plane with the aid of anisotropic crystal geometry. Herein, the intrinsic but undesirable parallel carrier flow was changed into the orthogonal one, resulting in spatial charge separation and a significant enhancement of the photocatalytic activity. The present work provides a deeper understanding on, and a new insight for charge separation in semiconductor photocatalysts.

In Chapter 5, the charge transfer at the interface of $Bi_4NbO_8Cl$ and Rh cocatalyst is further improved. The chromium oxide between $Bi_4NbO_8Cl$ and Rh selectively transfer the photoexcited electrons in $Bi_4NbO_8Cl$ to the Rh cocatalyst, suppressing the undesirable hole transfer to the cocatalyst, which results in the improved photocatalytic $H^+$ reduction activity. The concept of electron transport layer as employed in the field of solar cells was successfully introduced to the particulate photocatalyst system for selective carrier transfer between photocatalyst and cocatalyst, which resulted in efficient utilization of the photoexcited carrier.

In Chapter 6, earth abundant iron oxide can also be applied to facilitate the charge separation in an oxychloride. The iron oxide loaded on the oxychloride photocatalyst selectively captures photoexcited electrons in the CBM, leaving holes in the VB of the photocatalyst and enhancing the charge separation in the photocatalyst. Moreover, the iron oxide catalyzes the multi-electron reduction of $IO_3^-$ on the surface of the oxychloride, allowing the oxychloride to oxidize water and to reduce $IO_3^-$ under visible light irradiation. Z-scheme water splitting was demonstrated by using the iron oxide loaded oxychloride as a water oxidation photocatalysts, Ru-loaded and Rh-doped $SrTiO_3$ as a $H_2$ evolution photocatalyst, and $IO_3^-/I^-$ redox shuttle. Chapter 6, in combination with Chapter 5, shows transition metal oxide loaded on the Sillén–Aurivillius oxyhalides facilitates the charge separation in the photocatalyst by selectively capturing one of the photoexcited carriers, improving photocatalytic activities.

These strategies developed thorough the present thesis for broadening the absorption range of visible-light (Chapter 1, 2) and efficient utilization of the photoexcited carrier of Sillén–Aurivillius oxyhalide (Chapter 3-6) not only pave the way for the future of the Sillén–Aurivillius photocatalysts but also provide a deeper understanding on, and a new insight for controlling band gap and facilitating charge separation in semiconductor photocatalysts.

# *List of Publication*

## Chapter 1

Ogawa, K.; Suzuki, H.; Zhong, C.; Sakamoto, R.; Tomita, O.; Saeki, A.; Kageyama, H.; Abe, R.
"*Layered Perovskite Oxyiodide with Narrow Band Gap and Long Lifetime Carriers for Water Splitting Photocatalysis*"
*J. Am. Chem. Soc.* **2021**, *143*, 8446–8453.

## Chapter 2

Ogawa, K.; Zhong, C.; Suzuki, H.; Tomita, O.; Kageyama, H.; Abe, R.
"*Tuning of Conduction Band via Inter Layer Interaction in Layered Perovskite Oxyiodide Photocatalys*"
*To be submitted*

## Chapter 3

Ogawa, K.; Nakada, A.; Suzuki, H.; Tomita, O.; Higashi, M.; Saeki, A.; Kageyama, H.; Abe, R.
"*Flux Synthesis of Layered Oxyhalide $Bi_4NbO_8Cl$ Photocatalyst for Efficient Z -Scheme Water Splitting under Visible Light*"
*ACS Appl. Mater. Interfaces* **2019**, *11*, 5642–5650.

## Chapter 4

Ogawa, K.; Sakamoto, R.; Zhong, C.; Suzuki, H.; Kato, K.; Tomita, O.; Nakashima, K.; Yamakata, A.; Tachikawa, T.; Saeki, A.; Kageyama, H.; Abe, R.
"*Manipulation of charge carrier flow in $Bi_4NbO_8Cl$ nanoplate photocatalyst with metal loading*"
*Chem. Sci., doi.org/10.1039/D1SC06054F*

## Chapter 5

Kotani, T.; Ogawa, K. (co-first author); Suzuki, H.; Tomita, O.; Kato, K.; Yamakata, A.; Abe, R.
"*$CrO_x$ layer promoting electron transfer from photocatalyst to noble-metal cocatalysts for efficient charge separation and $H_2$ evolution*"
*To be submitted*

## Chapter 6

Murofushi, K.; Ogawa, K. (co-first author); Suzuki, H.; Sakamoto, R.; Tomita, O.; Kato, K.; Yamakata, A.; Saeki, A.; Abe, R.

"*Earth-Abundant Iron(III) Species Serves as a Cocatalyst Boosting the Multielectron Reduction of* $IO_3^-/I^-$ *Redox Shuttle in Z-Scheme Photocatalytic Water Splitting*"

*J. Mater. Chem. A* **2021**, *9*, 11718–11725.

## *Papers not included in the thesis*

Ogawa, K.; Tomita, O.; Takagi, K.; Nakada, A.; Higashi, M; Abe, R.
"*Improved Activity of Hydrothermally-Prepared $WO_3$ Photocatalysts by Sodium Salt Additives*"
*Chem. Lett.*, **2018**, 47, 985-988.

Nakada, A.; Suzuki, H.; Vequizo, J. J. M.; Ogawa, K.; Higashi, M.; Saeki, A.; Yamakata, A.; Kageyama, H.; Abe, R.
"*Fe/Ru Oxide as a Versatile and Effective Cocatalyst for Boosting Z-Scheme Water-Splitting: Suppressing Undesirable Backward Electron Transfer*"
*ACS Appl. Mater. Interfaces* **2019**, 11, 45606−45611.

Zhong, C.; Mizushima, D.; Hirata, K.; Ishii, Y.; Kurushima, K.; Kato, D.; Nakajima, H.; Mori, S.; Suzuki, H.; Ogawa, K.; Abe, R.; Fukuma, T.; Kageyama, H.
"*Domain observation in the visible-light photocatalyst $Bi_4NbO_8Br$ with the layered perovskite structure*"
*App. Phys. Exp.*, **2020**, 13, 091004.

Ogawa, K.; Wakisaka, Y.; Suzuki, H.; Tomita, O.; Abe, R.
"*Visible-Light-Responsive Oxyhalide PbBiO2Cl Photoelectrode: On-Site Flux Synthesis on a Fluorine-Doped Tin Oxide Electrode*"
*ACS Appl. Mater. Interface* **2021**, 13, 4, 5176–5183.

Ozaki, D.; Suzuki H.; Ogawa, K.; Sakamoto, R.; Inaguma,; Y.; Nakashima, K.; Tomita, O.; Kageyama, H.; Abe, R.
"*Synthesis, band structure and photocatalytic property of Sillén−Aurivillius oxychlorides $BaBi_5Ti_3O_{14}Cl$, $Ba_2Bi_5Ti_4O_{17}Cl$ and $Ba_3Bi_5Ti_5O_{20}Cl$ with triple-, quadruple- and quintuple-perovskite layers*"
*J. Mater. Chem. A*, **2021**, 9, 8332–8340.

Zhong, C.; Kato, D.; Ogawa, K.; Tasel, S.; Izumi, F.; Suzuki, H.; Kawaguchi, S.; Saito, T.; Saeki, A,; Abe, R.; Kageyama, H.
"*$Bi_4AO_6Cl_2$ (A = Ba, Sr, Ca) with double and triple fluorite layers for visible-light water splitting*"
*Inorg. Chem.*, **2021**, 60, 15667–15674

# *Acknowledgement*

The present thesis summarizes my studies conducted during 2016–2022 at Department of Energy Hydrogen Chemistry, Graduate School of Engineering, Kyoto University.

Firstly, I would like to express my sincere gratitude to my supervisor Pro. Ryu Abe for the contentious support and patience during my Ph.D. study and related research. His invaluable guidance and immense knowledge pushed me to sharpen my thinking and brought my work to a higher level.

Besides my advisor, I would like to thank the rest of my thesis committee: Prof. Hiroshi Kageyama and Prof. Koji Fujita, for their insightful comments and encouragement, but also for the hard question which incented me to widen my research from various perspectives.

I would also like to thank Prof. Ryota Sakamoto for his helpful discussion and heartwarming encouragement. My sincere thanks also go to Dr. Osamu Tomita, Dr. Hajime Suzuki, Dr. Akinobu Nakada, Dr. Masanobu Higashi, for their valuable discussion and helpful support. Without their precious support it would not be possible to conduct this research.

I am deeply grateful to Prof. Akinori Saeki for his technical support and advice in the time-resolved microwave conductivity measurement. My sincere thanks also go to Dr. Akira Yamakata, and Dr. Kosaku Kato for the contribution to the time-resolved absorption spectroscopy. I would like to express my sincere gratitude to Dr. Takashi Tachikawa for his help and valuable discussion in single-particle and single-molecule imaging in Chapter 4. My thanks also go to Dr. Kouichi Nakashima and Mr. Takaaki Toriyama for the contribution to the transmission electron microscopy images. I wish to thank Dr. Shunsuke Nozawa and Dr. Tomoki Kanazawa for their technical support in the X-ray Absorption Fine Structure measurements in Chapter 5, 6. I would also like to thank Mr. Chengchao Zhong, Dr. Daichi Kato, and Dr. Daichi Ozaki for useful discussions. I would also like to express my sincere gratitude to Pro. Aron Walsh for his kind support.

I would like to thank all members of Abe laboratory for their kind encouragement, support, and collaboration. Especially, I am deeply grateful to my junior fellows, Mr. Yusuke Wakisaka, Mr. Katsuya Murofushi, Mr. Tetsu Kotani for their assistance and useful discussions. I also thanks Secretary Eri Minoda for her kind support.

Kanta Ogawa
2022